Processing–Structure–Function Relationships in Solid–State Batteries

By

Marm Dixit

Dissertation

Submitted to the Faculty of the

Graduate School of Vanderbilt University

in partial fulfillment of the requirements

for the degree of

DOCTOR OF PHILOSOPHY

in

Mechanical Engineering

December 12, 2020

Nashville, Tennessee

Approved:

Kelsey Hatzell, Ph.D.

Haoxiang Luo, Ph.D.

David Cliffel, Ph.D.

Peter Pintauro, Ph.D.

Douglas Adams, Ph.D.

Dedication

I dedicate this thesis to

Hemendra Dixit and Yogesh Shukla

and

those whom we lost.

Eventually,
I realized that you don't need the trees
for their shadows to linger,
they stay there with us,
in spite of everything.

Acknowledgment

I would like to start this acknowledgement by thanking my advisor, Prof. Kelsey Hatzell for her mentorship and guidance throughout my doctoral journey. The immense faith she showed in me when picking me up as her first PhD student following two brief Skype interviews and through the subsequent years was inspiring and helped me persevere throughout my degree. Her passion and enthusiasm for our work is inspiring as well as contagious. I would like to thank her for the constant support and constructive criticism that she has offered to make me a better researcher. Her drive for excellence in research pursuit has helped me tremendously towards constantly improving myself as a researcher. It is also important to thank Prof. Marta Hatzell for facilitating the first interaction between Prof. Kelsey Hatzell and me. I would also like to thank my dissertation committee: Prof. Douglas Adams, Prof. David Cliffel, Prof. Haoxiang Luo and Prof. Peter Pintauro : who have supported my research through the years by providing excellent inputs, grounding feedback and valuable suggestions.

My deepest gratitude is also to my fellow labmates who have been valuable sources of knowledge and support over the years. Wahid Zaman, the longest standing partner of late-night at synchrotrons, my heartiest thanks for suffering me through the years and providing excellent support and feedback when I needed them. I do hope that all your cells work great under pressure! Dr. Fengyu (Kris) Shen: thanks are due for showing me the ropes in the early days and your help in kickstarting a lot of the projects I have worked on. Brice Harkey, Nicholas Hortance, Yanjie Zheng, Dr. Yuxun Ren: I thank you for sharing your time and expertise with me and for being receptive towards the countless tomography reconstruction sessions and other didactic stuff that I keep doing. And while they were around for a shorter duration, I would also like to acknowledge the support and feedback provided by Matthew Galazzo and Katie Browning over the many discussions we have had. Thanks are also due to the amazing undergraduates with

whom I had the pleasure to work with: Matthew Regala, Nafisa Ibrahim, Stella Vujic, Xinlin Zhong, among others. It was a pleasure working with all of these wonderful folks at Inks and Interfaces Laboratory and it will be missed dearly.

This work would not have been possible without the tremendous help and support offered to me by a large number of collaborators. I would like to thank all the instrument scientists I have worked with over the years for their patience and sharing their expertise with me. Specifically, I would like to thank Jonathan Almer, Jun-Sang Park, Peter Kenesei, Andrew Chuang, Jon Okasinski, Pavel Shevchenko, Xianghui Xiao, Vincent de Andrade for their extensive help in making this thesis possible. The selfless dedication with which they facilitated our experiments and their deep passion for science is inspiring and I am forever grateful to them for sharing this with me. A big shout-out to Timothy Arthur and Nikhilendra Singh from Toyota Research Institute of North America for unreservedly sharing their expertise and for assembling cells way into the night with me. Thanks to Dr. Ankit Verma and Bairav Vishnugopi from Prof. Partha Mukherjee's group for their readiness to work with me and for fielding odd, weird questions about polycrystalline models. A big thanks also to all collaborators at Oak Ridge National Laboratory, Georgia Tech, Purdue University and Lawrence Berkeley National Laboratory.

Next, I would like to thank a group of people who are collectively responsible for making this exertion in the United States a not-so-alienating experience. The Harrogate gang of Abhishek, Anand, Dhrupad, Sai Mani, Rohan, Ruhani, Nisha: who have constantly been around for the last few years whether I wanted them to be or not. Thanks also to occasional partners in crime and remote accomplices: Kushan, Vaishal, Ganesh, Bhumil, Raj and Anuj Bisht. I would have written this entire document twice as faster if it weren't for these wonderful folks but it would not have been half as much fun. Thanks for all the crazy times, the non-crazy times (were there really any?) and everything in between. A lot of this work is owed to these folks but I am owed back equally so we have decided to

call it evens.

A toast of dry Martini is mandated for Jait Dixit (as Nick Charles would have it), who through countless movies and endless discussions over weekends of the past four years helped preserve my sanity. He offered a good ear when I needed it and sage advises (unlike what you would think) when he was in his element. The paths that I walk are clearer for his vision and I am deeply grateful for that. I am not entirely grateful for the earworm thread, though. And while we are talking about movies, I do not think I would have been able to work effectively, if it were not for the very periodic cinematic interludes at the Belcourt Theatre (many of them courtesy FLICx) and the genius of WILTY- so a huge thanks to them for the magic they brought to my life.

I guess, I also need to thank my family for whatever it was, that they did to me - the results seem to be satisfactory. So thanks to everyone back at 237, Manekbaug - I would not have made it this far without knowing who the first cousin of the second daughter of the fifth brother of the neighbour of the friend of the guy whom one of you crossed on the street yesterday is getting married to. Jokes apart though, I do feel lucky to have such an eclectic collection of people to call home. Thanks to Lata Dixit (a.k.a. Lataben) for being an absolute joy and reminding me to get back to India every time I called; to Barin Dixit (a.k.a. bapa) who egged me on through his poetry and (occasionally) extremely well-sung songs; to Gita Dixit (a.k.a. bagita) for correcting my grammar since 1991 and for providing valuable information regarding bollywood musicals; to Mainak Dixit (a.k.a. Kakufoi) for identifying all the auspicious times and for making sure we get wake up on important dates; to Maaz Dixit (a.k.a. Sumi) for sharing the best of new-age bollywood music and for keeping buildings sustainable. Shoutout to Urjita and Ishwar Patel and Ahiri Jain as well for all their support during the whole time here. And as with all good things, we end by this:

GNU Terry Pratchett.

TABLE OF CONTENTS

LIST OF TABLES

LIST OF FIGURES

Chapter 1

Introduction

1.1 Global Warming and Electrification

The Paris Agreement mandates the participating countries to "hold the global average temperature increase well below 2 ° C ...and to pursue efforts to limit the temperature increase to 1.5 °C....to achieve a balance between anthropogenic emissions by sources and removals by sink of greenhouse gases in the second half of this century" (United Nations (2015)). Over the years, anthropogenic contributions to particulate matter emissions, greenhouse gases and other human endeavor has led to a sustained increase in average global temperatures (Schleussner et al. (2016); Jacquet & Jamieson (2016)). Climate change is already causing significant stress on the world's ecosystems, and unless curbed, can lead to unrecoverable damages like rising sea levels, altered weather patterns, differences in geo- and hydro-chemistry which can significantly impact local ecosystems leading to species decline and even extinction (Rogora et al. (2003); Berner & Berner (2012); Harley (2011)). Capturing and mitigating greenhouse gas emissions arising from dangerous anthropogenic interference' (DAI) is crucial to achieve a long-term temperature goal (LTTG) outlined in the Paris agreement (Schleussner et al. (2016); Jacquet & Jamieson (2016)). In this regard, climate change is one of the most complex collective action problems that requires addressal at various levels from policy and law making, economic aspects as well as from a technological viewpoint (Bolsen et al. (2014); Åhman et al. (2017); Huang et al. (2017)). Of this, the chief technological challenges are linked with decarbonization as well as carbon capture and storage (Jackson et al. (2018); Schiffer & Manthiram (2017)).

Almost all the greenhouse gas emissions are a result the energy sector (Jackson et al. (2018)). Transportation accounts for 28% of greenhouse emissions of 2018 of 1869 million metric tons of CO_2 equivalent, followed by electricity generation, and industry in the

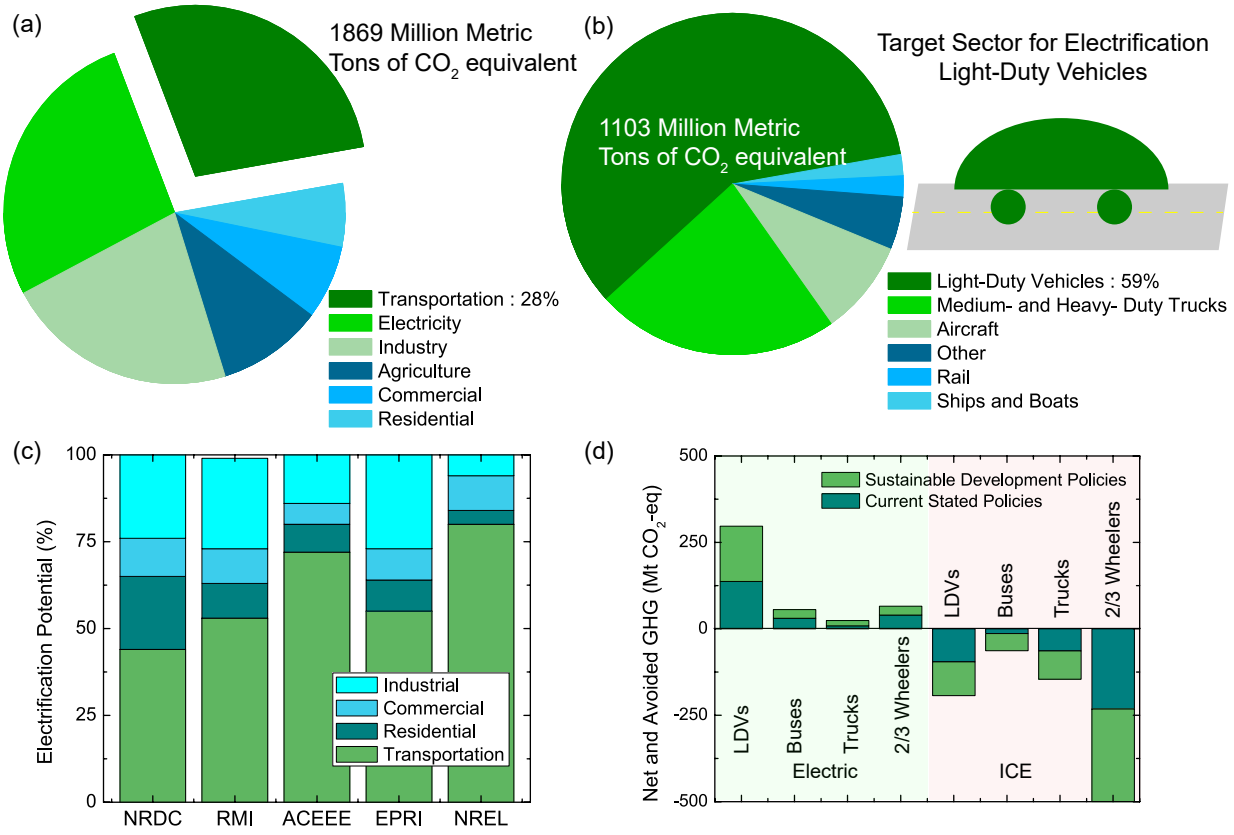

Figure 1.1: (a) Greenhouse gas emissions in the United States in 2018 distribution by sector. Transportation contributed to 28% of total greenhouse gas emissions at 1869 Mt CO_2 eq. (b) Distribution of green house gas emission in transportation sector by vehicle type. Light duty vehicles (LDVs) contribute significantly to the transportation sector GHG emissions with 59% (1103 Mt CO_2 eq.). (c) Agency reports on potential of electrification based on the sectors. Across multiple studies, transportation shows an average electrification potential of 61%. (d) GHG emission saved and emitted in transitioning from internal combustion engines (ICE) to electric vehicles. Data for these graphs were sourced from International Energy Agency (IEA), Environmental Protection Agency (EPA), and American Council for an Energy-Efficient Economy (ACEEE).

United States (Fig. 1.1a, Agency (2020)). Internal combustion engines in light duty vehicles contribute nearly 59% of greenhouse gases emissions from the transportation sector in United State in a year (1103 million metric tons of CO_2 equivalent) (Fig. 1.1b). Primary cause for greenhouse gas emissions across sectors occurs through burning of fossil fuels. Electrification of the transportation sector is crucial in order to achieve the emission goals set in place by the climate change agreement (Needell et al. (2016)). Theoreti-

cal analyses predict a high electrification potential for transportation amongst industrial, commercial, and residential sectors. Typically, such analysis incorporates cost and performance perspectives to understand how the electrification of sectors can affect quantities like greenhouse gas emissions over time. A bottom-up stock taking toolkit for infrastructures that consume, produce, delivers/converts energy is utilized. The average electrification potential for the transportation sector as predicted across modeling forecasts from five agencies (National Renewable Energy Laboratory (NREL), Rocky Mountain Institute (RMI), American Council for an Energy-Efficient Economy (ACEEE), Electric Power Research Institute (EPRI) and Natural Resources Defense Council (NRDC)) is 61% (Fig. 1.1c, Billimoria et al. (2018); Nadel & Ungar (2019); Gowrishankar & Levin (2017); Mai et al. (2018); Howard (2018)). Enabling and implementing sustainable development policies can enhance the reduction in emissions arising from electrification(Fig. 1.1d).

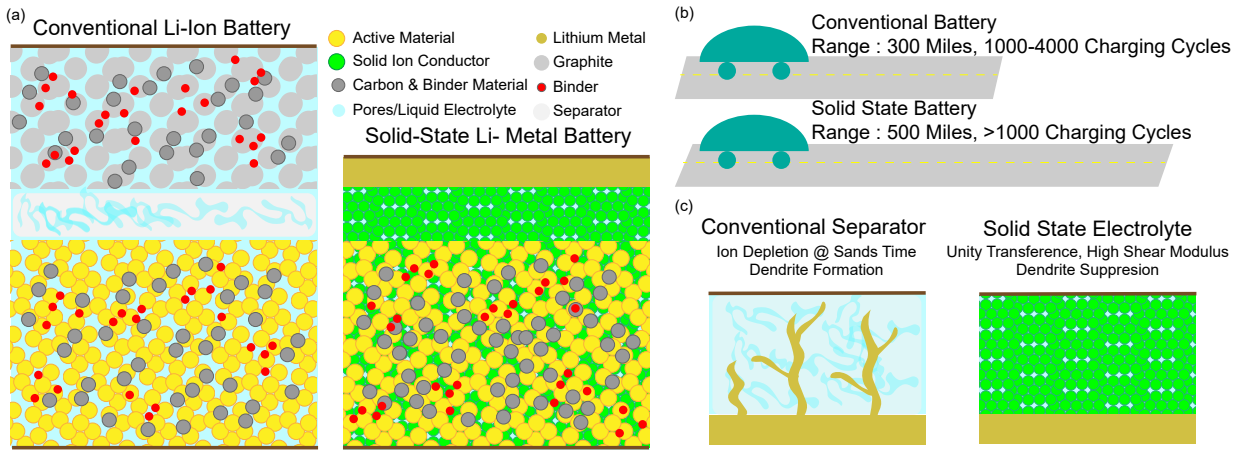

Figure 1.2: (a) Schematic diagram showcasing difference in architectures of conventional Li-ion batteries and solid state batteries. Schematic diagram highlighting differences in (b) range and (c) safety of Li-ion batteries and solid state batteries.

Electric vehicles are primarily classified as following: (a) battery electric vehicles (BEVs), (b) plug-in hybrid electric vehicles (PHEVs), (c) range-extended electric vehicles (REEVs) and (d) PHEV utility vehicles (Thielmann et al. (2013)). Each EV category require specific battery technology in terms of gravimetric and volumetric energy density as well as capacity and rate performance. Adoption of electric-mobility alternatives are contin-

gent on the range offered, durability, charging times and safety. Over the recent years, introduction and diffusion of electric vehicles in the automotive market has steadily increased from around 0.7 million EVs in 2015, to approximately 7 million EVs in 2019 (Mohn (2018)). Current EVs have a battery capacity between 5-95 kWh and ranges up to 300 miles. These EVs employ conventional Li-ion technology which typically employs a (Nickel Manganese Cobalt Oxide) NMC/ (Nickel Manganese Aluminium Oxide) NCA cathode, graphitic anode, and liquid electrolyte (Fig. 1.2a,Løvvik et al. (2019)). DOE's Vehicle Technology Office (VTO) projects 750 Wh/L cell packs (>1000 mAh/g anode, >300 Wh/g cathode, >5 V cell voltage) for next generation electric vehicles (EVs) (Boyd (2018); Howell et al. (2016)). Technology roadmaps emphasize that these next generation energy storage systems will need to leverage high energy density anodes, like Li metal (high theoretical capacity (3860 mAh g^{-1}) and low density (0.54 g cm^{-3}), as well as multivalent cation chemistries to achieve the required performance metrics (longer vehicle range, long life, production costs, safety; Løvvik et al. (2019); Thielmann et al. (2013)). However, lithium metal is incompatible with liquid electrolytes leading to dendrite formation that can cause catastrophic failures of the battery (Fig. 1.2c, Frenck et al. (2019)). Solid electrolytes (SEs) offer a promising route towards realization of these chemistries due to their wide electrochemical stability window as well as propensity to mitigate dendrite formation (Janek & Zeier (2016)). Additionally, high voltage cathodes (S, NCA) can be integrated with solid electrolytes to achieve higher energy densities. To this end, solid-state batteries are envisioned as a key technology for enabling metallic anode resulting in high energy density batteries that can lead to an extended range of EVs coupled with safer operations.

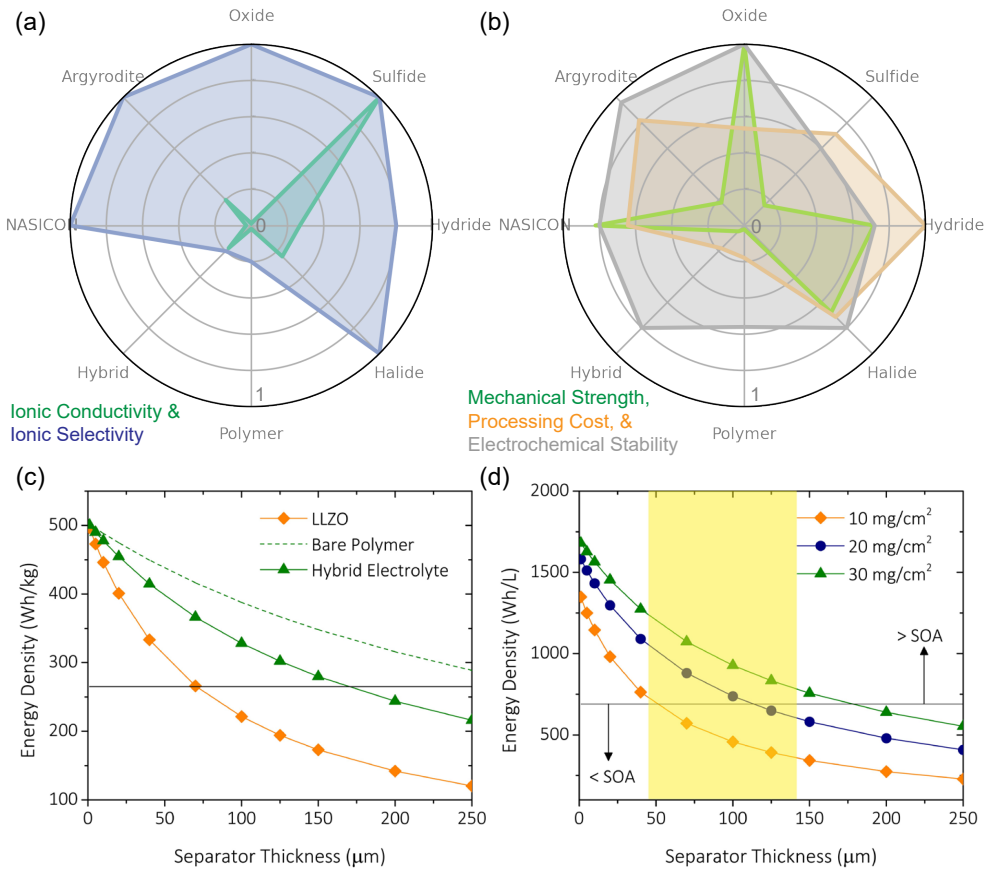

Figure 1.3: (a-b) Radar plot highlighting differences in material properties for key solid electrolyte material alternatives. Note that the ionic conductivity values are on a linear scale thus showcasing a large difference between sulfides and the other material alternatives. All values are normalized to unity for representation. It should be noted that the representation is purely qualitative in nature. (c) Gravimetric energy density calculations for LLZO, polymer and hybrid electrolytes at 10 mg/cm^2 cathode loading. (d) Volumetric energy density calculations for hybrid electrolytes with different cathode loadings. Li metal-NCA chemistry is assumed. Cathode composition is assumed to be 96:2:2 for active material:binder:C. State of the art (SOA) is assumed to be Graphite-NCA based battery system.

1.2 Solid State Batteries

1.2.1 Solid Electrolytes: A Brief Introduction

Conventional Li-ion battery systems have retained their basic architecture and material systems since they were introduced in the 1970s (Fig. 1.2a). These systems use a host material (e.g. graphite anode) to reversibly insert ions (Li+) within their matrix during charging and discharging. Transitioning from a host material to using lithium metal can

lead to almost a 3x increase in energy density extending the range capabilities of end-use systems. However, conventional electrolytes are unstable against lithium metal and can lead to catastrophic failures. All solid-state batteries have gained a lot of traction due to their potential to work with Li metal and high voltage cathode along with inherent safety. ASSBs employ a solid ion conductor that has comparable ion conduction properties, superior ion transference properties and high mechanical strength that can facilitate the use of lithium metal directly. These systems offer potential pathways to achieving high range, durable and safe energy storage systems that can be used for electro-mobility applications in the next decade.

Solid ion conductors are synthesized in a wide range of chemistries (Fig. 1.3a-b, Zheng & Hu (2018)) that are chiefly divided into three different categories (a) organic, (b) inorganic and (c) hybrid. Ionic conductivity of several material families are comparable to conventional liquid electrolyte conductivities. Notably, room temperature conductivity of thio-LISICON type solid electrolyte ($Li_{10}GeP_2S_{12}$) is 1.2 x 10^{-2} S cm^{-1}, with a low activation energy of 0.25 eV (Quartarone & Mustarelli (2011)). Argyrodites, perovskites, sulfides, anti-perovskites, NASICONs and oxides have all shown mS cm^{-1} range ionic conductivities (Famprikis et al. (2019); Fan et al. (2018); Zheng & Hu (2018); Zhang et al. (2018); Keller et al. (2018); Kerman et al. (2017)). Additionally, most inorganic solid ion conductors show very high ion selectivity reflecting a transference number of nearly 1. This nullifies concentration gradients inside the battery and improves the rate performance of the system. In comparison, polymer and hybrid electrolytes show comparably lower ionic conductivity ($\approx 10^{-6}$ S cm^{-1} for polymer and $\approx 10^{-4}$ S cm^{-1} for hybrid) and transference numbers ($\approx$ 0.1-0.5; Keller et al. (2018)). Electrochemical stability is typically higher for solid-state electrolyte (SSEs) due to their chemical affinity to lithium and stability against high voltage cathode material. Garnet oxides are typically most stable against lithium metal, while materials like sulfides and polymers generally undergo reduction reactions against lithium metal. Similarly, oxides are generally more stable against high voltage

cathodes compared to other electrolyte materials. Inorganic solid electrolytes typically have significant processing costs due to multi-step and high temperature processing (Kerman et al. (2017)). Polymer and hybrid type SSEs have lower processing and integration cost due to available commercial benchmarks for polymer manufacturing. Several other characteristics like mechanical properties (Young's modulus, fracture strength), electronic and ionic area specific resistance, thermal stability that dictate the electrochemical performance of the system show differences based on material family (Manthiram et al. (2017)). Garnet type ($A_3B_2(XO_4)_3$) SSEs possess high conductivity and stability against Li-metal electrode (Liu et al. (2018)) and are one of the most promising SSE material system. These ceramics have a shear modulus of >50 GPa, which is significantly larger than the shear modulus of Li metal. Monroe and Newman predicted that a shear modulus exceeding 8.5 GPa is sufficient to inhibit dendrite formation through the electrolyte (Monroe & Newman (2005)). A large series of garnet oxides have been developed as SSE of which one notable composition is $Li_7La_3Zr_2O_{12}$ (LLZO; Tan & Tiwari (2012)). This material exhibits two structures: a low temperature tetragonal symmetry with low ionic conductivity and a high temperature cubic structure which has a high ionic conductivity (Sun et al. (2015)). Aliovalent substitution into this matrix can help stabilize the cubic phase at low temperatures (El-Shinawi et al. (2017)). Limited reaction with lithium metal and relative ease of handling make this an ideal material to undertake fundamental studies.

Design and engineering of solid state batteries are strongly dependent on the material under consideration. To illustrate this, a comparison of theoretical energy density of SSB with polymer, hybrid and garnet oxide- solid electrolyte is carried out (McCloskey (2015)). The garnet ceramic system shows high ionic conductivities and transference numbers. However, to achieve comparable or better performance than state of the art graphite based battery systems extremely compact form factors with thickness ≤ 50 μm need to be achieved (Fig. 1.3c-d). Processing these ceramics with high densities in these form factors at scale is challenging. The hybrid electrolytes have an inferior electrochemical perfor-

mance, but they can be scalably manufactured using existing infrastructure. This makes them an attractive material system for large scale systems. Further, the hybrid electrolytes can be scalably processed for a wide range of thicknesses (50-150 μm) enabling higher performances compared to the state-of-the-art graphite-based battery systems. These calculation highlights the need for holistic development of solid electrolytes from synthesis to device integration is required to achieve high density energy storage systems.

1.2.2 Current Challenges in Solid State Batteries

Material families that can meet ion transport criteria comparable to the state-of-the-art liquid electrolytes are identified for solid ion conductors (Fig. 1.3a-b), but their integration into high-performance battery packs is still far from realization. The primary limitation in this regard is their poor performance which partly arises from side reactions and poor reversibility for which there is a lack of fundamental understanding, specifically at the electrode | electrolyte interfaces. Unfavorable chemo-mechanical behavior at the solid | solid interface leads to non-optimal material utilization and poor ion transport. These phenomena transcend several orders of magnitude in time- and length- scales, are poorly understood (Fig. 1.4). Characterizing and diagnosing these responses are pivotal towards design of high-performance energy storage system. A fundamental understanding of interfacial design with regards to these physical processes is needed to rationally engineer a high performance ASSB in terms of driving range, safety and durability.

Solid-state batteries rely on the ability to work with high energy density anodes (Li metal) to achieve techno-economic feasibility. Specifically, morphology control of Li metal during electrodeposition and electrodissolution at the Li|SE interfaces is imperative in order to achieve high energy density batteries. However, achieving the required performance metrics of $\approx$5 mAh cm^{-2}of reversible cycling capacity at 5 mA cm^{-2} plating current density with high coulombic efficiency is far from realization (Randau et al. (2020)). The primary concern with Li metal is its propensity to form filaments that grow through the

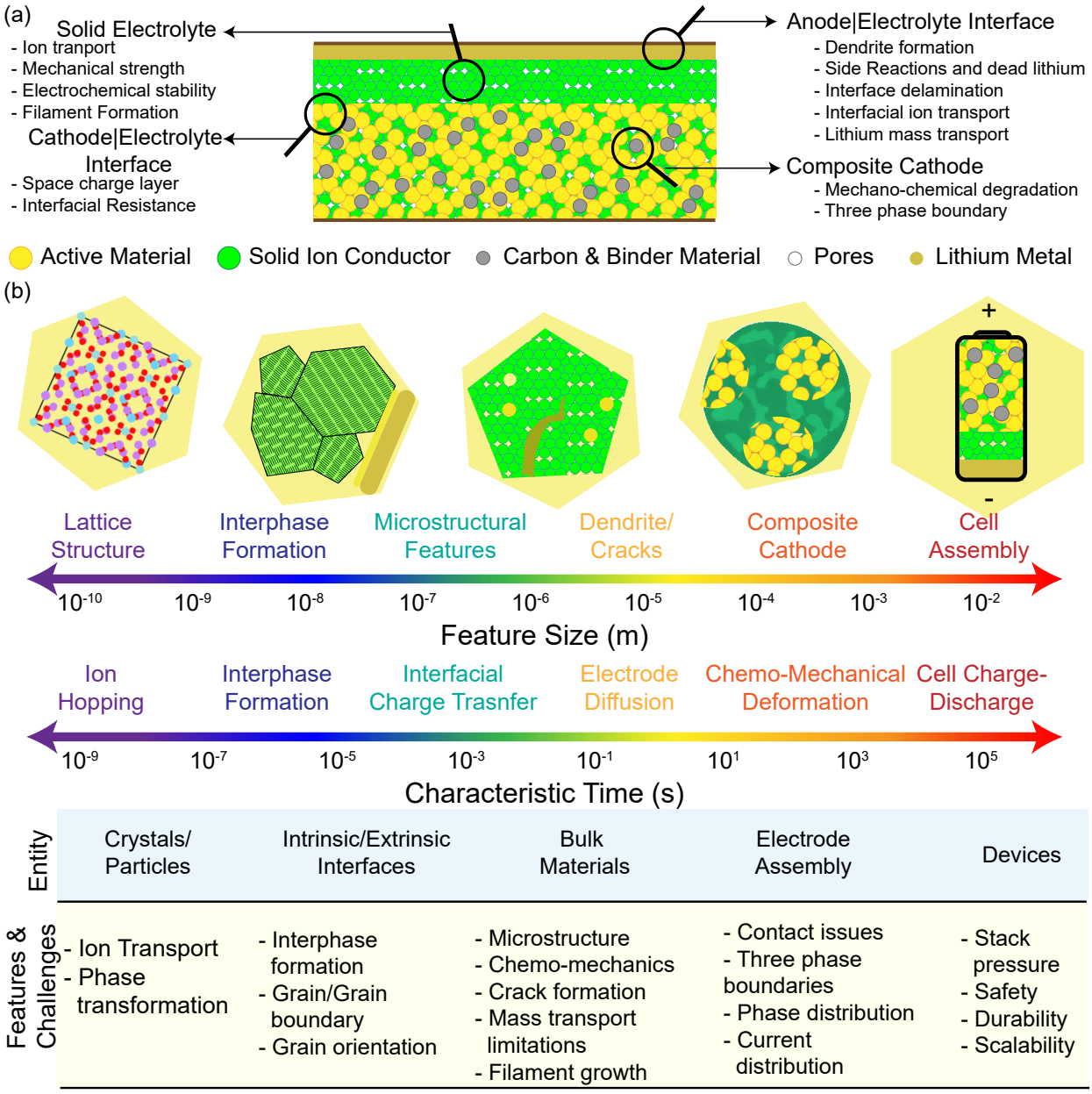

Figure 1.4: (a)Key challenges in solid state batteries outlined w.r.t. the different components of the SSB. (b) Spatial and temporal distribution of the challenges.

electrolyte thickness causing cell failure (Wang et al. (2019); Kasemchainan et al. (2019); Kazyak et al. (2020)). Filament formation can significantly limit the rate performance, power density as well as coulombic efficiencies of the solid state batteries (Hatzell et al. (2020); Sharafi et al. (2016)). In addition to filament formation, side reactions of Li with SE can lead to ionically insulating products, as well as formation of dead lithium, both of

which cause unrecoverable capacity loss (Tippens et al. (2019); Lewis et al. (2019); Singh et al. (2020)). Interfacial kinetics of Li metal with solid electrolyte is still a significant challenge limiting the high rate performance of the SSBs. High rate electrodissolution from the Li metal can lead to formation of pores that can cause onset of failure (Kasemchainan et al. (2019); Spencer Jolly et al. (2020)). Mass transport within the Li metal is also a key challenge and understanding creep and flow behavior of Li is necessary to tune the performance of the system (Wang & Sakamoto (2018); LePage et al. (2019)).

A wide range of solid electrolyte materials are investigated in order to maximize ionic conductivity, transference number and critical current density of the materials (Fan et al. (2018); Lau et al. (2018); Keller et al. (2018)). However, electro-chemo-mechanical degradation of the solid electrolyte still remains one of the key concerns with solid electrolytes (Ma et al. (2018); Lewis et al. (2019)). Operational stresses generated in the system from electrodeposition/dissolution of Li metal (Mistry & Mukherjee (2020b)) and/or with the composite cathode volume modulation (Koerver et al. (2018)) can lead to significant deterioration of the solid electrolyte. Primary concern with solid electrolytes is consistent with the Li metal and concerns filament propagation (Pervez et al. (2019); Ke et al. (2020a); Jana & García (2017); Frenck et al. (2019)). Mechanical strength of the solid electrolytes generally does not counter the propagation stresses of filament and can lead to fracture and catastrophic failure of the material. In general, an improved understanding of ion transport within the solid electrolyte and the chemo-mechanical response to cycling is necessary for high performance systems.

Composite cathodes also offer significant challenges towards realization of high energy density solid state batteries (Tian et al. (2020)). Literature indicates the need for high active material loading cathode (>70 %) with areal capacities of 5 mAh m^{-2} are required (Randau et al. (2020)). Primarily, the composite cathode architecture for the necessary three-phase boundary within the cathode is largely unresolved. In contrast to conven-

tional cathodes, wherein pores are filled with an ionically conducting liquid electrolyte, the composite cathode needs to function with a solid electrolyte with pores acting as ion blocking domains (Dixit et al. (????)). Interfacial transport and kinetics of these solid|solid interfaces are largely unexplored. Integration of high voltage cathode with solid electrolytes can lead to formation of space-charge layers that can impede ion motion through the electrode|electrolyte interfaces. Chemo-mechanical response of a dense composite cathode is still not clear and the impact of operating conditions (stack pressure, temperatures) needs to be ascertained.

Whilst significant work is carried out in the field of solid state batteries in the recent years, several fundamental challenges need to be resolved. Chemo-mechanical response of individual components are largely unresolved. Specifically, stable electrodeposition and electrodissolution of anode and stable cycling of high voltage cathodes are required. Studies that look at end-to-end of the battery production line, from synthesis, processing and integration of battery components in a scalable fashion are needed. The wide range of spatial and temporal physical phenomena underlie these challenges. Understanding and diagnosing these phenomena at these varied time- and length- scales is important to rationally design and engineer high performance solid state batteries. As discussed here, anode and cathode interface transformations and electro-chemo-mechanics there-of signficantly impacts the cell performance, durability as well as safety. Characterization of buried electrode|electrolyte interfaces in solid state batteries is an experimentally challenging task. Physical location of the solid | solid interfaces, relevant spatial and temporal scales for physical phenomena (compared to technique resolutions) as well as the operating environment are the chief obstacles limiting the studies of solid|solid interfaces. Dynamic interfacial tracking of electrode|electrolyte interface as well as interfaces within the same phase (grains, grain boundaries, etc) require the use of sophisticated *ex situ, in situ*, and *operando* characterization tools. Additionally, accessing 'buried' interfaces within the ASSBs require significant effort towards designing systems to access the electro-chemo-

mechanical transformations. Fundamental insights obtained through such characterization techniques can help enable high energy density solid state batteries. The following section provides a brief summary of the key characterization studies of ASSBs divided into sections on electrolyte failure, anode interface and transformations and cathode interface and transformations.

1.3 Literature Review

Most of the chemo-mechanical degradation mechanisms that limit performance of the solid state batteries occur at the electrode|electrolyte interfaces. These solid|solid interfaces are difficult to probe experimentally and are thus referred to as 'buried interfaces'. In order to assess and diagnose the operational chemo-mechanics in solid state batteries, it is imperative for advanced characterization of these buried interfaces. Various characterization techniques are leveraged with respect to the spatial and temporal characteristics of the phenomena they are probing. Additionally, constraints regarding sample geometry and working environments dictate what techniques can be leveraged to study particular phenomena. Over the years, significant advancement has been made in characterizing physical and chemical transformations at solid|solid interfaces (Fig. 1.5a). Characterization of Li|SE interfaces has progressed from optical images to chemical specific imaging with ^{7}Li chemical shift imaging and neutron depth profiling (Hatzell et al. (2020)).

Some of the earliest work on *in situ* observation of filament growth in Li metal systems involved optical cells coupled with microscope and CCD camera to enable simultaneous measurement of concentration gradients and polarization growth (Brissot et al. (1999)). Subsequently, optical/scanning electron microscopy techniques have been extensively used for imaging of the solid state battery systems (Ren et al. (2015); Aguesse et al. (2017); Lewis et al. (2019); Porz et al. (2017); Kazyak et al. (2020)). The optical cell can be used for planar/sectional imaging of the solid state battery and can resolve μm-scale features in the μm scale sharply. Primarily these studies are aimed to provide visual evidence

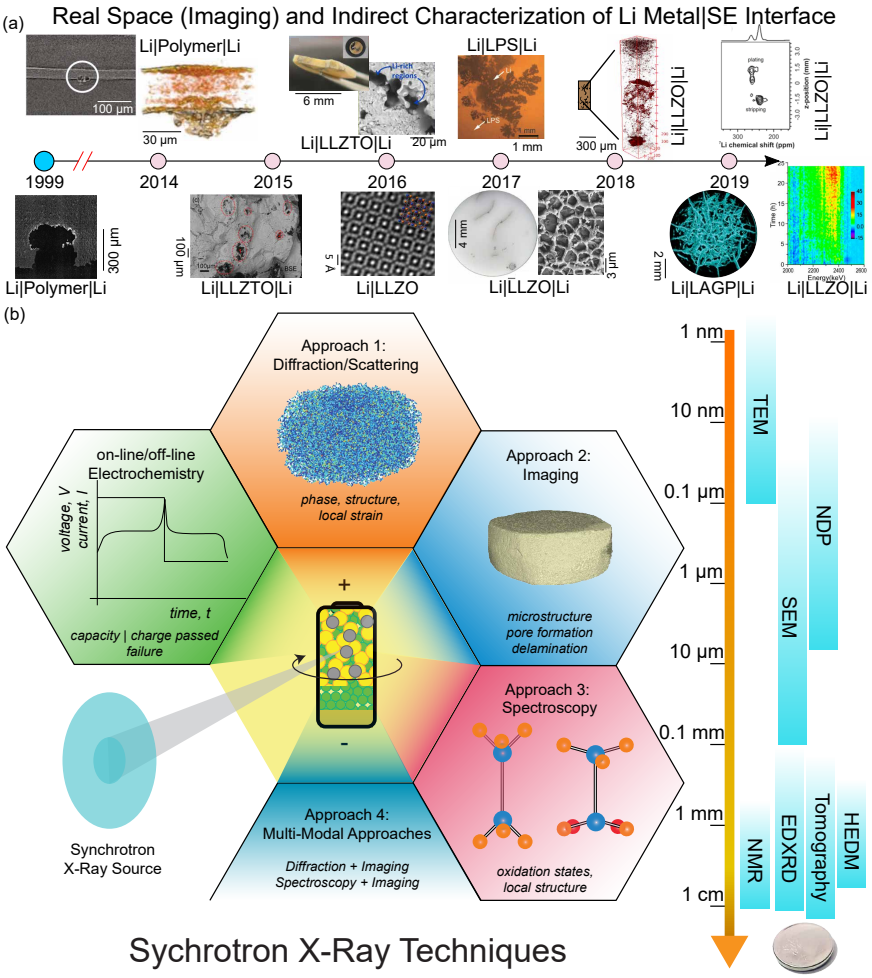

Figure 1.5: (a) Timeline of imaging and characterization of Li-metal | SE interfaces. Optical techniques and X-ray tomography reveal morphology of Li filaments at a polymer SE interfaces. Ex situ scanning electron microscopy revealed subsurface deposition in inorganic electrolytes. Transmission electron microscopy experiments reveal structural transformation at LLZO interfaces in contact with Li metal. Optical techniques demonstrate dendritic growth of -Li_3PS_5 polycrystals . Lithium metal extruding out of intergranular regions in LLZO and microstructural representation of Li metal forming in pores from X-ray tomography experiments. Large mechanical fracture of LAGP solid electrolyte and evidence of lithium penetration across a LLZO electrolyte imaged with NMR. Neutron depth profiling enabling tracking of lithium at subsurface regions in a SE. Figures are reproduced from Brissot et al. (1999); Harry et al. (2014); Porz et al. (2017); Shen et al. (2018); Tippens et al. (2019); Aguesse et al. (2017); Marbella et al. (2019); Wang et al. (2017); Ren et al. (2015); Cheng et al. (2017b). (b) Schematic diagram showcasing accessible length scales by key characterization techniques for solid state battery characterization as well as the key synchrotron techniques.

for filament growth within the system and no other information is accessed (Ren et al. (2015); Aguesse et al. (2017); Lewis et al. (2019); Porz et al. (2017)). Additionally, synchronizing electrochemical signatures during cycling to *operando* optical microscopy can provide insights into growth and morphology of Li filaments (Fig. 1.6d,Kazyak et al. (2020)). Specifically, three different morphologies of Li filaments, reversibility as well as onset mechanisms are identified based on the *operando* results. Optical cells are generally easier to construct and are economical. However, optical studies require the material to be transparent/translucent in the visible light spectrum which is not always possible. Nanometer and atomic level investigations are pursued by transmission electron microscopy (Ma et al. (2016)). TEM, SEM, and optical microscopy cover a wide range of spatial length scales from atomic to macroscopic. The access to these instruments is readily and economically available making them ideal tools for characterization. Coupling of SEM with tools like energy dispersive spectroscopy (EDS; Cheng et al. (2014)) and focused ion beam milling (FIB; Ebner et al. (2013)) can provide additional elemental and three dimensional information regarding the sample. However, the latter is a destructive technique and cannot be employed for *in situ* or *operando* tests. TEM can also be coupled with EDS as well as other analytical tools like selected area electron diffraction (SAED; Chen et al. (2020)) or electron energy loss spectroscopy (EELS; Wang et al. (2016)) that can provide additional information about structure and chemical moieties of the sample over and above the morphological information. The key challenge with microscopy studies is developing a technique compatible with an *operando* solid state battery cell. Planar and sectional batteries, as well as, particle-scale electrochemical cells are investigated with optical as well as scanning electron microscopy. *In situ* and *operando* studies on TEM are carried out on thin film batteries as well as using custom built biasing cells. Adequate care needs to be taken in design of ASSB systems for microscopy studies to ensure that the field profiles in the *in situ* cells resemble the anticipated field patterns in a laminar battery cell. Edge and surface effects at the electrode|SE interface can significantly alter the local

field configurations dictating the observed electrochemical performance. Neutron depth profiling has seen tremendous use in the solid state battery community recently (Whitney et al. (2009); Oudenhoven et al. (2011)). Thermal neutrons are bombarded on a planar sample, and the charged particles emitting from the interaction of neutron with ^{6}Li (α and ^{3}He) are detected and energy discriminated. Between production and detection, the emitted charge particles lose energy due to interaction with the sample. Sample knowledge and stopping power can be used to computationally obtain depth profile density with the obtained energy spectrum with nm precision. However, there are limited number of thermal neutron sources with end-stations capable of NDP measurements making this technique harder to pursue. Additionally, no in-plane information regarding Li distribution can be ascertained from this method. Nuclear magnetic resonance is a non-destructive technique that is extensively used in battery research to provide quantitative chemical species identification, and information regarding local symmetry, electric field gradients, interatomic distances and atomic connectivity (Pecher et al. (2017); Wiemers-Meyer et al. (2019)). NMR experiments can also be extended to 2D maps allowing to assess metallic lithium growth within the solid electrolyte (Marbella et al. (2019)).

X-rays interact with materials proportionally to the electron cloud density resulting in minimal interaction with low Z- elements and strong interactions with high Z- elements (Willmott (2011)). Depending on the sample configuration and X-ray energy, photons can either be transmitted, absorbed or scattered by the probed material. This results in three typical configurations of X-ray experiments: (i) imaging, (ii) scattering, and (iii) spectroscopy (Fig. 1.5b, Lin et al. (2017)). Traditional X-ray imaging typically leverages absorption and phase contrast mechanisms to enable reconstructions of three dimensional structures of the probed material (Leahy et al. (2009)). Depending on the X-ray energy, flux and optics: resolution from μmShen et al. (2018) to nm range (Dixit et al. (2020); Zaman et al. (2019)) can be obtained. Leveraging energy selection facilities available at synchrotrons (monochromator) allows to carry out absorption edge- or XANES imaging

that can provide elemental information in addition to the morphological information obtained from X-ray imaging (Kimura et al. (2020)). Scattering methods typically probe materials and yield structural information in reciprocal space. X-ray diffraction is a scattering technique that probes the Bragg reflection peaks for ordered, crystalline materials within the system and provides information regarding structure and phase of the material investigated (Li & Johnson (2019)). XRD at synchrotrons can provide spatially and temporally resolved information within the samples (Paxton et al. (2015)). Diffraction tomography can also be leveraged to assess three dimensional phase distribution within the investigated materials (Finegan et al. (2020)). X-ray spectroscopy is widely used to investigate the local coordination environment of materials using absorption, florescence or photoelectron spectroscopy (Kirshenbaum et al. (2015); Matsuyama et al. (2016); Freiberg et al. (2018); Bak et al. (2018)). Hard x-ray spectroscopy is typically preferred for heavier elements with absorption edges > 5 keV while soft and tender X-rays are used for lighter elements (Bak et al. (2018)). By studying the signal from the sample emanating few eV below absorption edge to approximately 50 eV above (XANES) insight into oxidation state, site symmetry and bond strength. While signals from 50 ev to 1 keV above the absorption edge (EXAFS) can provide information regarding short-range local structure, coordination number, bond distances and nearest neighbor atom identities. XPS, similarly can provide insight into surface composition, near surface variation composition, and oxidation state (Shutthanandan et al. (2019)). While some soft X-ray spectroscopy requires UHV conditions, there is a potential for studying materials in near ambient conditions with a variety of environments with ambient pressure XPS (Lu et al. (2012)).

Hitherto, key characterization techniques that are leveraged in understanding and diagnosing the chemo-mechanical deformations in solid state electrolytes are described briefly. In the following subsections, key results that discuss electrolyte failure, anode transformations and Li|SE interface, as well as composite cathode and operational chemo-mechanics are discussed.

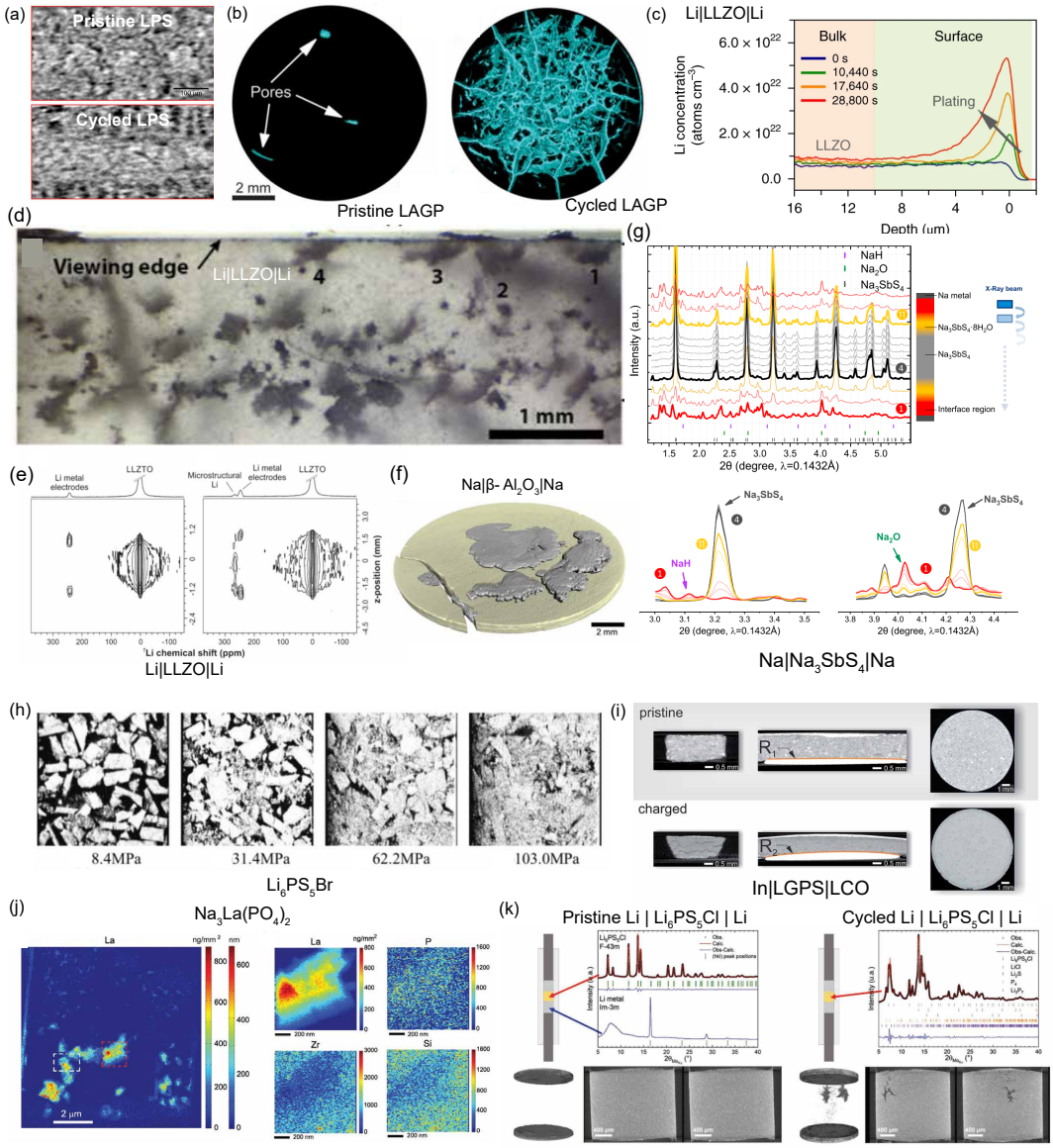

Figure 1.6: Summary of solid electrolyte chemo-mechanical degradation investigations. (a) Cycled LPS shows higher concentration of X-ray transparent regions (Seitzman et al. (2018)) (b) Radial and circumferential crack generation in LAGP solid electrolytes (Tippens et al. (2019)). (c) Isolated Li deposition in bulk LLZO evidenced by NDP (Han et al. (2019)). (d) Filament growth in symmetric Li|LLZO|Li cells (Kazyak et al. (2020)). (e) Metallic lithium growth in LLZO evidenced by ^{7}Li chemical shift imaging (Marbella et al. (2019)). (f) Crack formation in Na β-alumina observed by XRT (Haas et al. (2019)). (g) Hydration of Na_3SbS_4 characterized by spatially resolved X-ray diffraction Tian et al. (2019). (h) Impact of pressure on Li_6PS_5Br electrolyte microstructure (Kodama et al. (2020)). (i) Effect of cycling on structural integrity of LGPS solid electrolyte evaluated by XRT (Zhang et al. (2017a)). (j) TXM-XANES maps of self-forming NASICON solid electrolyte (Zhang et al. (2017a)). (k) XRT and diffraction study of impact of high pressure cycling on structure of Li_6PS_5Cl (Doux et al. (2020)).

1.3.1 Solid Electrolyte Failure

Stresses coupled with volume changes of electrodes can lead to mechanical degradation in solid electrolytes (Fig. 1.6). Significant studies have focused on characterizing the bulk microstructural changes in the solid electrolyte in response to electrochemical cycling. X-ray tomography is a powerful tool that is extensively used to investigate microstructural transformations in bulk solid electrolyte. Li|LPS system was studied using XRT to assess the morphological changes in the anode as well solid electrolyte (Fig. 1.6a,Seitzman et al. (2018)). Comparison of cross sectional images from the reconstructions at different cycles showed a decreasing thickness of lithium foil. Pristine cell showed Li thickness of 100 μm which reduced to 10-15 μm on the first cycle and was indistinguishable from LPS for subsequent cycles. Lithium insertion into the porous electrolyte matrix is proposed to modify the LPS material significantly giving rise to an increased concentration of dark gray, rounded features (lower density) at the Li|LPS interface compared to the pristine cell. *Operando* imaging further showcases monotonic increase of dark features identified as grain boundaries of LPS. The monotonic increase of the line features is proposed to be an evidence of growth of Li features within the LPS layer and propagation of the cracks in the LPS solid electrolyte. Lower beam energies used for this study, coupled with significant X-ray scattering limit the extraction of physical descriptors (porosity, tortuosity) of the Li|LPS cell. This study showcases morphological changes occurring both in the Li metal as well as solid electrolyte during electrochemical operation. Similar study was carried out on Li|LAGP|Li system (Fig. 1.6b,Tippens et al. (2019)), Na|Na- β alumina|Na (Fig. 1.6f, Haas et al. (2019)), In|$Li_{10}GeP_2S_{12}$|$LiCoO_2$ (Fig. 1.6i, Zhang et al. (2017a)) and Li|Li_6PS_5Cl|Li (Fig. 1.6k,Doux et al. (2020)). An extensive crack network growth was observed in the cell extending through the thickness of the LAGP pellet (Tippens et al. (2019)). Distinct circumferential and radial cracks were observed in the LAGP pellet with the circumferential cracks forming at the outer perimeter of the pellet while radial cracks focused at the center of the pellet. The crack volume is found to correlate with the cell

impedance with impedance rising from approximately 2.81 kΩ cm^{-2} to 256 kΩ cm^{-2}. The authors indicate that mechanical fracture can be the source of the electrochemical failure of the cell. Fracture initiation was linked to the edges of the Li|LAGP contact area which was evidenced from the tomography reconstructions as well as simulations. Overall, the results indicated that the structure and morphology of the Li metal driven interphase formation dictated failure in LAGP. In addition to interphase morphology, solid electrolyte microstructure can also influence cell degradation. A large crack in the Na- β alumina SE was proposed to act like a nucleation site for Na dendrite formation and eventual short-circuiting and failure of cell (Haas et al. (2019)). Crack formation was assumed to occur due to electrochemical stress arising from electrodeposition/electrodissolution of Na at the interface. Synchrotron radiography over long-term plating/stripping show electrode thickness change and SE displacement consistent to the amount of Na cycled (Zhang et al. (2017a)).A tilt in the SE is observed that is anticipated to lead to stress generation in case of long-term stripping/plating due to uneven contact with the cell housing. Tomography results showed a densification of the $Li_{10}GeP_2S_{12}$ solid electrolyte during charging consistent with the pressure changes measured for the cell. The porosity of the solid electrolyte decreases from 5.5% for the pristine sample to 2.6% after cycling. Measured height fluctuations of the cell are consistent with the densification mechanism with a significant asymmetric change in cell height observed in the initial cycles. In addition, the charged cell shows a significant bending indicating a strong pressure build up at the electrode|electrolyte interfaces. The cells are assembled in absence of stack pressure and thus reflect the change in the shape of the cell reflects the mechanical forces acting on the cell during charging. The solid state battery showed bending towards the cathode side due to higher volume expansion at the anode. Further, cracking of the SE was observed at the edges of the charged cell. For Li_6PS_5Cl, tomography measurements show the presence of low density region within the bulk solid electrolyte consistent with dendrite formationDoux et al. (2020).

Ex-situ imaging of solid electrolytes can also provide relevant information. High pressure, laboratory *in situ* XRT study of Li_6PS_5Br solid electrolyte was carried out to elucidate the influence of microstructure on ion transport properties of the solid electrolyte (Fig. 1.6h, Kodama et al. (2020)). Ionic conductivity of LPSBr increased from $\approx$ 0.2 mS cm^{-1} to $\approx$ 0.8 mS cm^{-1} on increasing the pressure from 10 to 100 MPa. XRT images showed porosity decreased while the particle|particle contact increased on increasing the pressure from 8.4 to 100.3 MPa. Densification of the solid electrolyte measured by the decreasing thickness of the electrolyte showed a non-linear behavior with strain increasing rapidly between 0-30 MPa, but more slowly between 30-100 MPa. Mechanical breakdown of the LPSBr particles is expected at 25 GPa (Young's Modulus) which accounts for the large increase in strain. The results highlight the influence of microstructure on ion transport properties of solid electrolytes.

Neutron depth profiling has been extensively employed to understand distribution of low Z- element, specifically Li in solid state batteries. Monte carlo simulation models in combination with NDP energy profiles are used to generate Li concentration depth profiles to generate further insight into the battery mechanisms (Danilov et al. (2020)). Validation of the proposed methodology on available data enables identification of Li accumulation in the $LiPO_4$ (LPO) electrolyte as the origin of aging mechanism in thin film ASSBs. This mechanistic origin identified by combining MC models with the measured energy profiles correlates very well with the electrochemical results. Li enrichment zone at garnet surface and adjacent depletion zones are identified in LLZO garnets undergoing ALD coating of Al_2O_3 by NDP (Han et al. (2017)). Surface Li reaction with ALD precursor trimethyl alumina (TMA) and water generate a Li-Al-O layer adjacent to the Al_2O_3 layer which is observed as a sub-nm region in SAEED images. Al_2O_3 coated LLZO is shown to contain higher concentration of Li in the surface region compared to bare LLZO. Li loss in LLZO due to high-speed thermal pulse treatment process was identified by NDP(Wang et al. (2019)). NDP identified surface loss of Li on the high temperature pulse to be 1.59$\pm$0.14%

and no change to the bulk composition. Lithium deposition in bulk solid electrolytes was investigated by time resolved, *operando* NDP (Fig. 1.6c,Han et al. (2019)). LCO|LiPON|Cu, Li|LLZO|Cu and Li|LPS|Cu are investigated. LiPON sample did not show any shorting behavior while LLZO sample shorted at 1.06 mA cm^{-2} after a cumulative charge of 4.6 mAh cm^{-2} (23 μm) and LPS sample shorted at 2 mA cm^{-2} after a cumulative charge of 1.2 mAh cm^{-2} (6 μm). *Operando* visualization of NDP energy profiles indicate nucleation and growth of Li dendrites inside LLZO and Li_3PS_4. High electronic conductivity of these materials is identified as the cause of lithium deposition in the SEs. Chemical shift imaging show dense Li microstructures grow into electrolyte prior to apparent electrochemical signature of shorting as well as metallic lithium growth into the electrolyte at current densities lower than the critical current densities suggesting it is a continuous process (Fig. 1.6e,Marbella et al. (2019)).

Ex situ spatially resolved XRD was carried out for Na|Na_3SbS_4|Na cells to characterize the Na|SE interface (Fig. 1.6g, Tian et al. (2019)). The work investigated the influence of hydration of Na_3SbS_4 solid electrolytes and its impact on stabilization of the Na|SE interface. XRD results show presence of decompsition products like NaH, Na_2O as well as $Na_3SbS_4.8H_2O$ in the layers closest to Na metal. Layers further in the bulk of the sample shows presence of combination of the hydrated solid electrolyte with pristine Na_3SbS_4 and only the pristine solid electrolyte is found in the bulk. Hydrated solid electrolyte mitigates degradation of the Na metal anode against the Na_3SbS_4 solid electrolyte. Further, presence of Na metal was validated highlighting the protection of Na metal by hydration of the electrolyte. Similar study with coupled, *ex situ* XRT and diffraction measurements of pristine and cycled Li|Li_6PS_5Cl|Li cells was carried out to assess the impact of high pressure cycling to the phase as well as the microstructure to the solid electrolyte (Fig. 1.6k,Doux et al. (2020)). Diffraction from the pristine bulk solid electrolyte shows only the presence of Li_6PS_5Cl while the cycled sample shows evidence of presence of numerous phases like LiCl, Li_2S, and reduced phosphorous species. Li dendrite growth through

the solid electrolyte bulk introduces fresh Li|SE interfaces where SEI generation can lead to formation of decomposition products identified by the XRD results. Additionally, the impact of pressure on the performance of Li|Li_6PS_5Cl|Li cells is investigated. High stack pressures > 25 MPa were shown to accelerate failure due to Li creep through electrolyte pores. An optimal stack pressure of 5 MPa was identified for the Li|Li_6PS_5Cl| (Lithium Niobate) LNO-coated NCA system that enabled long-term cycling with 80.9% retention at 100 cycles.

TXM-XANES imaging was used to determine the elemental distribution of self-forming $Na_{1+n}Zr_2Si_nP_{3-n}O_{12}$ ($0 \leq n \leq 3$) NASICON electrolyte (Fig. 1.6j, Zhang et al. (2017a)). La addition to NASICON-type $Na_{1+n}Zr_2Si_nP_{3-n}O_{12}$ ($0 \leq n \leq 3$), can improve ionic conductivity of NASICONs by inducing a concentration variation of mobile ions in the pristine phase, enhancing the density of the composite electrolyte and by creating faster grain boundary conduction pathways. TXM images of the two-phase solid electrolyte showed a heterogeneous distribution of the secondary phase ($Na_3La(PO_4)_2$) with considerable size disparity. La, P, Zr and Si elemental mapping was also carried out over smaller subvolumes which showed a correlation of La distribution with the P distribution spatially. This indicates a higher concentration of P in the secondary phase which is consistent with the anticipated stoichiometry of the secondary phase. Zr and Si spatial distributions are anti-correlated with the La and P distributions confirming that Zr and Si both belong to the primary phase.

1.3.2 Anode| Solid Electrolyte Interface and Anode Transformations

Controlling the morphology of electrodeposited and electrodissoluted metallic anode is crucial to achieving high coulombic efficiency batteries. Inherent interfacial resistance, slow kinetics as well as chemical decomposition at the SE|anode interface leads to non-uniform electrodeposition of Li metal. Significant work is carried out on ameliorating interfacial resistance by active (interlayer coating, surface preparation) and passive ap-

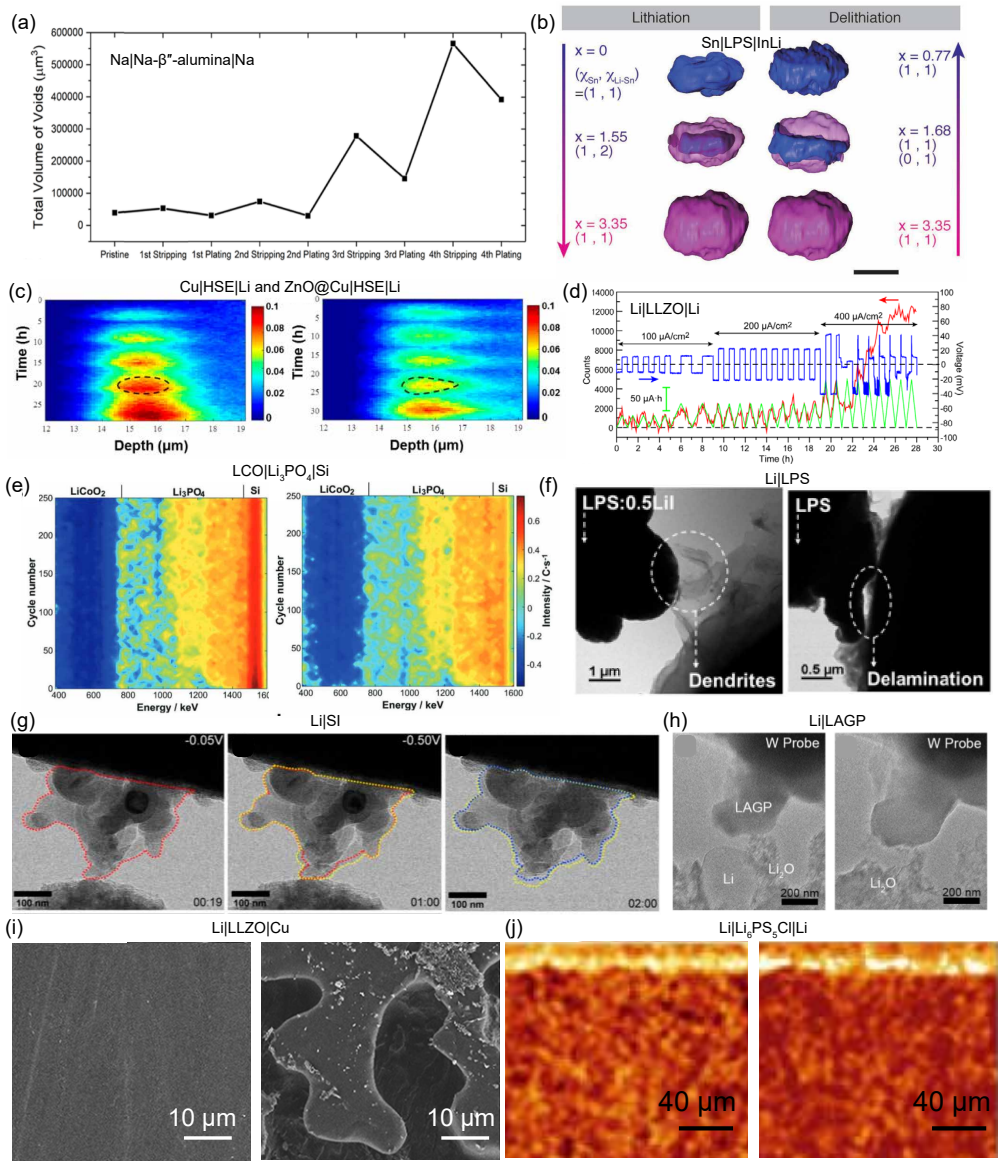

Figure 1.7: Summary of investigations on anode|SE interface and anode transformations. (a) Porosity in Na electrode during cycling measured by synchrotron XRT (Spencer Jolly et al. (2020)). (b) Sn structure transformation and oxidation state measured during electrochemical cycling by TXM-XANES (Wu et al. (2019)). *Operando* NDP studies investigating Li plating in (c) Cu|HSE|Li (Liu et al. (2020)), (d) Li|LLZO|Li (Wang et al. (2017)) and (e) $LiCoO_2$|Li_3PO_4|Si Chen et al. (2018). *In situ* TEM studies on (f) LPS|Li (Singh2020), (g) Si|Li (Basak et al. (2020)) and (h) Li|LAGP (Lewis et al. (2019))systems. (i) Transformation in Li metal anode observed by *ex situ* SEM (Krauskopf et al. (2019)) for Li|LLZO|Li and XRT (Kasemchainan et al. (2019)) for Li|Li_6PS_5Cl|Li.

proaches (doping). Polishing in inert atmospheres (garnet oxides) Sharafi et al. (2017), ALD coating of Al_2O_3 (garnet oxides, Han et al. (2017)) and Si coating have been re-

ported to mitigate this issue (garnet oxides, Luo et al. (2016)). LLZO is reactive with H_2O and CO_2 on exposure to atmosphere affecting their ionic conductivities as well as interfacial resistance against Li metal (Cheng et al. (2015); Sharafi et al. (2017); Cheng et al. (2014); Wang & Sakamoto (2018)). LiF addition to LLZO prior to sintering can inhibit these parasitic reactions (Li et al. (2017)). Engineering electrolyte microstructure and electrode|electrolyte interface is crucial for achieving high rate-performance systems. This requires understanding the underlying ion transport and failure mechanisms associated with the anode|SE interfaces.

Morphological changes in composite Sn anode material in $InLi_x$|LPS|Sn solid state battery were tracked using *operando* synchrotron TXM studies (Fig. 1.7b, Wu et al. (2019)). The solid-state battery was charged and discharged between 2 and 0.1 V. A strong correlation in the observed lateral strain in the working electrode is observed compared to the theoretical expansion of equivalent quantity of Sn. This indicated a strong influence of volume change of active material on macroscopic deformations of the electrode. Morphological evolution of the active material showed a strong spatial heterogeneity with the Z- axis showing preferential expansion (up to 90 %) compared to X- or Y- directions (approximately 10%). The preferential expansion might arise from cell constraints as well as electrode aspect ratio. Topological analysis of Sn particles indicated a core-shell evolution of the lithiation process. Furthermore, a reaction gradient is observed in the electrode with Sn particles near the separator showing higher concentration of Li-Sn, while those at the current collector remain almost inactive. Horizontal (XY- plane) and shell voids were observed in the working electrode that showed a cyclic behavior during cycling. Lithiation caused an increase in the crack density, while delithiation caused the cracks to disappear. Horizontal cracking is proposed to occur due to z- oriented expansion of the active material, while the shell voids occur due to non-reversible morphological changes to the Sn particles. Na|Na β-Al_2O_3 interface was characterized using *operando* lab-scale XRT measurements (Fig. 1.7a,Spencer Jolly et al. (2020)). Na metal anode showed poros-

ity at the pristine interface in the tomography scans. Void number density as well as sizes increases during stripping while a complementary behavior is observed during plating. The interfacial contact between Na and SE shows a consistent decrease with increasing cycles with the total void volume showing a system increase during cycling. In addition, pore size distribution during cycling shows persistence of smaller pores even during plating cycles which suggests a partial filling of larger pores during the electrodeposition step. Persistence of the smaller pores indicate the mechanism for void growth and accumulation at the interface during cycling. Loss of active contact area of Na | SE can lead to increased local current density that can cause filament formation and cell short. These results highlight the morphological variations in anode|SE interface and its impact on failure mechanisms.

Similarly, impact of ZnO ALD layers on lithium metal electrodeposition stability on copper with a PEO-LAGP based hybrid solid electrolyte (HSE) was investigated by NDP (Fig. 1.7c,Liu et al. (2020)). *Operando* NDP results show a that for the bare copper current collector, the average Li density, as well as the thickness of the deposits, rapidly increase upon cycling, reflecting buildup of inactive lithium- metal and Li-species at the HSE side. Introduction of ZnO layer on the current collector, results in improved affinity between the Li metal with the ZnO-covered current collector leading to a reduced accumulation of dead Li metal deposits. Additionally, integration of the observed density profiles allows for calculating plating/stripping efficiency which is approximately 45% for Cu current collector and 80% for ZnO@Cu current collector. Similar measurements to investigate electrodeposition stability at anode interfaces were carried out to understand plating/stripping behavior of Li in solid state battery working with Ti and carbon nanotube interlayers in Li|LLZO|Li (Li & Johnson (2019); Wang et al. (2017), Fig. 1.7d) as well as for LCO|Li_3PO_4|Si thin film batteries (Fig. 1.7e,Chen et al. (2018)). Ti|LLZTO|Li cell was cycled up to a cummulative charge passed of 600 μAh (Li & Johnson (2019)). NDP energy profiles as well as fitting results suggests Li preferentially deposits within

the holes of the patterned Ti electrode as opposed to the Ti|SE interface. This architecture can significantly reduce interfacial stress due to electrode volume change and mitigate dendrite formation. Li plating behavior at the electrode|electrolyte interface is evaluated for Li|Li symmetric and Li|CNT asymmetric cells by NDP (Wang et al. (2017)). NDP energy profiles indicate the formation of a reversible layer near the SE|CNT interface that shows reversible cycling. Plating in excess of this region is left behind and accumulates in the CNTs. At low current density (100 μA cm^{-2}) net change in charge passed in Li|Li symmetric cells and the integratred NDP counts turn out to be near zero at end of cycle indicating reversible plating/stripping behavior. At higher current density (200 and 400 μA cm^{-2}) no accumulation of Li at end of each cycle is observed until failure indicating complete reversibility. After short circuit, inner layers show an increase in counts indicating Li accumulation in garnet pellet. During the initial two formation cycles in LCO|Li_3PO_4|Si thin film batteries, the intensity profiles follow expected trends with respect to lithiation and delithiation (Chen et al. (2018)). However, high lithium content cathode and Li- free anode are not realized after the first two cycles indicating presence of immobilized Li in the anode. In addition, an immobilized interlayer is also identified at the anode|electrolyte interface. *Operando* NDP scan of the charged battery over long term cycling highlight stability of the cathode over the duration of the cycle while a monotonic decrease in lithium content at the anode. In addition, a generation of increasingly concentrated immobilized Li containing interlayer at the anode|electrolyte interface is identified. NDP map of the discharged cell over the cycling duration show consistent behavior. Si-migration to the solid electrolyte is identified as the cause of generation of the Li rich interlayer by XPS measurements. Si-containing interfacial layer can trap higher amount of Li that cannot be extracted during normal battery operation limiting the capacity of the battery.

Significant work on understanding the chemical transformations at SE|anode interfaces is carried out with *in situ* SEM and TEM measurements. Dendrite formation and delam-

ination of Li metal against LPS electrolyte was recently showcased (Fig. 1.7f,Singh et al. (2020)). LPS forms a reactive interphase with Li metal that leads to interfacial degradation. Addition of Li halides is shown to stabilize the interphase and enable higher rate performance. *Operando* TEM results highlight the local redistribution of Li during cycling (Fig. 1.7g,Basak et al. (2020)). Results indicate that over a length scale of few hundred nms, contact of active material with electrolyte is not necessitated. Facile lithium redistribution is shown between interconnected active particles. Generation of reactive interphase is visualized by TEM measurements for LAGP|Li system (Fig. 1.7h,Lewis et al. (2019)). Interfacial delamination and pore formation in Li metal at high stripping current density is visualized by *ex situ* SEM and XRT measurements (Fig. 1.7i-j,Krauskopf et al. (2019); Kasemchainan et al. (2019)).

Studies on anode transformations, anode|SE interface and solid electrolyte failure highlight filament formation as one of the key issues with solid state batteries. Over the years, several mechanisms/pathways are proposed for dendrite nucleation and growth in solid electrolyte (Fig. 1.10). Earliest filament growth mechanisms in Li metal were outlined for solid polymer electrolytes (Brissot et al. (1999)). At high current density, ion concentration at anode drops to zero at Sand's time. However, a different behavior for the anionic and cationic species leads to an excessive concentration of positive charges at the anode. This results in a local space charge associated with a large electric field that leads to instabilities like filament formation (Brissot et al. (1999)). However, most of the inorganic solid electrolytes discussed here are single ion conductors eliminating concentration gradients within the system.The general consensus for dendrite growth and nucleation follows these steps: (1) Limited mass transport within the metallic anode creates a mass transport imbalance at the anode|SE. (2) This causes formation of pores/voids at the SE|anode interfaces resulting in poor or delaminating-type contact at the interface (3) improper contact leads to high interfacial resistance that results in localized generation of hot-spots of current densities (3) high local over-potentials in this regions can lead

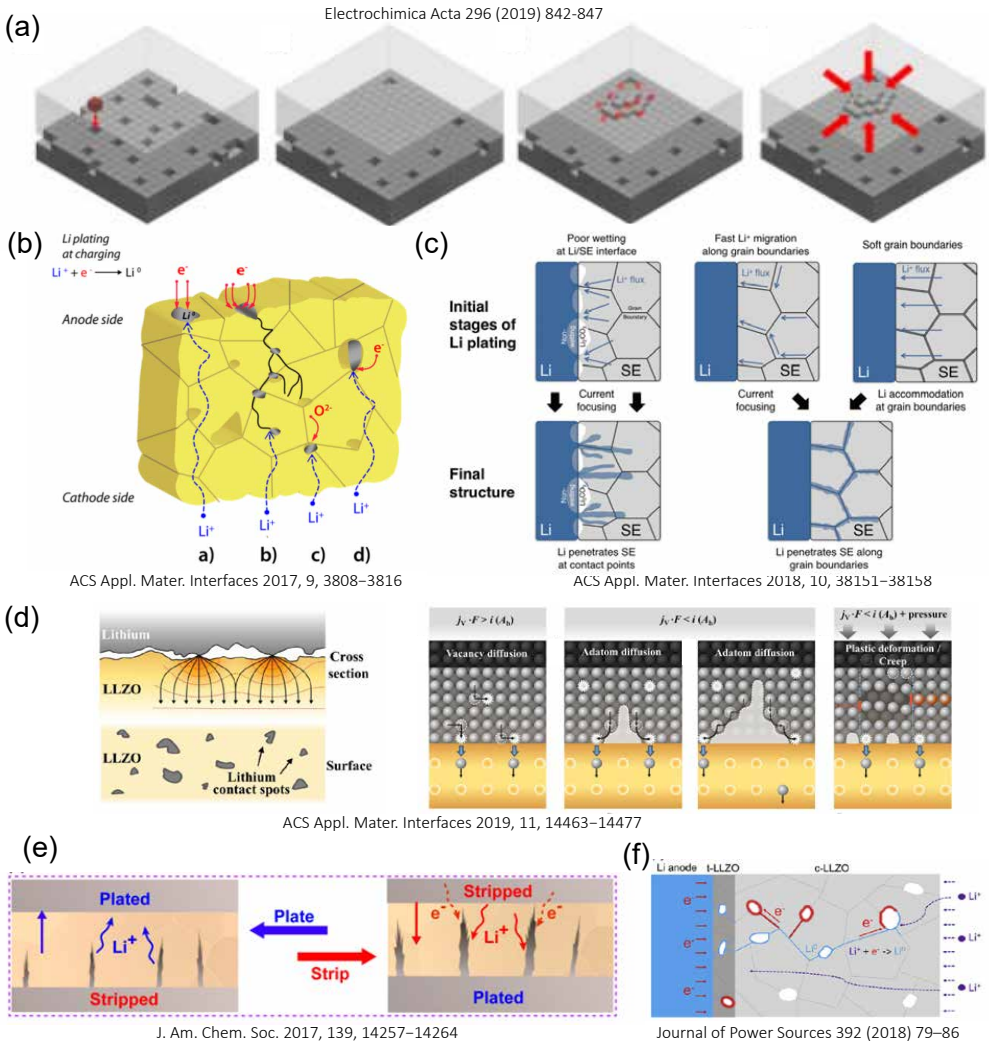

Figure 1.8: Summary of mechanisms for filament onset and growth in solid electrolytes in the literature.

to nucleation and preferential growth of lithium through these sites. This mechanism is proposed by several studies (Wang et al. (2019); Krauskopf et al. (2019); Kasemchainan et al. (2019)). However, limited experimental evidence is available for this hypothesis. Li deposition in bulk solid electrolyte due to trace electrons is an alternative hypothesis proposed by modelling (Aguesse et al. (2017); Tian et al. (2018)) as well as experimental studies (Han et al. (2019); Shen et al. (2018)). Grain boundaries, grain sizes and orientation have been investigated for their impact on dendrite mitigation with contradicting results (Sharafi et al. (2017); Cheng et al. (2015)). DFT studies shows grain boundaries

have 50% mechanical properties of the bulk material (Yu & Siegel (2018)). This results in initial plating along GB which further reduces the mechanical properties along which dendrites grow. The model considers homogenous Li distribution, unlike other models which assume the presence of high ion-flux hot-spots. Instead, the model predicts Li will preferentially migrate to grain boundaries via interfacial diffusion leading to Li protrusions. These protrusions would have locally stronger electric fields that can lead to dendrite growth.

^{7}Li chemical shift imaging provide evidence of continuous filament growth at current density below the critical current density (Marbella et al. (2019)). In contrast, random current spikes observed in the operation of the symmetric cell suggests a sharp dendrite propagation event termed 'dendritic arc' as opposed to continuous dendrite growth through the whole electrolyte (Aguesse et al. (2017)). The arc-ing induces stresses in the electrolyte that leads to fracture and eventual shorting of the cell. The reaction of solid electrolyte with lithium involves (electro)chemical reduction of the SSE to form a non-conducting interphase. During this process, the solid electrolyte can undergo volume expansion that induces mechanical stress that can induce fracture. Nonuniform growth of the reacted interphase occurred within the bulk of the solid electrolyte at higher current density can cause localized stress concentrations and accelerate mechanical failure (Singh et al. (2020); Lewis et al. (2019); Tippens et al. (2019)). Moreover, dendrite growth is also reported for single crystal solid electrolytes (Porz et al. (2017)). This suggests that while grain size and boundaries play a role in poly-crystalline solid electrolyte, the fundamental reason for can be due to Griffith-like fractures induced from inherent defects in the crystals.

Significant work is carried out in understanding anode transformation and stabilizing the anode|SE interfaces in solid electrolytes. However, the ability to track transformations in low Z- element anodes as well as characterizing the intra-material interfaces (grain

boundaries, pores) and inter material interfaces (electrode|electrolyte) are essential to unravel the exact mechanisms for instabilities at the anode|electrolyte interface. Fundamental understanding of interfacial kinetics, anode transformations and chemo-mechanics of solid electrolytes can enable engineering of systems with controlled electrodeposition and electrodissolution of metallic anodes at the required capacity.

1.3.3 Composite Cathode| Solid Electrolyte Interface and Cathode Chemo-Mechanics

Electrochemical potentials of typical cathode materials are quite different from that of the bulk solid electrolytes. The difference in electrochemical potentials and underlying stability window of the cathode material can lead to significant chemical decomposition of the cathode and electrolyte (Vardar et al. (2018); Wang et al. (2016); Choi et al. (2019); Yamamoto et al. (2010); Sakuda et al. (2010); Koerver et al. (2018, 2017)). Investigation into the generation, nature and impact of this cathode electrolyte interphase (CEI) is crucial towards development of high performance solid state batteries. Local lithium concentrations in the electrolyte and electronic structure of cathode material and electrolyte at the interface dictate the stability windows of the cathode-electrolyte interface. Additionally, during operation cathode active materials undergo volume expansion that leads to significant chemo-mechanical stresses on the cathode as well as the electrolyte (Koerver et al. (2018)). High strain in the cathodes can lead to fracture, delamination and/or loss of active material leading to poor battery performance. Characterization and diagnosis of cathode microstructure transformations and interfacial charge transfer dynamics are crucial for rational design of high performance batteries.

Many of the techniques used in investigation of anode|electrolyte interfaces can be utilized for studying the cathode electrolyte interphase (CEI). Specifically, SEM and TEM have been extensively used to study the cathode electrolyte interphase. Imaging results show that particles of the active material lose contact with the solid electrolyte due to the prolonged cycling and associated structural changes (Fig. 1.9a-b,Koerver et al. (2017,

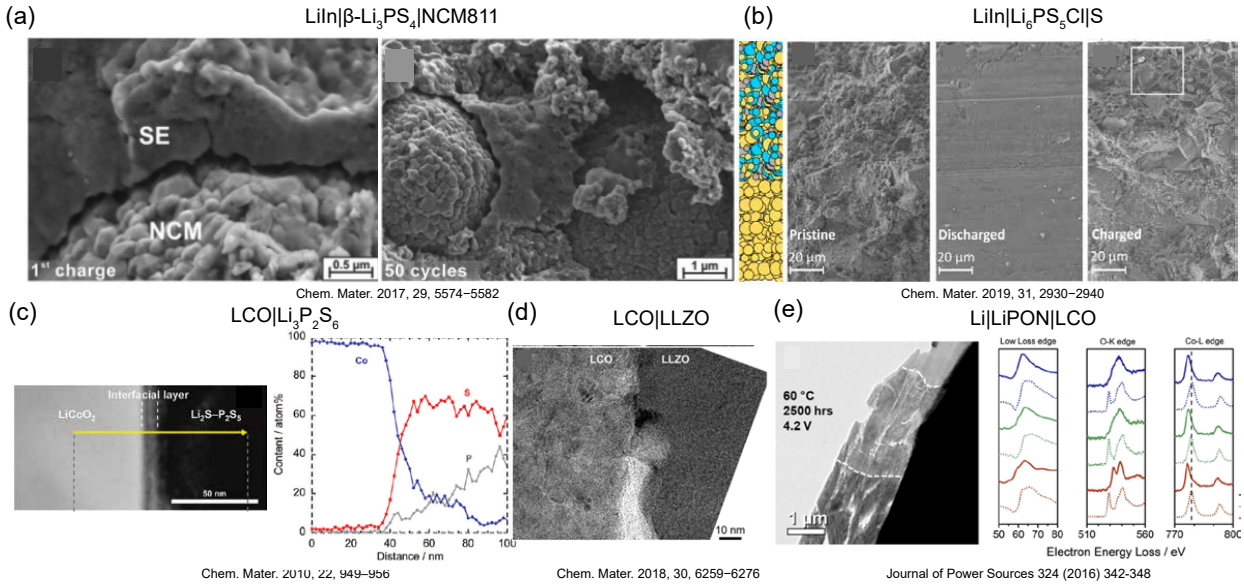

Figure 1.9: Summary of cathode chemo-mechanics and cathode|SE interface studies by microscopy techniques. (a) Delamination of cathode particles from solid electrolytes observed for LPS|NCM system by *ex situ* SEM imaging (Koerver et al. (2017)). (b) Microstructure variation in composite cathode for LiIn|LPSCl|S system observed by *ex situ* SEM imaging (Ohno et al. (2019)). Interphase formation between cathodes and solid electrolyte visualized by TEM for (c) LCO|Li_2S-P_2S_5 (Sakuda et al. (2010)), (d) LCO|LLZO (Vardar et al. (2018)), and (e) LiPON|LCO (Wang et al. (2016)).

2018); Ohno et al. (2019)). *Operando* X-ray diffraction showed the crystallographic volume change of single materials (Koerver et al. (2018)). Electro-chemo-mechanical FEM simulations suggest that fracture is prevented if electrode-particle's expansion is lower than 7.5% (Bucci et al. (2017)). Microstructural inhomogeneities, such as particle-to-particle misalignment and particle asperities are sufficient to cause tensile and shear stress in the solid electrolyte matrix that can lead to fracture. Additionally, the loss of three-phase contact leads to capacity fade in these systems. Cathodes|electrolyte interface shows a presence of a highly resistive interphase in the cathode which is formed by oxidation of the SE during the charging periods which is evidenced by TEM measurements (Fig. 1.9c-e,Vardar et al. (2018); Sakuda et al. (2010); Wang et al. (2016)). Mutual diffusion of transition metals from the cathode to the electrolyte are observed highlighting the chemical instability of the interface. Addition of interlayers can help in mitigating the reaction

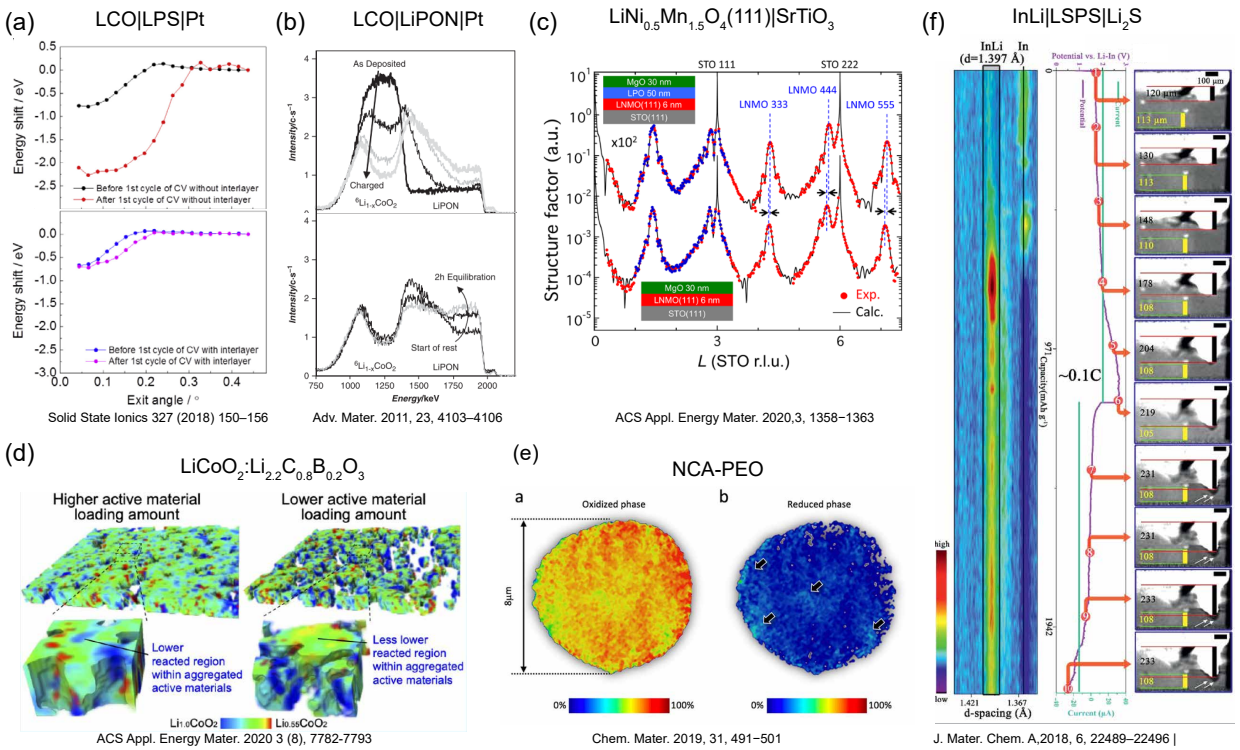

Figure 1.10: Summary of cathode chemo-mechanics and cathode|SE interface studies by neutron and X-ray techniques.(a) Energy shift in XANES spectra for LCO|LPS|Pt system with and without Li_3PO_4 interlayer (Chen et al. (2018)). (b) NDP studies of Li distribution in LCO|LiPON thin film batteries (Oudenhoven et al. (2011)). (c) Crystal trucation rod profiles evaluated at LNMO|$SrTiO_3$ interface (Kawasoko et al. (2020)). (d) Lithiation distribution and reaction front propagation in composite LCO cathodes based on loading differences visualized by TXM-XANES (Kimura et al. (2020)). (e) Chemo-mechanical effects and SoC distribution of NCA cathode was investigated using *ex situ* XANES imaging (Besli et al. (2019)). (f) Energy dispersive XRD and tomography for InLi|LSPS|Li_2S system (Sun et al. (2018)).

layer formation and stabilize the interface (Fig. 1.9f,Chen et al. (2018)).

Lithium concentration in a thin film LCO|LiPON|Cu battery was investigated by neutron depth profiling (Fig. 1.10a, Oudenhoven et al. (2011)). The thin film battery is charged at 10 μA ($\approx$ 0.3C) to 4.2 V. To further understand the lithium migration between cathode and solid electrolyte, LCO was fabricated with 100% ^{6}Li which results in higher intensity for the cathode compared to the solid electrolyte. No interaction between cathode and electrolyte is observed during passive hold between fabrication and testing (one week). Upon

charging a significant decrease in intensity at the cathode is observed consistent with depletion of Li from the cathode. In addition, the depletion is stronger at the SE|cathode interface which is proposed to arise from ^{6}Li migration from cathode to solid electrolyte as well as the charging reaction. Similar analysis was carried out on LMO|LiPON|LNO thin film battery (Fig.1.10b, Tomandl et al. (2020)). NDP scans were take for fully charged and discharged battery. Comparison of the two scans indicate that most change in lithium concentration is observed in the two electrodes (approximately 14-16%) with minimal change in the electrolyte (0.1%). 31% of the total calculated lithium concentration is estimated to participate in the redox reactions. Spatial 2D imaging of NDP profile indicates inhomogeneous distribution of Li in the ASSB with Li being concentrated near the center of one half of the sample (28% of lithium in 8% the total cell area). These results highlight the need to understand spatial distribution of lithium migration within solid state batteries.

Atomic level LPO|LNMP interface characterization was carried out by synchrotron X-ray crystal truncation rod scattering analysis (Fig. 1.10c, Kawasoko et al. (2020)). LNMO (111) epitaxial thin film growth is verified by the CTR profiles and introduction of LPO amorphous solid electrolyte does not damage the cathode thin films. LPO introduction lowers the cubic lattice constant of the LNMO from 8.23$\pm$ 0.02 Åto 8.18$\pm$0.01 Å. Lower lattice constant for LNMO without LPO deposition arises from lithium deficiency (30%) which gets slightly replenished on LPO deposition. Further quantitative analysis of the CTR profiles indicate an atomically sharp interface between LNMO and LPO that can facilitate Li^{+} transport. Comparing LPO|LNMO(11) interface to LPO|LNMO(001) interface, spontaneous migration of Li was lower for the (111) system. Additionally, anisotropy in the interface is observed with (111) system interface showing 5x larger resistance than the (001) interface. Similar study was carried out on the interface of LPO|LCO system to understand the origin of the resistance (Shiraki et al. (2018)). Two samples were evaluated corresponding to different LPO deposition rates 105 nm/h at 5 Hz repetition rate

and 450 nm/h at 20 Hz repetition rate. Impedance spectroscopy results show the 20 Hz-LPO|LCO system has a significantly (33x) higher interfacial resistance than the 5 Hz-LPO|LCO system (5.5 Ω cm^{-2}). The origin of the high interfacial reistance is attributed to a dead layer in the 20 Hz-LPO|LCO system with low crystallinity at the interface. These results highlight the need for tailoring the cathode|electrolyte interface with atomic precision to facilitate Li^+ transport through the solid|solid interface.

InLi|LSPS|Li_2S cell was investigated by *operando* energy dispersive X-ray diffraction and tomography (Fig. 1.10f,Sun et al. (2018)).The cell was cycled at 1C, 0.5C, 0.25C and 0.1C during the *operando* measurement. During charge process, principle diffraction line of In disappears with the appearance of InLi diffraction peak. Additionally, volume change in the electrode cause build-up/release of stress at the electrode | electrolyte interface causing mechanical degradation. *In situ* X-ray diffraction is used to study Bi|LiPON|Li thin film solid state batteries (Goonetilleke et al. (2018)). Diffraction data indicates presence of a series of phase transitions from Li_3Bi-LiBi-Bi along with presence of phases like Li_2Bi. These results highlight the importance of phase transformations in alloy electrodes and XRD as a tool to investigate binary alloy systems. Similar study was carried out on an Li|Li_3YCl_6|LCO cell (**?**). The cell was operated between 3.6-1.9 V at 135 μA cm^{-2} (0.1 C). LCO diffraction peaks show behavior similar to those observed in conventional liquid electrolyte systems with the (003), (006), and (104) peaks shifiting to lower angle while the (101) peak shifting to higher angle. No variation in the signal from LYC solid electrolyte indicated absence of side reactions within the system.

X-ray diffraction was proposed as an indirect measure for state-of-charge (SOC) of ASSBs (Bartsch et al. (2019)). In|Li_6PS_5Cl|NMC was assembled and cycled between 2.3 and 3.8 V at C/20 rate. Uncoated as well as $LiNbO_3$ coated NMC is evaluated using *operando* as well as *ex situ* measurements of SSB as well as conventional liquid electrolyte cells. $LiNbO_3$ coated NMC delivered higher specific charge capacity and coulombic efficiency (165 mAh

g^{-1}, 81%) compared to the uncoated NMC (154 mAh g^{-1}, 72%). High charge transfer resistance for the uncoated NMC due to side-reactions and partial contact loss with SE can lead to lower capacities for the initial cycles and poor coulombic efficiency. Presence of inactive cathode active material is identified by comparing *ex situ* and *operando* diffraction patterns of SSBs with conventional liquid electrolyte cells. Refinement of the XRD considering the inactive phase leads to estimation of SOC of the coated and uncoated materials as 173 and 162 mAh g^{-1} which are consistent with the experimental results. These results indicate that XRD is a potential tool for reliably assessing SOC of SSBs and to investigate presence of inactive CAM within the composite cathode. *In situ* XRD was used to estimate unit cell volume change for NCM, NCA and LCO cathode materials (Koerver et al. (2018)). Unit cell volume reduction of 4-6% is observed for NCM and NCA electrodes, while a non-monotonic response ($\pm$2%) is observed for LCO material. Cathode expansions identified by XRD experiments are correlated to chemo-mechanical stress generation in ASSBs.

Exothermic reactions of LPS solid electrolyte with $LiNbO_3$ coated NMC111 were investigated by *in situ* high temperature synchrotron XRD (Tsukasaki et al. (2019)). Composite cathode consisting of LPS:NMC (25:75) was initially charged to 3.8 V against In at 0.13 mA cm^{-2}. The charged cathode sample was extracted and investigated by synchrotron XRD in a control N_2 atmosphere as well as vacuum. The diffraction patterns were obtained in the 2θ range of 5°-25° between temperatures of 20 °-500 °C. In N_2 atmosphere, $CoNi_2S_4$, Li_3PO_4, MnS, β-Li_3PS_4 and Li_2S phases appears after 300 °C with a reduction in the NMC phase peaks indicating exothermic reactions between LPS and NMC between 300 °-500 °C. In contrast, no reaction products are observed for the temperature study in vacuum. In particular, the formation of the LPO oxide phase is derived from the LPS reaction with the O_2 gas generated during NMC decomposition. These results dictate the necessity of oxygen tolerant solid electrolytes for practical solid state batteries.

Impact of loading on active material utilization in composite cathodes was investigated by XRT-XANES imaging (Fig. 1.10d,Kimura et al. (2020)). $LiCoO_2$ (LCO) was used as cathode active material and $Li_{2.2}C_{0.8}B_{0.2}O_3$ (LCBO) was used as a solid electrolyte. Two cells were assembled with cathode compositions of LCO:LCBO = 5:5 and 8:2, LCBO solid electrolyte and Li metal anode. Cell with 8:2 cathode composition showed a specific discharge capacity of 57 mAh g^{-1} (48% theoretical capacity) while the 5:5 cathode composition cell showed a specific discharge capacity of 85 mAh g^{-1} (70% theoretical capacity). XRT-XANES results for both cells observed no reaction distribution in the through plane direction of the electrode indicating a ion-diffusion limitation. However, a heterogeneous distribution of in-plane active amterial utilization is observed. In particular, the 8:2 system shows larger active material aggregates with the central regions of these aggregates showing a lower degree of lithiation. In comparison, 5:5 system showed lower aggregation due to the reduced active material loading leading to smaller aggregates and a more homogeneous reaction distribution within the active material aggregates. Similar studies are caried out for NCA|PEO|Li (Fig.1.10e, Besli et al. (2019)), NMC|LTAP system (Li et al. (2018)). The NCA|PEO|Li ASSBs showed a significant drop in capacity over 20 cycles from 180.36 mAh g^{-1} to 83.09 mAh g^{-1}. The cathode materials were harvested from pristine, single-charged and cycled cells. TXM cross-sectional images for secondary particles from the cathode show presence of irregular patterns throughout the particles ascribed to the cracking of the secondary particles. This cracking is concentrated in the center of the secondary particles. XANES imaging of 2D cross sections over the Ni K-edge indicated presence of domains containing discharged cathode material even though the samples were harvested from a charged cell. 2D XANES imaging shows a heterogeneous utilization of the secondary particles with isolated, discharged domains that seem electrochemically inaccessible. Additionally, 3D-TXM-XANES images show a correlation between morphological cracking of the particle and the inactive domains identified in the 2D XANES maps. The results indicated loss of electrochemical activity in the core of

the particle driven by loss of ionic diffusion pathways due to cracking of the particle. Ex situ TXM study of LTAP|NMC composite cathode was carried out to understand spatial distribution of the individual phases and identify transport bottlenecks in the structure (Li et al. (2018)).Geometric analysis showed poor three phase interface between the components that is required for achieving electrochemical access of the active material. LTAP coverage on NMC improves from 55% to 59% on increasing the assembly pressure from 700 to 1300 psi. These results highlight the need for careful design of the composite cathode to ensure high utilization and rate capabilities in ASSBs. XRF imaging was used to investigate the Zr and Mn distribution of NMC infiltrated LLZO scaffolds (Shen et al. (2019)). Complementary distribution of Mn and Zr is observed indicating that NMC has infiltrated the voids present in the LLZO scaffold. Lab-scale XRT was used to image LPS based composite cathodes which were used for microstructure-resolved simulations (Neumann et al. (2020)). Visual analysis of the reconstructed cathodes indicated fluctuations in in the in-plane composition.

1.4 Research Questions and Expected Outcome

Next generation energy storage systems will use solid state electrolytes to achieve high energy and power densities. Advances in material synthesis, production as well as device engineering will be needed to achieve these goals. The literature survey included here focuses specifically on characterization of solid state batteries and components. Majority of the degradation is happening at the buried solid|solid interfaces and in the bulk of the solid electrolyte. Understanding the transport and failure mechanisms that occur at the buried solid|solid interfaces and bulk solid electrolytes is a challenging experimental task. The underlying hypothesis of this work is that the knowledge of structure-function dependence in solid state batteries can be leveraged towards engineering of high performing systems. Processing-structure-function relationships investigated in this thesis refer to the interplay of electrolyte microstructure and electrode|electrolyte interfaces on

transport and kinetic bottlenecks that limit the performance of the system.

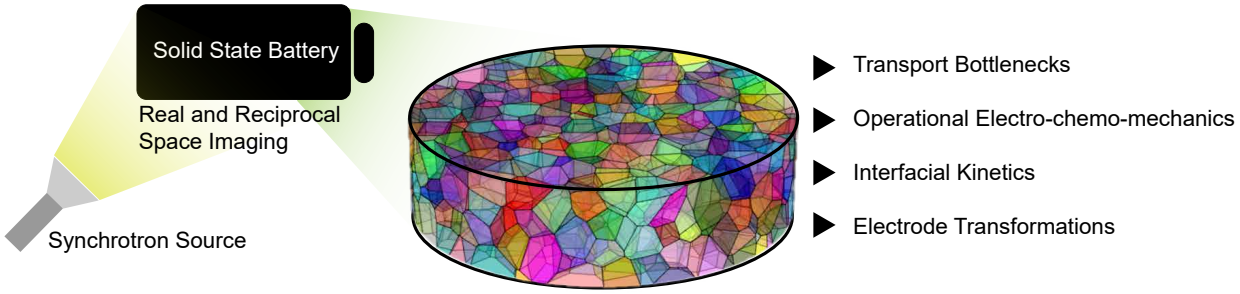

Figure 1.11: Schematic diagram highlighting the research methodology and investigated research questions.

The key research question addressed will be evaluation of the internal structure of the state batteries and transformations of the components during electrochemical cycling (Fig. 1.11). Experimental evaluation of these buried interfaces and interior bulk of the solid electrolytes necessitate the use of advanced characterization techniques. Synchrotron X-rays offer a high energy source with the capability of accessing these regions experimentally. Synchrotron experiments allow for extended range of spatial and temporal characterization capabilities that are crucial to understand the underlying fundamental processes of transport, failure and mitigation in battery systems (Pietsch et al. (2017); Hapuarachchi et al. (2018); Mcbreen (2009); Tripathi & Hwang (2018); Li et al. (2017)) which will be leveraged for this purpose. The second research question addressed will be correlating the microstructure of solid electrolytes with their performance. Electrochemical testing as well as modeling will be carried out to evaluate these relations. Furthermore, *operando* studies are proposed to evaluate evolution of structure in ASSBs as a function of their performance. The third research question to be addressed is leveraging the information derived from the previous studies to engineer high performance electrolyte systems. Emphasis will be put on development of scalable production methods that can tailor the structure during processing for manufacturing high performing solid electrolytes. The overarching goal of the proposed research is aimed at understanding the fundamental processing-structure-function correlations in solid state electrolytes. The results of these

studies are expected to inform rational design of next generation of solid state battery systems. Further, the proposed research will contribute towards enabling scalable production of high performance solid electrolytes and contribute towards commercialization of these systems.

Chapter 2

Methods and Technique Fundamentals

This chapter offers a broader understanding of the key synchrotron techniques leveraged and the underlying fundamentals for those techniques. Details regarding material synthesis and processing methods used in this thesis are included in subsequent chapters for the specific materials and methods used for those studies.

2.1 Electrochemical Testing

The primary aim of the solid electrolyte is to shuttle ions and offer electrical insulation between the two electrodes. In this regard, there are a few measurements that are extensively used for characterization of solid electrolyte materials. The details of these properties and their standard measurement protocols are described here.

2.1.1 Ionic Conductivity Measurements

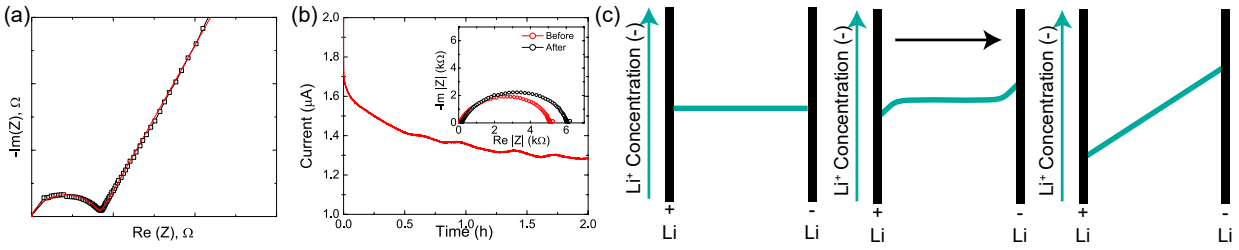

Figure 2.1: (a) Typical experimental measurement for ionic conductivity. The AC impedance measurement is carried out on solid electrolyte sandwiched between two blocking electrodes. Bulk resistance is estimated by equivalent circuit fitting (solid line) of the experimental data (markers). (b) Typical experimental measurement for transference number. Experiment is run on a symmetric Li|SE|SE cells. AC impedance measurements are carried before and after long term polarization. This method is only used for solid electrolytes showing both anion and cation transport. (c) Concentration gradients within the solid electrolyte during the transference number measurement.

The ionic conductivity of a material, σ is directly proportional to the concentration of the

mobile charge species and their mobilities (Famprikis et al. (2019)), given as

$$\sigma = \sum n_i q_i u_i \tag{2.1}$$

where q_i us the charge of the ionic species, u_i is the mobility of the ionic species and n_i is the number of the charged species. Ionic conductivity is traditionally measured by AC impedance measurements of electrolyte sandwiched between blocking electrodes. In this configuration, the cell acts like a resistor with a specific bulk resistance R_b with an interfacial capacitance C_{dl}. The bulk resistance is related to the ionic conductivity of the electrolyte σ by the following relation:

$$\sigma = \frac{1}{\sigma} \frac{l}{A} \tag{2.2}$$

where, l is the thickness of the electrolyte and A is the interfacial surface area. The bulk resistance value (R_b) is generally identified by fitting the impedance response to an equivalent RC-circuit (Fig. 2.1a). Typically these measurements are carried out over a range of temperatures to estimate the activation energy of ion motion through the solid electrolyte. Typically, Arhennius behaviors are observed for the solid electrolytes under study.

2.1.2 Transference Number Measurements

Transference number is defined as the fraction of the total current carried by a specific charge carrier. Thus, by definition the sum of transference numbers is 1 and transference number is between 0 and 1. In the limit of low ionic concentrations, the Nernst-Einstein equation relates the partial conductivities, and the diffusion coefficients and the transference number is typically given as:

$$t_+ = \frac{\mu_+}{\mu_+ + \mu_-} = \frac{\sigma_+}{\sigma_+ + \sigma_-} = \frac{D_+}{D_+ + D_-} \tag{2.3}$$

where, μ is the mobility of the specific charge carrier, σ is the specific ion conductivity, and D is the diffusion coefficient. High transference numbers are generally preferred for batteries to minimize concentration gradients within the system. Bruce and Vincent method is the most common method for measurement of transference numbers of solid electrolytes (Bruce & Vincent (1993)).This method involves polarization of a symmetric cell by a small potential difference to induce a concentration gradient within the system until a steady state is reached (Fig. 2.1c).

The initial current flowing through the system can be given as,

$$I_0 = \frac{\sigma}{k}\Delta V \tag{2.4}$$

where k is the cell constant (ratio of inter-electrode distance and surface area of electrodes). At steady state, the concentration gradient does not change with time; that is ion motion through migration under electric field is compensated by the diffusion due to concentration gradient. Thus, the steady state current can be given as

$$I_{SS} = \frac{t_+\sigma}{k} \tag{2.5}$$

which is simplified to,

$$t_+ = \frac{I_{SS}}{I_0} \tag{2.6}$$

The initial and steady state currents at very low polarization ($<$ 10 mV) are measured experimentally (Fig. 2.1b). However, interfacial resistances from contact resistance and charge transfer resistance can modify the initial and steady state currents. AC impedance spectra are obtained before and after the long term polarization (Fig. 2.1b). The initial and steady state current formulations are suitably modified as follows:

$$I_0 = \frac{\Delta V}{k/\sigma + R_{p,0}} \tag{2.7}$$

and

$$I_{SS} = \frac{\Delta V}{k/\sigma t_+ + R_{p,ss}} \tag{2.8}$$

Combining the initial and steady state current equations, we obtain the formulation for transference number as given by the Bruce-Vincent method:

$$t_+ = \frac{I_{SS}(\Delta V - I_0 R_{p,0})}{I_0(\Delta V - I_0 R_{p,ss})} \tag{2.9}$$

It should be noted that this measurement is only useful for conductors that show anion and cation transport. Lack of concentration gradients in single ion conductors make this measurement fundamentally inapplicable. In case of single ion conductors, transference numbers are estimated from the ration of electrical to total conductivity.

2.1.3 Critical Current Density Measurement

Another key metric for solid electrolytes reported generally is called the critical current density. Generally, critical current density is defined as the current density above which filament growth through the solid electrolyte occurs (Hatzell et al. (2020)). This current density offers the upper bound of operating currents with the solid electrolyte thereby dictating the rate performance of the solid electrolyte in a solid-state battery. Typically, critical current density is identified by galvanostatic cycling of a symmetric Li|SE|Li at increasingly higher current density until filament growth is observed.

2.2 Synchrotron Techniques

Chemo-mechanical degradation in solid state batteries occurs at the buried solid|solid interfaces and within the electrolyte bulk. Synchrotron X-ray sources have high energy and brilliance making them an ideal probe for solid electrolytes under relevant operating conditions. X-ray transmission is necessary for experimentation, thus, while typical lab experiments employ a solid electrolyte with a diameter around 10 mm, synchrotron

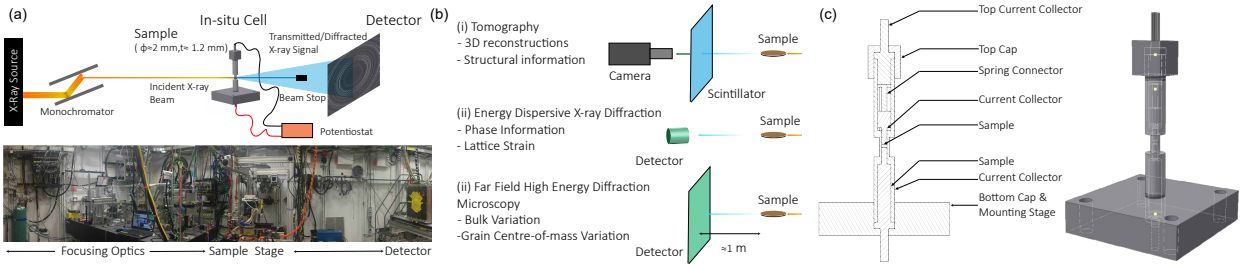

Figure 2.2: (a) Schematic diagram and actual experimental station at 1-ID beamline at Advanced Photon Source at the Argonne National Laboratory. (b) Schematic diagram showing end-station configurations for the synchrotron X-ray techniques employed in the thesis as well as the expected information from the technique. (c) Cross-section view of the proposed *in situ* cell. Key structural elements are shown. Additional control and measuring devices for pressure and temperature will be incorporated. 3D rendering of the proposed *in situ* electrochemical cell for synchrotron studies on all solid-state batteries is also shown.

experiments may require a diameter closer to 2 mm for effective imaging of high density polycrystalline materials (Fig. 2.4a). This is orders of magnitude of larger than other lab-based characterization techniques (TEM), where sample dimensions need be on the micron scale. Synchrotron experiments also benefit from excellent spatial resolutions (microns) which makes it ideal for tracking meso-scale transformations. The versatility offered by a beamline in terms of *in situ* and operando electrochemistry is extremely valuable and is typically not possible with laboratory X-ray /electron sources due to the vacuum environments (Fig. 2.4a).

X-rays exhibit three principle interactions with matter: a) absorption/attenuation, b) scattering/diffraction and c) transmission. Designing an *in situ* x-ray cell requires geometry optimization to maximize the signal/noise ratio. A key undertaking to assess the operando transformations in solid-state batteries was to build an electrochemical cell capable of *in situ* imaging and diffraction (Fig. 2.4b). X-ray imaging relies on absorption contrast to generate three-dimensional reconstructions of the sample. To ensure enough absorption contrast the transmitted intensity should be at least 1/e of the incident energy. The length of sample across which the intensity of the X-ray falls to 1/e of its initial

value is called the attenuation length. The attenuation length for LLZTO for 30 keV X-rays is ∼1.5 mm. Incident X-ray energy is fixed based on the diffraction experiment and is typically much higher (typically 70-80 keV). Sample size of ∼1.5 mm will yield good transmission intensity for imaging experiments at these energies. Correspondingly for diffraction experiments the X-ray absorption (μR) between 1-5 is obtained in the 70-80 keV range for LLZTO (ϕ=∼1.5 mm). Sample size influences acquisition times, data-set sizes and data analysis complexity. Considering these factors, a sample size of ∼1.5 mm is proposed for the *in situ* cell.

During imaging and diffraction microscopy experimentation, the electrochemical cell rotates 360° in small step sizes (typically 0.1-0.5°). A tubular design is ideal for *in situ* experimentation which requires a constant electrical connection. The developed design which contains two vertically aligned stainless steel rods that enable electrochemical connection and rotation (Fig. 2.4c). Polyether ether ketone (PEEK) has a low absorption to X-rays and is easy to manufacture and was used as the *in situ* cell encasement. The solid-state battery resides in the PEEK encasement between two stainless-steel current collectors. An additional spring element is placed on one side in the *in situ* cell to apply a constant pressure on the battery. The pressure value is dependent on the spring constant and the area of the battery investigated. The key limitations of this cell is the limited stack pressure it allows during operation (≈ kPa) is significantly lower than the typical stack pressures used in solid state battery systems (5-10 MPa). Additionally, assembling small aspect-ratio cells is a significant experimental challenge. In spite of these limitations, this cell can enable proof-of-concept measurements as well as generate new insight about chemo-mechanical degradations within the solid-state system.

2.2.1 X-Ray Tomography

In a typical tomography experimental setup (Fig. 2.4a-b), X-rays pass through the sample where they are partially absorbed based on the density distribution inside the sample.

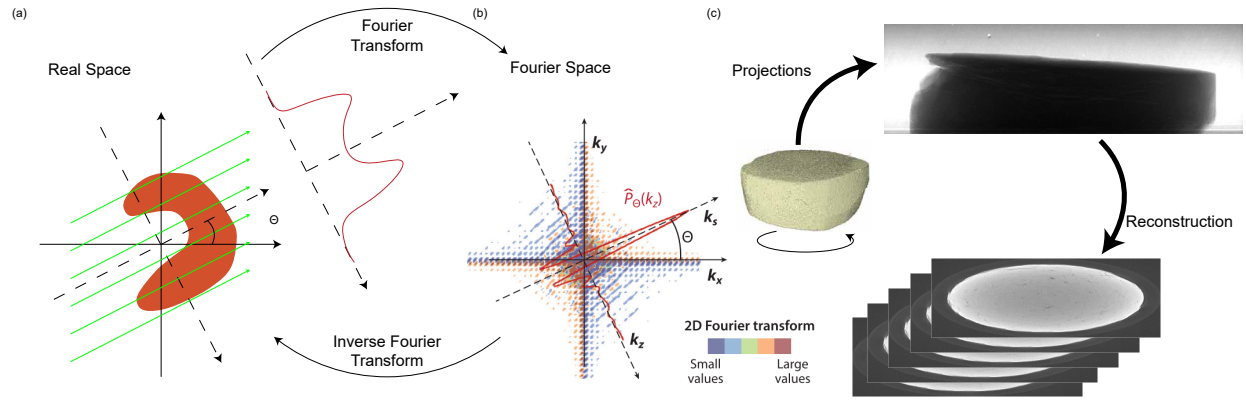

Figure 2.3: (a-b) Illustration depicting the Fourier slice theorem which forms the basis of tomography measurments. (a) Illustration showing a sample with attenuation co-efficient distribution ($\mu(x,y)$) penetrated by a parallel X-ray beam. The corresponding projection at an angle Θ is also shown (PΘ(z)). (b) 2D Fourier transform of attenuation coefficient distribution (colored map) and 1D Fourier transform of the projection through the origin of the coordinate system orthogonal to the X-ray beam direction. According to the Fourier slice theorem, it is possible to tomographically reconstruct $\mu(x,y)$ from the set of projections $P_\Theta(z)_{0\leq\Theta\leq\pi}$. (c) Schematic diagram showing a 3D pellet with a sample of the projection images recorded during a tomography scan and the resultant reconstruction slices. Figure adapted from Pietsch et al. (2017).

The transmitted X-rays are converted to visible light by a scintillator which can be optically magnified and capture with a camera (CMOS, CCD detector). An image taken at a fixed-angle of rotation yields a so-called projection which provides information regarding the absorption of sample through the transmission thickness at that orientation. The sample is then rotated and projection images are acquired over small intervals. In principle, X-ray tomography can be employed to any interaction between the material in the sample and X-rays. This physical quantity can be the X-ray attenuation co-efficient (as described here) or it can be diffraction patterns (diffraction tomography), real part of X-ray refractive index (phase contrast tomography). The fundamental principle that is leveraged in reconstruction is the Fourier slice theorem which is described briefly here.

A parallel X-ray beam propagating in the X-Y plane in direction s penetrates a sample with a given attenuation coefficient distribution (μ(x,y)) at an angle of incidence Θ. At each point along the orthogonal direction to beam propagation (Z), the X-ray intensity

will fall exponentially according to the Beer-Lambert Law as the X-ray beam penetrates through the sample,

$$I_\Theta(z) = I_0 e^{-\int_{-\infty}^{\infty} \mu(x,y)ds} \tag{2.10}$$

The resultant projections of the attenuation coefficient distribution along the beam path are thus given by,

$$P_\Theta(z) = \int_{\infty}^{\infty} \mu(x(\Theta,s,z),y(\Theta,s,z))ds = -ln\Big(\frac{I_\Theta(z)}{I_0}\Big) \tag{2.11}$$

where relation between x, y, s and z are formulated from basic trigonometry and orientation of the X-Y and S-Z coordinate system as depicted in Fig. 2.3a.

The ability to reconstruct physical quantity distribution from a set of projections arises from the Fourier slice theorem which states that the 1D Fourier transform $\hat{P}_\Theta(k_z)$ of a projection $\mathrm{P}_\theta(z)$ is equal to the 2D Fourier transform $\hat{\mu}(k_x,k_y)$ of the attenuation coefficient distribution evaluated along the slice through the origin that is orthogonal to the beam direction (Fig. 2.3b).

$$\hat{P}_\Theta(k_z) = \hat{\mu}(k_x = k_z sin(\Theta), k_y = -k_z cos(\Theta)) \tag{2.12}$$

here, the variables k_i where i = x,y,s, z are the Fourier space counterparts of the real-space variables. The set of Fourier-transformed projections $\left\{\hat{P}_\Theta(k_z)\right\}_{0\leq\Theta<\pi}$ thus entirely defines the 2D Fourier transform $\hat{\mu}(k_x,k_y)$ of the attenuation coefficient distribution. As the Fourier transform is bijective, there is a bijective mapping between the set of projections and the attenuation coefficient distribution.

For Fourier based reconstructions, the following steps need to be carried out:

1. Recording the set of projections by measuring X-ray transmission through the sample over a range of angles $0 \leq \Theta < \pi$
2. Carrying out 1D Fourier transform on the set of projections
3. Using Fourier Slice theorem and performing inverse 2D Fourier transform on the 1D FT projection set to obtain the attenuation coefficient distribution.

In practice, discretized data sets requires iterative and noniterative algorithms to perform the specified tasks efficiently and accurately. In a typical tomography experiment, projections of the sample are collected over the full rotation of the sample w.r.t. the incident beam. The projections reflect the attenuation of the X-rays though the sample, effectively capturing the radon transform of the material density (Fig. 2.3c). The solution of the inverse radon transform problem can be used to reconstruct the original density distribution from the projection data (Leahy et al. (2009)). There are several open-source packages that employ various algorithms to compute this solution: gridrec (Carlo et al. (2014); Rivers (2012)), SIRT (Rivers (2012)), FBP (Pelt & De Andrade (2016)) among others. Phase retrieval, ring artifact removal, noise removal algorithms can also be utilized during reconstruction to improve reconstruction image quality (Munch & Holzer (2008a)). Raw projection data, center of rotation and other necessary parameters for ancillary algorithms (beam energy, sample-detector distance, factors for artifact removal) are fed to the reconstruction algorithm. Typical reconstructions for 2048x2048x1500 pixel image can take from few minutes to several hours for reconstruction based on the setup parameters and the computational power accessible. Reconstruction yields a stack of images sliced along the vertical direction in the sample (parallel to projection axis).

There are multiple segmentation methods available based on the features that need to be segmented. Segmenting between high contrast features (polycrystalline LLZO and voids) can be effectively carried out using conventional thresholding methods available within open-source image processing software (Schneider et al. (2012a)) or common program-

ming packages (MATLAB, Python). This method is applicable if there are strictly two phases within the system with a sharp difference in the respective grayscale values. For segmenting into more than two phases or to segment between low-contrast phases advanced image processing methods are required. Multi-component segmentation is most effectively managed by identifying grayscale intensity range corresponding to each phase from the stack histogram. The images are subsequently labelled according to the identified ranges by leveraging common programming packages. Segmentation between low contrast systems (lithium metal and pores) cannot be carried out using the techniques described so far. Machine learning methods, specifically convolutional neural networks can be effective in such segmentation problems. Neural networks are trained and validated on a dataset that can be generated using manual segmentation or competent unsupervised machine learning methods (k-means, edge-based segmentation), or a combination thereof. Subsequent to training, the neural networks can be employed to carry out high accuracy and rapid segmentation of low contrast phases within the reconstruction images.

2.2.2 Energy Dispersive X-ray Diffraction

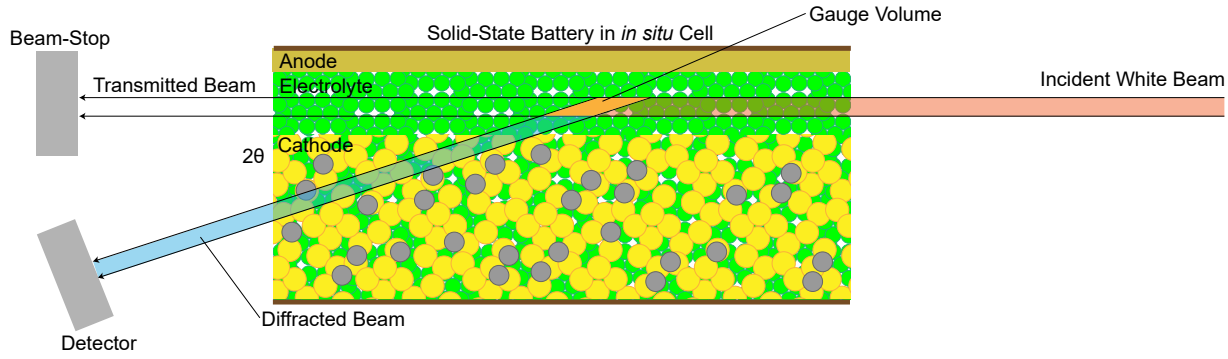

Figure 2.4: Schematic diagram highlighting the mechansim of energy dispersive X-ray diffraction.

Energy-dispersive X-ray diffraction is typically used for *in situ* phase evolution and stress analysis for polycrystalline materials. Phase evolution primarily involves recording the

diffraction patterns from the sample as a function of external stimuli (electrochemsitry, temperature, pressure) and identifying difference in them over time. Experimental configuration of measurement also allow for spatial profiling of the sample by rastering the X-ray probe through the sample thickness. Stress analysis, on the other hand, is based on the measurement of diffraction patterns and evaluation of the strains from peak-shifts corresponding to specific <hkl> plane, given as

$$\epsilon^{hkl} = \frac{d_t^{hkl} - d_0^{hkl}}{d_0^{hkl}} \tag{2.13}$$

where, d_0^{hkl} is the stress-free lattice spacing. In an energy dispersive XRD measurement, a white beam with a continous energy spectrum is incident on the sample, while the detector angle (2θ) under which the diffracted beam is measured is fixed during the measurement. Bragg condition for scattering is,

$$d^{hkl} = \frac{\lambda}{2sin(\theta)} \tag{2.14}$$

Using the equation E = hc/λ (where, h = Plank's constant, c is velocity of light in vacuum), the energy disperive relation for d-spacing is given as,

$$d^{hkl} = \frac{hc}{2sin(\theta)} \frac{1}{E^{hkl}} \tag{2.15}$$

Using this equation for the lattice strain equation, we obtain,

$$\epsilon^{hkl} = \frac{d_t^{hkl} - d_0^{hkl}}{d_0^{hkl}} = \frac{E_0^{hkl}}{E_t^{hkl}} - 1 \tag{2.16}$$

where, E_0^{hkl} refers to the energy corresponding to the strain-free lattice spacing d_0^{hkl}. The real-space location of the diffracting material (gauge volume) is identified by the relative positions of the incident beam and the fixed angle detector (Fig. 2.4). Spatial profiling of

the sample is achieved by translation of the sample through the gauge volume which is fixed for a given experimental setup.

Chapter 3

The Effect of Pore Connectivity on Li Dendrite Propagation Within LLZO Electrolytes Observed with Synchrotron X-Ray Tomography

3.1 Introduction

The elasticity, morphology, and structure of solid|solid interfaces are important for understanding the fundamental mechanisms that promote dendrite formation and propagation across ceramic electrolytesRen et al. (2015); Yu et al. (2016). All-solid-state lithium ion batteries (LIBs) are promising candidates for electric vehicle applications because they may enable the use of metallic lithium as an anode. Li metal is thermodynamically unstable in conventional liquid electrolytes but is stable against some garnet-type solid electrolytes (i.e. $Li_7La_3Zr_2O_{12}$ or LLZO)Cheng et al. (2017b); Ma et al. (2016); Sharafi et al. (2016, 2017). Doped LLZO materials have fast ionic conductivity (1 mS cm^{-1} at 298K)Thangadurai et al. (2014) and a high shear modulus (60 GPa). Theoretical studies have predicted that solid electrolytes with shear moduli greater than 8.5 GPa could negate lithium filament initiationMonroe & Newman (2003). However, recent experimental studies on ceramic-based materials have contradicted these findings and revealed preferential lithium growth along grain boundaries in electrolytes with shear moduli exceeding 60 GPaRen et al. (2015); Cheng et al. (2017a). While there is a significant interest in decreasing the interfacial resistance in all-solid state batteries with rationally designed coatingsMa et al. (2016); Han et al. (2017), there is an increasing need to understand how lithium dendrites grow and plate within ceramic electrolytesYulaev et al. (2018); Leite et al. (2014); Santhanagopalan et al. (2013).

Dendrite formation and propagation in garnet electrolytes is microstructure driven (i.e. solid electrolyte density, grain size, etc.)Porz et al. (2017); Cheng et al. (2015); Kim & Srinivasan (2016); Ishiguro et al. (2014). This degradation pathway initiates at current densities

between 0.05-0.2 mA cm^{-2} and needs to be significantly improved before garnet electrolytes can be realized in commercial applications. The size and orientation of the grains as well as the relative densities of the electrolyte all contribute to dendrite propagation across the electrolyte. Currently, only destructive and ex-situ characterization techniques (i.e. TEM and SEM) have been employed to study lithium dendrites formed in solid electrolytesCheng et al. (2017b); Sharafi et al. (2017); Sudo et al. (2014). This is in part, because directly observing high Z-element materials (i.e. zirconium) with contrast is difficult even with high energy x-ray methods. Herein, we overcome these challenges by using a synchrotron x-ray tomography method which employs a white beam set-up. The white beam setup enables the solid electrolyte microstructure ex situ after lithium dendrite formation. Three-dimensional reconstructions show an increase in X-ray transparent region on failure which suggests that isolated Li-metal agglomerates can occur. Isolated deposition of lithium metal within the ceramic can mechanistically occur by gaining an electron from the oxygen backbone of the ceramic or through electron propagation through the electrolyte. These findings are important and motivate the need for manufacturing and processing methods that can ensure high-density electrolytes and enable grain boundary engineering.

3.2 Experimental Section

3.2.1 Material Synthesis

A conventional solid-state-reaction method was employed to prepare LLZO powder, using LiOH, La2O3, ZrO2, and Al2O3 as the starting materialsRen et al. (2015). Briefly, 2.5 g LiOH (Pre-dried at 200 °C for 6 h). 6.629 g La_2O_3 (Pre-dried at 900 °C for 12 h), 3.346 g ZrO_2, and 0.152 g Al_2O_3 were mixed and ball milled for 2 h at 500 rpm. The mixture was then annealed at 800 °C for 12 h. Cubic LLZO was obtained. The powder was ball milled again for 2 h at 500 rpm and pressed into pellets for the second annealing at 1000-1150 °C for 6 h. The pellets were covered with the same mother powder during annealing.

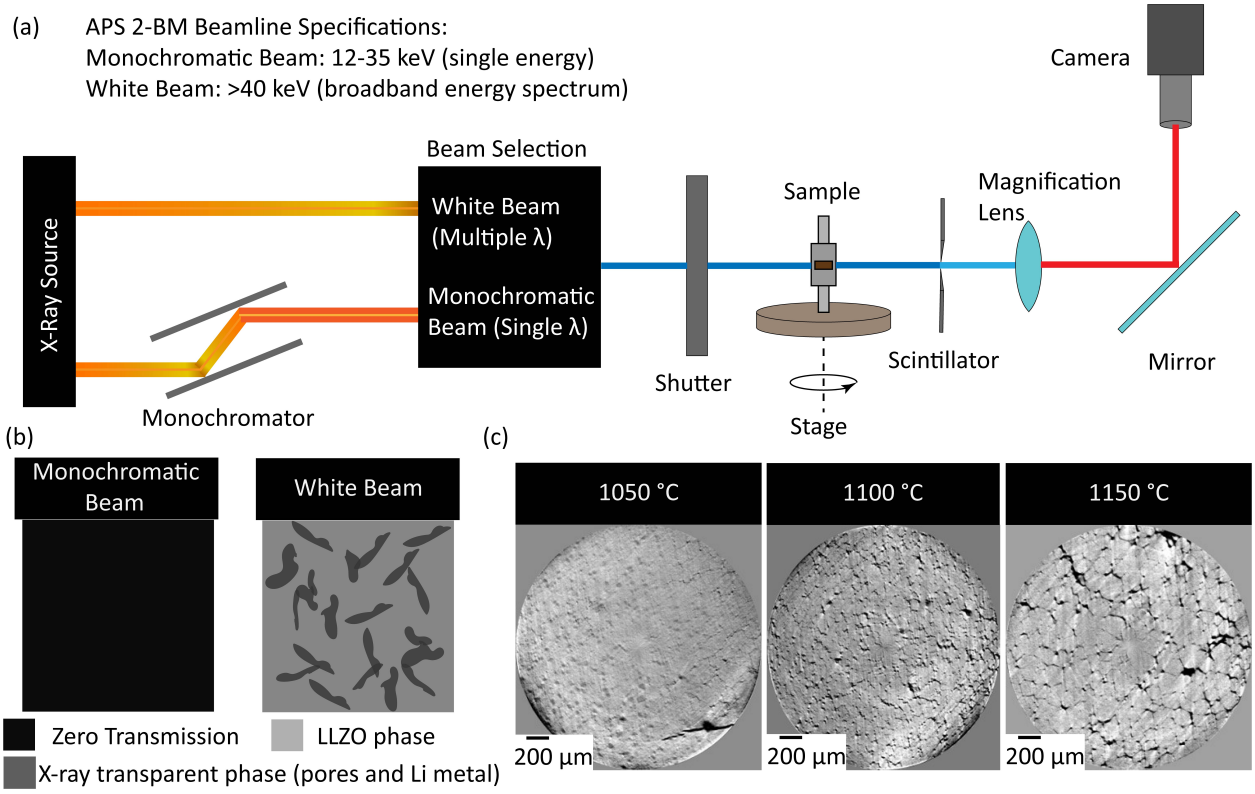

Figure 3.1: A diagram of the synchrotron X-ray tomography setup. The selection of the right beam energy and experimental set-up is important for resolving the morphological characteristics of a solid ceramic electrolyte (a). Garnet electrolytes dominated by heavy elements cannot attenuate X-rays and thus imaging is impossible. In contrast using high-energy x-rays at APS (white beam) we can resolve the pore phase and ceramic phase independently (b). Using the high-energy x-ray (white beam) we can resolve porosity, grains, and textural details (c).

3.2.2 Characterization

The crystal phase was detected by powder X-ray diffraction (Rigaku Smartlab, Tokyo, Japan) with a step of 0.01°. The microstructures of sintered LLZO pellets were examined by field emission scanning electron microscope (Zeiss Merlin, Oberhochem, Germany) with an Au conductive coating applied before imaging.Zheng et al. (2016)

3.2.3 Electrochemical Studies

The ionic conductivity was measured using an impedance analyzer (Bio-logic, VMP 3) with frequency from 1 MHz to 1 Hz at AC amplitude of 50 mV. Ag paste was deposited

on both sides of the finely polished pellets with Ag wires and dried at 175 °C for 0.5 h before test. The symmetrical battery cell was assembled by melting Li foils on both sides of the LLZO pellet. Charging/discharging cycling of the symmetric cells was conducted at a periodic increased current. EIS studies were carried out on the assembled cells before and after the charge/discharge cycling.

3.2.4 Tomography Studies, Reconstruction and Data Analysis

Synchrotron X-ray tomography was carried out at Beamline 2-BM-B of Advanced Photon Source at the Argonne National Laboratory. Filtered white beam X-rays were used to allow for X-ray penetration through the LLZO pellets. 1500 projections with an exposure time of 100 ms each were recorded evenly during 180° rotation of the sample. A pco.edge5.5 camera coupled with a mitutoyo long-working distance 10x magnification lens was used that gives a voxel size of 0.65 m and a total FoV of $\approx$ 1.6 x 1.4 mm^2. Under these experimental conditions, a single tomographic scan took approximately 15 to 20 minutes. The raw data obtained was processed with TomoPyGürsoy et al. (2014). Wavelet-Fourier filtering based ring removalMünch et al. (2009) and Paganin phase retrievalPaganin et al. (2002) were applied to the normalized projection images, and gridrec algorithmRivers (2012); Dowd et al. (1999) was used for tomographic reconstruction. The reconstructed images were binarized using autothresholding routines available in Fiji/ImageJSchneider et al. (2012a). Pore size distribution pluginMunch & Holzer (2008a) was used on the binarized image sets to identify and isolate solid phase in the sample. This is carried out by fitting the pore region of the binarized 3D data set with spheres of different radii. The histogram of the sphere radii acts as the continuous pore size distribution of the sample. The pore size distribution analysis of the failed samples was carried out on larger subvolumes (500 μm x 1.1 mm x 1.1 mm) to remove possible user bias.

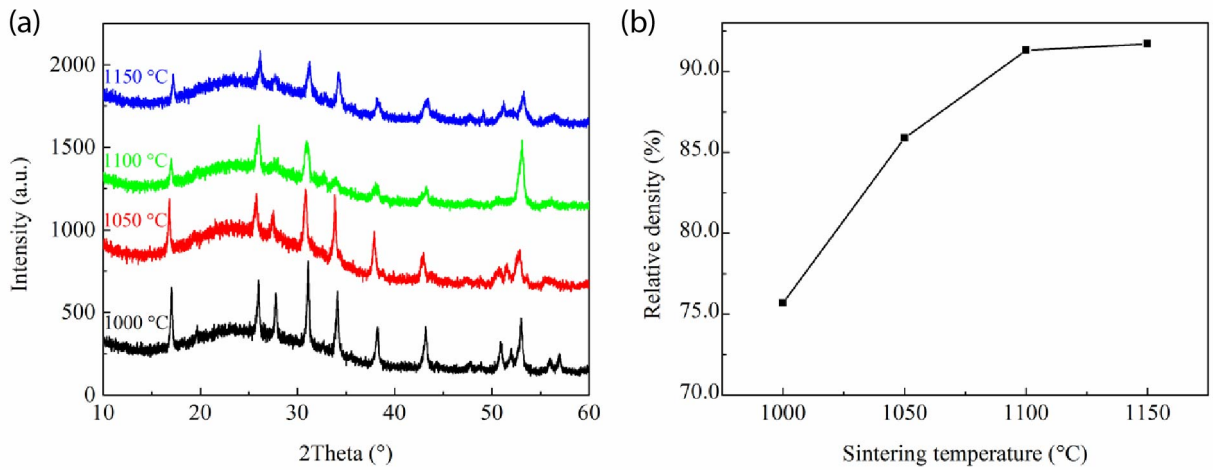

Figure 3.2: XRD patterns of LLZO pellets sintered at 1000, 1050, 1100, and 1150 ° C.(a). Density of LLZO pellet with sintering temperature (b).

3.3 Results and Discussion

The X-ray intensity through a sample exponentially drops following the Beer-Lambart law, $I = I_0 e^{d\mu}$, where $\mu = \mu$ (E) is the attenuation coefficient, E is the beam energy and d is the distance of propagation. Transmission needs to be optimized in order to obtain enough contrast for imaging and reconstruction. This can be achieved by manipulation of the beam energy (E) or the sample thickness (d)Aguesse et al. (2017). Synchrotron sources like those at APS-2BM allow a near-continuous selection of monochromatic beam energies or a polychromatic white beam with a broad band energy spectrum (Fig. 3.1a)(Hatzell et al., 2017). Due to the presence of heavy Z-elements in LLZO, the attenuation lengths for monochromatic beams energies available at APS-2BM are less than 200 μmPietsch et al. (2017). This is significantly smaller compared to the typical sample thickness used in this study ($\approx$1000 μm) and no transmission was observed for samples tested with a 35 keV monochromatic beam (Fig. 3.1b). In contrast, a polychromatic beam is able to distinguish between regions of high attenuation coefficient (ceramic phase) and regions of low attenuation coefficient (voids or lithium metal). The high incident energies attainable with the polychromatic white beam ensures good contrast between the ceramic and void

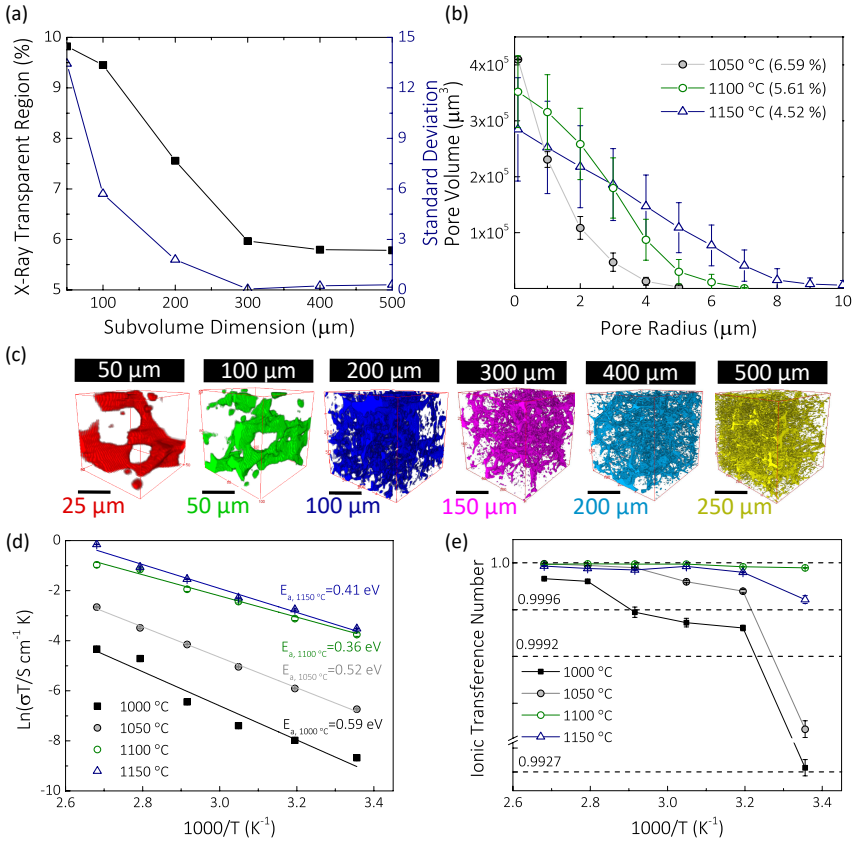

Figure 3.3: Field of view optimization for 3D reconstructions and solid electrolyte characterization. Small reconstruction volumes (50μm) cannot capture the heterogeneity of the material system and large reconstruction volumes (500μm) are computationally intense. The standard deviation between the experimentally measured density and porosity (tomography) is minimized for reconstructions ≈300μm (a). The pore size distribution for pristine LLZO samples sintered at different temperatures (b) and 3D representations of the X-ray transparent region (or pores) of the pristine LLZO (c). Different colors represent different reconstruction subvolumes between 50 and 500μm. Temperature dependent ionic conductivities and (d) transference number measurements for pristine LLZO (e).

region (pores and Li metal) (Fig. 3.1c). It should be noted that the shift to polychromatic beam is necessitated by the cut-off energy of the monochromatic beam (35 keV) at the APS 2-BM beamline.

The microstructural and grain size effects on Li transport and accumulation in LLZO electrolytes was systematically evaluated via sintering the electrolytes at different temperatures between 1000 and 1150 °C. The relative density of the ceramic electrolyte increased from 75% at 1000 °C to 92% at 1150 °C (Fig. 3.2). Previous reports have suggested a critical relative density of >93% can eliminate the formation of dendrites in LLZO electrolytesCheng et al. (2015); Tsai et al. (2016). However, further sintering at temperatures greater than 1150 °C did not yield any observable increase in density. Binarization of the tomography dataset enables quantitative analysis of the internal microstructure of the ceramic electrolyte. The binarization revealed two distinct regions. The first region is identified as the X-ray transparent region which is composed of pores and/or lithium deposits within the solid electrolyte. This region is transparent to x-rays because pores (air) and lithium metal both have low attenuation coefficients and thus are invisible when imaged with high-energy x-rays. The second region is the LLZO ceramic electrolyte which attenuates x-rays strongly. Herein, we specifically aim to monitor changes in the x-ray transparent region (pores and/or lithium metal) within the bulk of the solid electrolyte.

Geometric analyses are typically carried out on subvolumes of the total field of view as the analysis of the entire field of view is computationally not feasible. A systematic study was carried out to understand the effect of subvolume on the error of the geometric parameters estimated (Fig 3.3a). Small subvolumes cannot effectively capture the average microstructure and thus show very large standard deviations. By increasing the subvolume, heterogeneities in the material can be captured. A subvolume of 300 μm^3 was found to be optimum and was used for all subsequent analyses of the pristine samples. It should be noted that the estimation of the geometric parameters is strongly dependent on the binarization step, image processing, and analysisPietsch et al. (2018). Thus, to enable comparison across the samples, these steps have been kept consistent across all the samples.

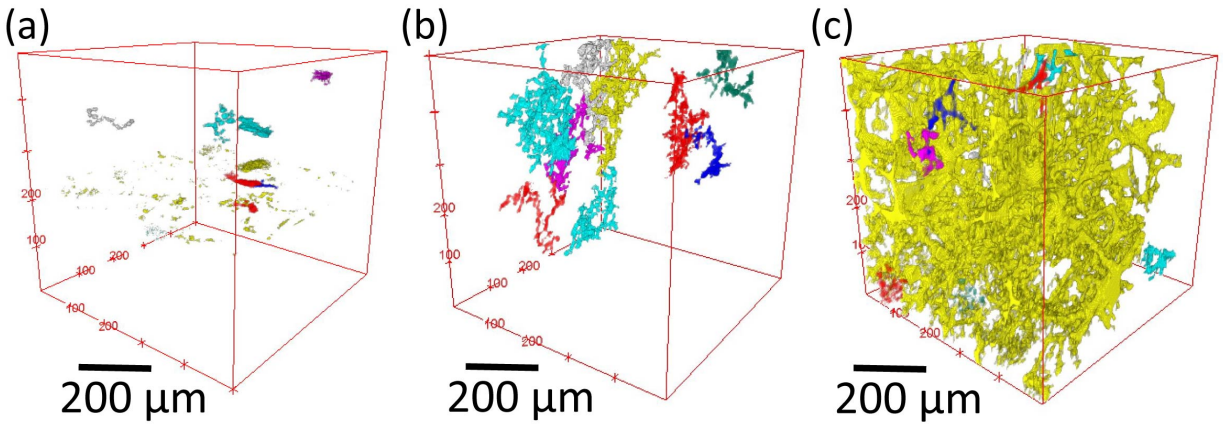

Figure 3.4: Ten largest connected pore structures for LLZO samples sintered at 1050 ° C (a) 1100 ° C (b) and 1150 ° C (c)

The X-ray transparent region can be identified for all sintered temperatures except for 1000 °C. Thus, it can be assumed that the solid electrolyte processed at 1000 °C is dominated by average pores sizes that falls below the resolution of the tomography setup used in this study ($\approx$ 0.65 μm), which is corroborated by the SEM images. The X-ray transparent region was calculated to be 6.59%, 5.61% and 4.52% for pristine samples sintered at 1050 °C, 1100 °C, and 1150 °C, respectively. As the samples are pristine, these values represent the fraction of void space inside the material, i.e. the porosity. The porosity trend matches the relative densities obtained from experiment well. The sample sintered at 1150 °C shows a broader range in in pore sizes than those obtained for samples sintered at 1050 °C (Fig. 3.3). It should be noted that the porosities identified here arise from fitting of the binarized dataset and are not linked to the resolution of the tomography set-up. Further analysis shows that the void structure in the samples sintered at 1150 °C is more connected compared to the samples sintered at lower temperatures (Fig. 3.4).

An increase in grain size was measured with increasing sintering temperature and the grains grew from $\approx$1 μm at 1000 °C to nearly $\approx$150 μm at 1150 °C (Fig. 3.5). Lithium ion diffusion kinetics along the grain boundaries is a large contributing factor to the formation of dendrites and the short-circuiting events in solid state batteries. The ionic con-

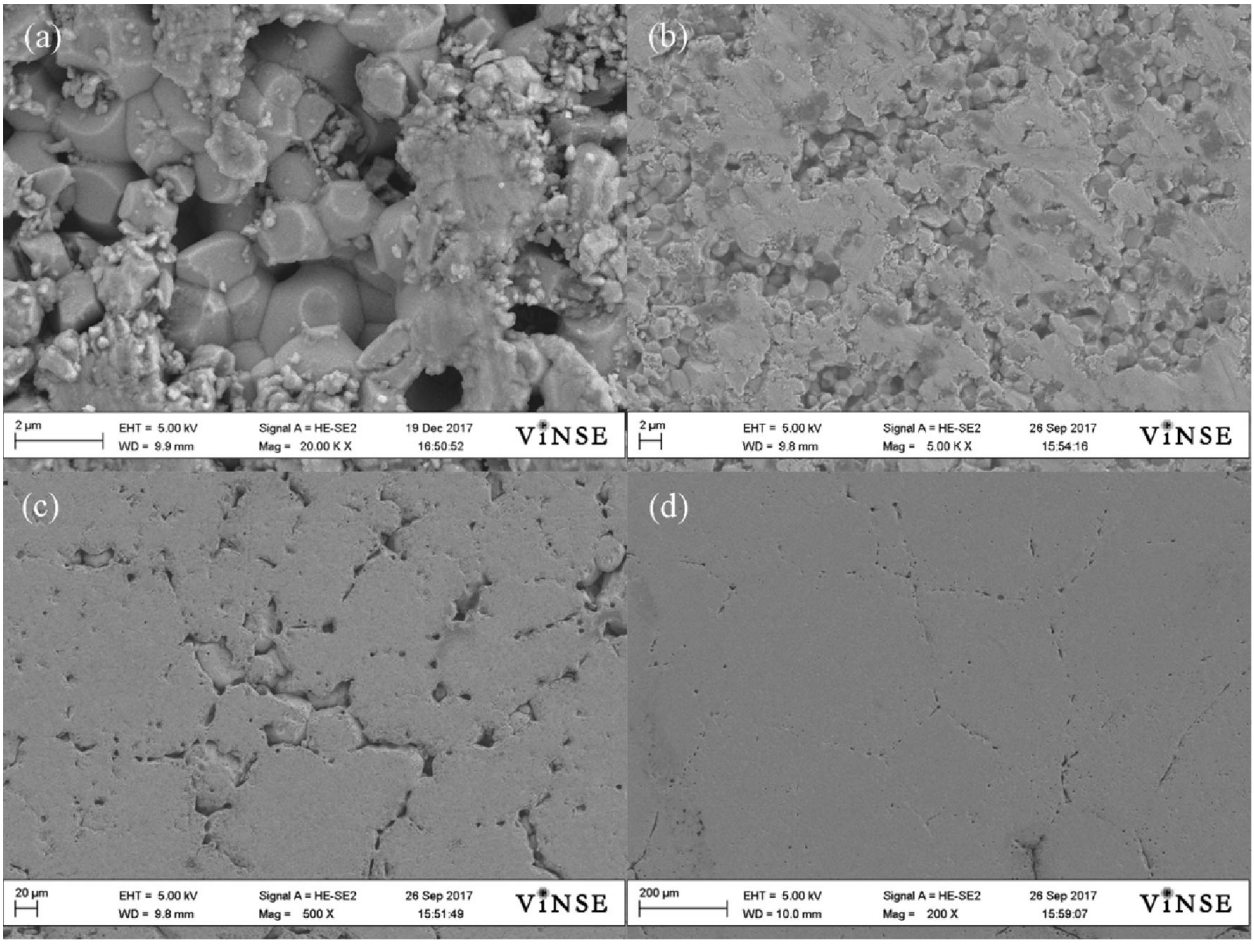

Figure 3.5: Microstructures of LLZO pellets sintered at different temperatures

ductivity for all samples increases from 25-100 °C and is proportional to the sintering temperature (Fig. 3.6). The crystal structure of the LLZO pellets demonstrates a shift in all peaks to higher angles when compared to the green LLZO powder. This could potentially be due to Li evaporation and possible alumina diffusion from the Al_2O_3 crucible, but there are no observed shifts in the XRD pattern. The increase in conductivity is therefore linked to modification in the microstructure of the electrolytes. Samples sintered at higher temperatures lead to larger densification, resulting in increased ionic conductivity. The highest room temperature ionic conductivity is about 1 x 10^{-4} S cm^{-1} for the pellet sintered at 1150 °C for 6 h. The activation energies decreased with sintering temperature from 0.59 (1000 °C), 0.52 (1050 °C), 0.36 (1100 °C), 0.41 eV (1150 °C), which are similar to

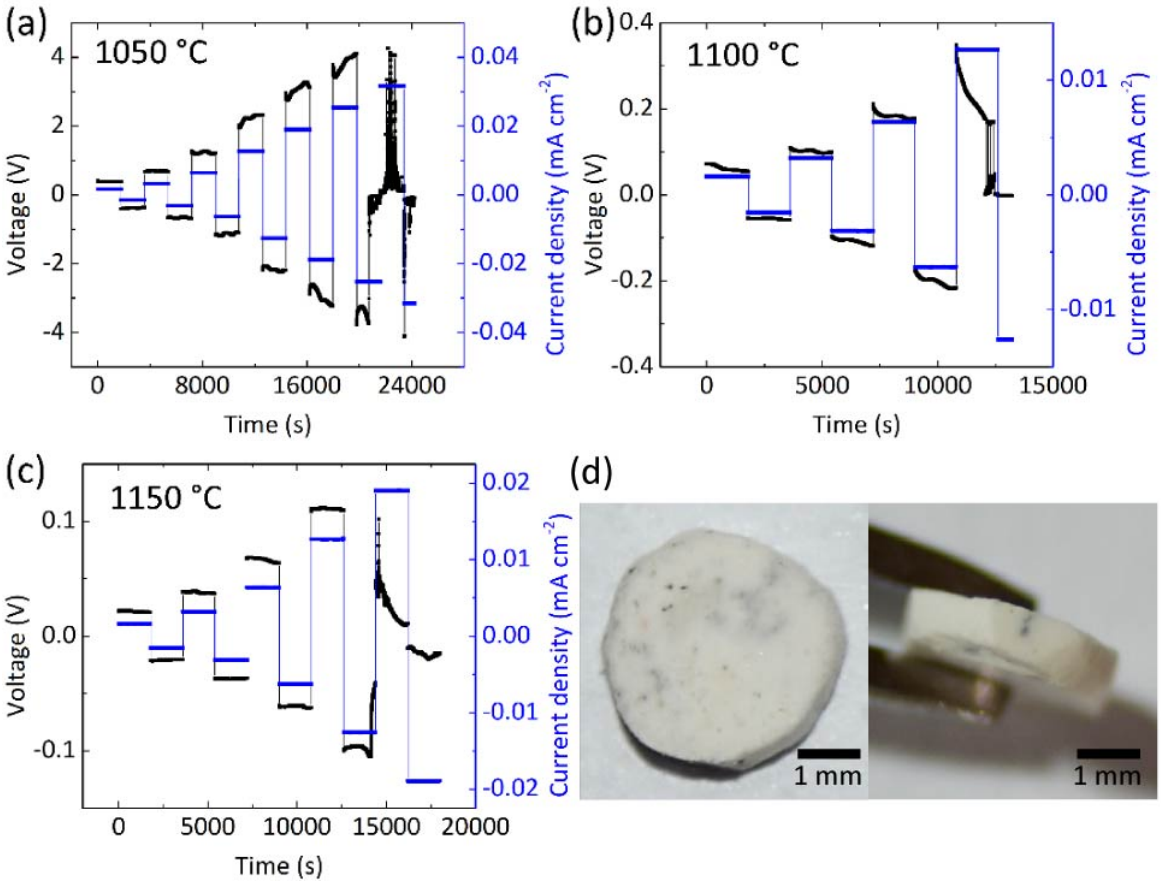

Figure 3.6: Galvanostatic cycling of Li/LLZO/Li symmetric cells at 20 °C with LLZO electrolytes sintered at 1050 °C (a), 1100 °C (b), and 1150 °C (c). The black line represents the applied voltage and the blue line represents the measured current response. Digital images of a cycled LLZO pellet on surface and cross section (d).

reported valuesEl-Shinawi et al. (2017); Xia et al. (2016). The electronic and ionic transference numbers are calculated as followsBuschmann et al. (2011):

$$t_e^- = \frac{\sigma_e^-}{\sigma_{total}} \quad and \quad t_{Li^+} = 1 - \frac{\sigma_e^-}{\sigma_{total}} \tag{3.1}$$

The electrolyte transference number increases with sintering temperature and nearly achieves a value of 1 at 1100 °C.

While the density of the electrolyte increases with sintering temperature, the critical current density (CCD) decreases (Fig. 3a-c). Grains and grain boundaries are more visible in samples sintered above 1050 °C. Li metal dendrites can penetrate solid LLZO along the grain boundaries and cause this short circuitYu et al. (2016); Sharafi et al. (2017, 2016); Yu et al. (2016); Kim & Srinivasan (2016); Yu & Manthiram (2017). At 1000 °C the CCD exceeds 0.08 mA cm^{-2} (Fig. S6). The CCD decreases to 0.025 mA cm^{-2} at 1050 °C (Fig. 3a) and 0.013 mA cm^{-2} at 1100 °C and 1150 °C (Fig. 3b and c). The voltage drops to almost zero after the CCD is achieved indicating an electrically shorted cell which no longer can be cycled. The samples sintered at higher temperatures had lower CCD values which can be attributed to their large grain boundaries which promote faster Li^+ transport. The presence of low resistance pathways provides a directed path for ionic current at the solid|solid interface. This leads to the accelerated Li deposition on these paths during plating and stripping and leads to a lower CCD value. Black spots can be seen on the cross-section and LLZO surface after CCD is achieved (Fig. 3.6). These spots are associated with metallic Li propagation and deposition.

X-ray tomography enables direct visualization of morphology changes in the interior of the solid ceramic electrolyte (Fig. 3.7). The use of a white beam significantly decreases the attenuation contrast sensitivity of the low Z elements (Li). This is because the bulk of attenuation occurs due to the high Z elements for the high incident energies encountered in white beam. Thus, it is impossible to identify directly the LLZO phase, lithium deposit, and the pore phase individually. While we cannot detect the difference between lithium and the pore region, we can detect differences in the ceramic and deposited lithium phase if it resides within the pore region and/or if it deposits in aggregation sizes greater the resolution limit of the experimental set-up ($>$0.65 μm).

To probe structural differences after solid electrolyte failure, we directly compared a pristine ceramic electrolyte with a failed sample (after failure). Ex situ comparison between

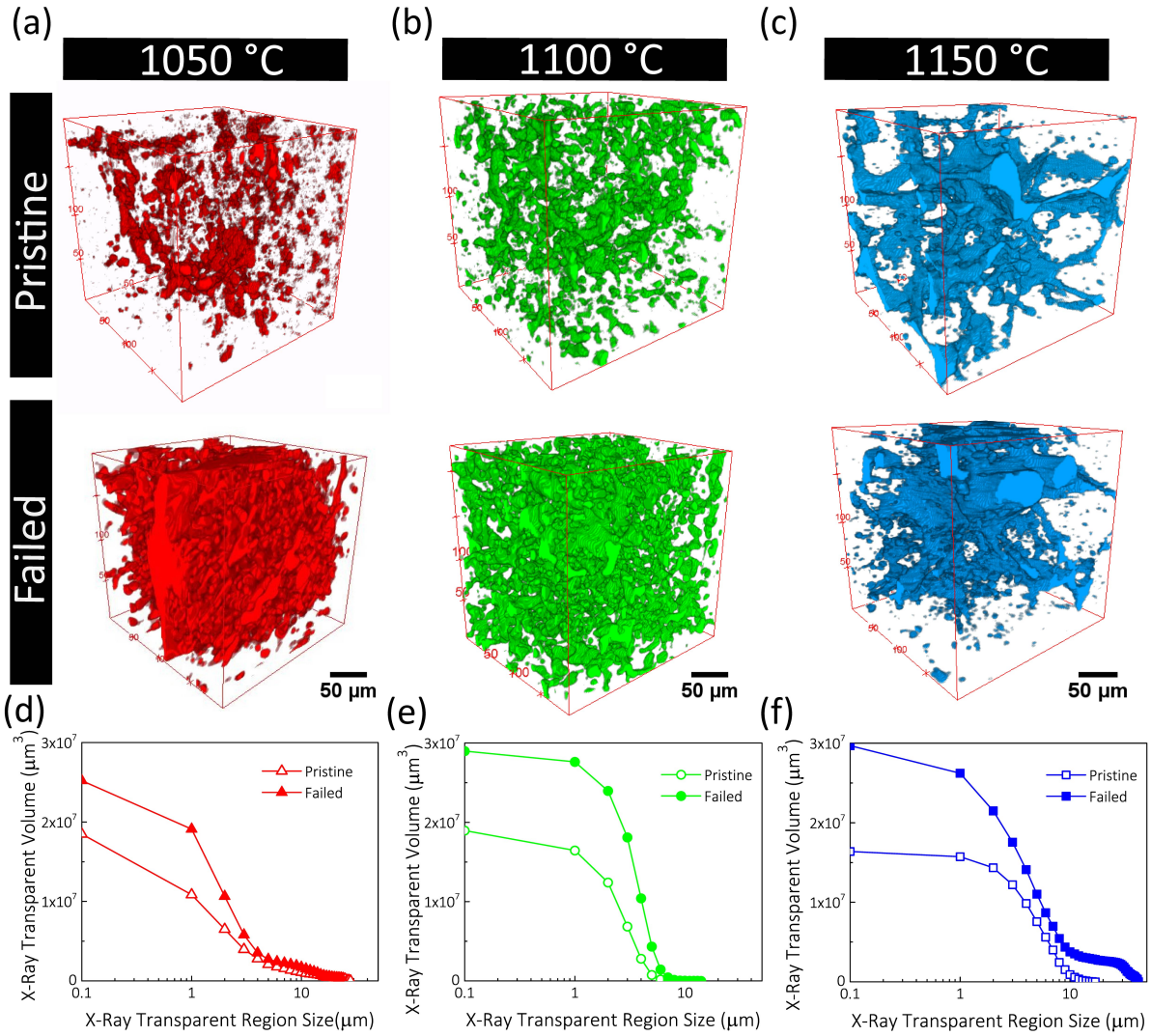

Figure 3.7: Microstructure changes after galvanostatic cycling. X-ray tomographic reconstruction of void phase in the interior of LLZO electrolytes sintered at (a) 1050 ° C (b) 1100 ° C and (c) 1150 ° C. Void phases before and after electrochemical tests are shown. Variation in the pore size distribution of the pristine and failed sample are shown in (d)-(f) for 1050 ° C, 1100 ° C and 1150 ° C respectively.

failed and pristine ceramic electrolytes enables quantitative comparisons between microstructural details (i.e. pores, grain, etc.). Any changes in the imaged void phase can be attributed to lithium deposition because lithium will be invisible to the high energy x-rays. Isolated lithium deposition can be seen in the individual subvolumes by an increase in the pore size distribution between the failed and pristine cells (Fig. 3.7d-f). A signifi-

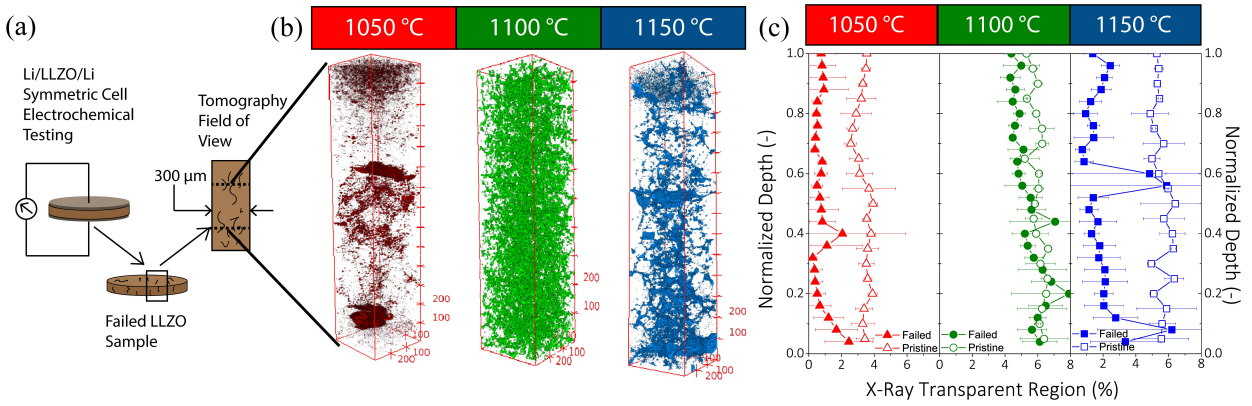

Figure 3.8: Sample field of View for sub volumes analyzed in terms of z-axis pore size distributions (a). Void structures obtained for failed samples (b) and fraction of X-ray transparent region for failed and pristine sample sintered at three temperatures (c).

cant change in the x-ray transparent region can be seen when evaluating across the entire thickness of the electrolyte (Fig. 3.8). We see distinct microstructural differences across the thickness of the electrolyte which is a potential signal of isolated lithium deposition within the electrolyte. Large deviations in x-ray transparent region are observed across the cross-section of the solid electrolyte in the failed sample, where a uniform porosity is observed in the pristine sample (Fig. 3.8). This heterogeneity across the sample suggests that metallic lithium can either be deposited in an isolated form or can accumulate within the pore region.

Ionic current at the Li/LLZO interface attempts to maximize flow through low resistance pathways. This preferential distribution of current leads to the formation of dendrites. While there are contradicting reports about the effect of solid electrolyte microstructure (grain character and pore size) on ionic conductivity and CCDSharafi et al. (2017); Porz et al. (2017), it is generally well understood that grain boundaries dictate transport. In this study, samples sintered at 1150 °C show a higher ionic conductivity and lower CCD then samples sintered at 1050 °C. This suggests that the failure could be microstructure driven. The larger distribution in pore sizes and large grain boundary size leads to greater

connectivity between pores in the solid electrolyte sintered at 1150 °C. The connectivity can be directly observed when imaging the largest ten connected pore structures within the electrolyte (Fig. 3.4). This connectivity, coupled with the higher ionic conductivity, facilitates lithium transport and dendrite growth within these microstructures and leads to a lower CCD. In contrast, even with a higher porosity, the sample sintered at 1050 °C shows a higher CCD due to the disconnected pore network. Local lithium deposition can result from leakage currents across the electrolyte or through the donation of an electron from the lattice oxygen network. It can also be caused by the presence of strong, local electric fields at the grain boundaries induced by the strain in the material. While this failure mode is not catastrophic like dendrite formation, it is expected to cause capacity fade due to loss of active material.

3.4 Conclusions

X-ray tomography is shown to be a powerful and versatile tool that can inform about sub-micron level microstructure within dense materials. Development of experimental setups that can allow for electrochemical measurements during sample rotation for tomography scans will enable in-situ studies for these systems. Further work will look into design and implementation of such experiments and is expected to provide significant insights into the failure mechanisms. Dendrite formation in solid state batteries is a microstructure driven event which is governed by the interfacial resistance and non-uniform contact between lithium metal and solid electrolyte. High-density electrolytes are favorable for increasing the critical current limit for solid electrolytes without sacrificing ionic conductivity. While lithium filament initiation can be avoided via low interfacial contact resistance, the formation of isolated lithium agglomerates within the interior is potentially a structurally driven phenomenon which is amplified when pore regions are connected within the electrolyte. Excess chemical potentials created within the interior of the electrolyte as a result of grain resistivity can potentially lead to isolated lithium deposition.

Furthermore, lithium within the electrolyte can be reduced either via leakage current or by recombination with a donor electron from the oxygen network. Further work on understanding localized deposition events created by the formation of holes, defects, and strain within the electrolyte will be important for achieving high critical current limits. In summary, density, grain size, and ionic conductivity of LLZO electrolyte increase with sintering temperature. Li penetration is observed using synchrotron X-ray tomography with white beam. Solid electrolytes with connected pore regions appear to promote dendrite formation and lower critical current densities.

Chapter 4

Tortuosity effects in Garnet-type $Li_7La_3Zr_2O_{12}$ Solid State Electrolytes

4.1 Introduction

Lithium-metal is the ideal choice for the anode in a lithium ion battery because it has the highest theoretical capacity (3,860 mAh g^{-1}), and lowest electrochemical potential (-–3.04V vs. SHE) Shen et al. (2018); Lin et al. (2017). All solid-state batteries may provide an avenue for enabling lithium metal batteries, if a solid separator (electrolyte) could be engineered to be thin (20-200μmMcCloskey (2015)), strong ($\geq$ 6GPa**?**), and highly conducting (10^{-3} S/cm) Janek & Zeier (2016); Yu & Manthiram (2017); Dawson et al. (2018). The rapid development of structural families of highly conducting solid electrolytes including agryditesCulver et al. (2018); Wenzel et al. (2013, 2015a), garnetsMurugan et al. (2007), and LISICON/NASICON-type structuresKanno & Murayama (2001); Kanno et al. (2000); **?** has stimulated research in solid state batteries. However, competitive energy densities and long lifetimes are necessary to displace the current state-of-the-art (liquid-based batteries).

Poor power densities in all-solid state batteries is associated with low ionic conductivity in the solid electrolyte. However, recent advances from the material science and inorganic chemistry communities have led to new solid ion conductors that are competitive with liquid electrolytes. Thus, the low energy densities and power densities are likely due to ineffective transport at the numerous interfaces in a solid state battery. There are two types of interfaces that exist in a solid state battery: (1) intrinsic and (2) extrinsic. Intrinsic interfaces are natural interfaces that occur in a material (i.e. grains, defects, void spaces) and extrinsic interfaces occur at material junctions (electrode|electrolyte)Hatzell et al. (2017); Dixit et al. (2018a). The nature of these interfaces can contribute to kinetic

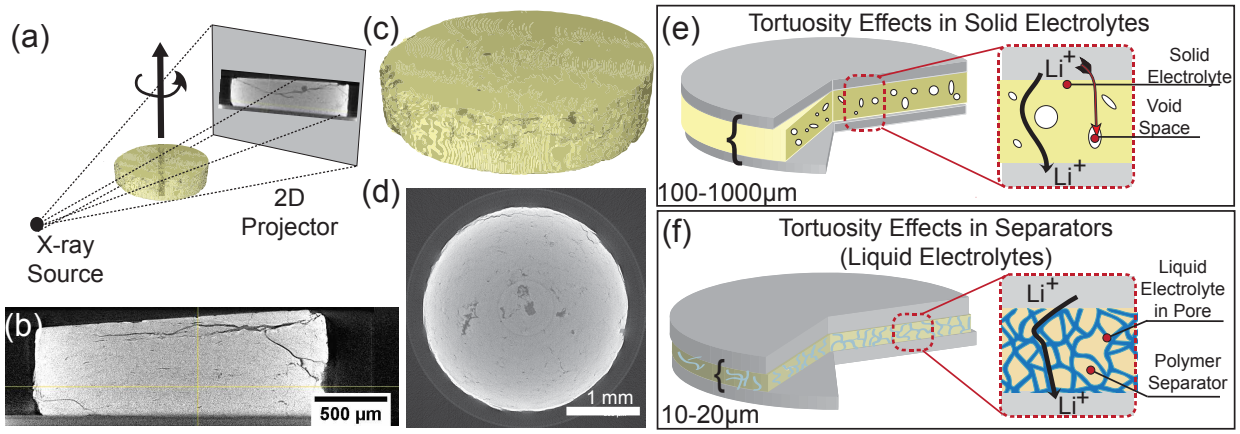

Figure 4.1: Tortuosity in a solid electrolyte is largely impacted by the formation of void phases or defects that emerge during processing (a). A porous separator is traditional batteries, and the pore region is filled with a liquid electrolyte (c). Synchrotron x-ray tomography enables probing the underlying microstructure of dense solid electrolyte characterized by heavy elements (c). A side view (d), a representative 3D reconstruction (e), and a cross sectional view of a solid electrolyte imaged at the Advanced Photon Source (f).

or mass transport limitations within the assemblyKasemchainan & Peter (2018) and can lead to large localized concentration and polarization gradients and accelerate failure. Examples of extrinsic interface instabilities include: (1) chemical decomposition and the formation of a solid electrolyte interphase at the electrode|electrolyte interfaceLotsch & Maier (2017); Han et al. (2016), (2) regions of excess and deficient lithium contentWang et al. (2017, 2016), and (3) poor or delaminating-type contact at the interface which can contribute to non-uniform current distributions and localized degradationOhta et al. (2007); Takada et al. (2003); Zheng et al. (2017); Zheng & Hu (2018). Each of these phenomena are likely to cause catastrophic cell failure (short circuit) through the formation of dendrites. Understanding how these interfaces and defects contribute to transport limitations in all-solid state batteries will enable design strategies for high performing batteries.

Lithium ion transport occurs through the electrolyte-filled pore phase in conventional

battery systems with polymer separators (Fig. 4.1b)Lagadec et al. (2016, 2018); Zahn et al. (2016). In contrast, the pore phase in a solid state battery is ion blocking because ions only transport through the solid phase (Fig.4.1a)Hlushkou et al. (2018); Shen et al. (2018). The presence of void phases acts as roadblocks to ion migration and decreases the flux through the system. Furthermore, these void spaces lead to the formation of highly tortuous pathways in the electrolyte and non-uniform ion distribution in the system. These generate strong, local concentration and polarization gradients in the system and can lead to electrolyte degradation. DFT studies have shown that the presence of such regions inside the electrolytes can lead to lithium metal deposition, especially near cracks and pores Tian et al. (2018). Further advancement of solid state batteries requires an acute understanding about how ions move within a solid electrolyte and strategies for controlling transport. The solid electrolyte tortuosity is a critical parameter that governs the effective transport properties. Tortuosity in battery electrodes is widely studied and follows the empirical Bruggeman' relationshipChung et al. (2013). Directional and anisometric tortuosity can emerge in battery electrodes as a result of the active material morphology. Directional tortuosity can affect the attainable power density in a battery and local transport rates. The latter mechanism can contribute to accelerated failure in battery systems Ebner et al. (2013); Kehrwald et al. (2011).

Tortuosity is conventionally estimated either with electrochemical methods Thorat et al. (2009); Vijayaraghavan et al. (2012) or by computational modeling of microstructures obtained with advanced imaging methods (X-ray tomography or FIB-SEM) Ebner & Wood (2014); Cooper et al. (2016). Effective transport properties derived using electrochemical techniques can be scaled to describe tortuosity in an electrode or electrolyte. These methods are comparatively quick and inexpensiveLandesfeind et al. (2018a,b); Kaiser et al. (2018); Kato et al. (2018). However, these methods are less versatile at

obtaining local or directional information. Tortuosity estimation from microstructural data can provide unique insight into local transport anisotropy and can help pinpoint bottlenecks to transport. There are several studies that focus on measuring tortuosity in composite cathodes for all solid state batteries. The cathode for a solid state battery is unique in that it contains the active material in addition to a glass and/or ceramic ion conductor. Results using analytical techniques reveal that lower tortuosity and better power densities are achieved when the ion conducting phase represents $\geq$40% of the cathode phaseKaiser et al. (2018). Studies using FIB-SEMChoi et al. (2018); Hlushkou et al. (2018) emphasize the impact of the cathode microstructure on cell performance. The presence of void phases that emerge because there is no liquid electrolyte in the electrode contributes to increases in the tortuosity. To overcome these challenges (void phase formation) at extrinsic interfaces (electrode|electrolyte) will require advanced processing and manufacturing techniques.

While there is growing interest in understanding the impact of extrinsic interfaces on transport in all solid state batteries, there are numerous intrinsic interfaces in solid ion conductors which play a significant role on ion transport. These intrinsic interfaces include grains, defects, and void spaces within the solid electrolyte and can govern localized concentration and polarization gradients within the cell. Understanding and controlling concentration gradients across the solid ion conductor as well as at the solid|solid interface is paramount for long lasting solid state batteries. In this study, we investigate the tortuosity of garnet-type $Li_7La_3Zr_2O_{12}$ electrolytes with the specific aim of understanding the impact of micropores on the tortuosity of the solid electrolyte. The microstructure of different garnet-type electrolytes processed between 1050°C and 1150°C are obtained using synchrotron X-ray tomography (Fig. 4.1c)Shen et al. (2018); Hatzell et al. (2017). The use of high energy x-rays enables full penetration of the sample and the genera-

tion of 3-D microstructures with sub-micron resolutions (Fig. 4.1d-f). COMSOL^{TM} and an open-source software TauFactor enable simulations of ionic fluxes in the solid electrolyteCooper et al. (2016). We evaluate idealized electrolyte microstructures (generated in-silico) to probe the impact of pore ordering (symmetry and packing) on ionic transport properties.

4.2 Experimental Methods

4.2.1 Material Synthesis and Electrochemical Studies

LLZO is prepared by mechanochemcial synthesis method Shen et al. (2018). Briefly, stoichiometric quantities of lithium, lanthanum and zirconium salts were ball-milled. 10% excess lithium salt was employed to mitigate lithium evaporation during the heating step. The ball-milled powder was sintered at 900 $^\circ$ C for six hours. This powder was subsequently ball-milled again to reduce the particle sizes. 12 mm pellets were made from this powder using a pellet press. The green pellets were sintered at three different temperatures: viz. 1050 $^\circ$ C, 1100 $^\circ$ C and 1150 $^\circ$ C for 12 hours respectively. The sintered pellets were polished using a sand paper to a thickness of $\approx$ 500 μm, and a diameter of $\approx$ 3-4 mm. The polishing was carried out to facilitate the tomography studies and ensure adequate transmission. Ionic conductivities were measured using ion blocking symmetric setup. Impedance measurements were carried out between 1 MHz to 1 Hz with 50 mV amplitude. Li|LLZO|Li symmetric cells were assembled for galvanostatic charge-discharge tests. Cycling of these cells were carried out over periodically increasing currents.

4.2.2 X-Ray Tomography

Synchrotron X-Ray tomography was carried out at APS 2-BM beamline. Tomography projections were obtained during 180 $^\circ$ of sample rotation in a white beam mode. Reconstructions, ring filtering and zinger removal was carried out using the TomoPy softwareGürsoy et al. (2014). Binarization and subsequent data analysis has been carried out in ImageJSchneider et al. (2012b). Cubical subdomains of side 50 μm were extracted from

the entire reconstruction. At least three subdomains of each size were evaluated to obtain statistics for the estimated physical properties. The BoneJ pluginMunch & Holzer (2008a) was employed to estimate the porosity and the pore size distributions of the solid electrolytes.

4.2.3 Ideal Domains

Ideal domains were developed in 3D CAD modeling software to enable understanding the effect of packing and arrangement on ion transport in these systems. Cubic domains of 50 μm size with isotropic body-centered cubic (BCC), face-centered cubic (FCC) and hexagonal close packed (HCP) pore structures were generated. Anisotropic domain included a parallelopiped (PP) structure consisting of tubular pores along the XX direction. Domains of these structures were developed at porosities ranging from 0.625% to 60%. Analysis of parallelepiped structures was also conducted with a constant porosity of 50% but varying the number and orientation of tubes in a pattern. Additionally, domains of body-centered cubic structures with different numbers of unit cells were compared to determine if the number of unit cells played a part in isotropic systems.

4.2.4 Computational Fluid Modelling

Computational fluid modeling was performed using COMSOL Multiphysics. Computational domains were obtained by subtracting the pore networks obtained from tomography reconstructions from regular cubic domains within COMSOL. Alternatively, for the ideal cases the domain geometry was directly imported into COMSOL. Subsequently, the geometry was subjected to refinement and cleaning to produce the meshed domains. Domain volumes of 50x50x50 μm^3 were created. A typical mesh contained between 1E5 to 5E5 elements and 2E4 to 3E4 vertices. Due to the complex nature of the imaged pore networks the refinement and cleaning steps necessary for each mesh different. Three domains were evaluated for samples sintered at each temperature and the average values are reported. Small concentration gradient was applied along the three principal axes for

each domain. The following equation was solved during the simulations:

$$\frac{\partial c}{\partial t} + \nabla . N_i = R_i \tag{4.1}$$

$$N_i = -D_i \nabla c_i \tag{4.2}$$

where, c_i is the concentration of species i, t is time, N_i is total flux, R_i is reaction source term, D_i is diffusion coefficient of species i. The steady state flux was computed and the effective diffusion coefficient was computed using Equation 2. This effective diffusion coefficient was correlated to primary diffusion coeffcient using the formulaShen & Chen (2007):

$$D_m = \frac{D_i}{\tau^2} \tag{4.3}$$

where D_m is the effective diffusion coefficient, D_0 is the ideal diffusion coefficient and τ is the tortuosity. D_0 was computed from Nernst-Einstein equation for LLZO and was found to be 2.15E-11 m^2/s.

4.3 Results and Discussion

The underlying microstructure of LLZO influences ion transport and electrochemical properties in the electrolyte Shen et al. (2018). Porosity and pore sizes of the electrolytes have been obtained from the reconstructed tomography data. Porosity decreases with increasing sintering temperature due to denser packing of the material (Table 4.1). However, the largest observed pore size is seen to increase with increasing sintering temperature. This can be correlated to the electrochemical performance of the material system. Ionic conductivity of LLZO increases from 0.54 μS/cm for the sample sintered at 1000°C to 97.9 μS/cm for the sample sintered at 1150°C. The increase in conductivity arises from the denser material packing seen in the systemYamada et al. (2016); El-Shinawi et al. (2017). In contrast, the critical current density is found to decrease from $\sim$90 $\mu A/cm^2$ to $\sim$15 $\mu A/cm^2$ for these samples. Understanding differences in transport through these

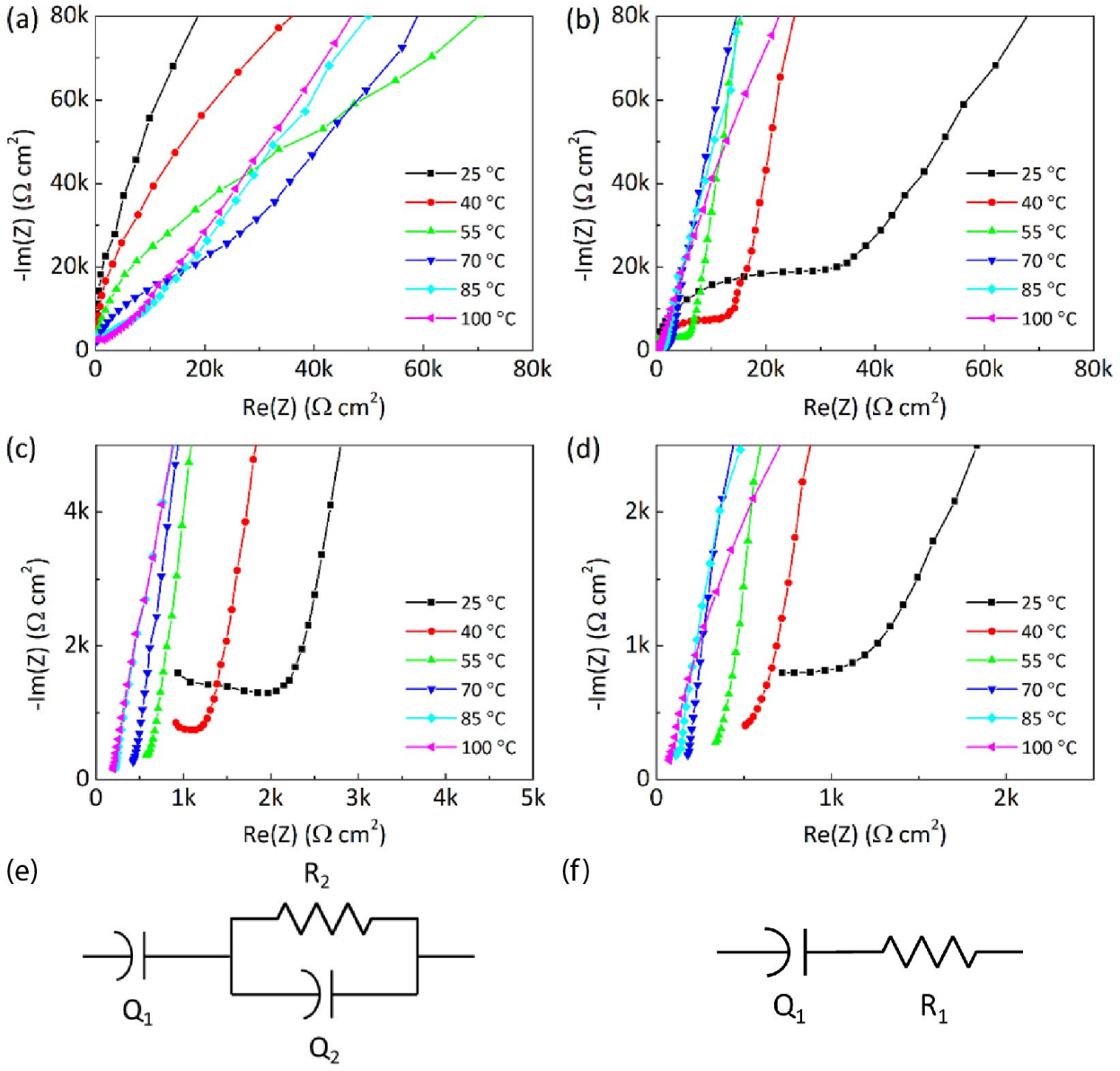

Figure 4.2: Nyquist plots for total ionic conductivity measurement for LLZO pellets sintered at (a) 1000 °C; (b) 1050 °C; (c) 1100 °C; (d) 1150 °C. (e) Equivalent circuit used for fitting low temperature data where high frequency semi-circle is visible (f) Equivalent circuit used for fitting high temperature data where high frequency semi-circle is not visible

varying microstructures can provide a lens into understanding the impact of micropores on local ionic and polarization gradients.

The pore network for the sample sintered at 1050° C shows smaller discrete pore network

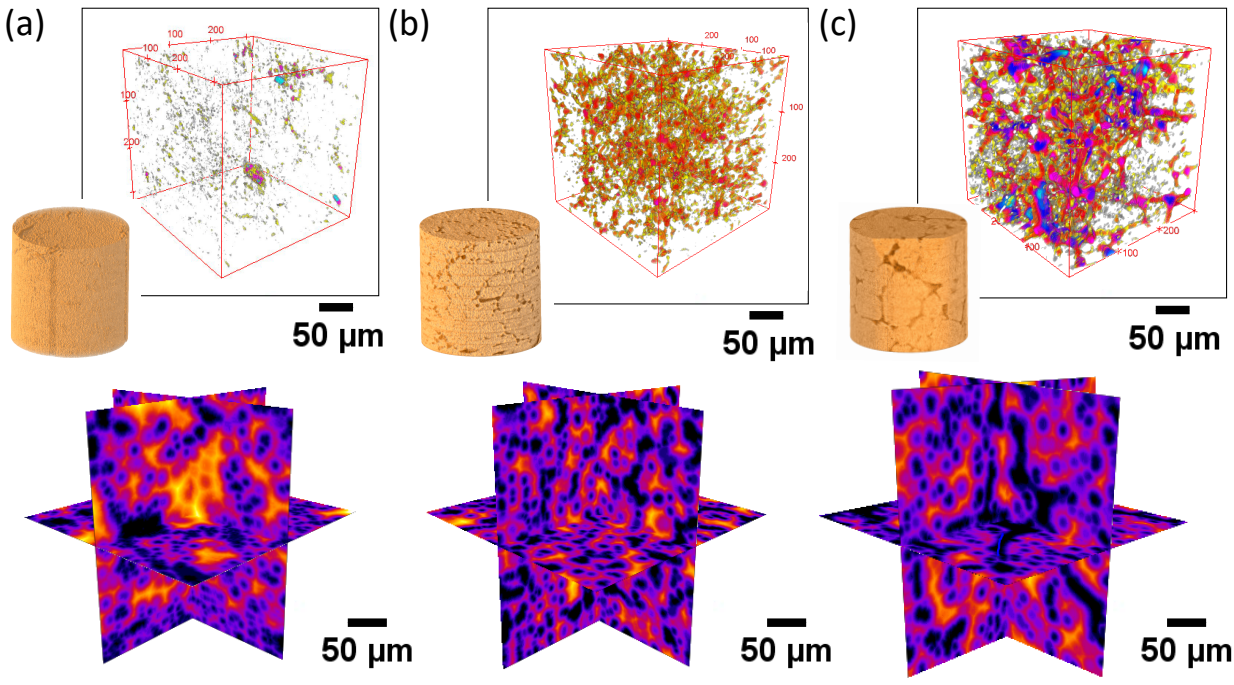

Figure 4.3: Pore-size color and distance maps for microstructure computed from reconstructed tomography data for SSEs sintered at (a) 1050 °, (b) 1100° and (c) 1150°C. 3D rendering of the electrolytes are also shown.

Table 4.1: Physical and Electrochemical Properties of LLZO Electrolytes

Sintering Temperature (°C)	Porosity (%)	Pore Size (μm)	Conductivity (μS/cm)	C.C.D. (μA/cm^2)
1000	24	-	0.54	>90
1050	14	8	3.9	40
1100	8	9	81.1	12
1150	7	12	97.9	15

(Fig. 4.3a). Pore network for the sample sintered at 1000° C could not be obtained from the tomography data. This could be due to the pore size in this sample falling under the resolution of the beamline. As the sintering temperature is increased, the pore sizes are increased and a greater connectivity is observed in the pore structure (Fig. 4.3b-c). This is further confirmed by evaluating the local thickness of the solid phase in the three samples. Local thickness is defined as the radius of the largest sphere that can be inscribed at a point while remaining within the domainHildebrand & Rüegsegger (1997). Cross

sectional views of local thickness are shown with lighter regions signifying larger local thickness (solid phase region) (Fig. 4.3a-c). The sample sintered at 1050°C shows largest light regions suggesting a larger solid domain. The intensity and spread of local thickness decreases with increasing sintering temperature suggesting that the solid phase in the samples sintered at 1150° C is less contiguous and is interspersed by the pore network. The pore networks shown here are representative volumes to highlight the differences in the microstructure. The average porosity trend is consistent with the experimentally measured porosities (Archimedes' method) as previously reported Shen et al. (2018) and decreases with increasing sintering temperature.

Mass transport in electrolytic systems can be described with the movement of mobile ionic species, material balances, current flow and electroneutrality. The flux density in a typical electrolyte can be given asNewman & Thomas-Alyea (2012):

$$N_i = -z_i u_i F c_i \nabla\Phi - D_i \nabla c_i \tag{4.4}$$

where, N_i is the flux of species i, z_i is the valency of species i, u_i is the mobility of species i, F is the Faraday's constant, c_i is the concentration of species i, $\nabla\Phi$ is the potential gradient, ∇c_i is the concentration gradient for species i and D_i is the diffusion constant. The first term on the right hand side of Equation 4.4 represents the migration term while the second term represents the diffusion term. Typically, these driving forces act in opposing directions and the transport of ions depend on the net electrochemical potentials. The effective transport properties needs to be scaled by tortuosity to capture microstructure-driven effectsDoyle & Newman (1996). To estimate the tortuosity through the solid electrolytes, it is necessary to compute the flux of Li ion through the samples. Only concentration gradients are applied in the simulations studies to reduce the computational efforts required. Incorporating both the driving forces in the simulation greatly increases the complexity due to the interdependence of the variables and exponentially increases the

computing power required. Since tortuosity is a property of the microstructure, neglecting the electric driving force in the system should not influence its measurement. Thus, the reduced form of Equation 4.4, i.e. Equation 4.1 and the material balance in Equation 4.2 are solved.

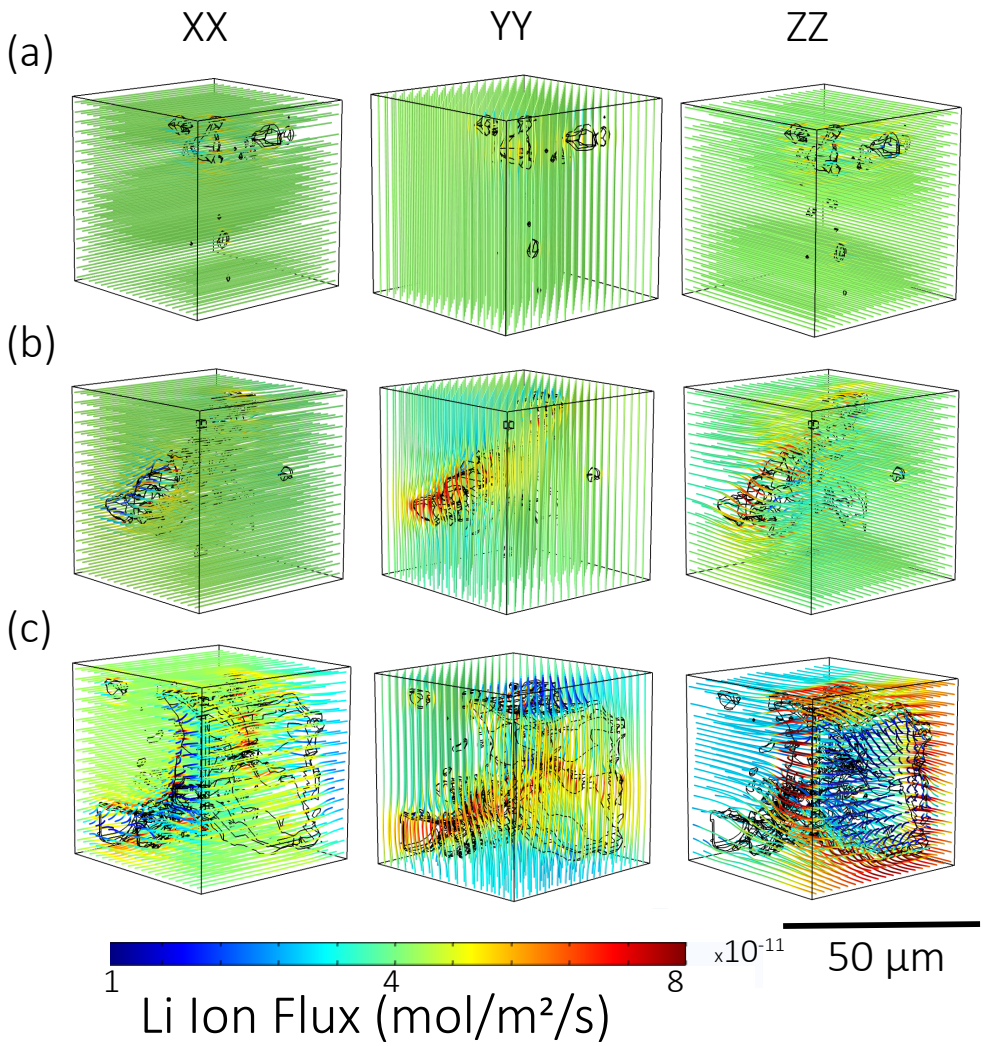

Figure 4.4: Li ion flux streamlines along three principal axes for microstructral domains of real LLZO electrolytes sintered at (a) 1050° (b) 1100° and (c) 1150°C

The results shown are for sample domains of 50x50x50 μm^3 size. Increasing the sample domain size to 100x100x100 μm^3 does not significantly change the simulated tortuosity values for samples sintered at 1050°C and 1100° C, while the tortuosity values for the sample sintered at 1150° C shows a slight increase. The dependence of physical prop-

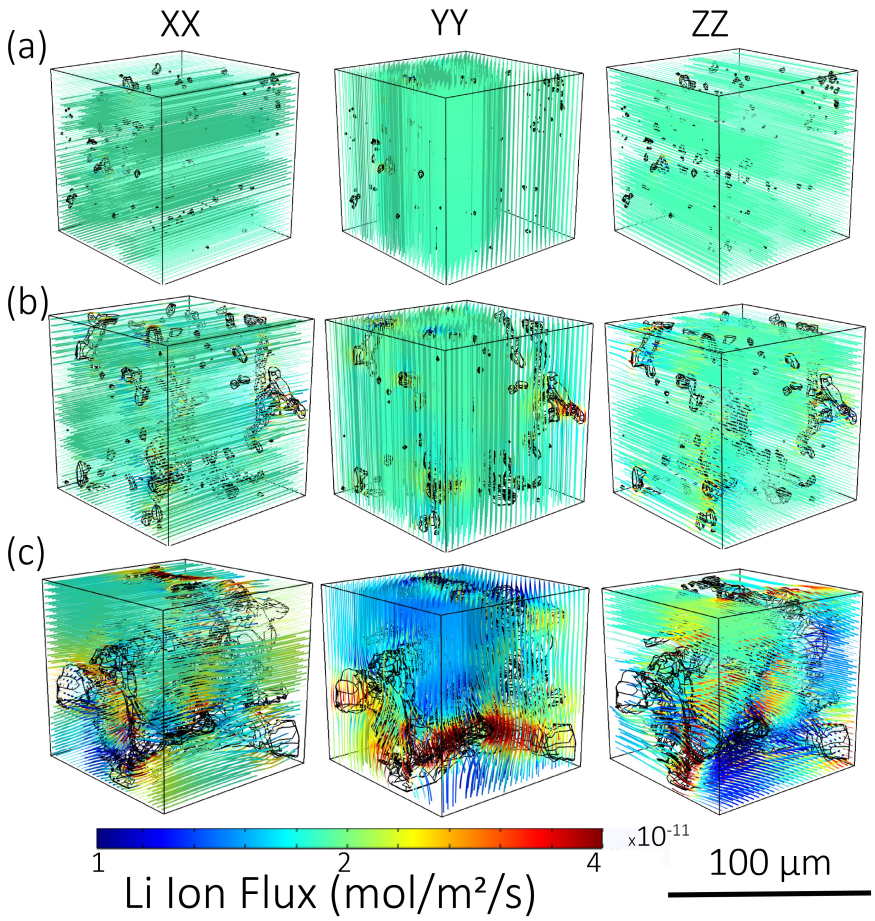

Figure 4.5: Li ion flux streamlines along three principal axes for microstructural domains of real LLZO electrolytes sintered at (a) 1050 °C (b)1100 °C and (c) 1150 °C. Domain size for these simulations is 100x100x100 μm^3.

Table 4.2: Simulated tortuosity for LLZO electrolytes

Sintering Temperature °C	XX	YY	ZZ
1050 (50x50x50 μm^3)	1.00	1.00	1.00
1100 (50x50x50 μm^3)	1.02 ± 0.006	1.03 ± 0.007	1.03 ± 0.001
1150 (50x50x50 μm^3)	1.05 ± 0.07	1.07 ± 0.09	1.06 ± 0.08
1050 (100x100x100 μm^3)	1.00	1.00	1.00
1100 (100x100x100 μm^3)	1.03 ± 0.02	1.03 ± 0.03	1.03 ± 0.02
1150 (100x100x100 μm^3)	1.05 ± 0.07	1.07 ± 0.09	1.06 ± 0.08

erties on the domain subvolume has been previously reportedShen et al. (2018); Pietsch et al. (2018). However, meshing of the reconstructed domains is extremely difficult for these larger volumes and subsequent computing power necessitated did not allow for

studying domains larger than 100x100x100 μm^3. Lithium ion flux is found to be uniformly distributed along the three principle axes for the sample sintered at 1050° C. This arises from the fact that this sample has small pore sizes that are dispersed through the material. The simulated tortuosity in this case is close to one and identical for all the directions (Fig. 4.4a). At 1100°C, anisotropy in Li ion flux is observed with the sample showing higher flux along the YY directions in certain regions compared to XX and ZZ directions. Correspondingly, small variations are seen in the tortuosity of the system along the three directions. At 1150° C, the pore cluster size is large and considerable variations in Li ion flux are observed along the three principle axes. The large, clustered pores lead to a non-uniform distribution of Li ion flux and higher values and wider spread is observed in the tortuosity along the three directions compared to the samples sintered at lower temperatures.

The anisotropic flux distribution arising due to higher tortuosity leads to a significant variation in the local concentration of Li ion in the electrolyte for the samples sintered at 1150°C. This results in strong concentration and polarization gradients at the edges of the pore structures. DFT studies suggest that the presence of excess electrons on pore surfaces can enable lithium metal reductionTian et al. (2018). These localized electrons on pore surfaces coupled with the strong concentration gradients arising from non-uniform mass transport can initiate deposition of lithium into the pores. These results confirm earlier work and sheds light on the lower critical current densities observed in these samplesShen et al. (2018). The samples sintered at lower temperatures do not show this anisotropic flux distribution and hence show higher critical current densities.

Tortuosity factors evaluated using the open-source package TauFactor were used to corroborate simulated values. The tortuosity factor computed with TauFactor is determined from the ratios of steady-state diffusive flux through a pore network, F_P to that of an equivalent fully dense control volume with the same physical properties. The software

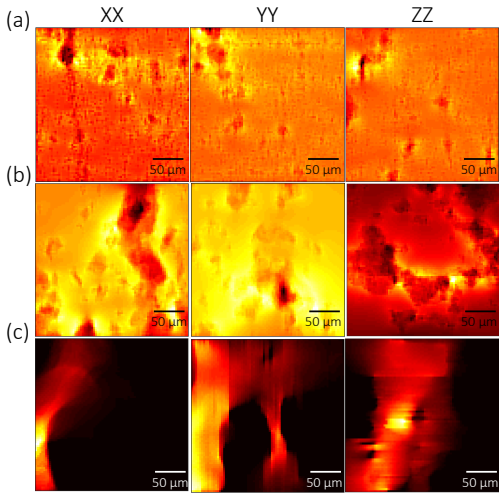

Figure 4.6: Projection of total flux along three principal axes for real LLZO electrolytes sintered at (a) 1050°C(b) 1100° C and (c) 1150° C. Scale bar is 50 μm and is common for all figures. The same domains shown in Figure 4.4 are used for this analysis. These results are obtained from TauFactor software.

computes these fluxes using the following equations:

$$F_P = -A_{CV} D \frac{\epsilon}{\tau} \frac{\Delta C}{L_{CV}} \tag{4.5}$$

$$F_{CV} = -A_{CV} D \frac{\Delta C}{L_{CV}} \tag{4.6}$$

where, D is the diffusivity of the dense phase, C is the local concentration, A_{CV} and L_{CV} are cross-sectional area and the length of the control volume respectively. The software considers each voxel as a distinct mesh element which mitigates the need for resampling and meshing. The samples sintered at 1050°C show a uniform distribution of flux through the three principal directions (Fig. 4.6a). The images represent the sum of the flux through the three principal directions projected onto a single slice. Brighter regions represent regions with high flux. The tortuosity value predicted by the software was $\sim$1.01 in all the directions. For the samples sintered at 1100°C, the simulated tortuosity values increased

to ∼1.06 and directional anisotropy becomes apparent along the ZZ direction where very low flux (high tortuosity) is observed (Fig. 4.6b). This corroborates well with the simulated data (Fig. 4.4). Large directional anisotropy and significantly higher tortuosity values were observed for the samples sintered at 1150°C. Tortuosity values predicted by this software were 9.13, 2.03 and 2.76 along the XX, YY and ZZ directions. While these values are considerably higher than those observed by the earlier method the trends are consistent. Both methods confirm that the magnitude of the electrolyte tortuosity increases and the anisotropy in directional tortuosity increases with increasing sintering temperature. The differences in tortuosity values predicted from the two methods could arise due to meshing differences as well as computational differences in the two methods.

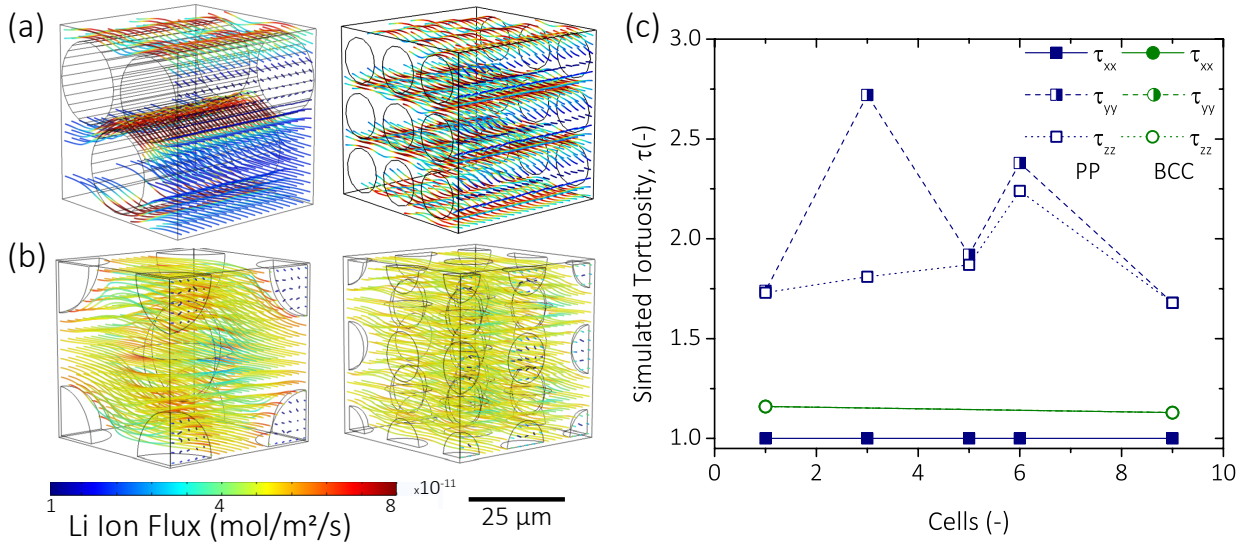

Figure 4.7: Flux streamlines for Parallelopiped pore configurations with 3 and 9 pore units at constant porosity (a) Flux streamlines for BCC pore configurations with 1 and 9 pore units at constant porosity (b) Simulated tortuosities along three principal axes for parallelopiped and BCC pore configuration with varying pore units (c).

Ideal solid electrolytes are completely dense with 0% porosity. However, practically achieving perfectly dense electrolytes is challenging and requires energy consuming high temperature sintering processes. The previous sections highlighted how the concentration profiles and ionic flux are impacted by the presence of pores. Thus, there may be opportunities for tailoring the ionic pathway between the electrode and electrolyte via

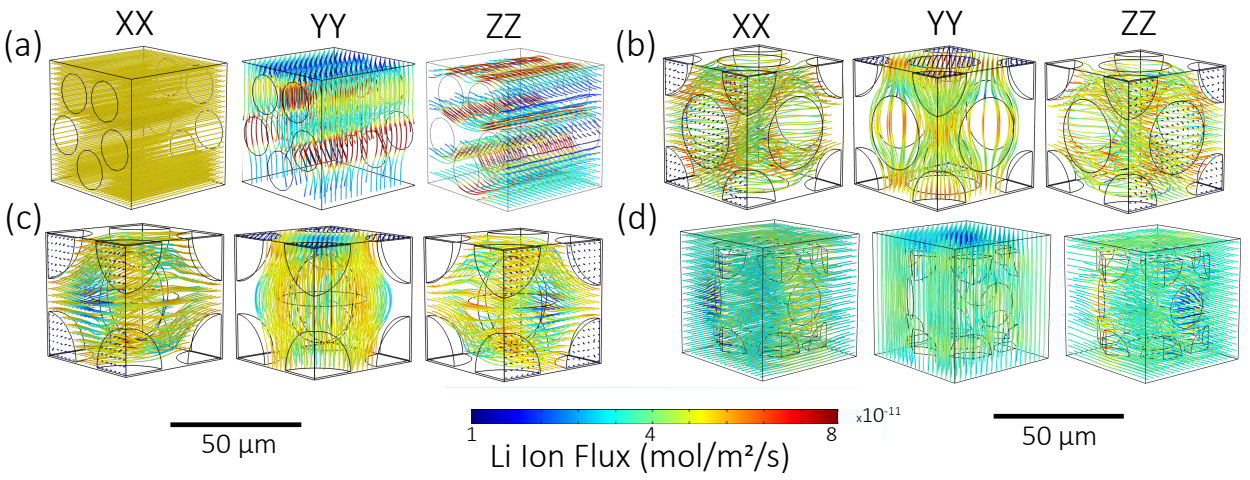

Figure 4.8: Flux streamlines for (a) Parallelopiped, (b) FCC, (c) BCC and (d) HCP pore configurations at constant porosity of 40%

tailoring the pore size and distribution. Symmetry and alignment in pore structures have been leveraged to develop high rate electrodesBillaud et al. (2016). Three times higher specific capacities are attained in electrodes with aligned pores than non-architectured electrodes. A similar principle can be leveraged in the design of solid electrolytes to enhance their rate performances.

To evaluate the impact of pore microstructures, domains with BCC, FCC, HCP and PP configurations of pores were developed *in-silico* over a range of different porosities. PP structure yields uniform striped fields along the direction of ion transport. This configuration is similar to the configuration identified as the upper-bound for the Wiener constraints of effective transport properties of porous mediaFerguson & Bazant (2012). The configuration can be equated to a parallel resistor network leading to maximized transport in this configuration. The simulated tortuosity along the XX direction is ≈ 1 for the PP case due to this reason. Along the transverse (YY and ZZ) directions, the tortuosity is higher to due the obstructions arising due to the longitudinal pores. This can be equated to the lower bound configuration of the Wiener constraints with phases arranged in a transverse fashion. This equates to a series resistance circuit lowering the effective trans-

port. Increasing the number of pores at a constant porosity results in oscillating tortuosity along the transverse directions. These variations arise from generation of symmetric microstructures (equivalent to upper bound configuration) within the domain. This can be visualized by the 3-cell and 9-cell architectures for PP configuration (Fig. 4.7a, 4.8). Ion flow paths observe a symmetric arrangement along the YY direction (streamlines shown) leading to low tortuosity value. However, non-symmetric phase arrangement is observed along the ZZ direction and the ion flow needs to be divided around each pore element leading to an increased tortuosity in this direction. In contrast, ion flow path sees identical structures while transversing along YY and ZZ directions for 9-cell architecture and hence identical, low tortuosity values are seen.

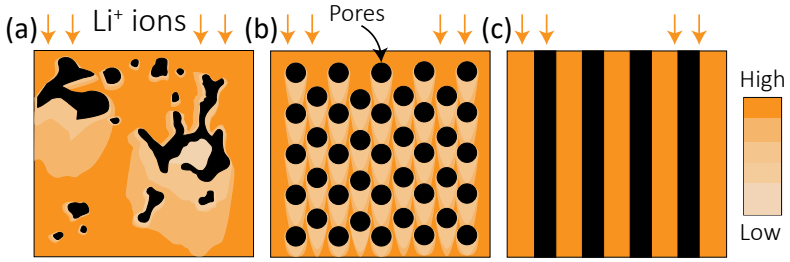

Figure 4.9: Distribution of Lithium ion flux through solid electrolyte for microstructures with (a) realistic pore network (b) isotropic pore network and (c) anisotropic pore network.

The tortuosity values remain constant irrespective of the number of repeat units of the pore structure at a constant porosity (Fig 4.7b,c) for domains with isotropic distribution of pore structures. This results from uniform flow profiles that are generated around the pores. It is observed that BCC pore structure offers a higher average flux through the system with smaller gradients in the transverse direction. Much higher concentration gradients are seen along ion transport through transverse directions of PP pores which can have detrimental effect to the stability and electrochemical performance of the electrolyte as discussed earlier. However, transport through parallelopiped domains along the direction of the pores results in maximum flux as well as uniform distribution. Real electrolyte microstructure are highly anisotropic with no regular shapes (Fig. 4.9a).

These result in strong flux gradients within the system that can lead to lithium deposition and failure. Isolated, isotropic pore domains (Fig. 4.9b) alleviate some of these, however flux gradients cannot completely be eliminated. Connected and aligned pore domains (Fig. 4.9c) can theoretically achieve high and uniform flux distribution through the solid electrolytes. These results reinforce the importance of controlling the alignment and symmetry of pore domains in improving transport rates through the electrolyte.

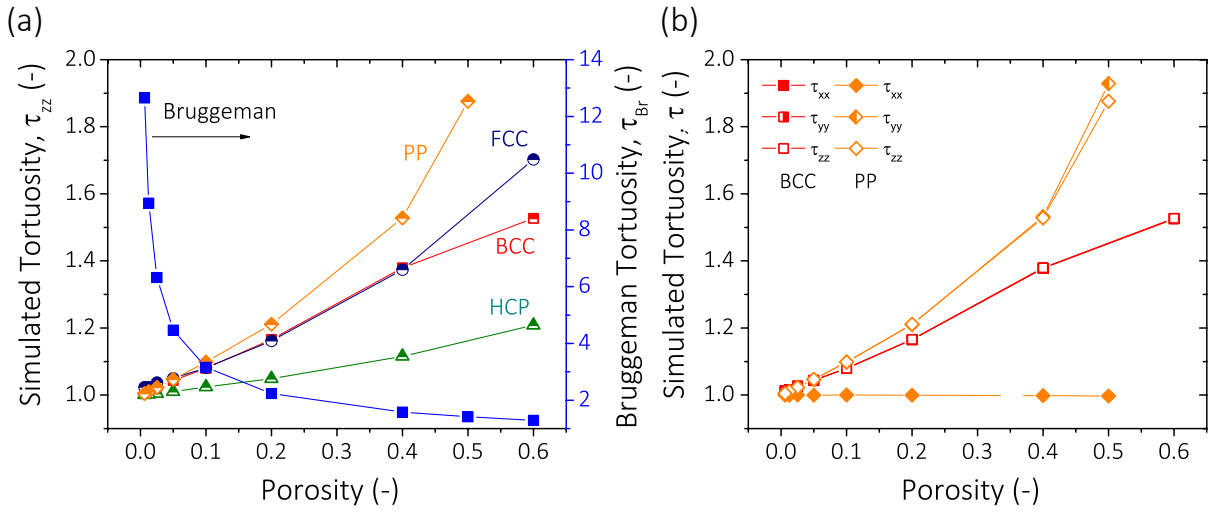

Figure 4.10: (a) Variation in simulated tortuosities along the ZZ direction for different pore configurations over a range of porosities. The Bruggeman tortuosity is also plotted on the secondary Y-axis as a reference (b) Directional anisotropy in tortuosity for the PP and BCC pore networks

Tortuosity decreases with increased packing of the pores (FCC>BCC>HCP) for isotropic domains (Fig. 4.10a). This effect can be explained by the Hashin-Shtrikman constraints on effective transport properties of porous mediumFerguson & Bazant (2012). According to these constraints, maximized transport can be achieved by core-shell type of configuration with phase with lower conductivity occupying the core site. BCC, FCC and HCP configurations achieve this kind of configurations and hence show lower tortuosity and higher transport rates. Further, HCP configuration results in highest packing for the solid phase and subsequently shows the lowest tortuosity values. To further understand the

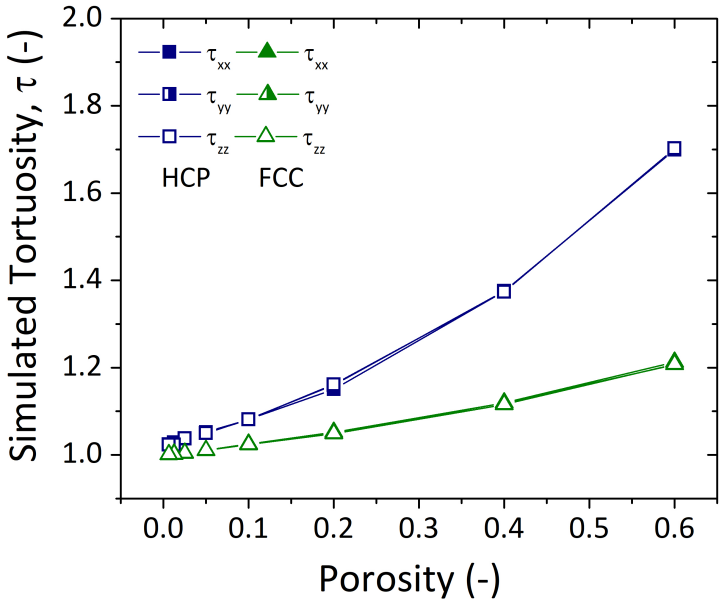

Figure 4.11: Simulated tortuosity along three principle axes for HCP and FCC pore configurations

effect of packing configurations, domains with a wide range of porosities were simulated to enable predictions of porosity-tortuosity relationships for solid electrolytes. The tortuosity increases with increasing porosity as expected. Modifying the Bruggeman' relationshipBruggeman (1937) to reflect that the transport is occurring through the solid phase, we get:

$$\tau = (1 - \epsilon)^{(1-\alpha)} \tag{4.7}$$

Using this equation, the exponent α is estimated to be 1.457, 1.59, and 1.209 for BCC, FCC and HCP pore structures (Fig. 4.10b, 4.11). A reasonable fit is obtained for all the datasets using these values. Further, these values are consistent over the three directions for these three microstructures. This is expected as these possess isotropic pore distributions. Bruggeman exponents can be correlated to the connectivity of the transport phase with higher Bruggeman exponent values signifying lower connectivityVadakkepatt et al. (2016). HCP configurations shows the lowest Bruggeman exponent implying a well

connected solid phase. This result corroborate the higher flux rates observed in this configuration. FCC configuration shows the highest Bruggeman exponent indicating a less connected domain. In contrast, the Bruggeman' exponent is 1, 1,93, and 1.89 in the XX, YY and ZZ direction for the PP case. The exponent of 1 along the XX-direction signifies a fully connected solid phase which is optimum for transport. Further, the wide spread of Bruggeman' exponents show the impact of alignment and symmetry in the reducing the tortuosity. Based on these results, it is proposed that architecturing pores along the direction of ion transport can help reduce the tortuosity and maximize the flux through the system. Further work on engineering these kinds of microstructures with solid electrolytes is needed.

4.4 Conclusions

Effect of microstructure on ion transport in LLZO solid electrolytes was evaluated. Computational Fluid Dynamic simulations are run on COMSOL Multiphysics software to evaluate the tortuosity factor. Samples sintered at lower temperatures have discrete pore structure with small feature sizes that lead to homogenous flux distributions within the sample. Samples sintered at higher temperatures show larger pore sizes with a connected pore network. These samples show higher tortuosity as well as greater directional anisotropies. These lead to development of large local concentration and polarization gradients that can initiate and accelerate failures in these systems. The tortuosity factor values are further corroborated with an open-source software. Ideal pore microstructures are evaluated by *in-silico* development of computational domains with BCC, FCC, HCP and PP distributions. Aligned pores along the transport direction can minimize tortuosity and improve the rate performance of solid state electrolytes.

Chapter 5

Synchrotron Imaging of Pore formation in Li Metal Solid State Batteries Aided by Machine Learning

5.1 Introduction

Metal anodes (Li, Na, Mg) benefit from high specific energy because the entire electrode volume is activeHatzell et al. (2020). However, high reactivity in liquid electrolytes and non-uniform electrodeposition severely limits its application. Electrodeposition instabilities and dendrite formation in liquid binary electrolytes can occur because of transport limitations and the formation of concentration gradients at high charge rates. Prior theoretical studies have hypothesized that using a rigid solid electrolyte with a shear modulus 2 $\times$ larger than metallic lithium could suppress lithium penetrationMonroe & Newman (2003). Numerous experimental studies contradict this resultShen et al. (2018) and demonstrate that both soft (polymers, sulfides) and hard (oxides) solid electrolytes can impact the the morphological evolution of lithium metal during electrodeposition and dissolutionHarry et al. (2014); Wang et al. (2019); Zhang et al. (2020); Chang et al. (2015). Thus, a solid electrolyte's stiffness or shear moduli (G) cannot completely describe lithium filament formation and growth in solid state batteries. Instead, unstable electrodeposition is related to chemo-mechanical properties at the anode-electrolyte interface that drives non-uniform Li^+ transport.

Mechanical stress at the anode-electrolyte interface impacts ion transport and reaction kinetics that governs lithium metal morphological evolutionHatzell et al. (2020); Schmalzried & Janek (1998); Kazyak et al. (2020). Recently, a set of chemo-mechanical design rules were proposed to achieve solid electrolytes with pressure-driven dendrite blocking or density-driven dendrite suppressing propertiesFu et al. (2020); Mistry & Mukherjee (2020a). Spatiotemporal evolution of an electrodepositing interface can be tai-

lored via control over the solid electrolyte's partial molar volume of Li^+ (V_{Li^+}) and shear moduli relative to lithium anode properties ($V_{Li^+}/V_{Li}, G_s/G_{Li}$). However, this theoretical framework assumes uniform material properties, continuous interfaces, and defect and contamination free materials. In reality, both the solid electrolyte and lithium metal contain chemical impurities and microstructure heterogenities (grains, defects, etc.) which will influence the morphological progression of the reaction interface.

Above a critical current density, Li metal morphological changes can lead to interface deterioration, contact loss, and an increase in the overpotentialYonemoto et al. (2017). Recently, contact lossKrauskopf et al. (2019) (Fig. 5.5a) and pore formationSpencer Jolly et al. (2020); Kasemchainan et al. (2019) in Li metal upon stripping (Fig. 5.5a) was experimentally observed using *ex situ* scanning electron microscopy and *in situ* x-ray tomography. Pore or "void" formation upon stripping may be the origin for interface deterioration, yet, there is little known about how pores form. It has been postulated that upon Li dissolution, vacancies can form at the anode|electrolyte interface. Limited self-diffusion of lithium atoms in metallic lithium can lead to accumulation of "voids" at high discharge currents (Fig. 5.5b) Hiratani et al. (1988) and possibly vacancy and pore gradients within the lithium metal anodeSchlenker et al. (2020); Jow & Liang (1983). With the exception to a few low resolution experimental observations (Fig. 5.5a), there are no *in situ* experimental observations that track pore evolution dynamics and gradients within lithium metal electrodes.

High-resolution imaging of lithium metal at buried solid|solid interfaces is challenging because low atomic number elements weakly interact with experimental probes. Additionally, for *in situ* and *operando* imaging, proximity to highly absorbing/scattering materials (steel current collector, LLZO electrolyte) significantly impedes extracting morphological information from lithium metal. Maintaining a stable, air-free environment during operation is also a key experimental challenge. Filament formation is typically character-

ized by *ex situ* optical/electron microscopy due to these experimental challengesLewis et al. (2019); Porz et al. (2017). Recent *operando* optical imaging of Li|LLZO|Li systems demonstrated how the morphology of the filament differed depending on the operating regime (e.g. current density) which suggests that there are a variety of failure mechanismsKazyak et al. (2020). While microscopy and optical imaging offer valuable material insight, it is challenging to resolve dynamic material processes that occur in sub-surface and bulk materials. Synchrotron X-ray tomography (XRT) is a potential method to resolve three-dimensional morphological transformations with adequate spatial and temporal resolutions relevant to solid state batteriesMaslyn et al. (2019); Harry et al. (2014). Recently, XRT was used to track morphological variation in Na- metal anodes during cycling which showed clear evidence of pore formation mechanismSpencer Jolly et al. (2020). There is some literature that leverages synchrotron imaging to evaluate transformations in lithium metal**?**Adair et al. (2020); Taiwo et al. (2017), but the reported studies use low density systems (graphite, polymer) in combination with lithium metal. Enabling lithium metal visualization by synchrotron imaging in combination with a high-density solid electrolytes (LLZO) has not been previously reported.

This work uses imaging techniques to track morphological transformations at lithium metal/solid electrolyte interfaces. A garnet (LLZO) solid electrolyte is chosen as the model electrolyte to image because it is one of the most stable solid electrolytes, and has minimal interphase formation. In order to process the low-contrast images (lithium metal and pores) advanced image processing and machine learning methods were developed for effective segmentation to extract quantitative metrics of the electrodes (current density, porosity and their spatial distribution) during cycling (Fig. 5.5c-e). Furthermore,*in situ* experiments allow for tracking Li metal morphological transformations at stripping and plating electrodes simultaneously. Advanced visualization combined with electrochemistry represents a important pathway toward resolving the role non-equilibrium defects and microstructure heterogenities impact rate capabilities of lithium metal anodes.

Spatial variation in microstructrural properties of the solid electrolyte are correlated to the hotspot generation within the lithium metal (Fig. 5.5a). Mesoscale simulations of the solid electrolyte reveal heterogeneous transport and mechanical properties. Failure onset at Li|SE interfaces occurs at regions with lower transport and mechanical properties.

5.2 Experimental Methods

5.2.1 Material Synthesis and Cell Preparation

Conventional solid-state method was used to synthesize $Li_{6.5}La_3Zr_{1.5}Ta_{0.5}O_{12}$ was synthesized using solid state reaction process. Stoichiometric amounts of appropriate solid precursors were ball-milled. Resultant mixture was dried and sintered at 900 °C. Ball-milled sintered powder was pressed in 3 mm diameter pellets and re-sintered at 1130 °C for ten hours. The pellets were subsequently polished to diameters of 1.5 mm for synchrotron experiments. Cells were assembled in a custom built *in situ* cell at the Advanced Photon Souce. Lithium metal foil was melted on both sides of the LLZO pellet for 30-45 min prior to assembly. No pressure was applied during Li metal integration with LLZO. Heating tape was coiled around the in-situ cell and a nominal temperature of 60 ° was maintained around the cell during experiments. Electronic impedance spectroscopy was carried out between 1 MHz and 100 mHz with a 50 mV amplitude. Galvanostatic plating/stripping tests were carried out for 30 minute duration at 6 and 25 μA cm^{-2} respectively. Impedance measurements were taken after individual plating and stripping cycles. Tomography scans were also taken at the end of each plating/stripping cycles. Diffraction pattern were measured between 10° - 70° (step size: 0.01°).

5.2.2 Synchrotron X-Ray Tomography

Tomography experiments were carried out at end station 1-ID-E endstation of the Advanced Photon Source at Argonne National Laboratory. Monochromatic, parallel beam (76.11 keV) was used for the tomography experiments. The imaging detector for tomography consist of a Pointgrey Grasshopper3 USB3 camera (GS3-U3-23S6M) , 5x objective

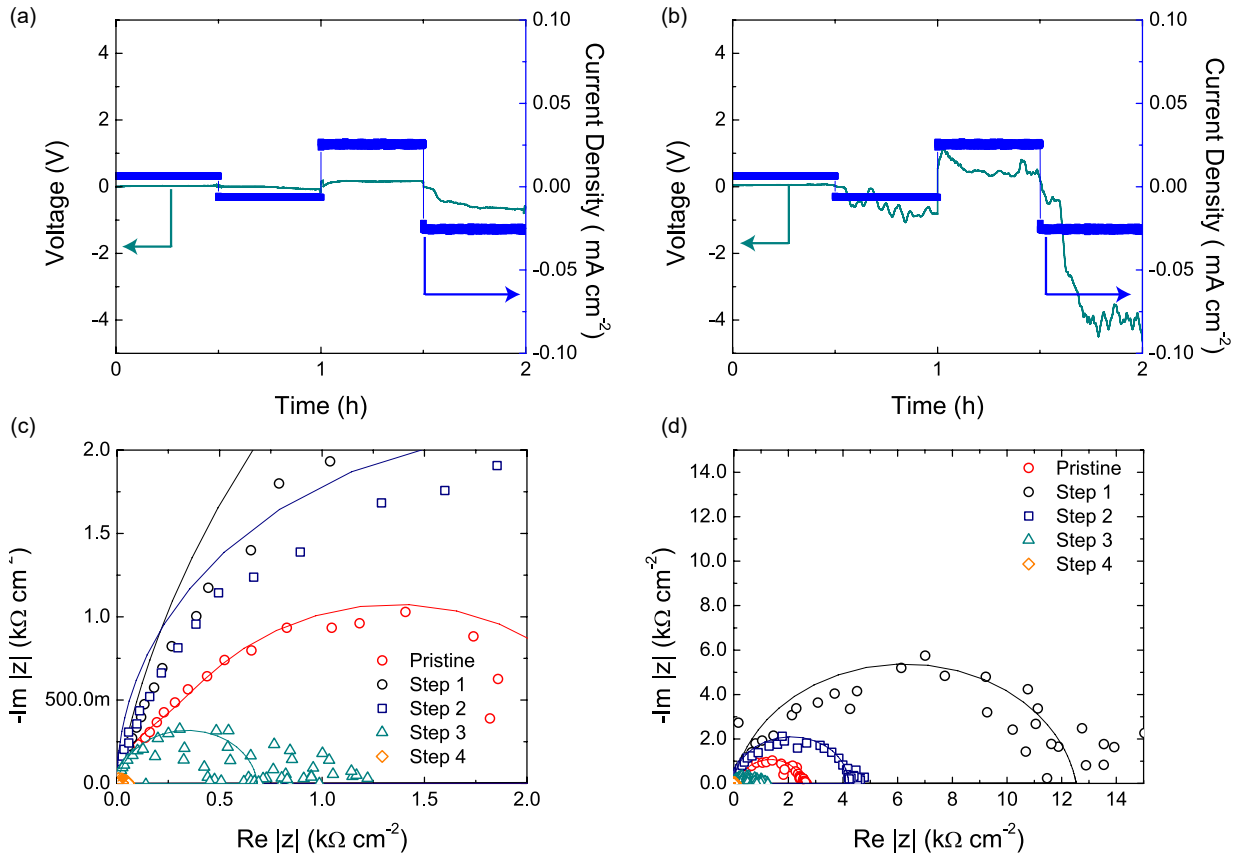

Figure 5.1: Galvanostatic cycling response of two samples (a-b) of Li | LLZO | Li cells run in *in situ* cell. First plating/stripping cycle is run at 5 μA cm^{-2} and second plating/stripping cycle is run at 26 μA cm^{-2}. The nominal environmental temperature of the cell was $\approx$ 60 °C. (c-d) Impedance scans for pristine cell and at end of each plating and stripping step for two samples.

lens and 25 μm LuAG:Ce single crystal scintillator. The measurement setup provides 1.8mm x 0.8mm x-ray beam size which fits into the field-of-view (FOV) of the detector with 1.172 μm pixel resolution which can cover the entire cell assembly. The in-situ cell was rotated from 0° to 360° and projections were recorded with exposure time of 0.17 s at every 0.1° steps. The total imaging time was approximately 15 minutes.

5.2.3 Data Analysis and Reconstructions

Tomography reconstructions are carried out using an in-house code TomoProcKhounsary et al. (2013) which is performing the pre-processing and post-processing steps in MAT-

LAB and using the GridRec reconstruction algorithmDowd et al. (1999) in between. Subsequent image analysis is carried out using ImageJ and DragonFlySchneider et al. (2012b). Identical post-processing and analysis steps were employed on all the datasets. All quantification measurements were carried out using MATLAB and python.

5.2.4 COMSOL Simulations

Transport simulations were run on COMSOL Multiphysics 5.4. A thin electrolyte domain was segmented into two regions; a central hot-spot region and the surrounding. An electrode domain of 5x20 μm was simulated adjacent to the electrolyte. Hot-spot region was provided a boundary current density 10x compared to the adjacent electrolytesMai et al. (2019); Yu & Siegel (2018). The physical domain and relevant boundary conditions are depicted graphically (Fig. 5.2). Steady state simulations were run and the resultant flux profiles are visualized.

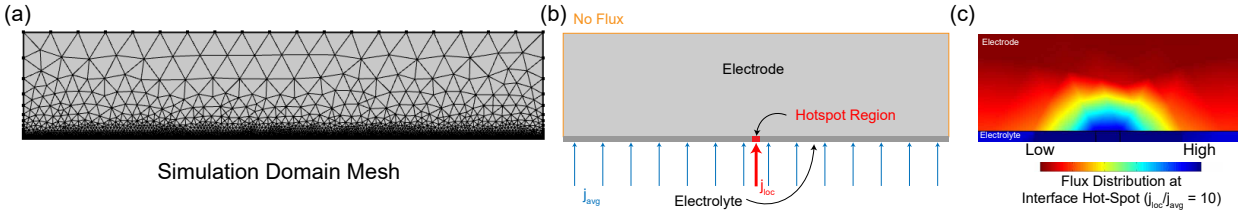

Figure 5.2: (a) Mesh and (b) corresponding boundary conditions for the simulation cases run on Interface | Electrode domain. (c) Simulations results showing flux contours in a thick electrode adjacent to an interfacial hotspot.

5.2.5 Spatial Tortuosity Factor Distribution Calculation

Direct numerical simulation tool was used to estimate tortuosity factors directly from binarized tomography dataCooper et al. (2016). Binarized pellet data-set was cropped to 100 μm thickness at the interface (Fig. 5.14d). This binarized data further cropped into 25x25x100 μm sub-domains and piecewise simulations were carried out using TauFactor software on individiual sub-domains. This enabled estimating the tortuosity factors over the entire solid electrolyte section. Tortuosity factors are obtained by comparing steady

state diffusive flux through a porous domain (F_P)), to that through a fully dense control volume (F_{CV}) of the same size, diffusivity and potential difference.

$$F_P = -A_{CV} D \frac{\epsilon}{\tau} \frac{\Delta C}{L_{CV}} \tag{5.1}$$

$$F_{CV} = -A_{CV} D \frac{\Delta C}{L_{CV}} \tag{5.2}$$

where D is the diffusivity of the solid electrolyte, C is the local concentration of diffusive species, A_{CV} and L_{CV} are the cross sectional area and length of the control volume, ϵ and τ are the porosity and tortuosity of the domain investigated. Steady state diffusion is evaluated through the domain with fixed value (Dirichlet) boundary conditions imposed at two parallel boundaries, with the other faces showing a zero flux boundary condition (Fig. 5.4a). Steady state diffusion equation $\nabla^2 C = 0$ is solved to identify the steady state flux through the domain.

5.2.6 Convolutional Neural Network

Resnet34 flavor conventional neural network architecture was utilized for semantic segmentationYakubovskiy (2019). The layer details for the CNN are detailed in Table 1. The network was trained on a dataset consisting of 800 training images and 200 validation images. Initial weights for the model were used based on the network's training on existing reference data-sets. Training data was generated by edge-segmentation of the raw reconstruction data and manual labeling. Training was run over 500 epochs and the resulting trained network was employed for subsequent segmentation purposes. Tensorflow and Keras backbones were used and the implementation was carried out in Python3 using Colab resources. Subsequent quantification from the segmented data was carried out using MATLAB and Python as required.

Table 5.1: Typical Resnet 34 Architecture

Layer Name	Output Size	Details
Conv1	112x112	7x7, 64, stride2
Pool1	56x56	3x3 max pool, stride 2
Conv2_x	56x56	[3x3, 64; 3x3, 64] x 2
Conv3_x	28x28	[3x3, 128; 3x3, 128] x 2
Conv4_x	14x14	[3x3, 256; 3x3, 256] x 2
Conv5_x	7x7	[3x3,512; 3x3,512] x 2
	1x1	average pool, 1000-d fc, softmax

5.2.7 Meso-scale Modeling

Figure show the representative microstructures for polycrystalline SE system (Fig. 5.4b). A polycrystalline structure comprises of grains (G), grain boundaries (GB) and pores (V) while the amorphous structure consists of grains and poresCheng et al. (2014); David et al. (2015). Experimentally, SEM images of the electrolyte can be used to characterize the grain and pore size while the relative density values can be used to compute the porosity of the electrolyte. The virtual microstructures are generated using the software suite DREAM.3D which allows for the screening of a wide range of grain size, pore size, and pore fractionsGroeber & Jackson (2014). As the grain size increases, the grain boundary density decreases. As the pore size increases, the number of pores for the same pore volume decreases.

Effective electrolyte properties are obtained by doing Direct Numerical Simulation (DNS) calculations on the reconstructed virtual SE microstructure. The effective electrolyte ionic conductivity and elastic modulus depends on arrangement of the grains, grain boundaries and pores and their instrinsic values. The DNS calculations involve the solution of Laplace equation on three-dimensional electrode microstructure grid with Dirichlet boundary conditions along the transport/stress direction and zero flux boundary conditions on the other four faces. We assign a finite thickness to the grain boundary for the effective property computations on a voxelated mesh, with the grain boundary thick-

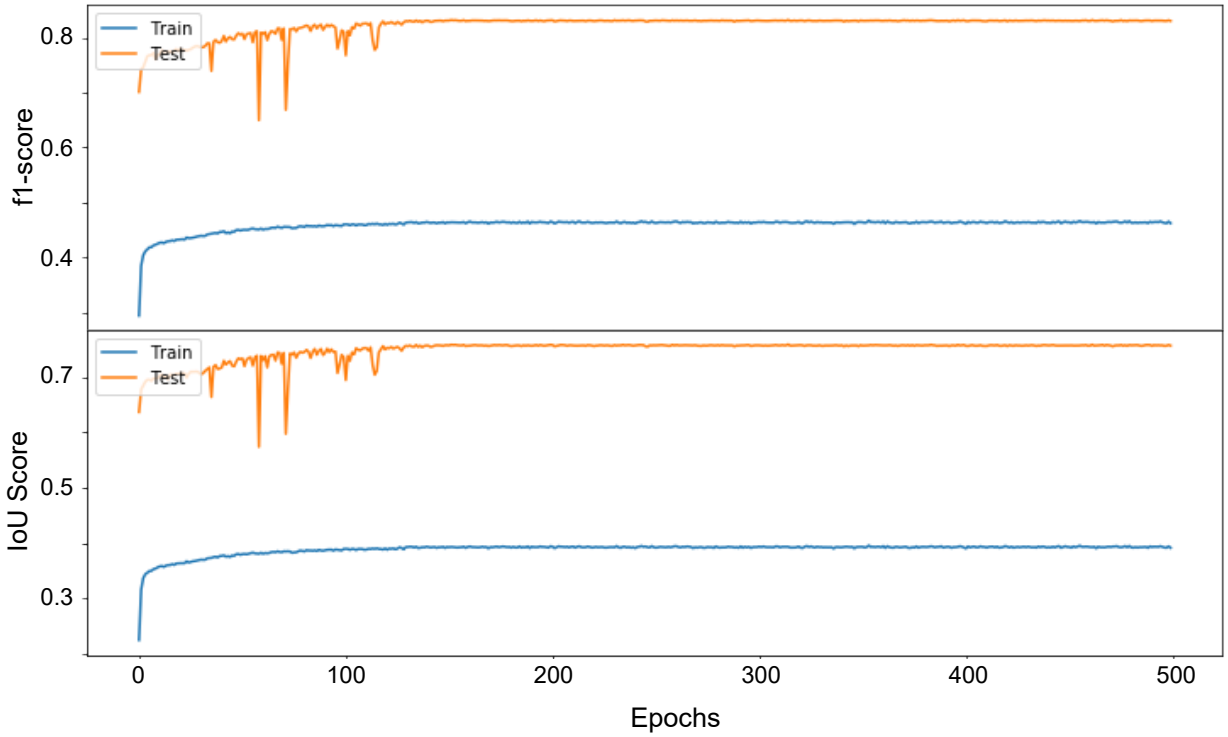

Figure 5.3: Convolutional neural network training metrics. f1-score and IoU metric are plotted against the training epochs. Higher f1-score and IoU metric indicate accuracy of prediction of the convolutional neural network.

ness of 10 nmLacaille et al. (2014). The grain boundary thickness of 10 nm represents the closest analogue to the realistic structure. In-house codes are used to characterize the effective ionic conductivity and elastic constants. The representative elementary volume is ensured to be approximately 10 times the biggest feature size to ensure grid independence of the properties, and the voxel resolution is kept equal to the smallest feature size, namely, the grain boundary thickness. High performance computing was utilized to enable effective property computations for large grid sizes. Domain generation is using DREAM.3D. and input parameters are given in equation 1. C++ was used to get the effective property computation. Since we are getting the ratio of effective to nominal conductivity, just assign a value of 1 to grain, grain boundary becomes 0.01 and void is 0 for conductivity calculations. The effective ionic conductivity can be calculated by solv-

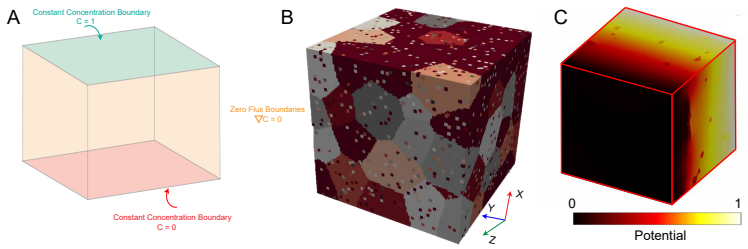

Figure 5.4: (a)Schematic diagram showing the boundary conditions used for estimating tortuosity. Constant value boundary conditions (C = 1, and C = 0) are used on two parallel faces. All the remaining faces have zero flux conditions imposed on them. (b) A typical physical domain used for meso-scale simulations. Polycrystalline materials with grain, grain boundary, and pore segregation are evaluated. Domain sizes of 100x100x100 μm^3 are used for the simulation. (c) Visualization of polarization gradient through the domain under constant potential difference.

ing the Laplace's equation for electrolyte potential $\nabla.(\kappa_{SE,ref}\nabla\phi) = 0$ with the individual phases assigned their intrinsic reference ionic conductivities.

$$\kappa_{SE,ref}(1ptr_xOcFFS) = \left\{ \begin{array}{c} \kappa_G \quad if, \quad 1ptr_xOcFFS \in G \\ 0.01\kappa_G \quad if, \quad 1ptr_xOcFFS \in GB \\ 0 \quad if, \quad 1ptr_xOcFFS \in V \end{array} \right\}. \tag{5.3}$$

$$\kappa^{eff}_{SE,ref,x} = \frac{L}{A(\Phi_{right} - \Phi_{left})} \int_{\Omega_x} \kappa_{SE} \frac{\partial \phi}{\partial x} dydz \tag{5.4}$$

Here, the grain boundary conductivity is assigned an intrinsic value of 0.01 times the conductivity of the grain in accordance with density functional theory computations of grain boundary transportYu & Siegel (2018); Dawson et al. (2018). They show that grain boundary transport of Li^+ is sluggish as compared to the Li^+ intragrain transport. The effective conductivities in the y and z-directions are computed in the usual fashion and an arithmetic mean is used to calculate the effective ionic conductivity of the full 3D structure, $\kappa^{eff}_{SE,ref} = (\kappa^{eff}_{SE,ref,x} + \kappa^{eff}_{SE,ref,y} + \kappa^{eff}_{SE,ref,z})/3$. Similarly, the effective elastic modulus can be calculated by solving the Laplace's equation for displacement $\nabla.(E_{SE}\nabla U) = 0$ with the individual phases assigned their intrinsic elastic modulus.

$$E_{SE,ref}(1ptr_xOcFFS) = \left\{ \begin{array}{c} E_G \quad if, \quad 1ptr_xOcFFS \in G \\ 0.5E_G \quad if, \quad 1ptr_xOcFFS \in GB \\ 0 \quad if, \quad 1ptr_xOcFFS \in V \end{array} \right\}. \tag{5.5}$$

$$E_{x,eff} = \frac{L}{A(U_{right} - U_{left})} \int_{\Omega_x} E_{SE} \frac{\partial u}{\partial x} dydz \tag{5.6}$$

Here, the grain boundary elastic modulus is assigned an intrinsic value of 0.5 times the elastic modulus of the grain in accordance with density functional theory computations by Seungho et alYu & Manthiram (2017). This complies with the grain boundary softening mechanism through which the dendrites can penetrate the SE.

5.3 Results and Discussion

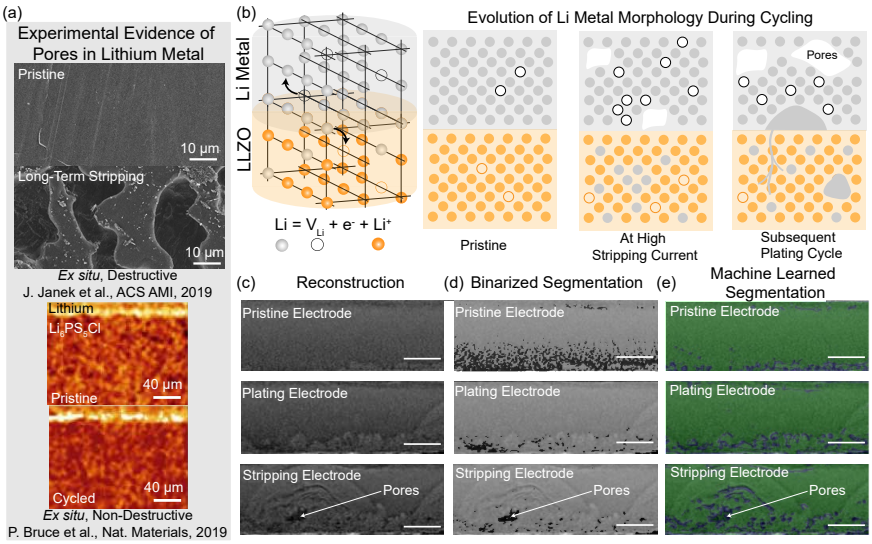

Figure 5.5: (a) State of the art (SoA) characterization for Li metal. *Ex situ* SEM and XRT show evidence of pore formation on Li metal after stripping. Adapted from Krauskopf et al. (2019) Copyright 2019 American Chemical Society and from Kasemchainan et al. (2019). (b)Schematic diagram of the interfacial transport challenges in lithium metal solid-state batteries. Lithium metal undergoes oxidation and migrates as Li^+ to the solid electrolyte leaving an electron and a vacancy in the lithium metal. During stripping at high current densities, the vacancies formed due to Li^+ migration accumulate faster than can be replenished by self-diffusion of Li metal. This results in formation of voids at the anode|SE interface. On subsequent cycling, the void acts as focusing regions for non-planar Li deposition. (c) Sample reconstruction slices of lithium metal electrode imaged for pristine, plating and stripping steps. Semi-circular morphologies are observed in the plating as well as stripping electrode and pore formation in the stripping electrode is observed. (d) Segmentation from conventional binarization process overlayed with raw reconstruction images. Darker regions in these images are identified pores/void phase while the lighter domains are lithium metal. (e) Segmentation results from convolutional neural networks overlayed with raw reconstruction images. Green phase is the identified lithium metal while the blue phase is the identified pore/void phases.

X-ray imaging relies on absorption and phase contrast to distinguish materials in the field of view of the beam. Absorption contrast captures differences in the attenuation of the X-rays along the trajectory from the source to the detector. The attenuation depends on the spatial density of the material, depth of the sample and the incident X-ray wavelength. Assuming there is one material in the X-ray beam, this attenuation is described by the Beer-Lambert law:

$$I(x,y,\lambda) = I_0(x,y)exp\big[-(\mu_0^\lambda - \mu_h^\lambda)T_0(x,y)\big] \tag{5.7}$$

where I is the attenuated intensity, I_0 is the incident intensity, μ_0^λ is the attenuation coefficient of air, μ_h^λ is the attenuation coefficient of sample for X-rays of wavelength λ, and T_0 is the projected thickness through point (x,y) in the direction of z, which is the propagation direction of the X-ray beam. In addition to attenuation, X-rays will undergo a phase shift after traversing a material. The phase shift is determined by the real part of the complex refractive index of the material which depends on the incident X-ray wavelength and local electron density. The phase shift imparted by the sample to the X-ray is given byEndrizzi (2018),

$$\Phi(x,y,\lambda) = -k\int_O dz\delta(x,y,z,\lambda) \tag{5.8}$$

where Φ is the phase shift, δ is the real part of the complex refractive index (in terms of n=1-δ+iβ), k is a proportionality constant and the integration is carried out over the extent of object O along the optical axis. While it is not possible to directly measure the phase of the transmitted X-rays, the interference pattern is captured and reconstructed. The phase contrast is enhanced specifically at the interfaces between materials. Distinguishing low density phases (pores, lithium metal) is challenging for larger sample sizes as well as without adequate phase contrast. The careful combination of absorption and phase contrast and experimental design enables lithium metal imaging at buried solid|solid in-

terfaces. Monochromatic, high energy X-rays (E = 76.2 keV) are employed for imaging the Li|LLZO|Li system. High monochromaticity ($\Delta E/E \approx 10^{-3}$) allows to distinguish low density phases (voids/Li metal). The transverse sample thickness was reduced to about 1.5 mm to match the field-of-view. Sample-detector distance was selected to ensure optimum phase contrast. GRIDREC reconstruction algorithm was used to ensure high quality reconstructionsDowd et al. (1999). Reconstruction across different electrochemical steps show marked differences in lithium metal electrode (Fig. 5.5d,5.6,5.7). Optimized experimental and reconstruction protocols enable visualizing of morphology variation in lithium metal as well as presence of pores within the electrode. Semicircular domains (Fig. 5.5c) are visualized in lithium metal on plating as well as stripping. This morphology closely resembles lithium ion flux profiles around a hotspot at the electrode|electrolyte interface (Fig. 5.2). Such deposition morphologies were postulated in earlier workWang et al. (2019). This is the first mesoscale experimental observation of such morphologies in lithium metal electrodes at solid electrolyte interfaces. Stripping from the same electrode leads to formation of a similar semicircular feature with the presence of voids (darker regions) near the interface (Fig. 5.5d). Regions in the center of a stripping hotspot would have higher mass flux leaving the domain leading to generation of voids due to flux imbalance.

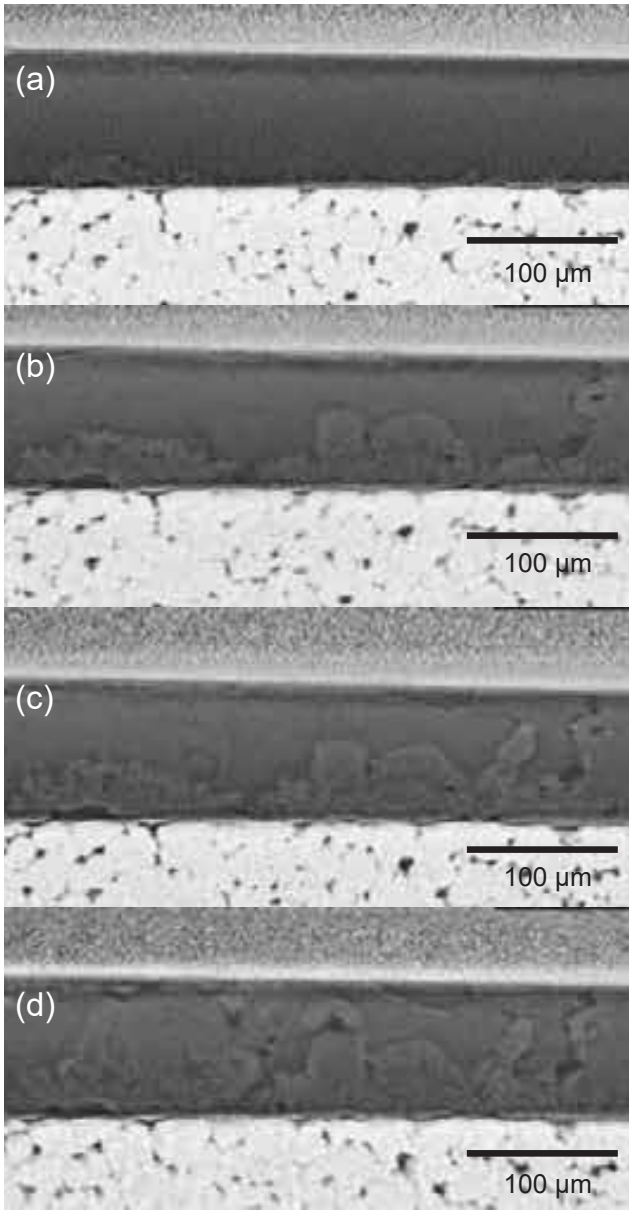

Figure 5.6: (a-d) Sample lithium electrode cross-sectional image over multiple cycling steps. The grainy regions at the top are from the steel current collector, and the porous material at the bottom is the LLZO electrolyte. Lithium morphology variations are clearly visualized within the electrodes.

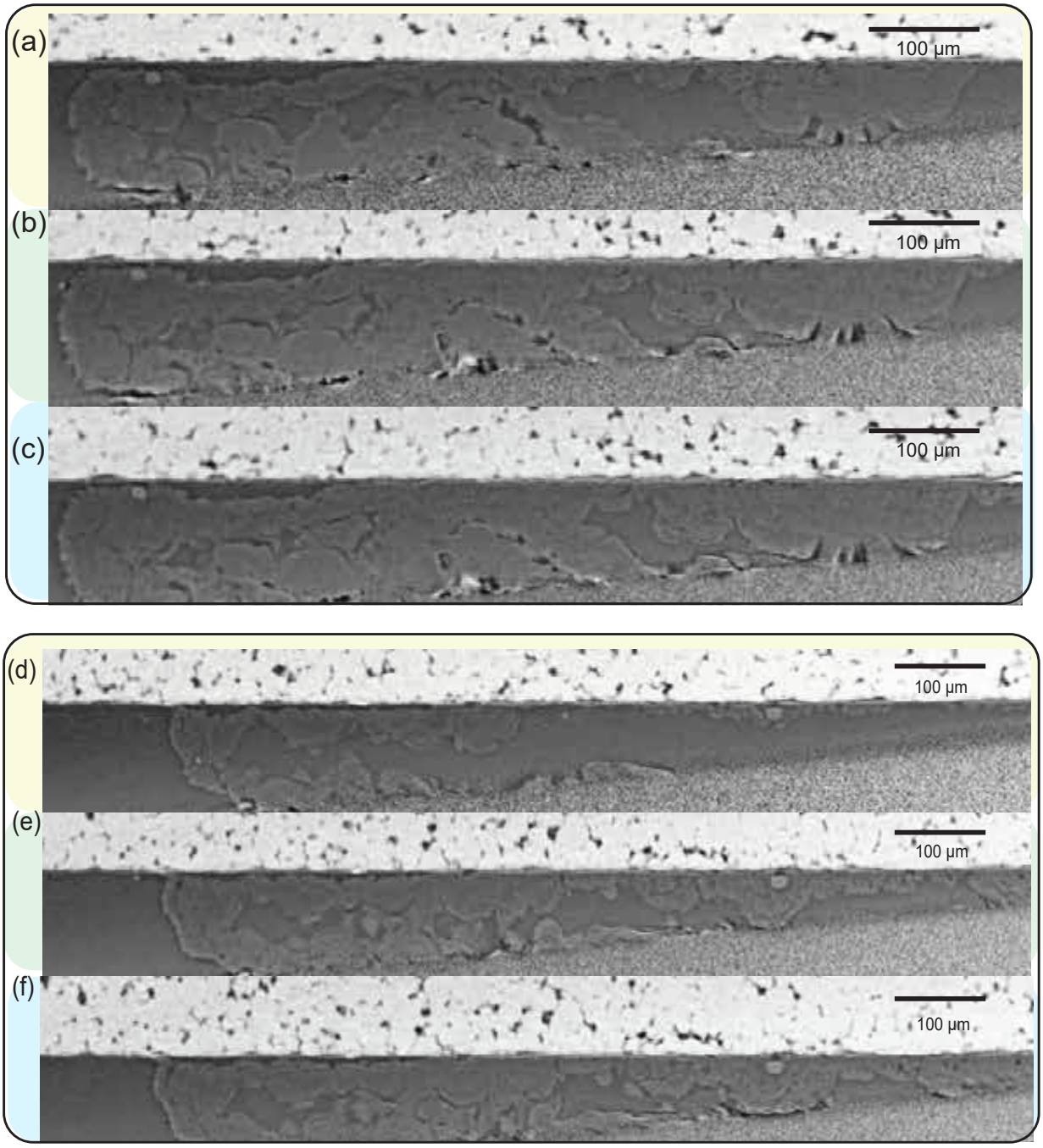

Figure 5.7: (a-c) Sample lithium electrode cross-sectional image over multiple cycling steps (pristine, plating, stripping) for top electrode. (d-f) Sample lithium electrode cross-sectional image over multiple cycling steps (pristine, plating, stripping) for bottom electrode. The lighter, porous regions at the top is the LLZO electrolyte, while the grainy region at the bottom right is the steel current collector. Cell assembly leads to some inclination in the sample alignment which is reflected in the current collector. Lithium morphology variations are clearly visualized within the electrodes.

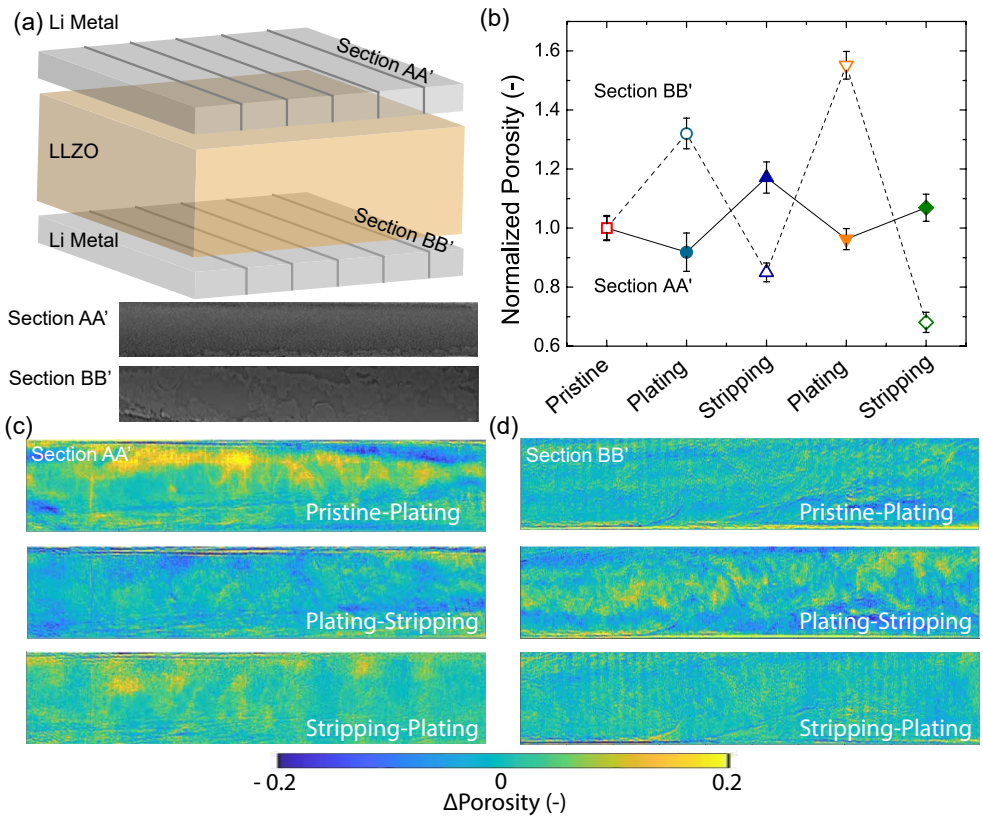

Figure 5.8: (a) Schematic diagram showing sections imaged from the two lithium metal electrodes in the Li|LLZO|Li system. Pore density difference maps are evaluated by averaging over a transverse thickness of approximately 500 μm. (b) Porosity variation of a single electrode at subsequent electrochemical cycling stages. This porosity is estimated near the solid electrolyte interface. This quantification is carried out on segmented Li metal images obtained from the convolutional neural network. Spatial pore density difference distribution for the (c) top and (d) bottom electrodes at various electrochemical cycling stages. The quantification metrics are evaluated from the segmented lithium electrodes obtained from the convolutional neural network. Identical pre-processing, segmentation and post-processing steps are employed for all the individual data-sets to enable comparison.

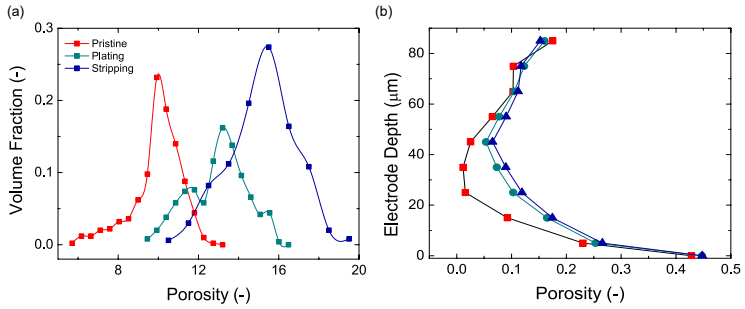

Figure 5.9: (a) Porosity distribution of a single electrode at various electrochemical cycling stages. This porosity distribution is visualized across the entire electrode section. (b) Porosity distribution as a function of electrode depth at various electrochemical cycling stages. The quantification metrics are evaluated from the segmented lithium electrodes obtained from the convolutional neural network. Identical pre-processing, segmentation and post-processing steps are employed for all the individual data-sets to enable comparison.

Quantification of microstructural properties (pores/voids) in the lithium electrode requires a rigorous and consistent segmentation procedure. Conventional thresholding methods cannot segment the phases (pores vs. lithium) reliably (Fig. 5.5c) and manual segmentation of the entire data-set is prohibitive. Convolutional neural networks is a machine learning method widely used for semantic segmentation in a wide range of disciplines that enable pixel-level classification of large data-sets. We implemented a resnet34 based deep convolution neural network for enabling lithium metal segmentation. The neural network processed individual cross-sectional images of lithium metal to yield a high confidence segmented image (Fig. 5.5e). Improvement in fidelity and accuracy of void phase identification for the machine learned segmentation is apparent in comparison to the conventional binarization process. Conventional binarization identifies a significant number of pixels as pores in the pristine sample, which are wrongly segmented while misses several, significant pore features in the stripping electrode. These images clearly highlight the importance of combining synchrotron XRT with machine learning methods to effectively track transformations within lithium metal anode. Machine learning methods required approximately 0.3 s for individual slice segmentation,

with greater than 80% confidence (Fig. 5.3). The segmentation times are an order of magnitude smaller than those typically needed for manual labelling of these images while the confidence statistics are competitive with the segmentation confidence obtained by state-of-the-art networks on standard data-setsZhang et al. (2018). The neural network was trained on 800 images from one electrode in a single electrochemical cycle and validated on a further 200 additional images from the same electrode. Training and validation labelled images were generated by computationally edge-segmented and manually corrected images. The quantification metrics discussed are obtained from the segmented images obtained by applying the trained network to all the subsequent data-sets. It should be noted that the segmentation introduces some error in quantification (80% confidence). Absolute quantification is not advised; however, relative trends between successive electrochemical steps can be ascertained. Pre-processing, segmentation, and post-processing steps are identical for all the evaluated data-sets enabling comparative evaluation.

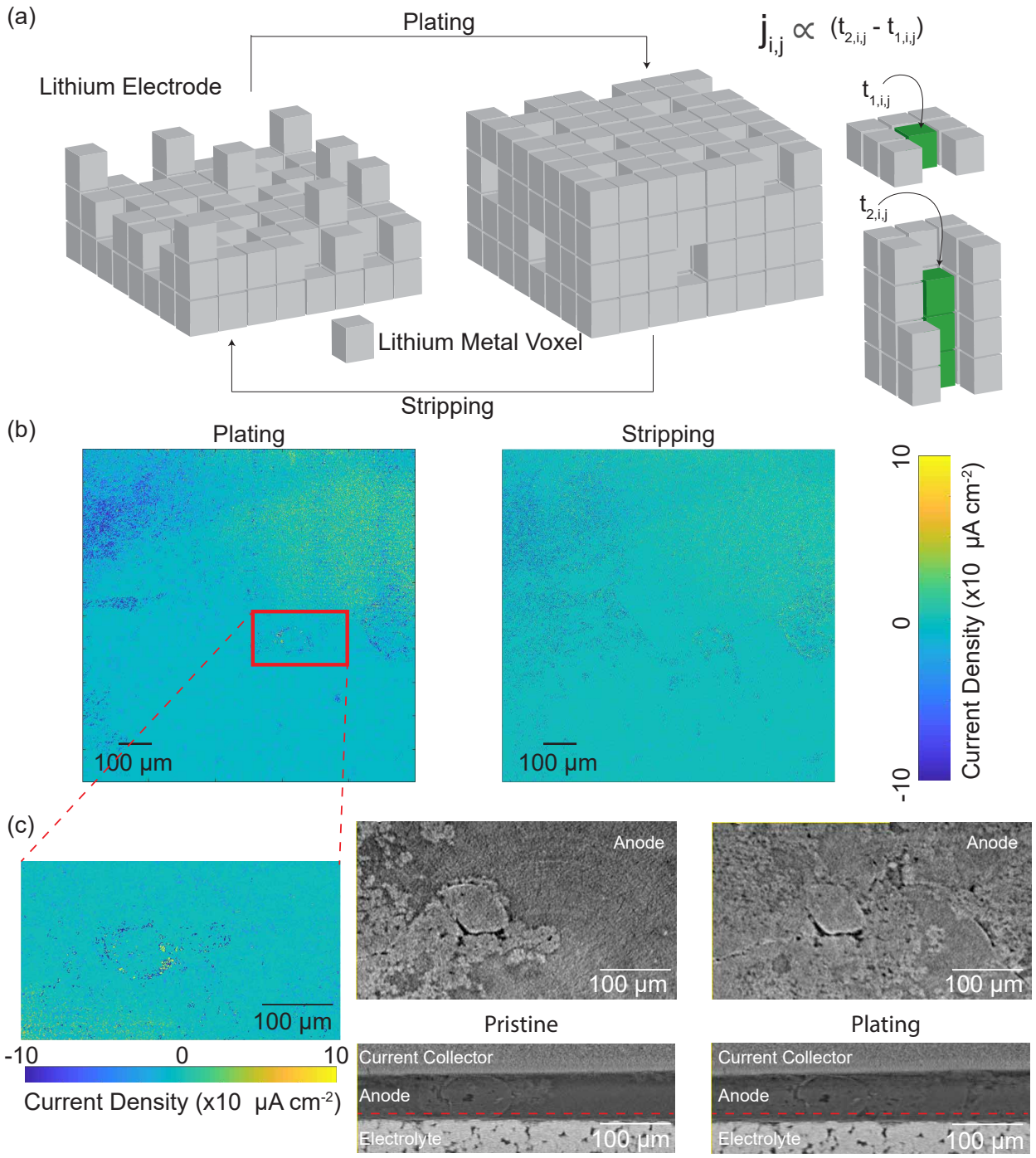

Figure 5.10: (a) Schematic diagram describing the current density quantification method. Difference in lithium electrode thickness are evaluated at each location across the electrode area. The local current density is proportional to the difference of the thickness of lithium electrode in successive image sets. (b) Current density maps for plating and stripping steps of a single electrode. (c) Expanded region identified as possessing potential hotspots region and the corresponding sectional images from the raw tomography data. Regions with uniform current density shows evidence of planar deposition, while the locations with lower current density directly correlate to the presence of pores/voids within the electrode. Additionally, differences in the sub-surface electrolyte microstructre in these sections are clearly visible.

The complete Li|LLZO|Li cell is imaged in a single scan allowing for simultaneous tracking of both the deposition and the dissolution electrodes (Fig. 5.8a). This is crucial for identifying key differences in morphological evolution and corresponding kinetics at the two electrodes simultaneously. Cross-sectional images of the lithium metal electrodes are cropped out from the reconstructions as identified for both electrodes (Fig. 5.8a). Spatial pore density distribution is evaluated by averaging over 500 μm depth of lithium metal electrode of such sections. The difference in the spatial pore density between successive electrochemical steps are visualized for the top and bottom electrodes (Fig. 5.8c-d). Both electrodes show a highly heterogeneous distribution of the porosity change spatially suggesting that the interfacial kinetics are highly non-uniform. Additionally, the two electrodes show complementary behaviors of porosity differences consistent with the electrochemical phenomena occurring at the two electrodes. Mass transport imbalance at the Li |SE interface is widely postulated to generate voids at the interface in solid-state batteriesKasemchainan et al. (2019); Wang et al. (2019). So far, limited cross-sectional imaging evidence is provided for this mechanismKasemchainan et al. (2019). *In situ* tomography configured specifically to track lithium metal enables quantitative assessment of this phenomena. Higher mass flux at the interface due to local high current density, poor lithium diffusion and creep can lead to pore formation. Inadequate metal diffusion and creep flow leads to generation of these voids. Normalized porosity measured near the interface (10 μm) clearly reflects this phenomenological model proposed, with plating showing a reduction in porosity and stripping leading to an increase in porosity in the lithium metal (Fig. 5.8b). Further, the importance of the developed convolutional neural network in discerning the pore features in lithium metal is investigated by quantification of porosity of binarized Li metal images. Otsu thresholding algorithm was employed for thresholding and the results show no trends during cycling (Fig. 5.18). Comparing the quantification results from the two methods (binarization, CNN) clearly showcases the usefulness of advanced ML methods in discerning pores from Li metal.

This behavior is also reflected over the entire electrode section as well with porosity increases from the plating step to the stripping step (Fig. 5.9a). Pristine lithium metal demonstrates a single modal porosity probability distribution while the plated and stripped samples have a non-uniform (tri-modal) distribution. The tri-modal distribution indicate larger spatial variation (variance) within the electrode section introduced due to electrochemical cycling. Additionally, the pore distribution along the electrode depth can be visualized using the segmented data (Fig. 5.9b). Individual data points in this graph are obtained by averaging the porosity over 10 μm thickness. The porosity at the Li|SE is greater than in the bulk metal regions. The high porosity at the interface suggests the formation of voids and interfacial delamination. Electrochemical cycling induced changes in the porosity depth profile are identified closer to the solid electrolyte interface. Porosity values at the current collector are consistent across the electrochemical steps suggesting that this region does not undergo active morphological changes during cycling. These results match well with the anticipated flux profiles in the vicinity of interfacial hotspots (Fig. 5.2c) where in flux gradients are concentrated near the solid electrolyte interface with less impact of the hotspot near the current collector end. Such behavior is only expected in systems with thick lithium foil electrode (higher excess lithium). Moving to systems with limited or no excess lithium, morphological changes are expected to propagate through the entire bulk of lithium metal. These morphological characterizations of bulk lithium metal are made possible due to the careful experimental design and the developed machine learning segmentation methods. Synchrotron XRT coupled with machine learning methods is likely to prove an essential tool for assessing and decoupling the effects of microstructure, operating conditions and interfacial kinetics on lithium metal anode.

Critical current density of approximately 26 μA cm^{-2} was identified from the *in situ* experiments (Fig. 5.1). It is important to note here that enabling Li metal visualization in *in situ* conditions by synchrotron XRT is extremely challenging due to the limitations in terms of sample size, environment and operating parameters. A brief summary of litera-

ture reveals a large variance in the reported critical current densities ranging from several μA cm^{-2} to mA cm^{-2} (Fig. 5.17). The latter are generally reported at high stack pressures and elevated temperatures. Additionally, several studies also employ interlayers at the Li|LLZO interface (ZnO, Al_2O_3, Au) to enable high critical current density. The metrics reported in this study arise from a model Li|LLZO|Li system run at significantly lower stack (kPa range) and the challenge of assembling a cell at the relevant physical dimensions (1.5 mm diameter). Achieving the operating conditions reported for the high critical current density require extensive experimental setup that is harder to couple with an *in situ* cell compatible with the beamline endstation. Interfacial resistances ($\approx 2000\ \Omega$ cm^{-2}) observed here are consistent with the reports for lower stack pressure systems. Further, low initial polarization is comparable to previous *ex situ* measurementsShen et al. (2018) and indicates an effective Li | LLZO | Li system for the characterization study. Thus, the results described here are characteristic transformations of lithium metal and solid electrolyte interface.

In situ tomography data set can generally be large in size particularly if the sample is large and many electrochemical steps are probed. A typical tomography scan of a symmetric cell results in a data-set greater than 30 GB. Tracking pixel level changes in morphology of lithium metal across these datasets is prohibitive. An analytical approach was developed to enable faster analysis via finding regions of interest (Fig. 5.10a). Regions of interest are considered location where either pores form in lithium metal, delamination may occur, and/or nucleation sites for filament formation. To identify these regions of interest we quantified a spatial current density profile across the lithium metal. This can be estimated by tracking the thickness of the electrode over different electrochemical steps given asMaslyn et al. (2019),

$$j_{i,j} = \frac{(t_{2,i,j} - t_{1,i,j}) * F}{\Delta t * V_{Li}} \tag{5.9}$$

where $j_{i,j}$ is the spatial current density at location specified by coordinates i and j, $t_{2,i,j}$ and

$t_{1,i,j}$ are thickness of lithium metal electrode at steps 1 and 2, F is Faraday's constant, Δt is the time duration of electrochemical cycle and V_{Li} is the molar volume of lithium. The thickness of lithium metal electrode was estimated by measuring intensity line-profiles at each location through the depth of the sample. Distinct absorption contrast between steel (current collector) and LLZO electrolyte enables identification of the electrode thickness. This measurement can be easily automated enabling faster tracking of the data-sets by providing qualitative information for easier identification of hotspots. Specifically, with the current data-set mapping current density over a 1 mm^2 area for both electrodes in a symmetric cell takes ≈20 min. Spatial current density maps for plating and stripping cycle show significant variation (Fig. 5.10b). Most of the lithium metal shows a uniform current density and is denoted by green/blue (Fig. 5.10b,c). There are isolated spots that demonstrate either a greater than average current density (yellow) or lower than average current density (blue). A potential hotspot region (yellow) is identified from the current density plots for further analysis of the raw projections (Fig. 5.10c). Comparing pristine and plating morphologies of the identified section shows the presence of interfacial pores as well as globular depositions. In addition to different plating morphologies, a clear difference in the electrolyte microstructure is observed for the hotspot region identified. Analysis of additional hotspot regions across multiple cycles show consistent results (Fig. 5.12,5.13). Spatial current density mapping aids in identifying local hot spots. Combining spatial current density mapping with imaging allows for directly tracking meso- and microstuctural properties that may impact the formation of hotspots while reducing the analysis time and computational power required for assessment of *in situ* tomography data.

Morphological changes captured in the lithium metal are intimately linked to the underlying solid electrolyte and the Li|SE interface. Understanding and evaluating the transformations in the electrolyte microstructure can help in identifying the origins of morphological transformations observed in the lithium metal electrode. The average porosity

of the pristine pellet was ≈5% indicating well-sintered, dense pellets. Normalized porosity shows a cyclic behavior with electrochemical cycles which decreases on plating and increases on stripping (Fig. 5.11a). The nominally X-ray transparent region (generically porosity) includes pores, voids as well as lithium deposition as these materials are difficult to distinguish within the bulk electrolyte. Modulation within this region can be interpreted as presence of electrochemically active lithium metal within the bulk electrolyte. The normalized pore density depth profile also shows spatial variation within the electrolyte domain with interfaces being more porous compared to the bulk. Higher amounts of X-ray transparent region at the interfaces can arise from crack/void generation from the mechanical stresses at the interface as well as from filament generation. Increasing the current density from 6 to 25 μA cm^{-2} on second plating/stripping cycles leads to greater penetration of the higher porosity regions into the bulk. This can reflect potential filament/crack propagation within the bulk. The spatial distribution is practically symmetric across the electrolyte depth suggesting identical mechanisms at both the plating and stripping electrodes. While the lithium metal electrode undergoes distinct morphological changes (void formation on stripping, non-planar deposition on plating), nominally identical response of LLZO electrolyte interfaces suggest they are influenced by the same underlying mechanics. Ion insertion and removal from the LLZO matrix at the interfaces causes stress generation within the solid electrolyte material. These phenomena lead to microstructural variations as evidenced by the tomography results. Further work on evaluating spatially resolved, grain-level chemo-mechanical response is required to understand the identical mechanical behavior at plating and stripping interfaces.

Sub-surface porosity maps reflect the porosity averaged through the Z direction (sample depth) at each pixel along the lateral (XY) section. The solid electrolyte shows a systematic increase in the sub-surface porosity consistent with the mechanism of filament propagation (Fig. 5.11b, 5.14)Shen et al. (2018). The location and size of the x-ray transparent region (porosity) across the pellet as well as in the interfacial regions show a cyclic

behavior with electrochemical steps (Fig. 5.11c, 5.14). Average porosity clearly reflects a difference in the microstructure between successive electrochemical steps in the interfacial regions which is effectively captured in the simulations. It is known that single ion conductors theoretically do not show concentration gradients due to the unity transference numbers. However, the presence of pores has been identified to influence transport and failure mechanisms strongly Shen et al. (2018); Dixit et al. (2018b). The sub-surface porosity maps clearly highlight the spatial microstructural variation, specifically at the interfacial regions. Additionally, tortuosity factors are extracted in the bulk and interfacial region of the solid electrolyte. Tortuosity factors are determined along the Z direction which coincides with the electric field direction in the cell (Fig. 5.14). Normalized tortuosity shown here is the relative change in local tortuosity factor compared to a completely solid domain (tortuosity factor = 1). This metric reflects the degree of obstruction the ions experience when traversing through the solid electrolytes. High tortuosity regions lead to an effectively lower effective lithium ion flux through the domain as given byTjaden et al. (2018),

$$æ_{eff} = -D_{bulk}\,\frac{\epsilon}{\tau^2}\frac{\Delta c}{\Delta x} \tag{5.10}$$

where, D_{bulk} is effective diffusion coefficient in the bulk, ϵ is the porosity, τ is the tortuosity, $\frac{\Delta c}{\Delta x}$ is the effective concentration gradient. Regions of lower tortuosity surrounded by high tortuosity domains correspond to hotspots as lithium ion flux through the low tortuosity domains will be higher to ensure mass balance through the cell section. Variations in tortuosity factors in the sample at individual plating and stripping steps indicate a strong heterogeneity in the underlying microstructure (Fig. 5.15). Tortuosity factor maps provide evidence for transport heterogeneity due to the underlying microstructure variations. Hotspot generation leading to void and filament formation within the lithium metal electrode is linked with the microstructural heterogeneity identified in the solid electrolyte.

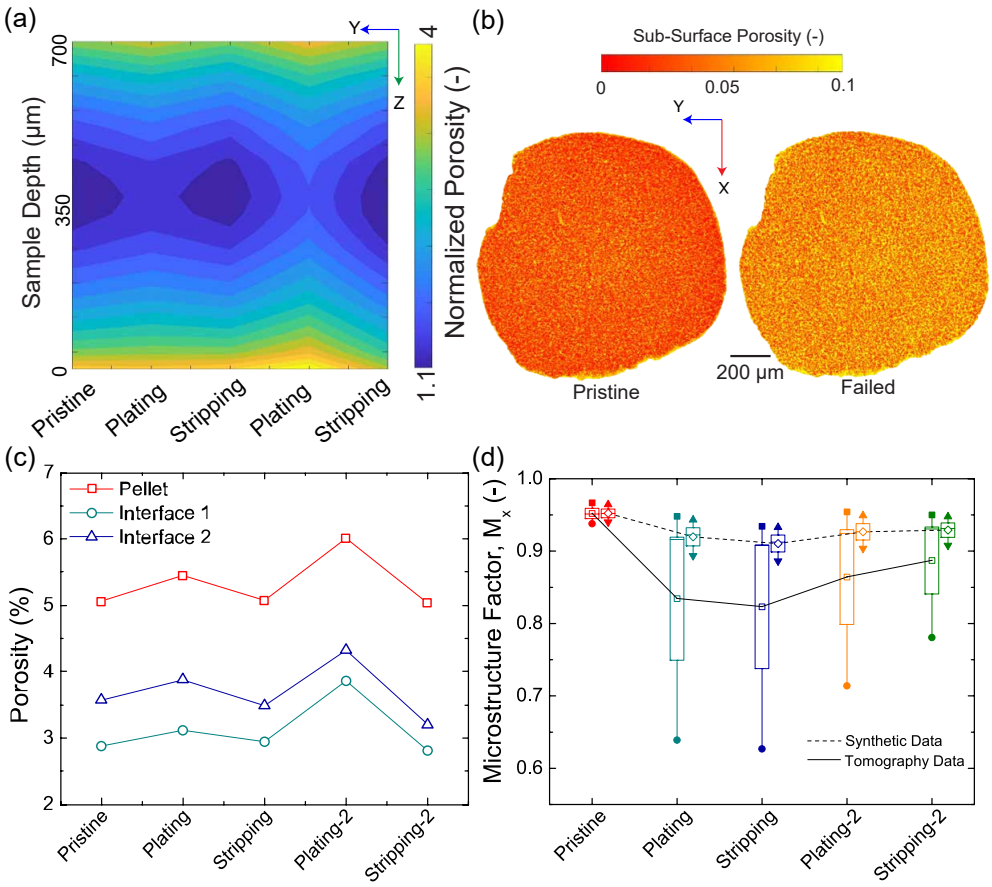

Figure 5.11: (a) Spatial microstructural variation within the sample evaluated across multiple electrochemical cycling steps. Normalized porosity is plotted which is defined as the ratio of the local porosity to the average electrolyte porosity. Spatial resolution of 36 μm was used to assess the microstructural variation through the depth of the electrolyte. (b) Sub-surface porosity map measured through the depth of the sample for the pristine and the failed electrolyte pellet. (c) Bulk pellet porosity and interfacial porosity evaluated across each cycling step. Interfacial regions of 100 μm are considered for this analysis to correlate with the results obtained from the tortuosity factor calculations. (d) Microstructure factor (ratio of local property/bulk property) estimated along the X-direction (along Li|SE|Li) of the domain from the tomography and synthetic data set. Tomography dataset uses the binarized reconstruction images as input for the simulations, while synthetic dataset uses isotropic domains generated from the quantified physical parameters.

To further ascertain the influence of the spatial heterogeneity, mesoscale modelling was carried out for representative simulation domains from interfacial region of LLZO electrolyte. Two data-set formulations were used: a) tomography data which employed the imaged domain directly and b) synthetic data which employed isotropic domains generated from physical parameters (porosity, pore size and grain size) identified from the experimental results. Mesoscale modeling enables explicit definitions of grains, pores as well as grain boundaries to ascertain effective bulk properties of materials (Fig 5.4b). Microstructure Factor (M_x, M_y and M_z) is defined as the ratio of the local conductivity/Youngs' modulus estimated along the X-, Y- and Z- direction in the simulated domain to the theoretical value for LLZO. Mean, maximum and minimum microstructure factors have been calculated during electrochemical cycling for both the synthetic and experimental datasets. A strong impact of sample microstructure anisotropy is seen in the tomography data-set with X- direction showing markedly higher variation across different electrochemical steps in microstructure factor compared to Y- and Z- directions (Fig. 5.11d, 5.16). In contrast, the synthetic data (isotropic domains) show only a small variation linked to the changes in the effective microstructure. Additionally, the tomography domains show a higher spread (minimum, maximum) compared to the isotropic domains signifying a large heterogeneity in local transport and mechanical properties. Identical behavior is seen for the for multiple Li|LLZO systems studied, with comparatively lower anisotropy related fluctuations (variations along X-, Y- and Z- direction). These results clearly show that macroscopic properties of conductivity and Youngs' modulus are affected by microstructural heterogeneity. Higher plating density is anticipated in regions around the domains showing lower transport properties to ensure mass balance across the interface. High plating density around these regions leads to stress accumulation which can subsequently lead to cracking/filament propagation through the electrolyte at the regions with the lower effective properties. The investigation of electrolyte microstructure yields strong evidence for origins of the heterogeneous current density observed in the lithium

metal electrodes. Microstructural variation in the solid electrolyte leads to regions with lower transport and mechanical properties that can act as nucleation sites for hot/cold spots at the Li|SE interface.

5.4 Conclusion

Careful experimental design enables high resolution X-ray imaging of lithium metal. Advanced machine learning methods enable segmentation of lithium and pores from the reconstructions in *in situ* conditions. This data provides physical insight into microstructure transformation in lithium metal and the solid electrolyte upon cycling. Heterogeneous interfacial kinetics are identified in lithium metal along with a validation of pore formation hypothesis on dissolution. Hotspots in lithium metal electrodes are correlated with the presence of anisotropic microstructures within the solid electrolyte. Mesoscale modeling results conclusively show local variations in effective properties of the electrolyte at the electrode interface. Local domains showing lower effective properties are construed to be regions where failure modes are initiated due to stress and flux distributions around these regions. Lithium metal electrode kinetics at solid electrolyte interfaces are distinct from liquid electrolytes. The imaging resolution and contrast described here lays the ground work for future studies capable of resolving the role microstructure heterogeneities in lithium metal impact electrodeposition stability and rate performance.

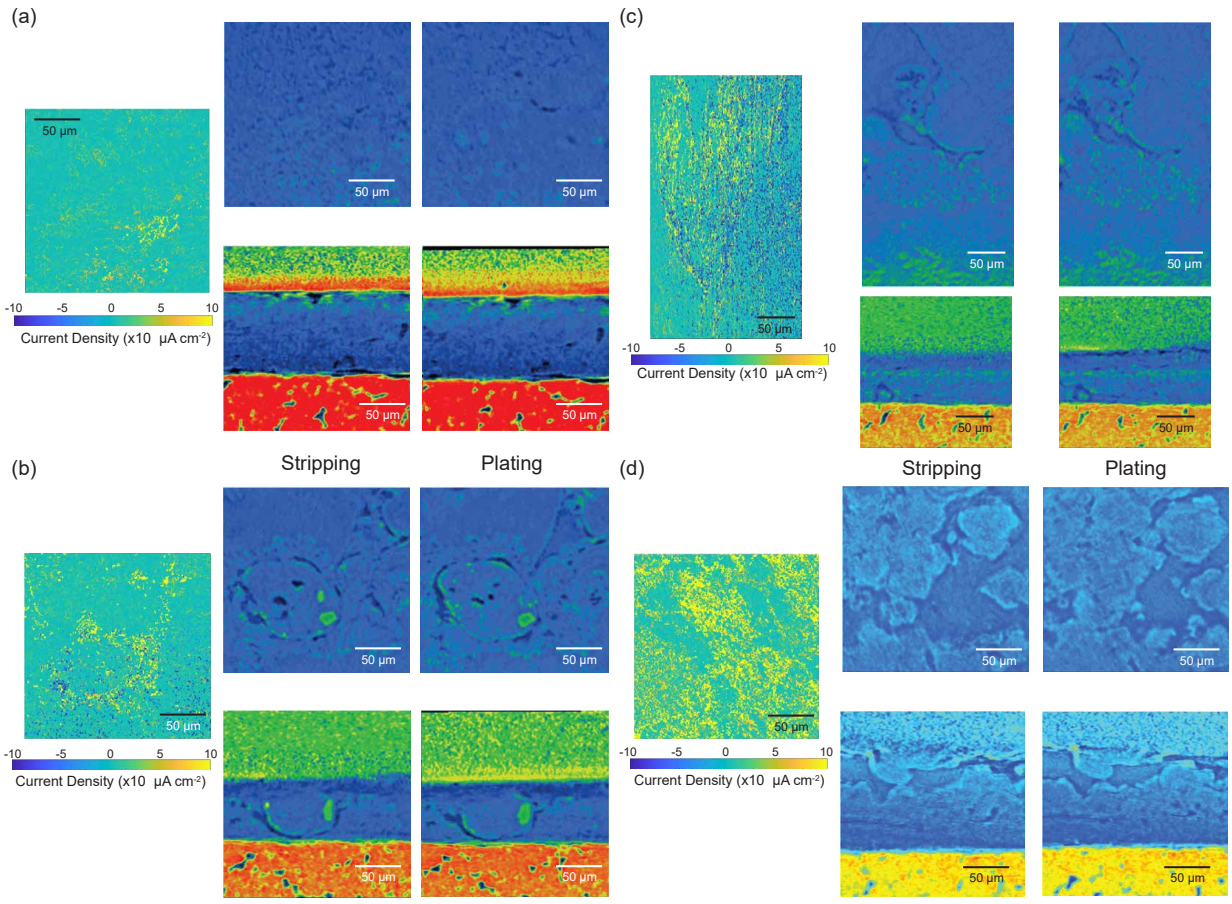

Figure 5.12: (a-d) Additional regions highlighting identified as possessing potential hot-spots region and the corresponding sectional images from the raw tomography data. Regions with uniform current density shows evidence of planar deposition, while the locations with lower current density directly correlate to the presence of pores/voids within the electrode. Additionally, differences in the sub-surface electrolyte microstructure in these sections are clearly visible.

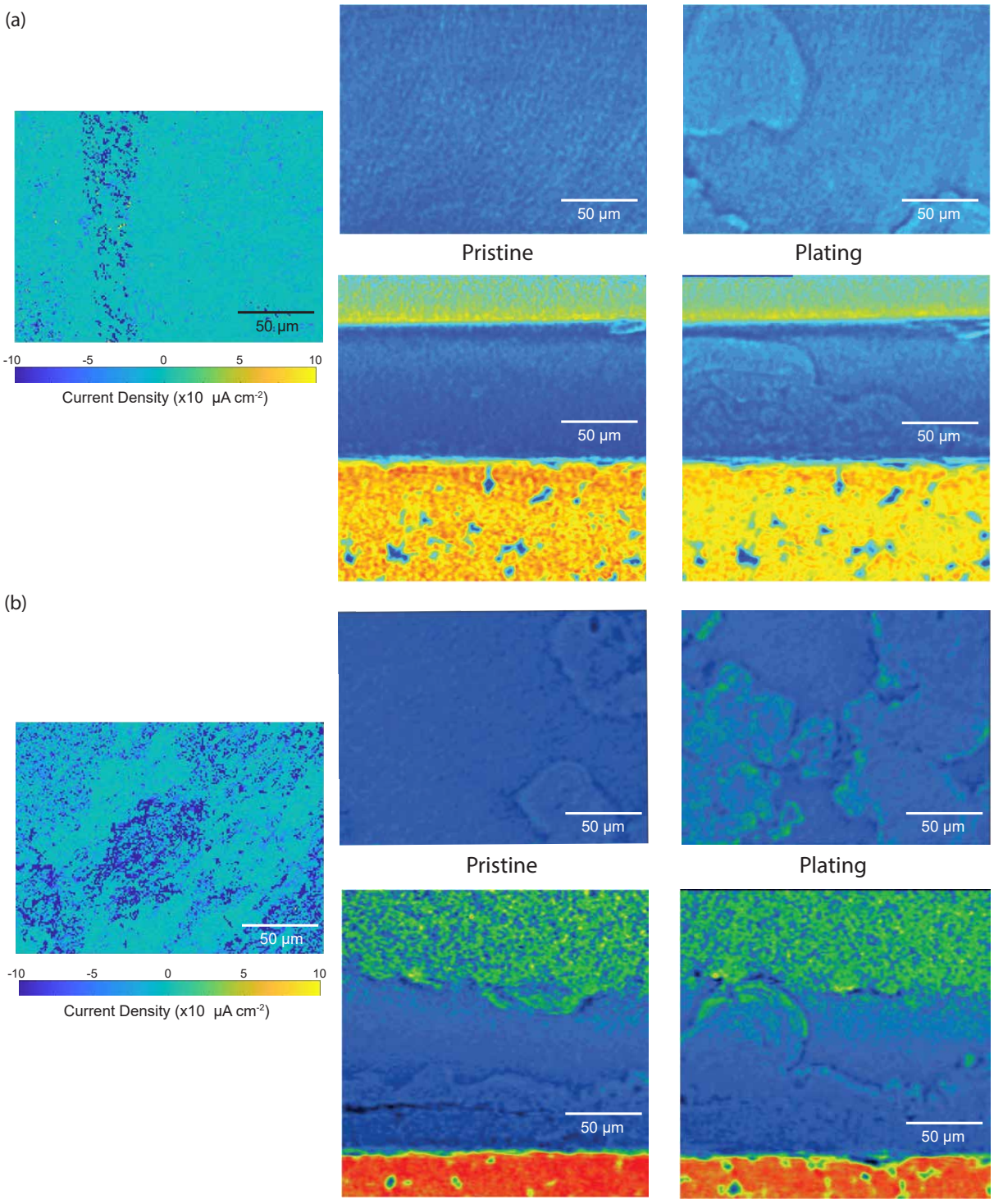

Figure 5.13: (a-b) Additional regions highlighting identified as possessing potential hot-spots region and the corresponding sectional images from the raw tomography data. Regions with uniform current density shows evidence of planar deposition, while the locations with lower current density directly correlate to the presence of pores/voids within the electrode. Additionally, differences in the sub-surface electrolyte microstructure in these sections are clearly visible.

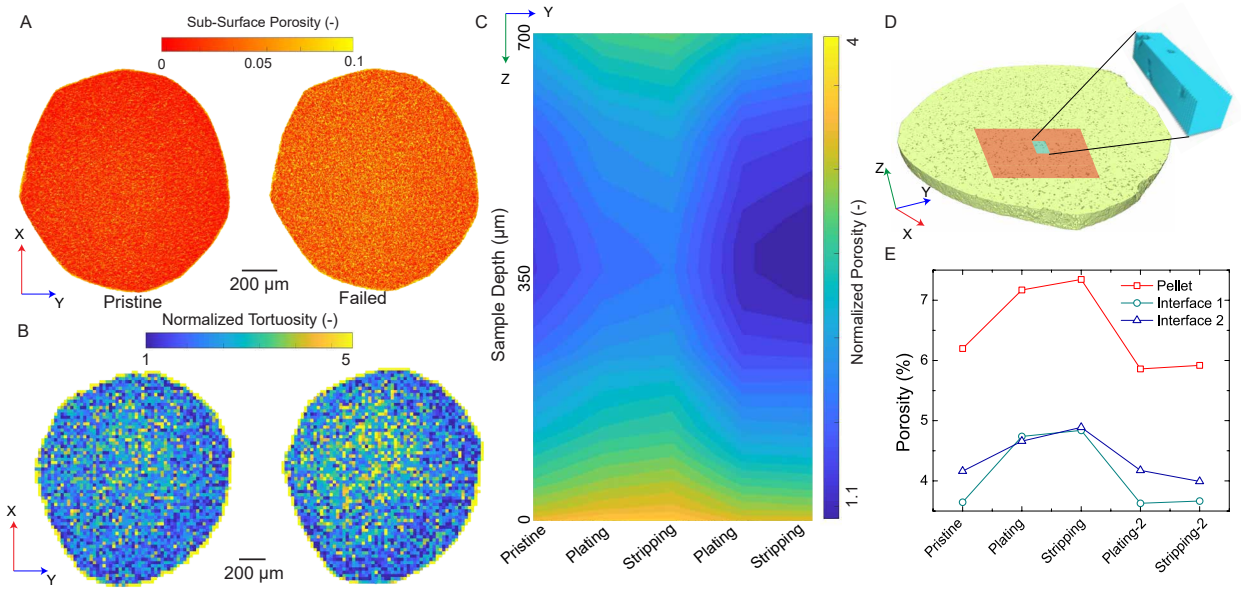

Figure 5.14: (a) Sub-surface porosity measured through the depth of the sample for the pristine and the failed electrolyte pellet. (b) Spatial tortuosity factor distribution for pristine and failed sample. Tortuosity factors are estimated by carrying out simulations over 25x25x100 μm interfacial regions across the entire cross-section of the pellet. Steady state simulations under a constant concentration gradient are performed. (c) Spatial microstructural variation within the sample evaluated across multiple electrochemical cycling steps. Normalized porosity is plotted which is defined as the ratio of the local porosity to the average electrolyte porosity. Spatial resolution of 36 μm was used to assess the microstructural variation through the depth of the electrolyte. (d) Schematic diagram showing the piecewise simulation method employed to estimate spatial tortuosity factor distribution. (e) Bulk pellet porosity and interfacial porosity evaluated across each cycling step. Interfacial regions of 100 μm are considered for this analysis to correlate with the results obtained from the tortuosity factor calculations.

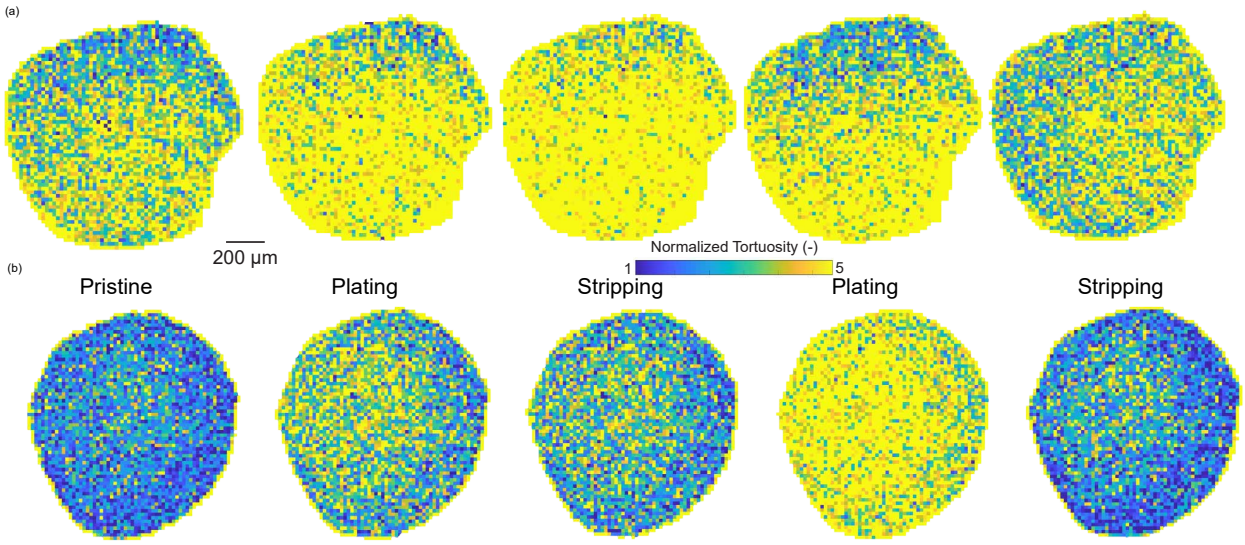

Figure 5.15: Spatial tortuosity factor distribution for sample 1 (a) and sample 2(b) across different electrochemical steps. Tortuosity factors are estimated by carrying out simulations over 25x25x100 μm interfacial regions across the entire cross-section of the pellet. Steady state simulations under a constant concentration gradient are performed.

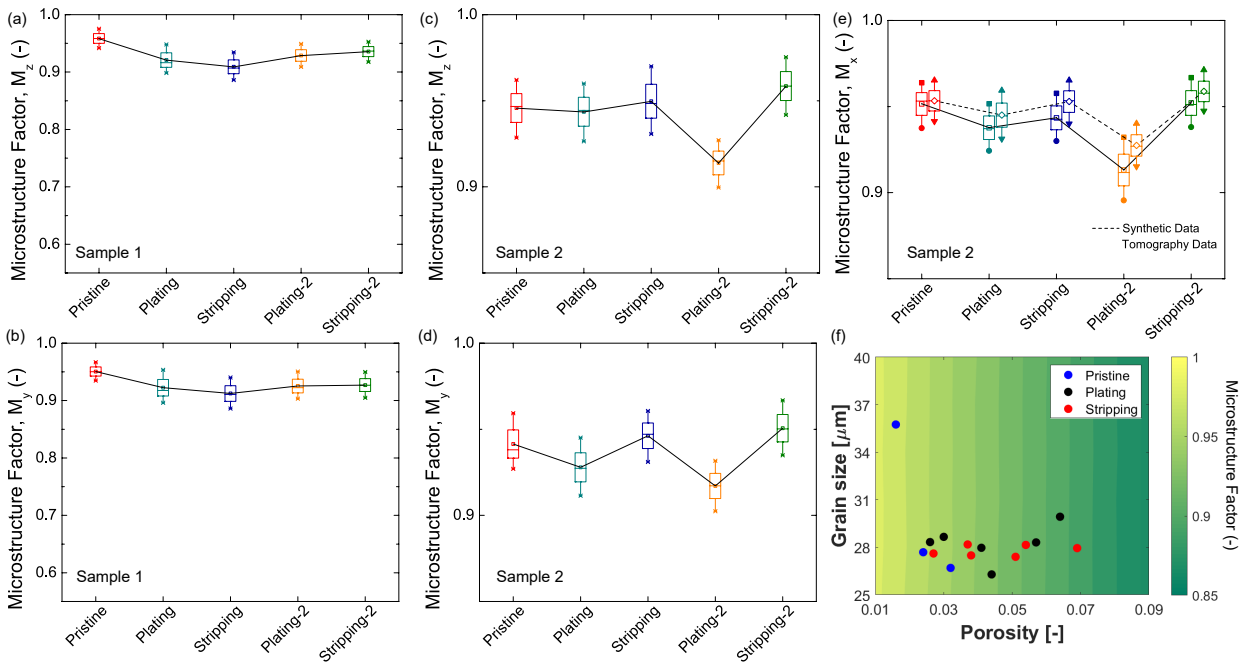

Figure 5.16: Additional mesoscale modeling results. (a-b) Y- and Z- directional microstructure factors for sample 1. (c-e) X-, Y- and Z- microstructure factors estimated for tomography data and synthetic data for sample 2. (f) Correlation plot between porosity and grain size for the microstructure factor estimated from the synthetic data.

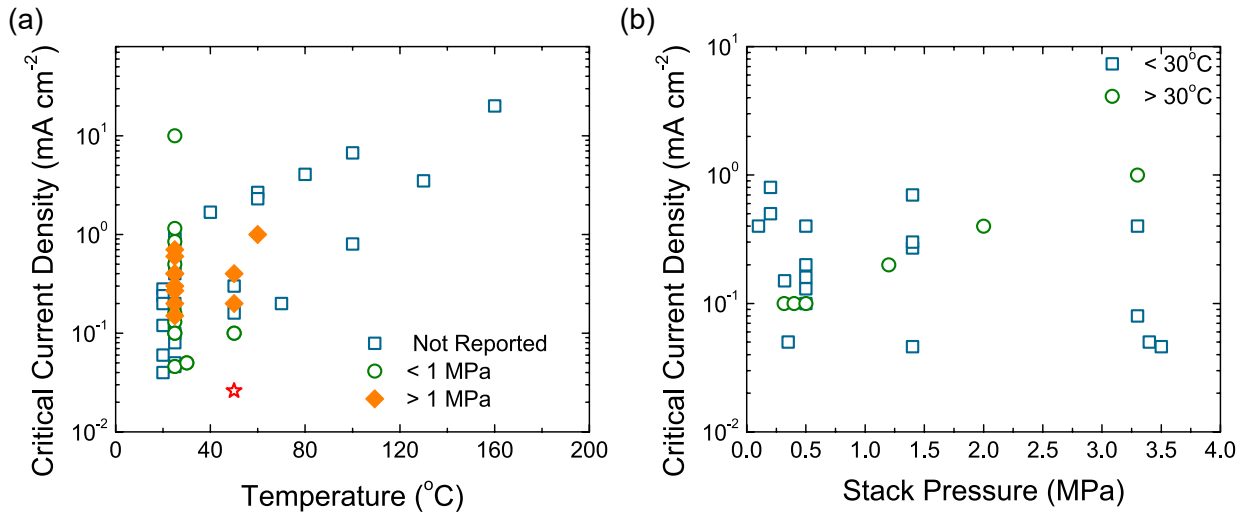

Figure 5.17: Critical current density as a function of (a) operating temperature and (b) pressure. The data are sourced from Cheng et al. (2014); Sharafi et al. (2017); Cheng et al. (2017b); Sharafi et al. (2016); Ren et al. (2015); Wang et al. (2019,?); Patra et al. (2020); Pesci et al. (2018); Taylor et al. (2018); Huang et al. (2018, 2019); Flatscher et al. (2020); Su et al. (2019). A stand-in temperature of 50 °C is used for reports where no operating temperature was mentioned as no reported studies used that operating temperature. The operating metrics of this study is indicated by a star symbol.

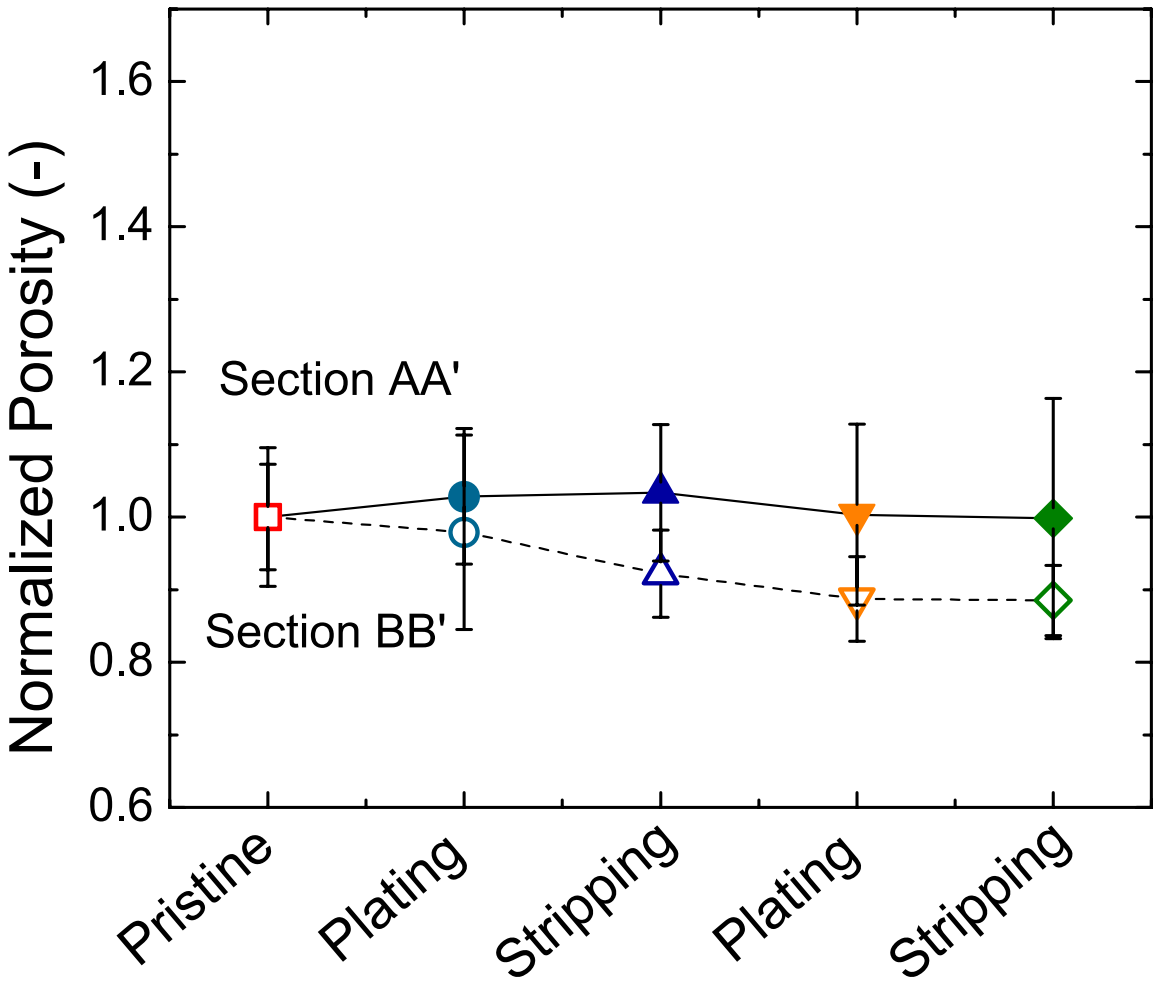

Figure 5.18: Porosity variation of a single electrode at subsequent electrochemical cycling stages. This porosity is estimated near the solid electrolyte interface. This quantification is carried out on binarized Li metal images.

Chapter 6

Chemo-Mechanical Transformations in All Solid State Batteries Studied by Combined Synchrotron Energy Dispersive X-Ray Diffraction and X-Ray Tomography

6.1 Introduction

Chemo-mechanical degradation that can occur during operation of an all solid-state battery (ASSB) is poorly understood hindering the development of high performance, durable systemsHatzell et al. (2020); Dixit et al. (2020); Lewis et al. (2019); Wang et al. (2019); Randau et al. (2020). This degradation is manifest in both bulk electrodes as well as at the electrode | electrolyte interfaces in all solid state batteriesXu et al. (2018); Wang et al. (2019); Lewis et al. (2019). Non-uniform contact at the electrode|electrolyte interface serve as hot spots of stress and concentration distributions and can accelerate failure through chemo-mechanical degradation Nie et al. (2018); Pervez et al. (2019); Xu et al. (2018); Zhang et al. (2020). Severe volume fluctuations as well as resulting contact loss are reported as causes for chemo-mechanical degradation for different ASSB chemistries Ohno et al. (2019); Koerver et al. (2017). Composite cathodes contain active material, ion and electron conducting additives, as well as binders. Active material undergoes volume changes during cycling that can disrupt the three phase contact necessary for active material utilization Zhang et al. (2017a); Koerver et al. (2018). Additionally, volume changes in the active material can lead to deformation, delamination as well as cracking of the composite cathode resulting in ion transport bottleneck and active material lossDixit et al. (2018b). At the anode, lithium metal undergoes large volume changes ($\Delta V \approx 100\%$, under no excess Li constraint) that can cause interfacial delamination upon cycling. Additionally, lithium metal deposition (planar or dendritic) leads to stress development at the anode interfaceLePage et al. (2019). Apart from these mechanical degradation pathways, side reactions between electrodes and electrolytes can also occur leading to chemical degradation in the systemZhang et al. (2017a); Tippens et al. (2019). Design of

compatible electrode|electrolyte interfaces are necessary to achieve realistic performance metrics (energy density, power density, cell lifetime) for ASSBs.

Cathode and anode interfaces in garnet solid electrolytes are widely studied with a viewpoint of materials and electrochemistry to alleviate the high interfacial resistance Walther et al. (2019); Xu et al. (2018). These studies employ coating of interfacial layers (graphiteShao et al. (2018), Al_2O_3Han et al. (2017), ZnOWang et al. (2017), $LiXO_3$Jena et al. (2018)), addition of dopant elements to electrolyteCai et al. (2015); Lu et al. (2018) and surface treatment of electrolytesSharafi et al. (2017). These strategies are primarily aimed to improve the Li metal|electrolyte interfacial contact challenges and limit the chemical degradation. Recently, application of high axial pressures (3-10 MPa) is identified as an alternative route to address the interfacial contact challenge in all solid-state batteriesKasemchainan et al. (2019); Wang et al. (2019). Smaller active material particle sizes are identified to effectively handle stress distribution and mitigate some chemomechanical degradation for a range of cathode ($LiFePO_4$, $LiMn_2O_4$, $LiCoO_2$) and solid electrolytes ($Li_{10}GeP_2S_{12}$, LLZO, Li_3PO_4) combinationsHao & Mukherjee (2018). X-Ray diffraction studies on volume change of active materials emphasizes the need to limit the effects of elastic and plastic deformations in the cathode active material and outlines the compensation requirements from solid electrolytes to ensure stable three-phase contact for durable ASSBs Koerver et al. (2018). FEA modelling identified an expansion limit of 7.5% for active materials in a sulfide electrolyte matrix above which the composite cathode is predicted to fractureBucci et al. (2017). Volume change in the InLi|LSPS|Li_2S cell tracked by tomography are shown to cause build-up/release of stress at the electrode | electrolyte interface causing mechanical degradation Sun et al. (2018). The cell was also investigated by *operando* energy dispersive X-ray diffraction which showed that the principle diffraction line of In disappears with the appearance of InLi diffraction peak during charging with altered d-spacing compared to pristine InLi which suggests mechanical degradation of the anode. Tomography studies usually provide spatial information with resolutions

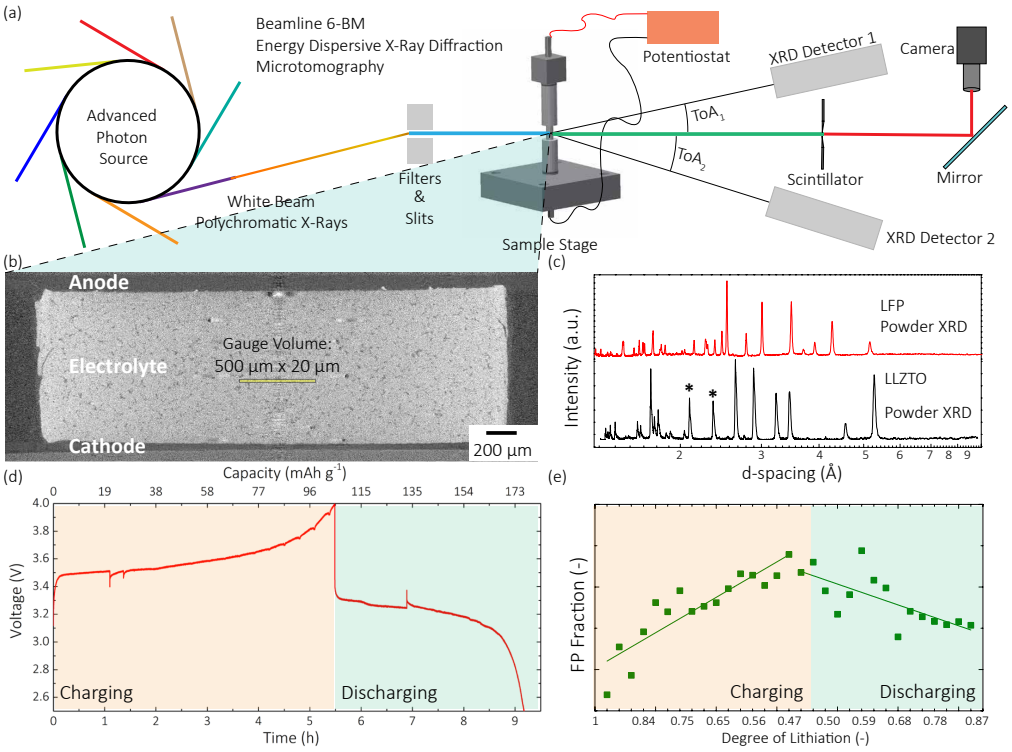

Figure 6.1: (a) Schematic diagram of the EDXRD and tomography experiment carried out at Beamline 6-BM of the Advanced Photon Source at the Argonne National Laboratory. (b) Sample reconstruction of the full cell with the gauge volume section size highlighted. (c) XRD patterns for LLZTO and $LiFePO_4$ (LFP) obtained from laboratory XRD instrument. (d) Galvanostatic charge-discharge response of the system in operando conditions. This cycle was run at 0.1 C-rate. (e) FP ratio as a function of degree of lithiation of this cycle measured from the EDD Data

around a micronWu et al. (2019); Zhang et al. (2017a,a); Seitzman et al. (2018); **?**); **?**); Sun et al. (2017); Li et al. (2018); Shen et al. (2018); Sun et al. (2018); Haas et al. (2019). In contrast, X-ray diffraction can provide information regarding state-of-charge of system as well as local microstrain in the material lattice and has been employed widely to study local strain phenomenon in batteriesZhu et al. (2018); Ulvestad et al. (2015); Glazer et al. (2015); Chen et al. (2014); Yu & Siegel (2018); Huie et al. (2017); Paxton et al. (2015); Kirshenbaum et al. (2015). Combining X-ray diffraction technique with tomography can enable complementary measurements of chemo-mechanical response of the solid state batteries over a wide range of length scalesMarschilok et al. (2020).

Herein, we report on cathode|solid electrolyte interfacial chemo-mechanics in Li|LLZO|LFP cells. *Operando* measurement of a full solid state battery using LLZO ceramic electrolyte with a multi-modal energy dispersive X-ray diffraction and tomography techniques was carried out (Fig. 6.1a). The effect of X-ray beam energy on sample electrochemistry is highlighted. Interfacial strain and phase fraction of $FePO_4$ are estimated as a function of cycling from the operando XRD data. Morphological differences in cathode and electrolyte are characterized along with volumetric variation in the electrodes. The chemo-mechanical strain in the electrolyte is quantified spatially and the extent of impact of interfacial strain in the electrolyte bulk is estimated. The results highlight the importance of designing resilient, conformal interfaces in these systems for high performance all solid-state batteries.

6.2 Experimental Methods

6.2.1 Material Synthesis and Cell Preparation

$Li_{6.5}La_3Zr_{1.5}Ta_{0.5}O_{12}$ was synthesized using solid state reaction process. Solid precursors were mixed in stoichiometric quantities (LiOH = 0.12 mol, La_2O_3 =0.02 mol, ZrO_2 = 0.02 mol, Ta_2O_5 = 0.004 mol) and were wet ball-milled for 8 hours. The resultant mixture was dried and sintered at 900 °C for 6 hours. The sintered powdered was further ball-milled for size reduction. Cubic phase of the powders was confirmed by powder XRD measurements (Fig. 6.1c). 6 mm diameter pellets were pressed from the size-reduced powder and sintered at 1130 °C for ten hours. The pellets were subsequently polished to diameters of 2.5 mm for synchrotron experiments. The average density of the pellets measured by Archimedes' principle was $\geq$ 85%. $LiFePO_4$ was sourced from MTI corporation and used without any modification (Fig. 6.1c). The cathode was solution cast from an ink consisting of $LiFePO_4$ (45 wt.%), LiTFSI (35 wt.%), conductive carbon (12 wt.%), and PVDF (8 wt.%), with n-methyl-2-pyrrolidone (NMP, Thermo Fisher) as the solvent. The ink was prepared by ball milling for 60 min. The cathode slurry was cast on carbon coated aluminium foil

and dried overnight under vacuum at 80 °C . Cells were assembled inside an argon-filled glove box at Advanced Photon Source. Li metal foil was scratched and melted on the LLZTO pellet and a 2 mm punch of the cathode was attached to the other side. A small quantity of liquid electrolyte (LiTFsi) was added on both sides of the electrolyte before cell assembly to ensure better contact. The full cell was sealed inside the in-situ cell and transported to the end station for experiments. The cathode loading for the cells is ≈ 1.3 mg cm^{-2}.

6.2.2 Material Characterization and Electrochemical Testing

X-ray diffraction (XRD) on synthesized LLZTO and as-received LFP was carried out on Rigaku Smart Lab (Cu Kα X-ray).The diffraction pattern was recorded between 10° - 70° (step size: 0.01°). Electronic impedance spectroscopy was carried out between 1 MHz and 100 mHz with a 50 mV amplitude. Galvanostatic charge-discharge tests were carried out at 0.1 or 0.2 C-rates. The cells were charged up to 4 V and discharged up to 2.5 V.

6.2.3 Synchrotron Energy Dispersive X-Ray Diffraction and Tomography

EDXRD and tomography experiments were carried out at end station 6-BM-A of Advanced Photon Source, at the Argonne National Laboratory. The end station has both tomography and EDXRD detectors that can be used alternatively (Fig. 6.1a). A white beam (40-150 keV) was used for both the techniques. For EDXRD measurements, the X-Ray beam was passed through appropriate optics to achieve a final gauge volume of 500x20x4500 μm^3 dimensions (Fig. 6.1b). XRD patterns were obtained from the cell in-operando conditions by keeping the detectors at a fixed angle and sweeping the energy range. The gauge volume was traversed from the cathode into the interior of the electrolyte. The typical acquisition time at each spatial step was 90 s. XRD patterns were recorded at two detectors placed at 2θ angles of 3.00° and 4.81° respectively. Tomography was carried out intermittently at the fully charged and discharged state of the battery. The imaging system for tomography consist of a Pointgrey Grasshopper3 USB3 camera

(GS3-U3-23S6M) , 2x objective lens and 100µm LuAG:Ce scintillator. The setup provides 4.3mm x 1.5mm Field-of-View (FOV) with 2.93 μm pixel resolution, which can cover the entire cell assembly. The in-situ cell was rotated from 0◦ to 180◦ and projections were recorded with exposure time of 0.1 s. The total imaging time was approximately 25-30 minutes. The acquisition times of a typical XRD pattern across the section is 90 s at a single location, while that for a tomographic scan is 25-30 minutes. Compared to the typical charge/discharge cycle times of several hours, the acquisition time for a complete tomography measurement did not provide enough time resolution for in-operando conditions. Thus, the EDXRD measurement was carried out in-operando while tomography was carried out at full charged and discharged state of the battery.

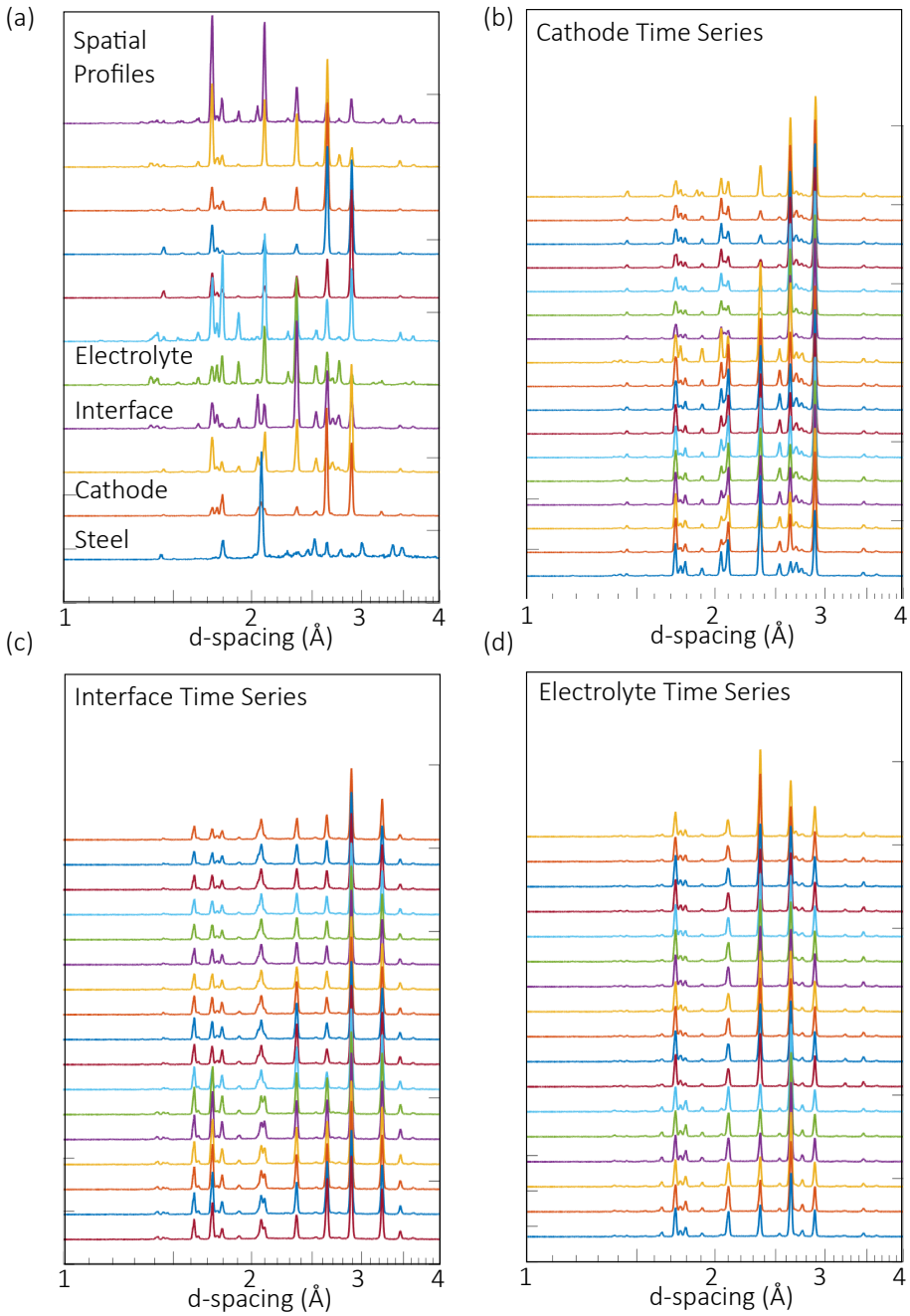

Figure 6.2: Typical EDXRD patterns collected. (a) Spatially resolved diffraction patterns. Steel current collector diffraction is the first profile from the bottom. Sequentially, the beam rasters through the cathode, interface and solid electrolyte. Time series diffraction patterns collected during a single charge-discharge cycle for (b) cathode, (c) interface and (d) solid electrolyte section.

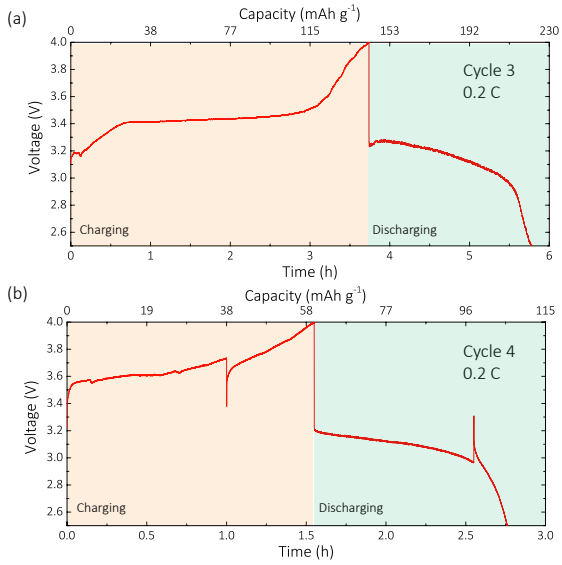

Figure 6.3: Galvanostatic charge-discharge response of two cycles (a-b) of LFP | LLZO | Li cell in operando conditions. This cycle was run at 0.2 C-rate.

6.2.4 Data Analysis and Reconstructions

EDXRD data set was analyzed using custom MATLAB routines. Energy was recorded during the EDXRD measurment, which are converted to d-spacing using Bragg's law. The XRD patterns are then filtered using a 1-D filter. Peak fitting analysis is carried out using the algorithms available within MATLAB. Strain is evaluated using the following equation:

$$\epsilon = \frac{d - d_0}{d_0} * 100 \tag{6.1}$$

where, ϵ is the lattice strain, d is the measured d-spacing and d_0 is the lattice spacing measured for the pristine sample. Tomography reconstructions are carried out using TomopyGürsoy et al. (2014). Subsequent image analysis is carried out using ImageJSchneider et al. (2012b).

6.3 Results and Discussion

Electrochemical performance of the operando cells were evaluated for 4 cycles (2 cycles at 0.1 C-rate and 2 cycles at 0.2 C-rate). The galvanostatic charge-discharge profiles for all

the four cycles show characteristic profiles with discharge capacities of 37, 40, 63 and 68 mAh g^{-1} (Fig. 6.1d, 6.6a, 6.3). Electrochemical cycling was suspended in order to carry out tomography imaging. The spikes observed in voltage profiles correlate to the pause in electrochemical testing to carry out the tomography scan. XRD patterns are collected during the entire charge-discharge cycle from within the gauge volume rastered across the sample in predetermined steps during cycling (Fig. 6.1b, 6.2). Typical powder-XRD patterns of LFP and LLZTO show anticipated structures (Fig. 6.1c). Bragg reflections in the EDXRD patterns are obtained at different energies with the incident beam energy having a non-linear distribution of photon flux and intensity across the energy rangeBruck et al. (2019). Additionally, the inherent sample motion due to electrochemical processes make the XRD pattern intensity vary over subsequent time steps for the same spatial location. These factors make quantitative analysis of phase fractions difficult. However, the relative phase fractions of $FePO_4$ (FP) signature are evaluated as area under the characteristic $FePO_4$ peak normalized to the peaks obtained for the $LiFePO_4$ (LFP) spectra. The FP fraction shows an increase during the charging step and a decrease during the discharging step (Fig. 6.1e, 6.8). This is characteristic behavior of LFP undergoing delithiation to form FP during charging and conversely lithiating and forming LFP during dischargingPaxton et al. (2015). Limited capacity attainable (<50% of theoretical capacity) at the low C-rates employed indicates improper active material utilization in the composite cathode. Charge/discharge profiles show a high ohmic loss in the discharge curve as well as a strong concentration overpotential drop (Fig.6.1d). This could arise from improper contact between active material and solid electrolyte limiting the ion transport and a suboptimal cathode microstructureLiu et al. (2016).

White beam flux at 6-BM range from 10-250 keV to 55-230 keV depending on the filters used (Fig. 6.4a). Two separately assembled cells were run with two different filter configurations with 0.25" and 0.5" steel filters. Both these cells show an similar as-assembled EIS spectra with interfacial resistance of $\approx$ 400 Ω cm^2 (Fig. 6.4b). When these cells are

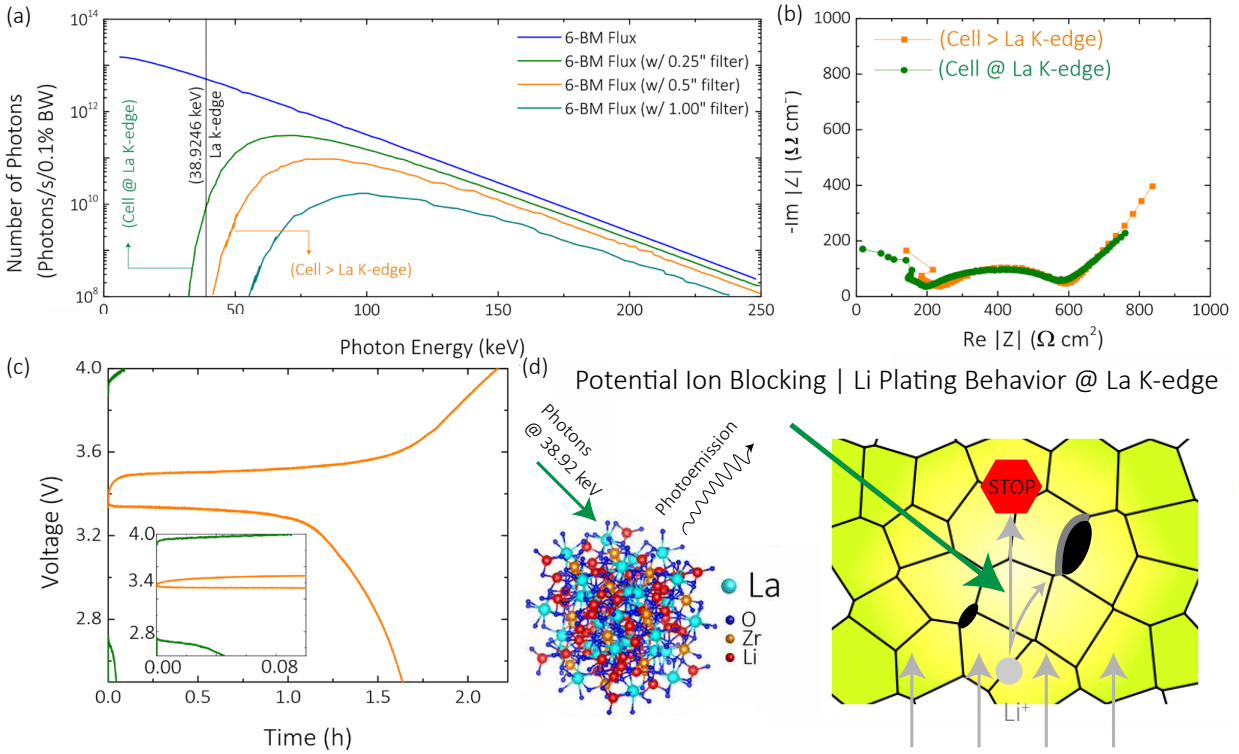

Figure 6.4: (a) Beam flux as a function of incident energy at 6-BM with different filter thicknesses. Cell 1 and 2 are run with 0.5" and 0.25" filters respectively. (b) EIS patterns of two cells assembled and tested with different filter sizes. (c) Electrochemical performance of the two full cells in-operando conditions. (d)Schematic diagram describing potential degradation mechanism with photons at the La k-edge incident on the system.

cycled in *operando* conditions with the two beam configurations both the cells show very distinct electrochemical performance. Cell > La K-edge which is run with a white beam with 0.5″ of steel as filter shows characteristic charge-discharge profiles with a discharge capacity of ≈37 mAh g^{-1} (Fig. 6.4c). In contrast, the cell run with the beam configuration 0.25″ of steel as filter polarizes almost instantly to the cut-off voltages with no effective charge storage (Fig. 6.4c). X-ray interaction with the material is causing the difference in the electrochemical performance of the system. Presence of La K-edge photons in the spectrum can lead to a systemic defect in the sample in spite of the small illuminated volume. The exact nature of this defect is unclear however, its impact on electrochemistry of the cell is evident. A potential ion-blocking mechanism or Li plating mechanism could be occurring (Fig. 6.4d). These results show that there is a strong impact of X-ray on

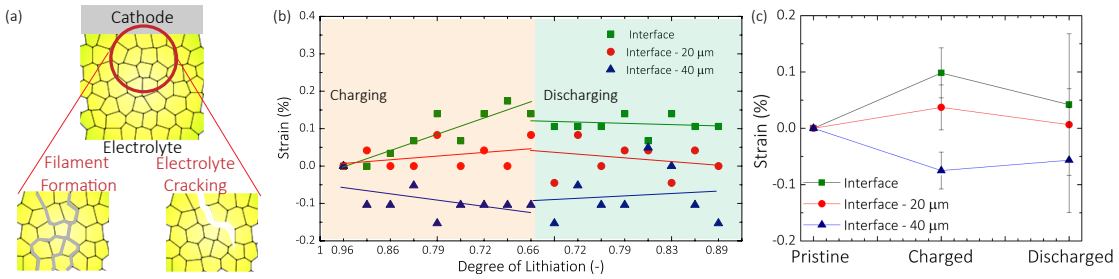

Figure 6.5: (a) Schematic diagram describing mechanical transformation that can potentially occur at the electrode|solid electrolyte interface. (b) Interfacial and sub-surface strain in electrolyte for Cycle 3 evaluated from the EDXRD data. (c) Average strain in the charged and discharged state for 4 cycles for a single cell.

the material electrochemistry that can significantly impact the results which needs to be carefully considered.

X-ray diffraction profiles typically provide information about the crystal structure and phase, local strain, crystallite size among othersLin et al. (2017). The strain measured from XRD profiles are a measure of local strain within the electrolyte lattice structure. Interfacial and sub-surface strain in the solid electrolyte is estimated from the XRD profiles obtained at the interface as well as at sub-surface locations(Fig. 6.5b-c, 6.10, 6.14b). The general trend observed in the spatial distribution of the strain is that the interfacial strain is typically tensile and transforms into compressive strain when measured ≈ 40 μm below the interface. The low strain values of the order of 0.1-0.2%, are consistent with the high Young's modulus of the solid electrolyte. Additionally, the trends of strain variation between the interface and the cathode are well correlated. During the charging step, when the cathode undergoes delithiation and contracts, the interfacial strain shows an increased tensile strain. During the discharge step, this trend is reversed as the electrode expands on lithiation. Electrochemical and mechanical stresses at the interface can lead to formation of filaments/cracks within the solid electrolyte network. These mechanical transformations are potentially captured by the strain evaluations with the XRD measurements. It should be noted that local strain gradients measured here can have impact on

the ion transport characteristics of the solid electrolyte. Recent modelling efforts have shown that cation flux through the solid electrolyte system is dictated both by potential as well as stress gradientsMistry & Mukherjee (2020a):

$$i = -\kappa \nabla \phi_e + \kappa \frac{\Omega_{Li^+}}{F} \nabla \sigma_{h,e} \tag{6.2}$$

where, i is the cationic flux, ϕ_e is the electrolyte potential, κ is the ionic conductivity, Ω_{Li^+} is the partial molar volume of Li ion, F is the Faraday's constant, $\sigma_{h,e}$ is the hydrostatic stress in the electrolyte. Strain gradients in the solid electrolyte captured with EDXRD measurements can induce currents which can significantly impact the electrochemical performance of the system by formation of local polarization hot-spots. Additionally, previous studies have shown that tensile strain can modify the conductivity of ion conductors and lower the activation barrier by approximately 0.1 eV by alleviating lithium diffusion barriers between the electrode material and the electrolyte O'Rourke & Morgan (2018). These results motivate the need for understanding and decoupling the electro-chemo-mechanical stresses at the electrode|SE interface. Controlled interfacial and sub-surface strain response is crucial for enabling durable all-solid-state batteries.

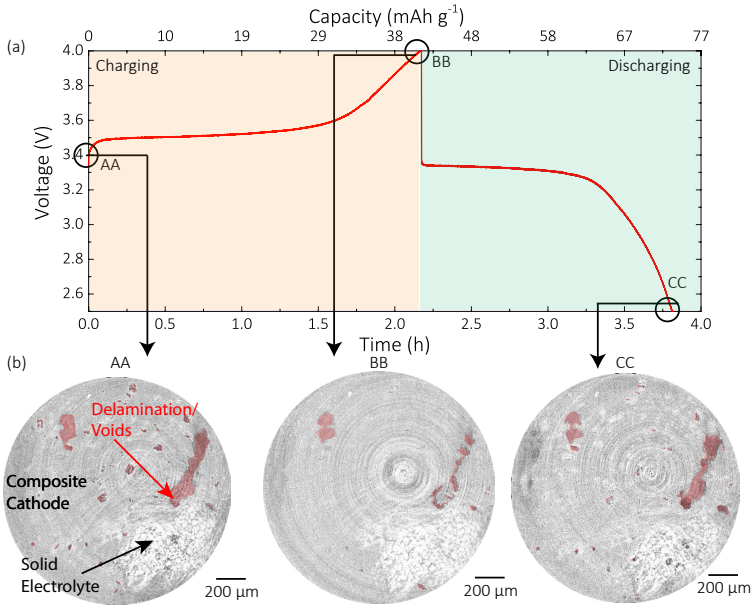

Figure 6.6: (a) Galvanostatic charge-discharge profiles for cycle 1 with locations for the tomography scans highlighted. (b) Cathode sections from the reconstructed tomography d at the pristine, charged and discharged state. The section of the cathode imaged here is immediately adjacent to the electrolyte (visible in patches). The features imaged here can potentially represent delamination of the electrode.

In addition to the EDXRD, tomography scans were also recorded intermittently during the electrochemical cycling (Fig. 6.6b, 6.11, 6.12). The cathode section images shown are in close proximity to the solid electrolyte (visible at lower right corner). The tomography reconstructions show regions of two distinct absorption contrast, where regions with lower grayscale value corresponds to the cathode material. The features with darker grayscale value range from 10 μm to having dimensions over 500 μm in size. These features are too large to be the pore structure of the electrodes which are typically in the order of a few microns (High resolution tomography at APS 2-BM, Fig. 6.13). The darker features imaged with lower resolution are associated with meso-scale structure and are considered to be an evidence of delamination/void formation at the interface. These features grow and contract during charge and discharge and are confined to the vicinity of the interface in the reconstructions confirming the claim that these are meso-scale delamination/voids forming at the interface. LFP material undergoes a phase change during cycling and the

resulting apparent partial molar volume, V_m (Li,delithiated phase α/lithiated phase) is +11.62 cm^3 mol^{-1}Koerver et al. (2018). Electrochemical cycling leads to volume changes in the active material which needs to be compensated by the composite cathode matrix. In absence of this, the active material volume change can lead to formation of voids, cracks and/or delamination. Even at low C-rates employed in this study as well as the few number of cycles, the degradation effects are severe in the cathode. These results confirm that the mechanical stability of the cathode is one of the pressing issues that need to be addressed for durable all-solid state batteries.

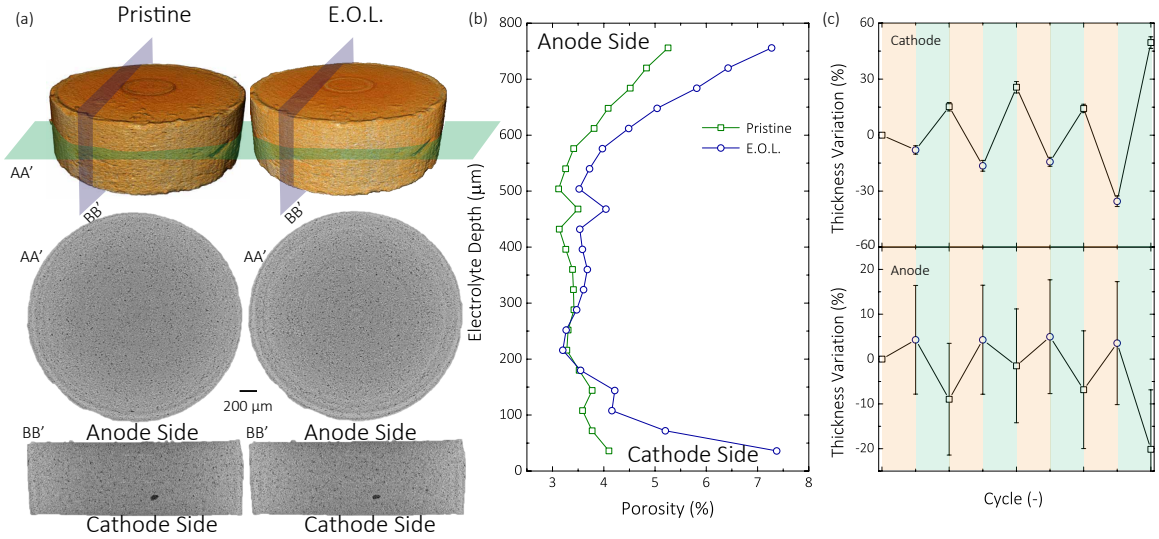

Figure 6.7: (a) 3D representation of LLZTO electrolyte for pristine and E.O.L. conditions. Sectional views from reconstructions are shown for both the electrolytes. (b) Average porosity measured over a thickness of 36 μm across the depth of electrolytes for the pristine and E.O.L. samples. (c) Variation of lithium and LFP electrode thickness during 4 cycles.

The differences in electrolyte microstructure is evaluated to assess the chemo-mechanical degradation impact on solid electrolyte. Earlier reports on in-situ tomography show that certain solid electrolytes consolidate pores upon charging and become denser Zhang et al. (2017a). Sectional images of pristine and end of life (E.O.L.) pellet after 4 cycles are shown (Fig. 6.7a). There is no apparent difference in microstructure or consolidation of pores in the two electrolytes. To quantitatively assess the difference, electrolyte porosity was estimated for the entire pellet in steps of 36 μm across the thickness for the pristine and the

E.O.L pellet (Fig. 6.7b). Typical porosity in the interior of the electrolyte is $\approx$ 4%. The porosity is higher at the interfaces for the pristine pellet (by $\approx$1-3%) compared to the interior of the sample. Since these measurements are taken over the entire pellet there are no error bars reported for this measurement. This effect could arise from the polishing or sintering steps employed for sample preparation. The E.O.L. sample shows similar trends, however, the porosity values at the interfaces are significantly higher compared to the pristine pellet(up to 2x). The bulk electrolyte still shows similar porosity values for both the samples. The increased porosity at the near the interfaces suggest a microstructure variation that could arise from mechanical strain/cracking/lithium deposition. Additionally, it is noted that the depth of impact is greater at the Li|electrolyte interface (400-750 μm) compared to the LFP|electrolyte interface (0-150 μm). This is expected as anodes undergo significantly higher volume expansion compared to cathode leading to higher stresses at the interface.

Electrode thickness fluctuations are tracked using the tomography dataset. Lithium interaction with X-rays is minimal making it difficult to evaluate the morphological difference in the anode during cycling. However, with the tomography dataset it is possible to quantify the thickness variation in the lithium metal. This is carried out by measuring line-scans of intensity values across the electrode sections (Fig. 6.13, 6.14a). This enables quantification of the electrode thickness during different system states. The trend in thickness variation of anode follow expected trends with increasing anode thickness during charging (plating) and reduction during discharging (stripping) (Fig. 6.7c). The larger standard deviations observed in the thickness variation arise from the fact that lithium does not plate parallel to the interface uniformly and there is an incline in that electrode. The thickness variations are symmetric for the most part between the charging and discharging cycle suggesting that there is no loss of lithium by deposits/dendrite formation in the system. Similar analysis is also carried out for the cathode section which shows complementary trends compared to the anode (Fig. 6.7c). The thickness variations in

cathode and anode ($\approx$ 20$\pm$12% for anode, 19$\pm$2% for cathode) are large compared to the theoretically expected fluctuations (5-8% for cathode, $\approx$5-10% for anode considering the depth of discharge and excess lithium). This indicates additional factors apart from thermodynamic and electrochemical driving forces are involved and further study is needed for decoupling these factors.

6.4 Conclusion

In summary, Li|LLZO|LFP full cells are investigated using operando synchrotron energy dispersive X-ray diffraction and in-situ tomography. Careful experimental design is needed to ensure non-destructive nature of X-ray probe during operando studies. Chemo-mechanical response of the electrolyte (interfacial and sub-surface) are quantitatively ascertained during battery operation. Lattice strain in the electrolyte at the cathode interface is tracked during cycling. Results indicate strained interfaces that can arise due to chemo-mechanical transformations like cracking or filament formation. Delamination effects are observed in cathode sections during operation which successively deteriorate on cycling. Volumetric expansion of the electrodes is estimated from the tomography data ($\approx$ 20$\pm$12% for anode, 19$\pm$2% for cathode). Microstructural variation (porosity) is found to be higher at the electrode|electrolyte interfaces between the pristine and E.O.L. sample. These results suggest that the electrode|electrolyte interfaces are pivotal in tailoring the chemo-mechanical response of the all solid-state batteries. Tailoring compliant interfaces is a potentially rewarding avenue towards designing all solid-state batteries with robust chemo-mechanical performance.

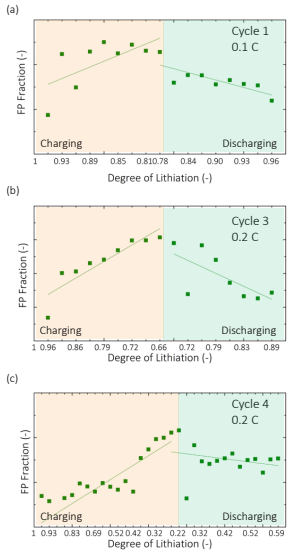

Figure 6.8: FP ratio as a function of degree of lithiation for three additional cycles measured from the EDD Data

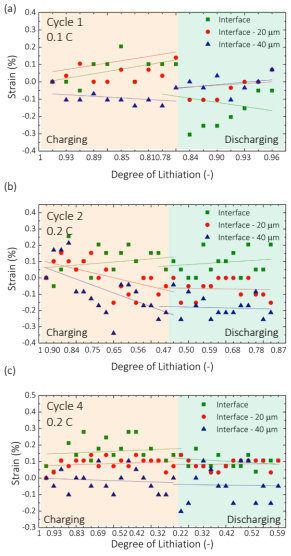

Figure 6.9: (a-c)Interfacial and sub-surface strain in electrolyte for three cycles evaluated from the EDXRD data.

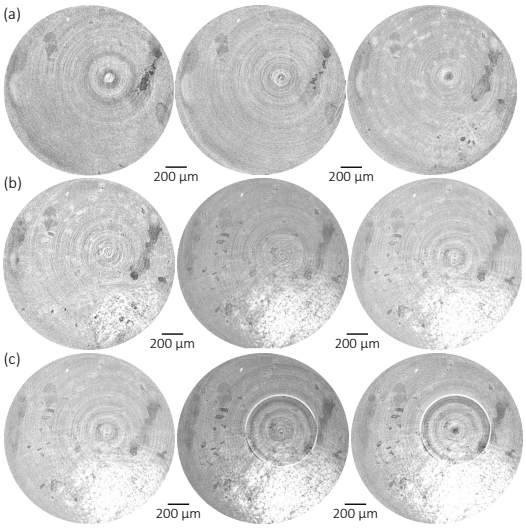

Figure 6.10: Cathode sections from the reconstructed tomography at the pristine, charged and discharged state from three additional cycles (a-c). The temporal locations of the imaged sections are identical to those shown in Figure 4 of the main text. The section of the cathode imaged here is immediately adjacent to the electrolyte (visible in patches). The features imaged here can potentially represent delamination of the electrode.

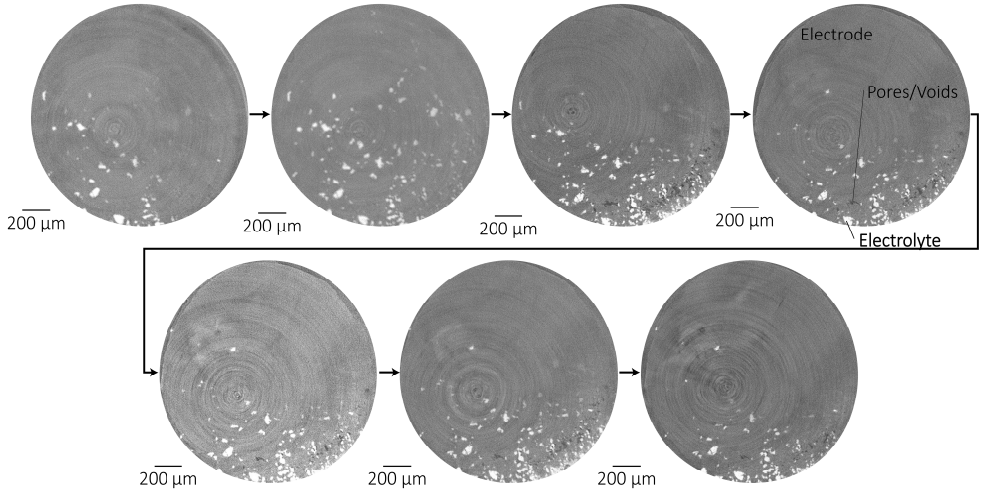

Figure 6.11: Cathode sections from the reconstructed tomography during cycling for additional sample. The temporal locations of the imaged sections are pristine and at the end of each charging and discharging cycle. The section of the cathode imaged here is immediately adjacent to the electrolyte (visible in patches). The features imaged here can potentially represent delamination of the electrode.

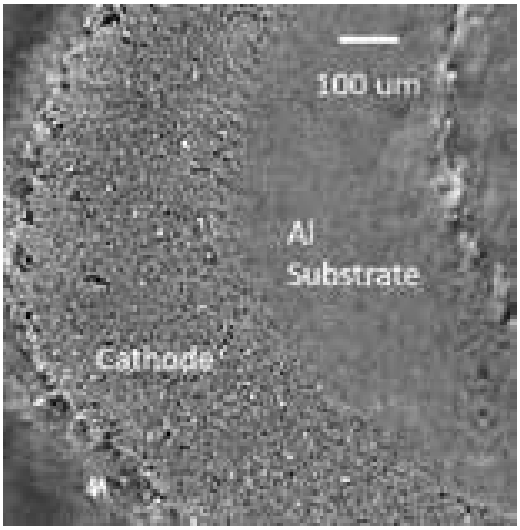

Figure 6.12: Cathode section imaged at APS-2BM microtomography beamline with higher resolution of 1 μm. This image was used to assess the features observed in the μ-CT at 6-BM beamline to be cracks/voids and not pores.

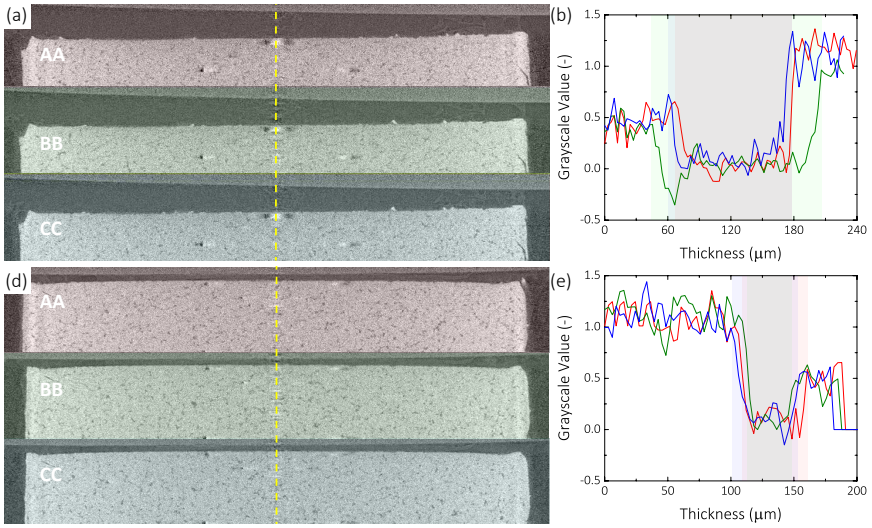

Figure 6.13: (a) Sectional images of lithium electrode at the pristine (AA), charged (BB) and discharged (CC) state for cycle 1. (b) Corresponding line intensity at identical sections from which the thickness of the electrode is evaluated. (c) Sectional images of LFP electrode at the pristine, charged and discharged state for cycle 1. (d) Corresponding line intensity at identical sections from which the thickness of the electrode is evaluated.

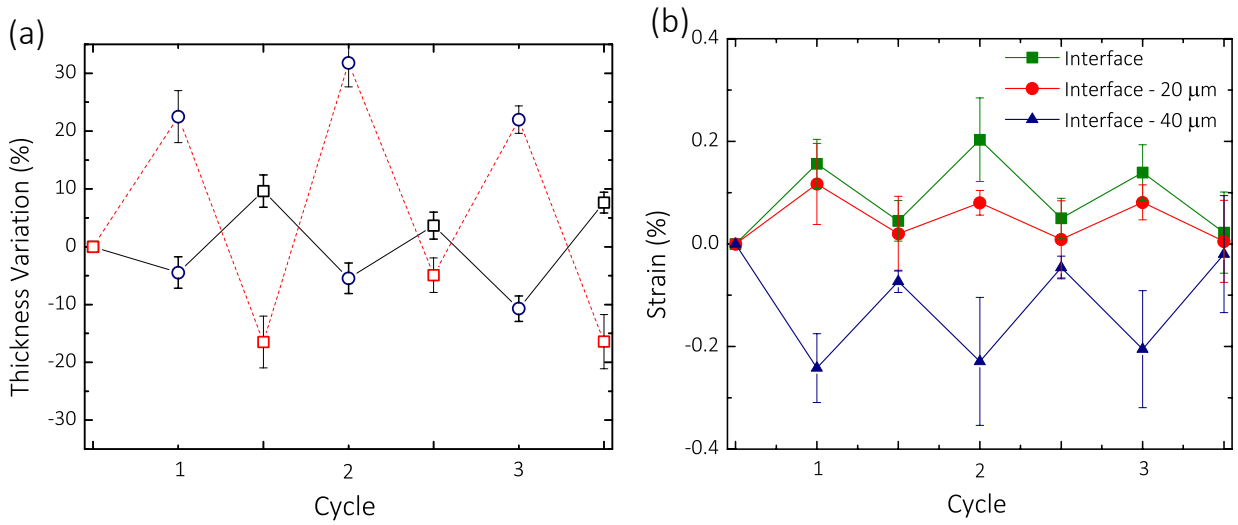

Figure 6.14: (a) Variation of lithium and LFP electrode thickness during 3 cycles.(b)Interfacial and sub-surface strain in electrolyte for three cycles evaluated from the EDXRD data. The results included here are for a second sample investigated.

Chapter 7

In situ Investigation of Interphase and Microstructure Effects on the Chemo-Mechanics of Thiophosphate Solid Electrolytes

7.1 Introduction

All-solid-state batteries can enable energy dense anodes for next generation energy storage systemsCheng et al. (2019); Hatzell et al. (2020); Masquelier (2011). Solid electrolytes, such as thio-LISICONs, lithium–phosphorous–sulfur (LPS) glasses, and argyrodites (Li_6PS_5X, X=Cl, Br, I), with high ionic conductivity ($>10^{-3}$ S cm^{-1}) and low electronic conductivity ($\sigma_e \approx$ nS cm^{-1}) Lau et al. (2018); Ujiie et al. (2013) are especially promising for lithium metal solid state batteries. However, despite excellent transport properties, the electrode|solid electrolyte chemo-mechanical stability remains a significant challengeHatzell et al. (2020); Koerver et al. (2018). Most inorganic solid electrolytes (ISE) are reactive with Li metal and form an interfacial decomposition product or interphase region. There are three prominent types of Li|SE interphases: (1) thermodynamically or kinetically stable (non-reactive), (2) unstable (reactive) Hartmann et al. (2013); Wenzel et al. (2016a), and (3) kinetically metastable (Fig. 7.1a)Wenzel et al. (2016b). Few solid electrolytes are non-reactive with lithium metal, with Garnet-type LLZO ($Li_7La_3Zr_2O_{12}$) being a possible exception Ma et al. (2016); Han et al. (2016). NASICON-type solid electrolytes (LAGP, LATGP, etc.) are examples of reactive electrolytes that form a mixed (ionic/electronic) conductivity interphaseHartmann et al. (2013). Finally, several types of solid electrolytes are metastable and form an interphase that is electronically insulating and ionically conducting. Li_3PS_4, for examples, is kinetically metastable as the interphase is primarily composed of electrically insulating lithium sulfide (Li_2S) and lithium phosphide (Li_3P)Wenzel et al. (2016a,b, 2018). While interphase structure, composition, and properties are not well understood, interphase growth leads to greater cell polarizationTippens et al. (2019); Wenzel et al. (2015b). The microstructure and transport

properties of the interphase can lead to non-uniform current densities, low power density, and local stress generation at buried electrode|electrolyte interfacesPorz et al. (2017); Sharafi et al. (2016). The latter can result in catastrophic failure via lithium filament formation, electrical shorting, and fractureKazyak et al. (2020).

Active or passive approaches during electrolyte synthesis and processing are commonly utilized to control interphase properties. Active approaches include the use of an interlayer barrier film Han et al. (2018); Pervez et al. (2019); Xu et al. (2018); Broek et al. (2016). Prior studies have investigated atomic layer deposition of interlayer materials (Al_2O_3, Si, $Li_xAl_{(2-x/3)}O$, $LiXO_3$(X = Ta, Nb)) to improve the surface wetting capability of metallic lithium and lower interfacial resistancesZhu et al. (2015); Sang et al. (2018); Han et al. (2016). Passive approaches such as halide doping or substitution have been reported to increase the stability of sulfide containing electrolytes with lithium metal through the formation of a nanometer-thin passivating interphaseAdeli et al. (2019); Wang & Sakamoto (2018). Halide doping has also been reported to improve the ionic conductivity, wettability with the Li metal as well as the electrochemical stability window Ujiie et al. (2013, 2014); Wu et al. (2015); Ujiie et al. (2012); Han et al. (2018); Mercier et al. (1981); Cai et al. (2015); Lu et al. (2018). Theoretical and experimental studies ascribe this increase in performance to the formation of an ionically conducting interphase with Li_2S, Li_3P and LiIHan et al. (2018). While transport in the interphase undoutedbly plays a role on performance, it is less clear how the chemo-mechanics of the interphase governs performance. Stress within individual battery components and/or at interfaces can occur because of physical volume changeKoerver et al. (2018); Wang et al. (2019), the formation of gasBartsch et al. (2018); Strauss et al. (2020), and/or mass (ion) transportMistry & Mukherjee (2020b); Tian et al. (2020); Larson et al. (2018). While concentration gradients do not exist in a single ion conducting electrolyte, there is the potential for stress-assisted diffusion at solid|solid interfacesLarson et al. (2018). Irregular interphase growth or Li^0 electrodeposition can lead to stress gradients in a solid electrolyte and alter the local en-

ergy level of the cation and contribute to directed ionic transportMistry & Mukherjee (2020b); Fu et al. (2020). Mechanical stresses can also affect the dissolution and deposition kinetics governed by molar volume mismatch between solid electrolyte and lithium metal electrodeMistry & Mukherjee (2020b). These chemo-mechanical effects can lead to non-uniform ionic flux at electrode|solid electrolyte interface and be a driver for mechanical degradation. Several competing hypotheses are proposed for chemo-mechanical degradation and failure of solid-state electrolytesXiao et al. (2020); Ke et al. (2020b). Unstable interphase formation due to reactivity between solid electrolyte and Li metal can cause mechanical stresses at the interface and cause fractureTippens et al. (2019). Trace electrical conduction in the solid electrolyte can cause isolated Li deposition which can subsequently grow through a connected pore network causing failureHan et al. (2019); Shen et al. (2018). Interfacial compatibility and irreversible electrode volume change can also cause chemo-mechanical degradation of solid electrolytesKe et al. (2020b). Preferential filling of local flaws and subsequent filament growth through the flaws can lead to fracture within the solid electrolytePorz et al. (2017). Modelling studies have highlighted that chemical and geometric defects at a Li|SE interface can cause decohesion of Li and/or fracture of SENarayan & Anand (2020); Klinsmann et al. (2019). Pressure build up at dendrite tips are shown by coupled transport, plastic and elastic deformation models to exceed hundreds of MPa which can potentially cause fractureBarroso-Luque et al. (2020); Tu et al. (2020); Athanasiou et al. (2020). *In situ* characterization of morphological changes in SE are required to assess the failure mechanisms.

The interdependent relationship between local ion transport, electrode|electrolyte contact, and solid electrolyte mechanical properties and cycle life is important for resilent solid state batteries. Thiophosphate solid electrolytes with halide substitution and/or doping have lower Young's modulus that can enable stress accommodating interfaces, better contact with metallic lithium, and longer cycle lifetime Kato et al. (2018). In the limit of absence of excess Li, the anode undergoes 100% change in thickness. While, ex-

act estimation of the associated strain on the electrolyte corresponding to this variation is difficult, a qualitative comparison of mechanical response for solid electrolytes with low and high Young's modulus can be made. Compliant interfaces, i.e. interfaces that maintain contact when subject to electrochemical stresses during cycling, require dissipation of the stresses within the material. With low Young's modulus (≈18 GPa,McGrogan et al. (2017)) solid electrolytes, the stresses generated by Li metal electrodeposition / electrodissolution can be accommodated by the solid electrolyte by deformation. This potentially can enable conformal deposition/stripping of Li metal at the interface. In contrast, with a high modulus material non-compliant nature of the solid electrolyte (low deformation to electrodeposition / electrodissolution stress) can lead to non-planar morphologies in the anode leading to instabilities. However, thiophosphate solid electrolytes have a low fracture toughness (≈ 0.2 MPa $m^{\frac{1}{2}}$) and are prone to fracture McGrogan et al. (2017); Hayashi & Tatsumisago (2018). It should be noted that mechanical response of the lithium electrode is generally in the flow/creep regimeLePage et al. (2019) and additionally molar volume mismatch of Li^+ and Li metalMistry & Mukherjee (2020b); Koerver et al. (2018) can impart electrochemical stresses at the interface. Prior work on the NASICON family of solid electrolytes has suggested that interphase instability can lead to non-uniform stress distribution which initiates fracture-induced failure Lewis et al. (2019). Other works suggest that operating conditionsWang et al. (2019); Kasemchainan & Peter (2018); Jow & Liang (1983) or the bulk solid electrolyte Garcia-Mendez et al. (2017); Porz et al. (2017); Sharafi et al. (2017); Cheng et al. (2015); Shen et al. (2018); Han et al. (2019) may be origins for fracture. Volume changes arising from electrodeposition and electrodissolution of lithium metal can lead to stress generation at the interphase. Additionally, mechanical stresses can arise from volume changes arising from chemical decomposition of the solid electrolyte, as well as due to molar volume mismatch between Li^+ and lithium metal. All of these factors can also contribute to mechanical failure of the solid electrolytes.

The influence of electrolyte microstructure heterogeneity on stress distribution and frac-

ture mechanics is not well known. This lack in understanding is primarily because there are limited experimental techniques capable of probing these dynamics at buried interfaces. One technique capable of *in situ* characterization of solid state batteries is synchrotron x-ray computed tomography (XCT) which offers resolutions ~ 1 μm. This resolution range is ideal for the detection of mesoscale material transformations in solid-state batteries Conder et al. (2018). Recently, *ex situ* studies revealed that pore connectivity in garnet-type oxides correlated with obtainable critical current densities Shen et al. (2018); Dixit et al. (2018a). Furthermore, XCT has revealed that mechanical deformation and irregular contact at electrode|electrolyte interfaces may drive filament propagation in Na^+ β-alumina and LPS electrolytes respectively Seitzman et al. (2018); Haas et al. (2019). Failure mechanisms transcend several length-scales, from nano-scale interfacial reactions to meso-scale crack and fracture propagation. Furthermore, these occur at disparate time scales which complicates experimental assessmentMa et al. (2018). Combining electrochemical measurements with (non-destructive) characterization techniques is crucial for deconvoluting the nature of chemo-mechanics in solid state battery systemsDixit et al. (2020).

Herein, we systematically study material transformation pathways which impact fracture in a series of thiophosphate solid electrolytes in order to understand the nature of interphase chemistry and microstructural heterogeneity on fracture. Thiophosphate solid electrolytes are systematically altered for interfacial chemistry (via halogen doping) and microstructural heterogeneity (milling and annealing). A multi-modal approach is employed to elucidate the role solid electrolyte microstructure and interphase impact fracture events. *In situ* transmission electron microscopy provides evidence for interphase formation mechanisms and provides nano-scale insight into pore formation in the interphase which drives edge fracture degradation modes at solid electrolyte|lithium interfaces. *In situ* synchrotron X-ray tomography experiments resolve fracture growth mechanisms. Fracture pathways in solid electrolyte are correlated with microstructure hetero-

geneities. The results demonstrate that the temporal onset of fracture is governed by interphase properties. However, the fracture-type was seen in all electrolytes independent of the interphase and the extent of fracture correlated well with microstructure heterogeneity. These local cracks are filled with electrochemically active Li metal. The active Li metal in the cracks can be cycled and thus contribute to localized stress within the solid electrolyte which accumulates and ultimately leads to catastrophic failure by fracture.

7.2 Methods

7.2.1 Sample Preparation

Synthesis of Li_3PS_4 (A-LPS)

Anhydrous lithium sulfide (Li_2S) (Aldrich, 99.98%) and anhydrous phosphorus pentasulfide (P_2S_5) (Sigma-Aldrich, 99%) first form a mixture (2.0 g total) containing a molar ratio of Li_2S:P_2S_5 = 3:1. This mixture was ground by hand in an agate mortar/pestle for 5 minutes and then transferred to a 45 mL zirconium oxide (ZrO_2) ball-mill pot along with 32 g of ZrO_2 balls (5 mm diameter). The mixture was ball-milled for 40 hours using a planetary ball mill (Pulverisette 7, Fritsch). Afterward, the yellow lithium thiophosphate (Li_3PS_4-LPS) powder was collected.

Synthesis of Li_3PS_4:0.5LiI (LPS:0.5LiI)

Anhydrous lithium iodide (LiI) beads (Aldrich, 99.999%) were added to an agate mortar/pestle and pulverized. Then, LiI was moved to a new mortar along with anhydrous Li_2S and anhydrous P_2S_5 to form a mixture (2.0 g total) containing a molar ratio of Li_2S:P_2S_5 : LiI = 3:1:1. This mixture was ground for 5 minutes and then transferred to a 45 mL ZrO_2 ball-mill pot along with 32 g of ZrO_2 balls (5 mm diameter). The mixture was ball-milled for 40 hours using a planetary ball mill (Pulverisette 7, Fritsch). Each cycle consisted of spinning the pot for 1 h at 550 rpm and then resting the pot for 5 min. Afterward, the LPS·0.5LiI (light yellow) powder was collected.

Synthesis of attrition milled LPS:0.5LiI (LiI-AT)

2 g of LPS:0.5LiI was transferred to a 45 mL ZrO_2 ball-mill pot along with 43 g of ZrO_2 balls (1 mm diameter). 6 g of dried heptane was added to the pot before sealing. The mixture was ball-milled for 12 hours using a planetary ball mill (Pulverisette 7, Fritsch). Each cycle consisted of spinning the pot for 1 h at 200 rpm and then resting the pot for 5 min. The white powder was collected and rinsed with 6 g of dried heptane and heated on a hot-plate while stirring at 100 °C for 3 hours. Afterward, the LiI-AT (white color) powder was collected.

Synthesis of annealed LPS:0.5LiI (LiI-AN)

2 g of LiI-AT was placed into a stainless steel can on a hot-plate. The mixture was heated at 185 °C for 3 hours while stirring every 20 minutes. Afterward, the LiI-AN (light-grey color) powder was collected.

7.2.2 Materials Characterization

Raman spectroscopy was performed with a Horiba LabRAM HR spectrometer equipped with an inverted optical microscope. A 50x lwr objective lens was used to focus a 532 nm laser onto the powder sample, which was pressed against the inside surface of a sealed cuvette to protect it from air. The back-scattered light was dispersed using a 600 grating/mm grating onto a CCD camera. Spectra were collected from three different spots on each sample and compared to confirm sample homogeneity. X-Ray diffraction patterns were collected on a lab diffractometer for $10^\circ < 2\theta < 90^\circ$.

7.2.3 Cell Assembly and Electrochemistry

Fabrication of impedance measurement cells

100 mg of solid electrolyte powder was added to the hole in a Macor ring (SA = 1.0

cm^2) and cold-pressed between two steel pistons into a pellet under 4 tons of pressure for 5 min. Then, carbon-coated aluminum foil (MTI corp.) disks were placed against both sides of the pellet and the stack was pressed again under 3 tons for about 1 min. After removing the stack from the press, the pistons were anchored in place by a cell top and bottom, held together by insulated bolts. The bolts were tightened to 2 N·m, which provides a stack pressure of about 88 MPa. Finally, the cell was sealed in an argon-filled container and placed into a temperature-controlled oven. Electrochemical impedance spectroscopy was performed using a Bio-logic VMP3 Potentiostat, with a frequency range from 100 mHz to 1 MHz and a potential amplitude of 10 mV. The electrolyte resistance was determined from the EIS plots by extrapolating the low-frequency, linear section of the curves down to the x-axis.

Fabrication of Li/Solid Electrolyte/Li symmetric cells

For LPS:0.5LiI measurements, 100 mg of solid electrolyte was added to the hole in a Macor ring (SA = 1.0 cm^2) and cold-pressed between two steel pistons under 4 tons of pressure for 5 min to form a pellet. Then a thick lithium (Li) disk (99.8%, Honjo Metal) of 10 mm diameter was polished with a toothbrush, punched from the flattened Li using a knife punch and placed on both sides of the pellet. The final thickness of the Li foil is 150 μm. Stainless-steel pistons were pressed against the Li to form a stack, which was then sandwiched between cell top and bottom. Finally, insulated bolts were used to compress the cell to 29 MPa before placing the cell into an argon-filled container, which was then moved from the glove box to an oven for electrochemical testing.

Critical Current Density (CCD) test

Li metal was plated and stripped at step-wise-increased current densities using a Bio-logic VMP3 Potentiostat. At 60 °C, the current density was increased in a stepwise

manner from 0.1 mA/cm^2 to 4.0 mA/cm^2 in 0.25 mA/cm^2 increments. Each current was applied using 1-hour half-cycles for 2 cycles. The CCD was ascribed to the current at which a sharp drop in potential was witnessed mid-half-cycle.

Fabrication of Synchrotron Cells

For synchrotron experiments, 3 mm electrolyte pellets were made by compressing the samples at 4 tons/cm^2 pressure. The samples were transferred to the beamline in Argon atmosphere sealed containers. Symmetric Li|Li cells were assembled in the *in situ* cell inside an Argon atmosphere glovebox ($<$ 0.1 ppm O_2 and H_2O) and sealed. The *in situ* cell was mounted on the sample stage at the end station. Electronic impedance spectroscopy was carried out before and after the complete testing of the symmetric cell between 1 MHz and 100 mHz with an amplitude of 50 mV. Plating and stripping experiments were carried out at current densities of 0.04 - 1.2 mA cm^{-2} for 30 minutes duration. A cut-off voltage of 10 V was kept for the tests. If the polarization exceeded this value, the current density was moved to the next step.

7.2.4 Tomography Studies

Synchrotron X-ray tomography studies were carried out at the 2-BM beamline of the Advanced Photon Source (Fig. 7.3a). Filtered monochromatic X-rays of 25 keV were incident on the sample. 1500 projections were taken evenly during a 180 $^\circ$ sample rotation with 100 ms exposure time for each projection. FLIR Oryx ORX-10G-51S5M camera was used with a 2x magnification objective lens. The resultant voxel size was $\approx$0.7 μm and a field of view of 1.4 x 0.8 mm^2. With these experimental conditions, a single tomography scan took approximately 7-10 minutes of acquisition time. The tomography scans were taken for the pristine and the failed sample. Additionally, tomography scans were obtained at the end of each plating and stripping cycle.

7.2.5 Image Reconstruction, Analysis and Quantification

Tomopy software was used for reconstruction of the raw dataCarlo et al. (2014) using Gridrec algorithm. Wavelet-Fourier ring filter removalMünch et al. (2009) and Paganin phase retrievalPaganin et al. (2002) methods were applied for raw image manipulation. Subsequent image processing was carried out using Image JSchneider et al. (2012a) and MATLAB. Binarization of all the samples were carried out using identical thresholding routines available in ImageJ. The thresholding protocols were kept identical across all the analysed tomography scans to reduce variability in the results. Subvolume optimization was carried out to estimate geometric parameters of the system. Pore size distributionMunch & Holzer (2008b) plugin was used to estimate the porosity of the samples. The details of the method used to describe porosity and pore size distribution is reported previously Dixit et al. (2018a). Identification cracks from the binarized data was carried out by filtering pores smaller than a specified threshold volume and subsequently by visual analysis. All quantification routines were developed and implemented in MATLAB.

7.2.6 Microscopy Imaging Methods

Scanning Electron Microscopy (SEM)/Energy Dispersive X-ray Spectroscopy (EDS)

SEM images were collected using a JEOL 7800 FLV microscope outfitted with an Oxford EDS system, operated at 5-20 kV for all samples. All samples were loaded into an air-free SEM holder (JEOL) within an Argon atmosphere glove box (< 0.1 ppm O_2 and H_2O) and transported directly to the SEM where they were analyzed under vacuum.

Transmission Electron Microscopy (TEM)/Energy Dispersive X-ray Spectroscopy (EDS)

HAADF STEM images were collected using a JEOL JEM-F200 microscope operated at 200 kV. Dual silicon-drift detector EDS systems with a large solid angle (100 mm2) were utilized for enhanced microanalysis of all samples via ex-situ and in-situ analysis modes. Specific to ex-situ TEM: All samples for ex-situ analysis were loaded onto 3 mm 300-mesh

lacy carbon coated copper grids (Ted Pella) within an Argon atmosphere glove box (< 0.1 ppm O_2 and H_2O). The loading was carried out by directly scooping the grid through the sample material contained within a glass vial. As such, this was a dry-casting method and no solvents were utilized during the process at any time to prevent possible reactions between sample materials and solvents. The material cast and analyzed using this process was Li_3PS_4:0.5LiI. In addition to general imaging and elemental analysis, ex-situ TEM was utilized as a benchmark to establish the necessary microscope settings (e.g. probe size, beam current, spot size, exposure time, etc.) to successfully image and analyze the materials without damage from the beam itself. It should be noted that each material is expected to have different behavior under the beam and as such should be benchmarked prior to in-situ TEM analysis efforts to ensure an optimized setup. Below, we provide a description of how the ex-situ holder (JEOL single-tilt) was setup for the experiments highlighted in this manuscript:

The holder was brought into the glove box using standard protocols and the holder tip was disassembled within the glove box to load a designated sample material. Specific tools for the holder were also brought into the glove box to ensure damage-free disassembly/assembly of the holder.

For all experiments, Li_3PS_4:0.5LiI material was loaded onto the grid using the procedure described above. The material loaded grid was then assembled into the holder component.

The reassembled holder was now secured for air-free transfer from the glove box by using a customized air-free holder cap. Once secure with this cap, the holder was removed from the glove box using standard protocols and immediately moved to the TEM for loading.

The holder was loaded into the TEM while the air-lock for the TEM holder vented either nitrogen or argon gas to ensure air-free entry of the holder into the TEM. The custom air-free holder cap was removed from the holder at the TEM point of entry immediately prior

to loading the holder into the TEM and pumping it down instantly to minimize sample exposure to air during this process. The total time that the sample was exposed to air was on the order of 5 to 10 seconds.

Specific to in-situ TEM: All sample analysis was carried out using a Biasing Nanomanipulator Holder designed by Hummingbird Scientific. The holder assembly was carried out within an Argon atmosphere glove box (< 0.1 ppm O_2 and H_2O). This in-situ holder utilized a 3mm 300-mesh lacy carbon coated copper half-grid (Ted Pella) and a tungsten (W) scanning tunneling microscopy (STM) probe (Bruker). The biasing capability of the in-situ holder allowed for the application and observation of a current and/or voltage between the half-grid and STM probe. The movable STM probe could be brought into contact with the half-grid to complete a circuit and conduct electrochemistry experiments within the TEM. Below, we provide a description of how the in-situ holder was setup for the experiments highlighted in this manuscript:

The holder was brought into the glove box using standard protocols and the holder tip was disassembled within the glove box to separate components for the half-grid and the probe. Specific tools (procured from Hummingbird Scientific) for the holder were also brought into the glove box to ensure damage-free disassembly/assembly of the holder.

For all experiments, Li_3PS_4:0.5LiI material was loaded onto the half-grid using the procedure described for ex-situ TEM. The material loaded half-grid was then assembled into the holder component designed for the half-grid.

The W probe was converted into a lithium (Li) coated W probe for our applications, as follows. Li metal foil (MTI Corporation) was first cleaned by mechanical scraping of the foil surfaces using the plastic cap of a standard 20 ml glass vial (VWR). This scraped Li foil piece was placed on top of a 100-micron thick nickel (Ni) foil (Alfa Aesar) which was contained within a glass petri dish (VWR). The petri dish, along with the Ni and Li foil materials were then heated using a hot plate until the Li was observed to melt at which

point the W probe was very gently dipped into the molten Li to procure the Li coated W probe. The dipping was accomplished by bringing the molten Li into contact with the probe, not vice-versa, to ensure safety of the fragile probe.

The holder was now completely reassembled within the glove box and the holder tip (containing the material loaded half-grid and Li probe components) was secured for air-free transfer from the glove box by using a customized air-free holder cap. Once secure with this cap, the holder was removed from the glove box using standard protocols and immediately moved to the TEM for loading.

The holder was loaded into the TEM while the air-lock for the TEM holder vented either nitrogen or argon gas to ensure air-free entry of the holder into the TEM. The custom air-free holder cap was removed from the holder at the TEM point of entry immediately prior to loading the holder into the TEM and pumping it down instantly to minimize sample exposure to air during this process. The total time that the sample was exposed to air was on the order of 5 to 10 seconds.

Once the holder was pumped down in the TEM, a suitable Li_3PS_4:0.5LiI sample was located on the edge of the half-grid closest to the Li probe, and the Li probe was moved into position to contact this sample using manual and electronic adjustments to the probe via Hummingbird Scientific software. Upon contact, the noted in-situ TEM electrochemical experiments in the manuscript were carried out using a Bio-Logic SP-200 Potentiostat.

7.3 Results and Discussion

Herein, we investigate a series of thiophosphate solid electrolytes with varying microstructures and interphase properties (A–LPS, LPS:0.5LiI, LiI–AT, LiI–AN) to assess the impact on mechanical failure (Fig. 7.1c). Mechanical failure in thiophosphate solid electrolyte manifests as cracks that traverse through the bulk of the material (Fig. 7.1b). Crack propagation through the bulk is spatially non-uniform in terms of density and

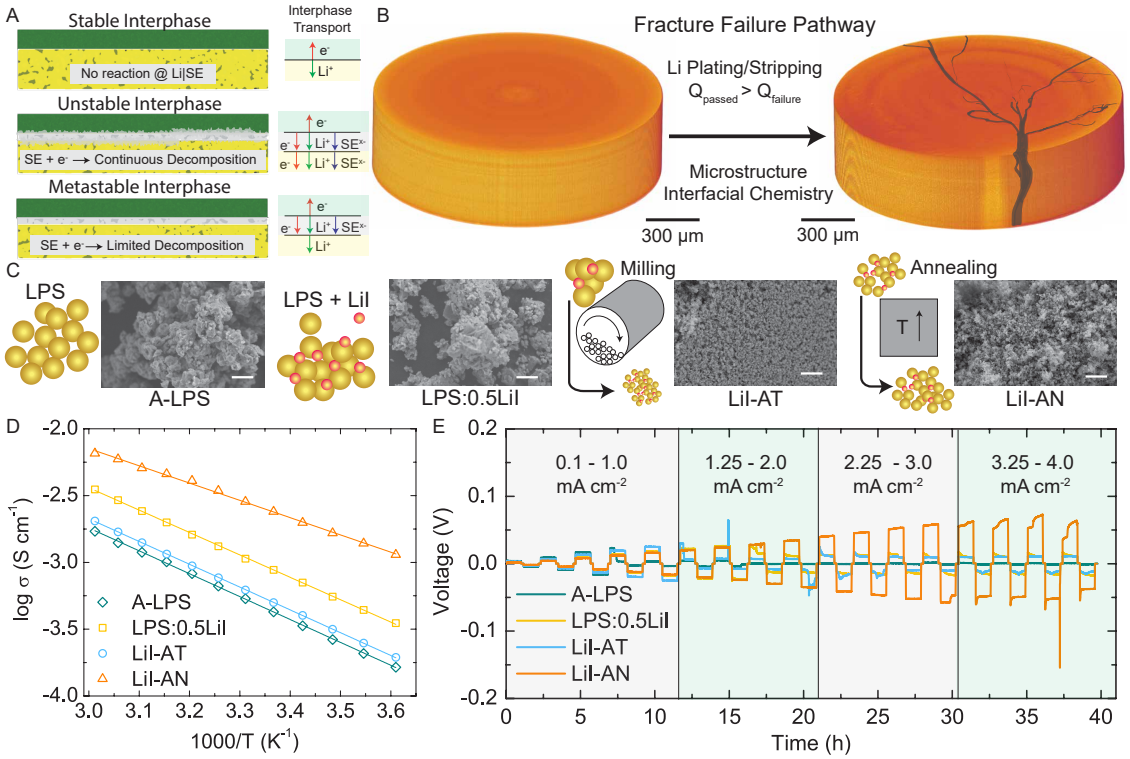

Figure 7.1: Investigation of Material Transformations in LPS Material. (a) Schematic diagram depicting Li metal and solid electrolyte interphase types. Stable interphase has no chemical decomposition of SE; unstable interphase shows continuous SE decomposition while kinetically metastable interphase shows controlled SE decomposition. Corresponding ionic and electronic conduction behavior are also indicated. (b) 3D tomography reconstruction of pristine and failed LPS electrolyte pellet. Effect of interfacial chemistry and microstructure on mechanical failure in LPS materials is investigated. (c) SEM images of powder materials in the study along with schematic diagrams highlighting processing used to synthesize the material. The scale bar on all images is 10 μm. A–LPS is amorphous sulfide material. LPS:0.5LiI is a mixture of amorphous LPS and LiI salt. LiI–AT material is obtained by mechanical milling of the LPS:0.5LiI material. LiI–AN is obtained by annealing the LiI–AT material. (d) Ionic conductivity, and (e) critical current density measurement for the solid electrolytes.

morphology. The material properties of the solid electrolyte (microstructure, density, interphase structure, etc.) can influence fracture events. A–LPS is an amorphous sulfide glass-ceramic electrolyte (Li_3PS_4) that is kinetically unstable and can form an lithiated interphase composed of Li_2S and Li_3P byproducts. An interphase can lead to an increase in cell polarization with cycling and cell failure. Extensive interfacial decomposition of A–LPS upon contact with metallic lithium is observed from tomography experiments

and is evidence of an unstable interphase (Fig. 7.8a-b). Solid electrolytes with kinetically metastable interphases can be obtained by doping LPS with LiI. LiI addition leads to higher mobile Li^+ concentration as well as interfacial decomposition to ionically conducting LiI along with the typical LPS decomposition products (Li_2S and Li_3P) . Thus, the ion conducting interphase coupled with better Li wettability contributes to better anode stability in the iodine-doped LPS (LPS:0.5LiI) Han et al. (2018); Ujiie et al. (2012); Mercier et al. (1981). In order to systematically change the microstructure of LPS:0.5LiI, two different post processing techniques were utilized. First, the LPS:0.5Li solid electrolyte was milled in order to reduce the primary particle size and improve the packing density (LiI–AT). Subsequently, the milled powders were annealed which resulted in a nano-crystalline phase with higher densification and lower porosity (LiI–AN). All samples studied (A–LPS, LPS:0.5LiI, LiI–AT, LiI–AN) show the formation of Li_3PS_4 through the presence of the PS_4 structural unit at 420 cm^{-1} (Fig. 7.9a). The lack of a diffraction peaks beyond small remnant reactant reflection (Fig. 7.9b) are characteristic of an amorphous solid-electrolyte. LiI addition induces some crystallinity in the samples. A–LPS material shows a porous structure with pores sizes >3-5 μm (Fig. 7.10). LPS:0.5LiI, LiI–AT and LiI–AN show consistently decreasing porosity and pore sizes (Fig. 7.10). Energy dispersive spectroscopy mapping of pellets reveals a uniform iodine distribution on all doped samples (Fig. 7.11).

The room temperature ionic conductivity increases as A–LPS<LiI–AT<LPS:0.5LiI<LiI–AN (Fig. 7.1d, 4.26×10^{-4}, 5.01×10^{-4}, 8.79×10^{-4}, 2.40×10^{-3} S cm^{-1}, respectively). The corresponding activation energy for the materials are 0.111, 0.144, 0.147, and 0.148 eV for LiI–AN, LPS:0.5LiI, LiI–AT, and A–LPS. LiI–AN shows almost a 5× increase in ionic conductivity and a 25% reduction in the activation energies compared to the amorphous material. Long-range order as well as the particle-particle adhesion in the material is improved in a dense matrix leading to improved ion transport propertiesGarcia-Mendez et al. (2017). Reduction of ion-blocking pores can also contribute to improved ion trans-

port properties (low tortuosity)Dixit et al. (2018a) and iodine doping increases the concentration of mobile Li^+ ions and reduces interactions with the glass network leading to improved ionic conductivityMercier et al. (1981).

The electrochemical response of all the investigated materials clearly show a decrease in polarization beyond the critical current density, with A-LPS showing an almost zero polarization. The electrochemical response is consistent with the formation of dendrites as reported previouslyKazyak et al. (2020); Brissot et al. (1999). No other mechanism was apparent with the short-circuiting cells. The critical current density (CCD) and cumulative charge passed before failure (charge-to-failure) follows a similar trend to the ionic conductivity (Fig. 7.1e) with LiI–AN showing a maximum CCD of 4 mA cm^{-2} (135.72 C cm^{-2}), and A–LPS showing the minimum CCD of 0.75 mA cm^{-2} (6.849 C cm^{-2}). LiI–AT fails at 1.25 mA cm^{-2} (19.62 C cm^{-2}) and LPS:0.5LiI fails at 1.75 mA cm^{-2} (41.67 C cm^{-2}). Halogen-doped solid electrolytes (LPS:0.5LiI,LiI–AT and LiI–AN) demonstrate an increased CCD compared to the undoped solid electrolyte (e.g. A–LPS). Considering current limit diagrams based on nucleation theory, the critical current density is given asRaj & Wolfenstine (2017),

$$j^* = \frac{(2\gamma\Omega_{Li}/r_c) + \sigma_F\Omega_{Li}}{fd(1-\alpha)|e|} \cdot \frac{1}{\rho} \tag{7.1}$$

where j^* is the critical current density, γ is the specific energy of the interface , Ω_{Li} is the volume per Li atom in the electrolyte, r_c is the critical radius, σ_F is the fracture stress, f is the contribution of grain boundary resistivity, d is the grain (particle/feature) size, α is the ratio of grain boundary to grain (void/particle) size, e is the charge on the electron, and ρ is the overall resistivity. The critical current density formulation arises from electro-chemo-mechanical potential of Li that can develop from high local resistivity or from physical irregularities in the shape of the Li interface. The model assumes a back stress that opposes the propagation of the dendrite and is considered as the fracture strength of

the electrolyte material. It should be noted that while this model proposes a nucleation-controlled fracture propagation model, other mechanisms for fracture propagation also exist. Chiefly, a toughness-limited fracture propagation model is also applicable to the system under study. There is an underlying uncertainty regarding the fracture propagation mechanism. However, the model can be utilized for the purpose of qualitative comparison of factors influencing critical current density for the studied materials. The critical current density (j^*) is proportional to the ionic conductivity and inversely proportional to the total resistivity. Highly dense LiI–AN with higher ionic conductivity shows improved critical current density as well as charge-to-failure over the other halogen containing materials (LiI–AT, LPS:0.5LiI). Increased particle surface area in the LiI–AT material compared to the LPS:0.5LiI material can lead to a higher effective grain boundary resistance for the milled material. This results in a lower ionic conductivity and critical current density for LiI–AT compared to LPS:0.5LiI. LiI–AN shows the highest critical current density due to the higher ionic conductivity, higher charge carrier concentration due to halide doping and lower grain boundary resistance due to improved densityBonnick et al. (2019). Interfacial effects of halogen doping can also aid in improving the critical current density. Uniform contact between the plating/stripping surface of the Li metal anode and the electrolyte leads to planar Li plating and stripping. Iodine can potentially act as a protective layer to ensure a congruent, contiguous interface between LPS and Li metal while also preventing the continuous decomposition of LPS in contact with Li metal.

A nanoscale understanding of interphase compositional and morphological transformations during electrochemical cycling is challenging because there are limited non-destructive techniques capable of probing these interfaces with adequate spatial and temporal resolutions. *In situ* TEM (Fig. 7.2, 7.12) is implemented to assess the chemo-mechanical response of the solid electrolyte during lithium stripping and plating. The solid electrolyte was benchmarked with *ex situ* experiments described in the support-

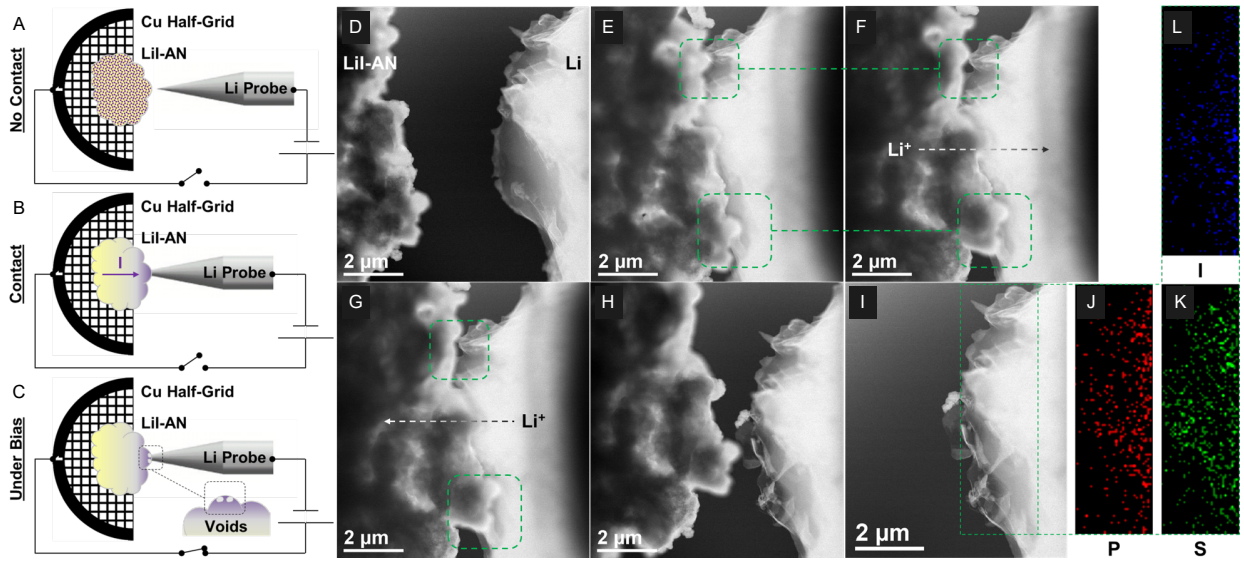

Figure 7.2: Interphase transformation tracked by *In Situ* TEM (a) Animation of the in-situ TEM Nanomanipulator holder highlighting the arrangement of Li and LiI–AN, (b) animation depicting the contact of Li and LiI–AN and resulting chemical processes (migration of iodine) within the TEM, (c) animation depicting the electrochemical processes (formation of voids) observed upon application of bias within the TEM, (d) HAADF STEM image of the Li probe and LiI–AN solid electrolyte prior to contact, (e) HAADF STEM image of the Li probe and LiI–AN upon contact, highlighting regions of interest for the purpose of this study, (f) HAADF STEM image of variations in the highlighted sections via appearance of voids along the Li/LiI–AN interface after plating of Li, (g) HAADF STEM image after the stripping of Li with the retention of formed voids during Li plating in the highlighted sections, (h) HAADF STEM image of the detached Li probe and LiI–AN after a Li plating/stripping cycle, (i) HAADF STEM image highlighting an area of interest on Li utilized for EDS mapping after Li plating/stripping experiments, and (j), (k), (l) phosphorus, sulfur and iodine EDS maps of the highlighted area in (i), respectively.

ing methods section, to ensure solid electrolyte stability for *in situ* studies. Li metal was placed on a metal probe while the solid electrolyte (LPS:0.5LiI) was mounted on a Cu TEM half-grid (Fig. 7.2a-c). LPS:0.5LiI and Li metal are imaged prior to contact (Fig. 7.2d), on physical contact (Fig. 7.2e), electrochemical reduction (Fig. 7.2f), electrochemical oxidation (Fig. 7.2g) and after probe retraction (Fig. 7.2h,i). When a reducing bias is applied to LPS:0.5LiI, Li^+ ions are drawn out of the solid electrolyte (LPS:0.5LiI) and deposited on the Li probe. A void or pore forms in the solid electrolyte region in contact with the metallic probe after electrodeposition and is highlighted with a green box (Fig. 7.2f). This void

is irreversible and remains after oxidation (Li^0 is stripped from probe) (Fig. 7.2g). The interphase void formation or loss of mass is evidence of edge chipping. Edge chipping, is a fracture mode, that most prominently occurs due to concentrated loadsChai & Lawn (2007) or from a sharp contactZhang et al. (2013). While the probe can be considered a sharp contact, there was no edge chipping observed upon initial contact (Fig. 7.2d). Pore formation and/or edge chipping only occured after electrochemical reduction of the solid electrolyte (Fig. 7.2f). This early stage fracture mode, observed within the interphase, is likely due to chemo-mechanical driving forcesFu et al. (2020). Local stresses within a solid electrolyte can impact dissolution and deposition kinetics ($Li^0 \xrightarrow{dissolution} Li^+$) and ionic transport pathwaysMistry & Mukherjee (2020b); Barai et al. (2017) and can lead to local 'hot-spots' for ionic fluxMasquelier (2011); Famprikis et al. (2019). This ionic flux directionality is postulated to be equivalent to an ionic concentrated load at solid|solid interface and be the origin for the observed edge-chipping.

HAADF STEM images and EDS maps of the solid electrolyte after cycling shows a uniform distribution of iodine, phosphorous and sulfur across the entire imaged area (Fig. 7.12). After electrochemical plating (Fig. 7.2f) and stripping (Fig. 7.2g) of Li^0, the presence of iodine remains evident in the Li metal (Fig. 7.2l). Iodine diffusion to the solid electrolyte|lithium metal interface is observed under both equilibrium (quiescent) and electrochemical biasing conditions. Iodine diffusion occurs at the point-of-contact between the solid electrolyte and metallic lithium and readily diffuses away from the point of physical contact (Fig. 7.2l). This indicates that iodine diffuses along the entire Li metal surface and is not restricted to the region of physical contact. Surface diffusion of iodine provides a uniform deposition surface for Li metal during cycling. A uniform interface reduces the cell impedance and results in a reversibly smooth overpotential response. The intimate contact afforded by an iodine rich interface between Li metal and the solid electrolyte can enable efficient ion transport through the interphase and lead to improved electrochemical performance.

In situ synchrotron X-ray tomography was carried out on all mentioned LPS-based materials to quantitatively assess the onset and growth of mechanical failure and observe sub-surface material transformation pathways upon Li cycling. It should be noted that the sample pellets ($\sim$2 mm) were slightly larger than the field-of-view (FoV, 1.8 mm) of the tomography setup, and consequently the imaged region is from the center of the pellet. Symmetric Li | SE | Li cells were assembled in the *in situ* cellShen et al. (2018) to observe plating and stripping behaviors at 0.5 and 1 mA cm^{-2} (Fig. 7.3a). The *in situ* cell shows a higher overpotential for Li plating and stripping, than the conventional coin cell due to the low applied pressure ($\leq$ 0.5 MPa) (Fig. 7.13). All the cells were run at increasingly higher current densities until either the polarization reduced to zero, or the overpotential value exceeded the range of the potentiostat. The shorting of the *in situ* cell was confirmed by electrochemical impedance spectroscopy (Fig. 7.14). The sample porosity before electrochemical cycling, computed from the reconstructed 3D images range from 0.48 for A–LPS sample to $\approx$ 0.05 for LiI–AN sample (Fig. 7.3b). It should be noted that the resolution of the tomography technique employed is 0.7 μm. Pores smaller than this size are not resolved and hence may lead to an under-estimation of the porosity values. The charge to failure values for *in situ* experiments follow the trend A–LPS<LPS:0.5LiI<LiI–AT<LiI–AN (25, 35, 40 and 90 mC respectively). The outer bounds of the trends are consistent between the lab-scale experiments and the sychrotron experiments. However, the LPS:0.5LiI and LiI–AT show different trends, with the latter showing a slightly higher charge to failure for the synchrotron experiments. The variation between the samples is small ($\approx$ 5 mC) and could arise from small differences in assembly in the *in situ* cell. All materials were stable during the course of the *in situ* experiment and did not show signatures of material degradation (Fig. 7.8). Inherent instability of LPS with Li metal can lead to interphase formation that manifests as material transformations (volume change, cracking, increase in porosity). Absence of extensive interphase formation enables the interpretation of the observed material transformations as arising from electrochemical cy-

cling. X-ray tomography works primarily on the principle of absorption contrast, where the intensity of a beam traversing through the sample is attenuated according to the Beer-Lambert law,

$$I = I_0 exp(-\mu(x)x) \tag{7.2}$$

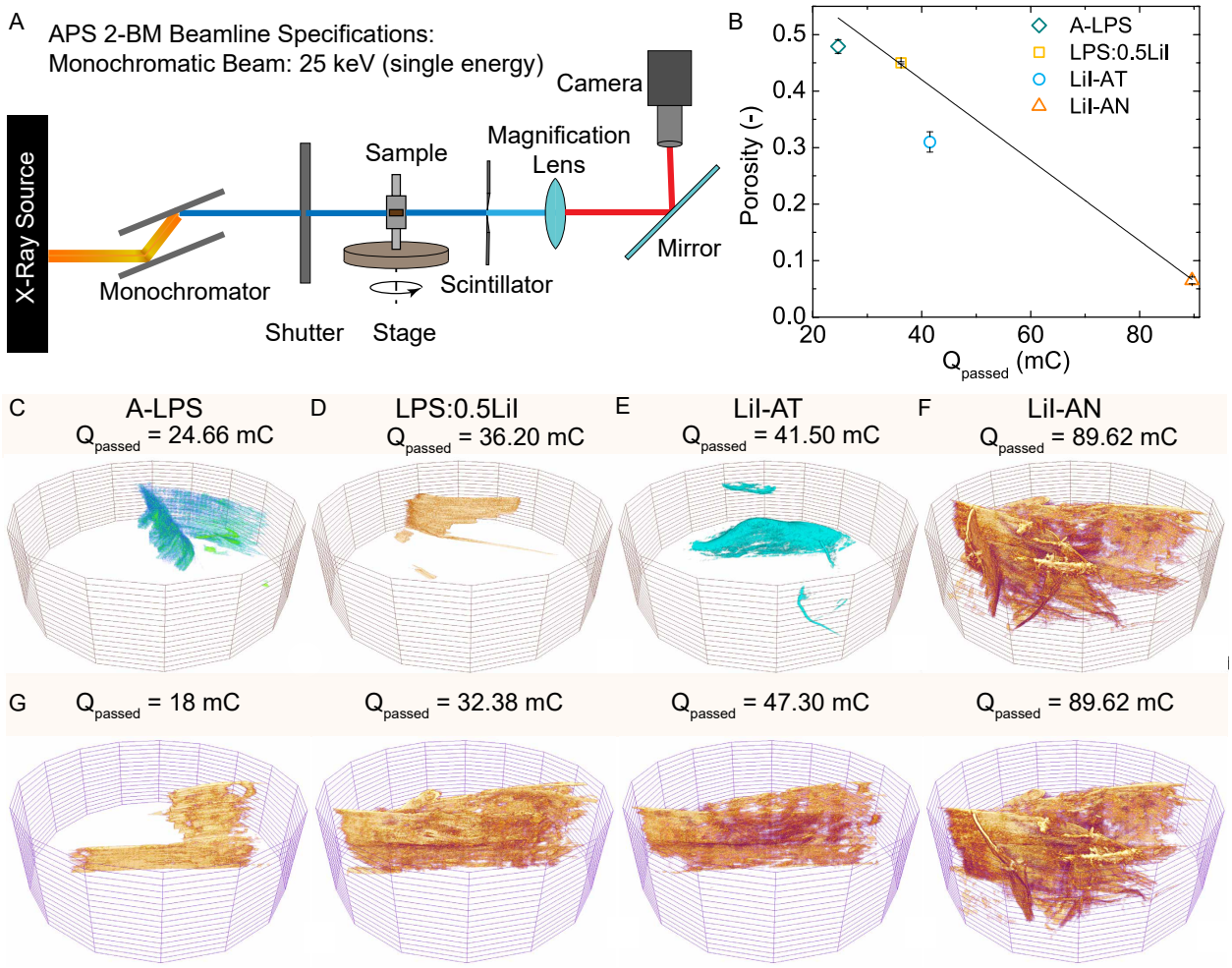

Figure 7.3: Failure onset and growth tracked by *in situ* synchrotron tomography. (a) Schematic diagram of the tomography setup used for *in situ* imaging of solid electrolytes (b) Correlation between the porosity measured from the tomography experiments and charge to failure. (c)-(f) 3D representation of cracks of the failed samples after cycling for A–LPS, LPS:0.5LiI, LiI–AT, and LiI–AN respectively. (g) Crack propagation through LiI–AN sample at various plating, stripping steps. The colors in (c-g) are only used to aid visualization.

where, I is the intensity of the transmitted beam, I_0 is the incident beam intensity and $\mu(x)$ is the absorption coefficient of the material. Denser materials characterized by high

Z-elements (solid electrolyte) attenuate the X-rays more than low-Z elements (Li metal and/or air). This difference in attenuation allows for tracking individual material transformations during electrochemical cycling. As the raw reconstructions show (Fig. 7.15), there are distinct features with significantly lower gray-scale value compared to the bulk solid electrolyte grayscale value observed in the pristine sample. The darker regions highlighted are thus identified as cracks/dendrites as this value corresponds to a less dense phase than LPS. The fracture regions were segmented out from the raw reconstruction images for visualization (Fig. 7.3c-f). The segmentation was carried using consistent semi-automated procedures for all the samples. Due to the small feature size of the fracture event and segmentation methodology, the crack regions are generally over-estimated (rather than underestimated). However, since the segmentation protocol is consistent at all steps and across samples, comparisons can be made between them. The cracks are concentrated in one region of the pellet for A–LPS, LPS:0.5LiI and LiI–AT, while the crack is uniformly distributed in the LiI–AN samples. The fracture region grows toward regions with high porosity during symmetrical cycling which mimics a Griffith crack like mechanismPorz et al. (2017). The overall mechanical strength of the solid electrolyte in regions with high porosity will be low and be more susceptible to fracture. All solid electrolytes have some level of meso- and microstructure which is introduced during materials processing. Although it is ideal to have a low porosity material, the way the material is pressed in a pellet can lead to non-uniform pore sizes throughout the pellet. Regions with high porosity contribute to tortuous ion transport that can locally magnify the current density and electric fields. The latter effect may promote localized ionic flux capable of chipping the solid electrolyte interface.

The cracks were also segmented at the end of individual charging/discharging step to visualize the onset and growth mechanism of crack propagation of the sample (Fig. 7.3g, 7.16). Based on these images, it was found that all the materials showed two distinct failure modes (Fig. 7.4a): (i) edge chipping failure of electrolyte section at

electrode|electrolyte interface and (ii) vertical crack growth through sample thickness originating from the chipped electrolyte section. The fracture onset via edge chipping is likely do to directed ion transport (chemo-mechanics) in the interphase as seen with *in situ* TEM experiments (Fig. 7.2f). Interphase void generation leads to regions of high current density and stress concentration that can lead to fracture of the solid electrolyte at the interface. Stress generation at the interphase typically arise from electrodeposition and electrodissolution of lithium metal. These processes are generally coupled with large volume changes that impart stress on the solid electrolyte. Interphase void generation mechanism is consistent over length scales and is effectively observed as the crack onset mechanism. *In situ* tomography corroborates microscopy observations and demonstrates initiation of edge chipping at the stripping electrode (Fig. 7.4b-c). Subsequently, from this region a lateral crack develops that grows through the thickness of the sample (Fig. 7.4d). Similar interface driven fracture was proposed previously for Na β-alumina solid electrolytesArmstrong et al. (1974). Surface irregularities were identified as potential stress concentration regions through which fracture can initiate. Metal flow through this surface-driven crack propagates the fracture through the thickness of the electrolyte leading to ultimate failure by shorting. Edge chipping failure mode is characterized by removal of material from a surface/edge section due to high stress concentrations and is widely observed in material shaping, tribology, anthropology and dentistryAl-Amleh et al. (2010); Choong et al. (2019); Cao (2001); Zhang et al. (2013); Chai (2015). The edge chipping was observed in all thioposphate electrolytes (independent of microstructure) and is likely chemo-mechanically driven. The through-plane or vertical fracture is a result of the solid electrolyte microstructure.

All samples showed an identical fracture initiation and propagation mechanism despite differences in microstructure and interphase properties (Fig. 7.4). These results indicate that while halide doping can kinetically stabilize the Li metal-LPS interface, the eventual failure mechanism for all the samples is identical. As this is a symmetric cell, these fea-

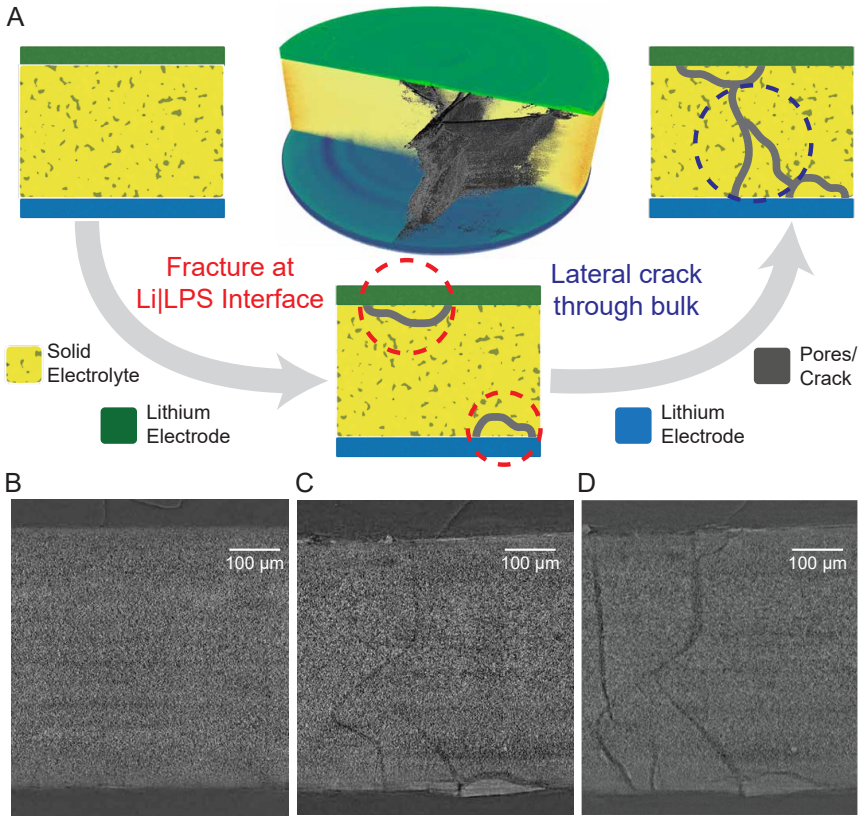

Figure 7.4: Failure mechanism in LPS. (a) Schematic diagram showcasing the failure onset and growth mechanism in LPS solid electrolytes. Pristine LPS pellet shows a heterogeneous distribution of porosity (darker regions). Mechanical failure initiates by chipping failure of an electrolyte block at the electrode|electrolyte interface. The chipping mechanism is initiated by active electrochemical oxidation and reduction and is not observed on passive contact. Further cycling leads to lateral crack growth from the regions showing chipping failure through the thickness of the electrolyte. Sectional reconstruction images of LiI–AN material clearly show these distince phenomenological mechanism: (b) pristine, (c) chipping failure and (d) lateral crack growth.

tures are found on both electrodes and the short happens when the propagating lateral cracks merge within the bulk. It should be noted that Li presence is possible in the crack features observed by tomography due to filament growth. Li penetration in to the crack features exposes additional SE surface to Li metal increasing the Li|LPS interfacial area. Solid electrolyte in contact with Li within these crack features can undergo interphase formation and related chemo-mechanical transformations as evidenced from TEM measurements. Additional interphase formation within the cracks can lead to an accelerated

failure. TEM and X-ray microscopy offer complementary insight into the mechanistic origin of failure within the material at cascading length scales which is vital to obtaining a complete understanding of the failure process. Specifically, the TEM results highlight differences in Li plating/stripping mechanisms with an electrochemically driven surface pitting reaction of the LPS material with Li metal. At the macro-scale, X-Ray tomography identifies a "interface chipping" mechanism as the mode through which all the investigated samples initiate failure. This mechanism is likely the manifestation of the interfacial pitting mechanism observed with the in situ TEM. In this way, TEM provides needed nano-scale interfacial chemistry information and XRT serves to compliment it as to look at real pelletized samples so we can observe the individual failure mechanisms from each technique, as well as how these mechanisms cascade into each other. Combining tomography and TEM provides unique collective insight into the failure onset mechanism in LPS electrolytes over several length scales.

In situ transmission electron microscopy revealed that iodine rapidly diffuse to the solid electrolyte|Li metal interface. This will result in a compositional gradient in the solid electrolyte. Prior work demonstrated that halide doping led to materials with lower Young's modulus and less elasticity due to a larger free volumeNose et al. (2015); Kato et al. (2018). Thus, iodine diffusion to the interface will lead to non-uniform mechanical properties throughout the solid electrolyte. Solid electrolytes doped with a halogen will have electrode | electrolyte interfaces with lower Young's modulus compared to the bulk. These interfaces will be more compliant and better accommodate the stresses associated with electrodeposition and electrodissolution of Li and maintain a conformal interface between the SE and Li. This can lead to the higher critical current density and charge-to-failure measured for the halogen-doped solid electrolytes. Iodine doping and improved packing density of annealed samples result in higher performance metrics (CCD, $Q_{failure}$). While the failure onset mechanism is identical for all mentioned LPS materials, the extent of crack propagation (density of cracks in the bulk) varies significantly between the dif-

ferent materials. This suggests that the lateral crack growth is governed by differences in bulk pellet microstructure.

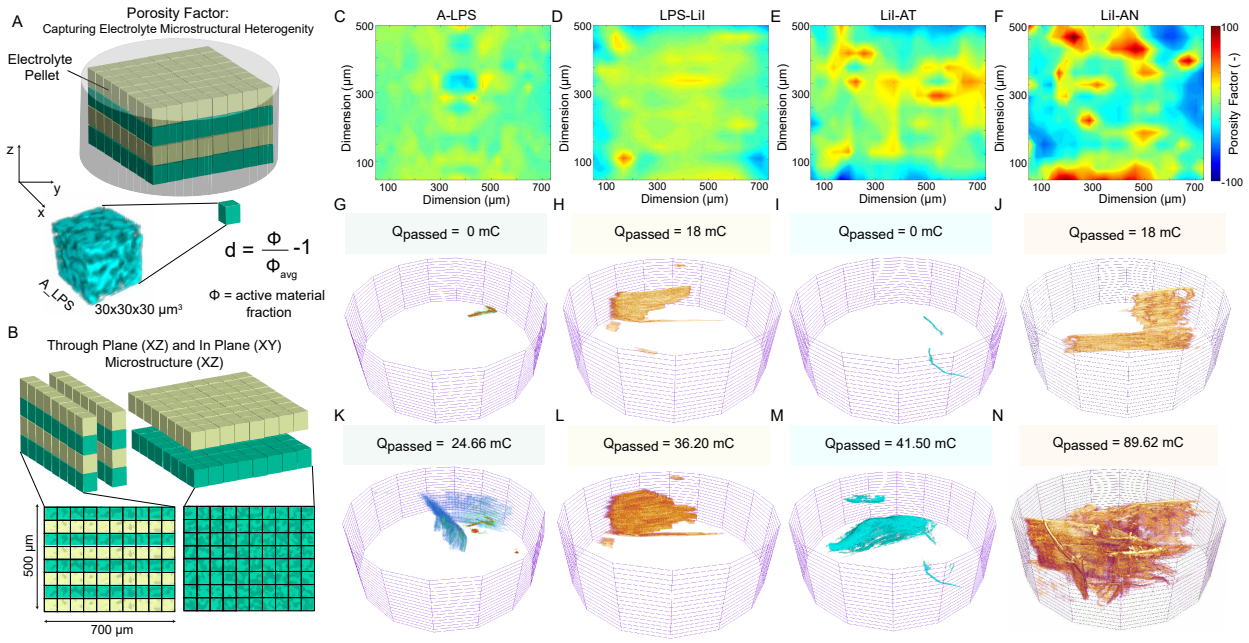

Figure 7.5: Assessing microstructural heterogeneity in solid electrolytes by porosity factor. (a) Electrolyte pellet is discretized into uniform sub-volumes of 30x30x30 μm^3 dimension. (b) Porosity factor is defined as the ratio of local porosity identified for the 30x30x30 μm^3 sub-volume to the average porosity of the pellet. Microstructure of a representative sub-volume of A–LPS pellet is shown. (c) Porosity maps are calculated across two normal planes in the electrolyte defined as through plane and in-plane directions. In-plane section are normal to the applied electric field and represent the horizontal cross section of the pellet. Through plane is parallel to the applied electric field and represents the vertical cross section of the pellet. Porosity factor variation in through-plane direction for A–LPS, LPS:0.5LiI, LiI–AT, LiI–AN (c)-(f). Initial crack formation in samples for A–LPS, LPS:0.5LiI, LiI–AT, LiI–AN (g)-(j). A–LPS and LiI-AT pristine pellets showed regions with microstructure distinct from the average microstructure. Hence, those morphologies are visualized. 3D representation of cracks of the failed samples after cycling for A–LPS, LPS:0.5LiI, LiI–AT, and LiI–AN respectively (k)-(n). See Figure S11-S13.

Solid electrolyte microstructure heteogenity can result in non-uniform mechanical stress. Regions with higher porosity have lower yield strength which results in larger deformation and damage in these regions. Thus, lateral crack growth tends to nucleate at porous regions (Fig. 7.16, 7.17). Microstructure variability can be quantitatively assessed with a porosity factor (Fig. 7.5a-b). Porosity factor is defined as the variation in local porosity

compared to the mean porosity:

$$d = \frac{\Phi}{\Phi_0} - 1, \tag{7.3}$$

where d is the porosity factor, Φ is the local porosity and Φ_0 is the mean porosity calculated on a binarized dataset. Porosity maps are calculated across two normal planes in the electrolyte defined as through plane and in-plane directions (Fig. 7.5b). In-plane section are normal to the applied electric field and represent the horizontal cross section of the pellet. Through plane is parallel to the applied electric field and represents the vertical cross section of the pellet. Mapping the porosity factor along the through-plane direction we clearly observe local regions with inhomogeneous microstructure compared to the average microstructure (Fig. 7.5c-f). A–LPS shows a more homogeneous distribution of porosity factor compared to LiI–AN which has a highly inhomogeneous distribution through the section. Porosity factors mapped here are local measurements that reflect the microstructural features at specific locations in the sample. It should be noted that the porosity factor shown here is a relative change in the local microstructural property compared to a mean microstructural property. Statistically, the absolute variation of local porosity should be identical because all pellets are processed in a similar way. Normalizing this value by the mean porosity gives an insight into the degree of structural heterogeneity. For A–LPS sample, with a mean porosity of 0.48, a local variation of 0.02-0.03 does not deviate significantly from the average microstructure. However, for LiI–AN, a local variation of 0.02-0.03 is comparable to its mean porosity (0.05) which is characterized as high structural heterogeneity (Fig. 7.5c-f). Statistical analysis of porosity factor was carried out on 40 distinct ≈750x500x30 μm^3 electrolyte cross-sections (Fig. 7.18). Statistical assessment of the porosity factor across this dataset shows consistent results with A–LPS showing a homogeneous, narrow distribution of porosity factor while LiI–AN shows a more heterogeneous, wide distribution of porosity factors. This is further

verified by in-plane assessment of porosity factor across different sub-volumes sizes for the raw gray-scale dataset to remove errors from the binarization process (Fig. 7.19, 7.20). These studies also show consistent results with LiI–AN having the most heterogeneous microstructure (compared to its mean value). The influence of porosity factor distribution is observed on the crack formation within the electrolytes (Fig. 7.5g-n). A–LPS, which showed a relatively homogeneous porosity factor, shows focused crack formation in the vicinity of a microstructural feature present in the pristine sample (Fig. 7.5g,k). In comparison, LiI–AN, which shows highly heterogeneous porosity factor distribution, shows extensive crack propagation through the entire bulk of the sample with no apparent focused crack growth (Fig. 7.5j,n). LPS:0.5LiI and LiI–AT show similar behavior in terms of crack formation and porosity factor distribution. Crack growth through the sample is dictated by the mechanics of the bulk electrolyte. The microstructural variation observed in the pellets indicate that cracks will preferentially grow through the regions with higher porosity (lower porosity factor) due to the reduced local yield strength and fracture strength. Additionally, higher porosity increases the local tortuosity in the region leading to an enhanced current density and electric field in the vicinity. These effects lead to crack formation in regions with high microstructural heterogeneity. It should be noted that for a Griffith-type approach larger (raw) defect size and volume fraction of the porosity is a critical factor dictating fracture growthHatzor & Palchik (1997); Yang et al. (2002); Lu et al. (2004); Carniglia (1972). Porosity factor is a measure of variation of the local microstructure from the average pellet microstructure. In this regard, a variation in the porosity factor (structural heterogeneity) will occur when the local domains show either a higher number density of pores (volume fraction) or larger pore sizes. Thus, both interpretations (porosity factor/Griffith mechanism) are analogous and identify the same mechanism for fracture. Controlling porosity and pore distribution within the pellet will be important to tailor solid electrolytes for high rate capability.

Current focusing, can occur because of solid electrolyte microstructure heterogenity or

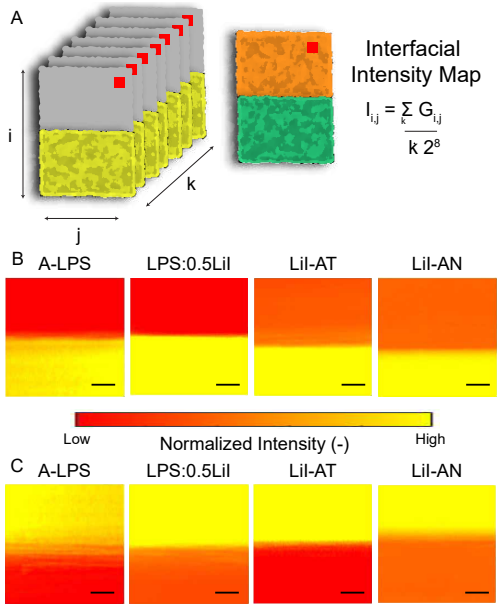

Figure 7.6: Interfacial intensity map at the solid | solid interface. (a) Schematic diagram explaining the measurement of intensity maps. Raw grayscale intensity is traced a 150x150 μm^2 section over at least 500 μm depth. This is normalized to the depth and the maximum theoretical intensity of an 8-bit image. The resultant image provides insight into the density variation and presence of pores/voids within the imaged section. Intensity map for the top Li | SE interface are shown in (b) while for the bottom SE | Li interface are shown in (c). All the scale bars in the figure are 30 μm.

constriction effects. Constriction effects can lead to polarization and is often due to distant active microcontacts (irregular contact) which leads to lower contact surface area, local regions with higher current densities, and high stress distributions Krauskopf et al. (2019); Kasemchainan et al. (2019). These non-conformal regions can accelerate material transformations leading to failure. To effectively rule out that sample contact had a role in current focusing, we created interfacial intensity maps (Fig. 7.6) similar to that reported earlierKasemchainan et al. (2019). Interfacial intensity maps qualitatively indicate the degree of interfacial contact and are generated by normalizing the gray scale intensity of a 150x150 μm^2 section at both Li | SE interfaces over at least a 500 μm thickness for the pristine cell (Fig. 7.6a). Regions with high normalized intensity signify high attenuation materials (solid electrolyte) while lower intensity materials signify transparent regions (air/voids). The resolution of this map is identical to the tomography resolution of 0.7

μm. Interface is generally estimated where a sharp change in intensity is observed in the 2D map corresponding to the step from Li (low intensity) to the solid electrolyte (high intensity). Some gradient exists within the high intensity region for A-LPS compared to the other electrolytes which reflects the porosity of the amorphous LPS material. The jump region (interface) is fairly sharp and similar for all the materials (Fig. 7.6b-c, 7.21) such that qualitatively they can be considered identical. More so, no regions of very low intensity are observed indicating that the SE | Li interfaces are identical for the tested materials. The identification of heterogeneity at the interface is limited by the size of the voids, resolution of the technique and the contrast available between Li and void regions. For the given experimental conditions, no discernible differences are observed in the average interface conformation for the four samples. This indicates that the crack formation mechanism are driven by inherent material microstructural heterogeneity and not due to variations in cell assembly (contact between electrode and electrolyte).

Resolving lithium filaments in the bulk solid electrolyte is challenge because both voids and lithium have low contrast and will be transparant. Thus, instead of directly tracking lithium filament within the bulk electrolyte, we indirectly monitor it via tracking the total transparant region. An increase in the transparent region will occur either via an increase in the void region (via fracture growth) or by the presence of lithium metal in the bulk solid electrolyte. X-ray transparent region volume within the solid electrolyte bulk is tracked during cycling to assess the presence of electrochemically active material within the LiI–AN solid electrolyte (Fig. 7.7a) and A-LPS,LPS:0.5LiI, LiI-AT (Fig. 7.22). The X-ray transparent region volume grows at crack onset and oscillates on subsequent cycles (Fig. 7.7c, 7.22) prior to failure by shorting for all the samples studied. It should be noted that the absolute crack volumes are most likely over-estimated due to segmentation challenges. However, the trends between individual steps can be compared as the same segmentation protocols were employed across all the samples. The X-ray transparent regions are areas showing lower absorption than the surrounding electrolyte material

which can be pores, cracks or Li metal all of which have low absorption coefficients. The volume modulation of the X-ray transparent region can be presence of electrochemically active material (Li) within the cracks (Fig. 7.7b). Presence of metal in crack is consistent with the failure mechanisms proposed for other solid electrolytes Armstrong et al. (1974). During the plating cycle, Li can be deposited in the crack onto a filament growth or deposit in an isolated formHan et al. (2019). On stripping, if this material is electrochemically accessible it will be oxidized and shuttled to the other electrode. Preferential plating and stripping from the filament lead to stress generation owing to material addition and removal from within a confined space (Fig. 7.23). If the extensive stress from the dendrite growth supersedes the restoring force offered by the fracture strength of the material, it can lead to propagation of fracture. Li filament growth into the solid electrolyte also increases the Li|LPS interfacial area. The regions with new interfacial contact between Li and solid electrolyte undergo interphase formation and chemo-mechanical transformations like void formations, iodine migration, and stress gradient formation as evidenced from the *in situ* TEM measurements.

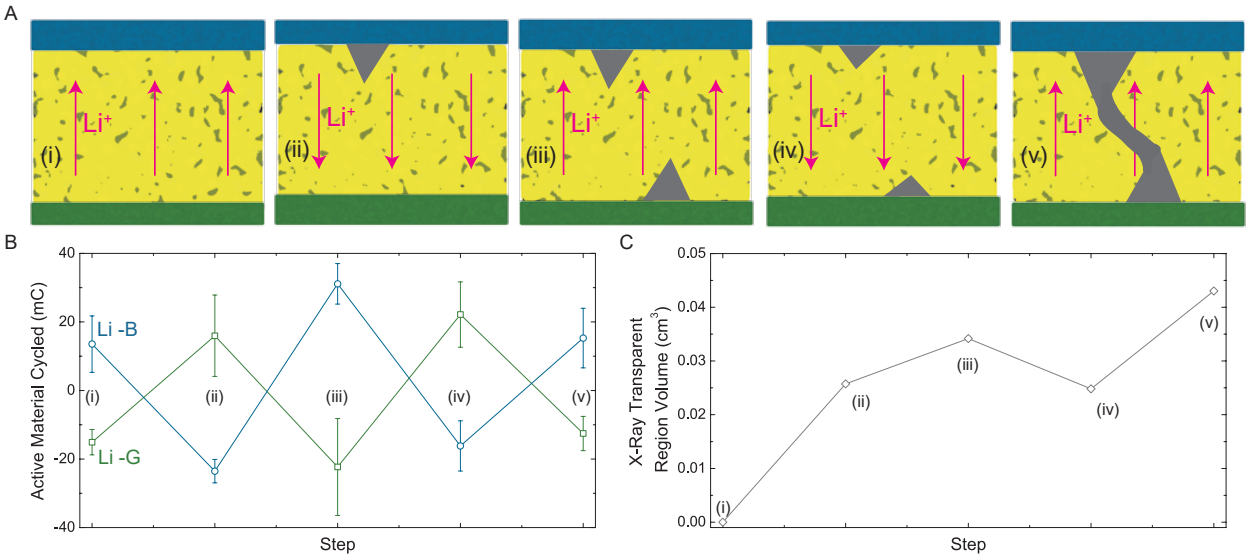

Figure 7.7: Crack Volume Modulation on Cycling in LiI–AN. (a) Schematic diagram representing the variation in imaged crack volume upon cycling. (b) Difference in average electrode thickness of the plating and stripping electrode as a function of cycle steps. (c) Absolute crack volumes measured as a function of cycle steps.

A validation of Li filament growth within the imaged cracks is carried out by assessing the cycled capacity from the individual electrodes of the symmetric cell at each step (Fig. 7.7b, 7.22). The cycled capacities are estimated from the change in thickness of the electrode between successive plating/stripping steps. The thicknesses of the electrodes are averaged over 15 spatial locations across the sample, assuming planar plating and stripping. While this assumption is not very accurate, it provides some information regarding the depth of discharge from individual electrodes. We clearly observe an unequal amount of plated and stripped charge for the individual electrode, especially for later steps. The excess charge can be thought to reside in the X-ray transparent regions imaged and thus account for the modulation of the crack volumes observed. Non-uniform crack formation and subsequent fatigue loading by cycling of active material through the cracks can lead to fracture of the solid electrolyte.

7.4 Conclusion

In summary, the effect of interfacial chemistry and microstructure on the mechanical failure of LPS-based solid electrolytes is investigated using advanced multimodal characterization techniques. Kinetically stable interphase and microstructural control is engineered by iodine doping, and milling and annealing respectively. The annealed samples with iodine doping show the highest room temperature conductivity of 2.4x10^{-3} S cm^{-1} and critical current density of 4 mA cm^{-2}. *In situ* TEM results show iodine migration to the Li metal surface and void formation at the LPS interface on electrochemical cycling. Void formation only occurs upon electrochemically cycling which suggest that the transformation is chemo-mechanically driven via local 'hot spots' in ion flux. Iodine migration to the Li metal surface affords nm-scale intimate contact with Li metal resulting in improved electrochemical performance of the LiI containing materials. Void formation at the LPS interface is an inherent material response to electrochemical cycling and is not observed on passive contact. Material transformations during cycling are evaluated using *in situ*

synchrotron X-ray tomography. A consistent failure mechanism across all materials is identified by tracking evolution of the crack features in the *in situ* tomography data. Mechanical failure is initiated with edge cracking at the interface and subsequent lateral crack growth through the surface. The onset of failure at the Li|LPS interface is consistent with the void formation observed in the TEM studies. Extent of crack propagation within the bulk solid electrolyte is assessed by tracking the porosity factor of solid electrolytes. Annealed sample shows large spatial microstructural heterogeneity leading to an extensive crack formation through the bulk dictated by the tortuous ion flux pathways and disparate local mechanical properties. Volume modulation of X-ray transparent region and non-symmetric depth of discharge on the two electrodes indicates Li filament growth and presence of active material in the crack features. Non-uniform crack formation and subsequent fatigue loading by cycling of active material through the cracks can lead to fracture of the solid electrolyte. *In situ* TEM and XRT corroborates the failure mechanism across cascading length scales. Multimodal characterization offers a unique insight into failure mechanisms of solid-state batteries. This work provides significantly new insight into fracture onset and growth mechanisms in sulfide solid electrolytes. These results are anticipated to inform future work on processing and operation of next generation solid-state batteries. While the decomposition product (e.g. interphase) between the solid electrolyte and electrode does impact failure, this work highlights the significance of microstructural heterogeneities on failure. Dense solid electrolytes with limited microstructure heterogeneity are imperative for high current density operation of all solid state batteries.

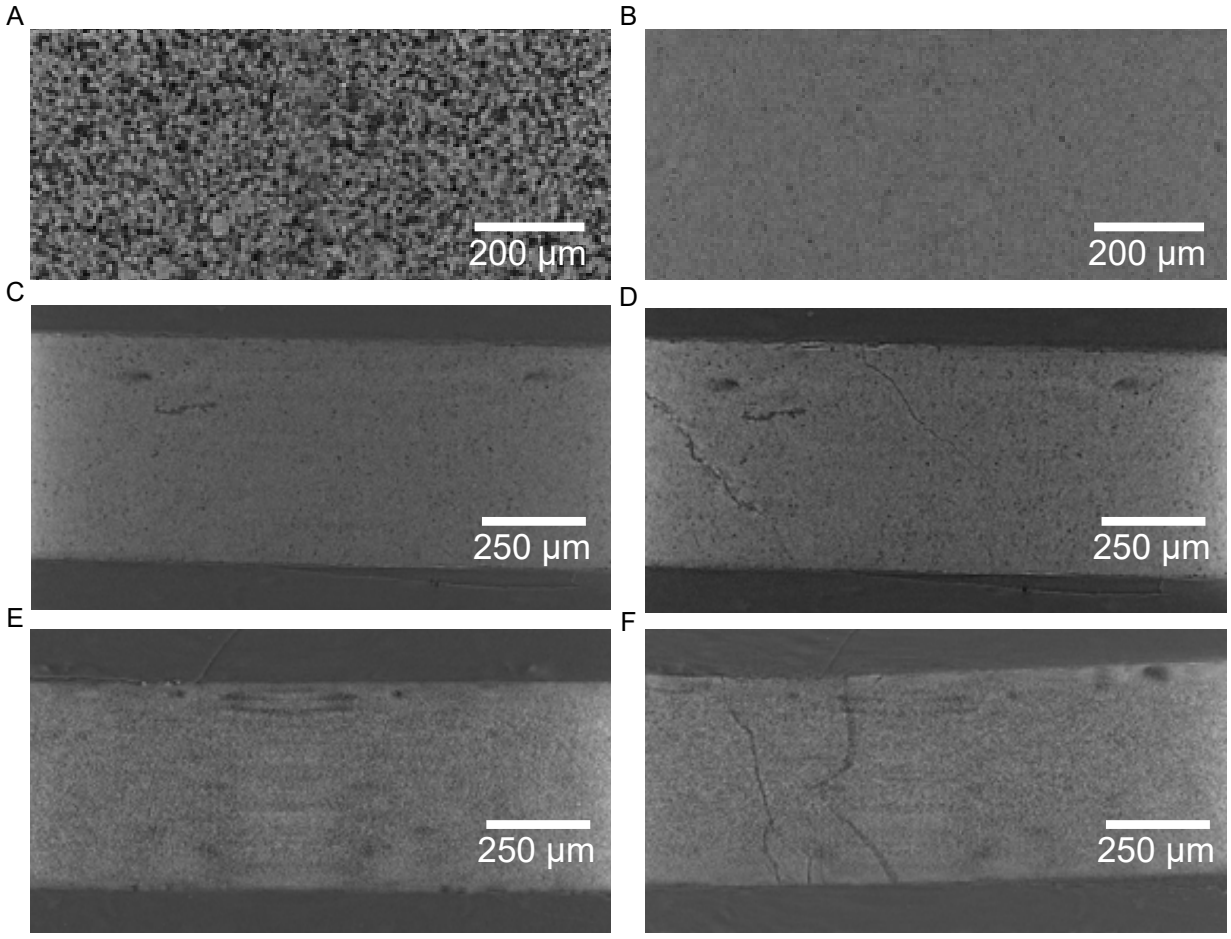

Figure 7.8: Sample stability during XRT measurement. Section of a reconstruction image for (a) amorphous LPS kept in contact with Li for extended duration (>5 hours) (b) amorphous LPS in contact with Li imaged within 15 min of cell assembly. Extended contact with Li metal shows decomposition of the LPS material into a highly porous material. Full cross-section image of Li | SE | Li cell assembled with A-LPS material in (c) pristine and (d) failed state and LiI–AN material in (e) prisitne and (f) failed state. No drastic variation in the microstructure is evidenced similar to that seen in the sample with extended contact (a). This allows for reliable interpretation of the data as electrochemistry driven material transformation as compared to the thermodynamics driven material degradation.

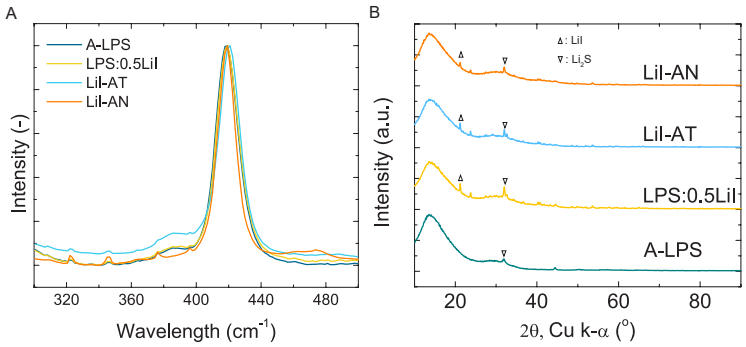

Figure 7.9: Material Characterization. (a) Raman and (b) XRD patterns of the materials investigated in this study.

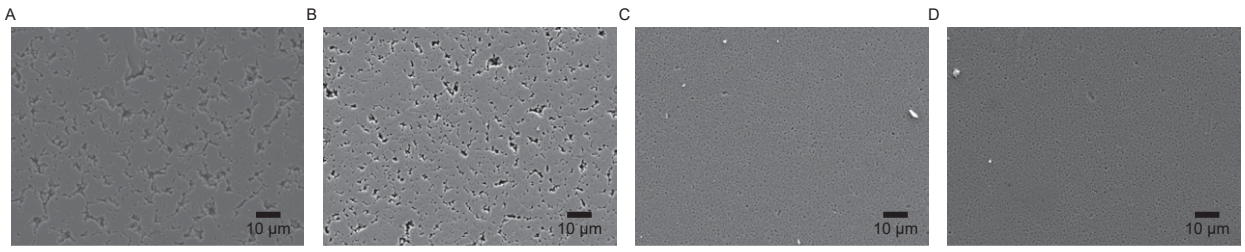

Figure 7.10: SEM images highlighting differences in material microstructure. (a) A–LPS, (b) LPS:0.5LiI, (c) LiI–AT and (d) LiI–AN.

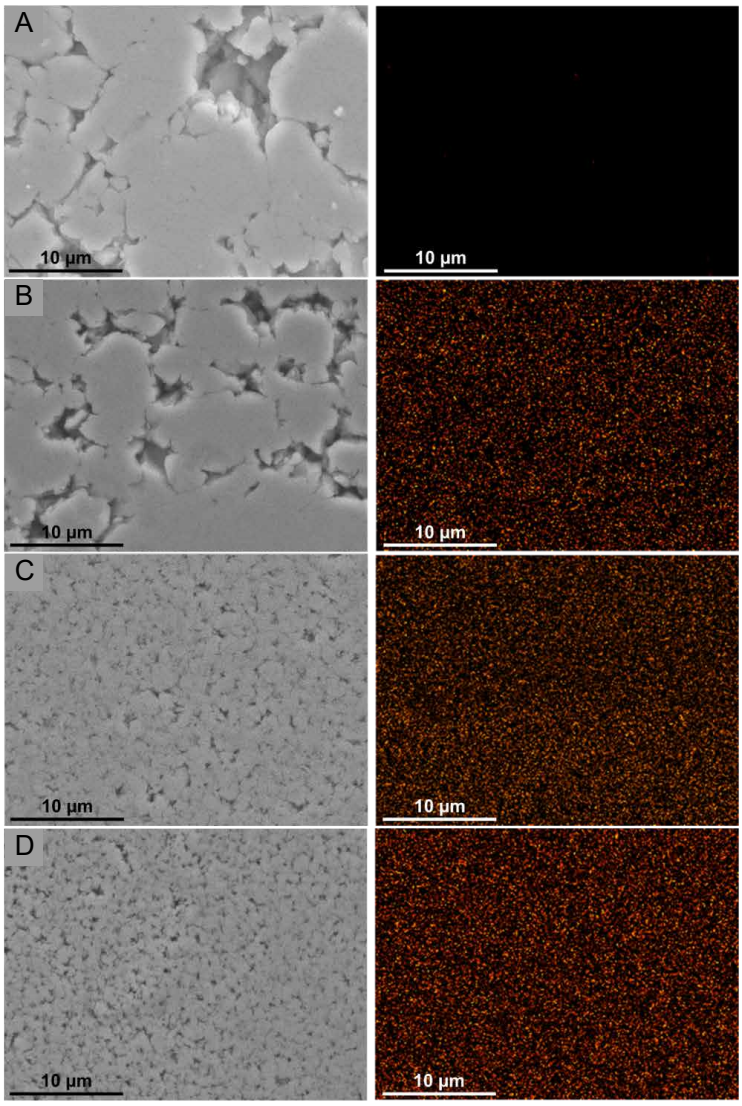

Figure 7.11: EDS maps for iodine. (a)A–LPS, (b) LPS:0.5LiI, (c) LiI–AT, and (d) LiI–AN pellets. Iodine distribution is uniform for all the LiI containing samples.

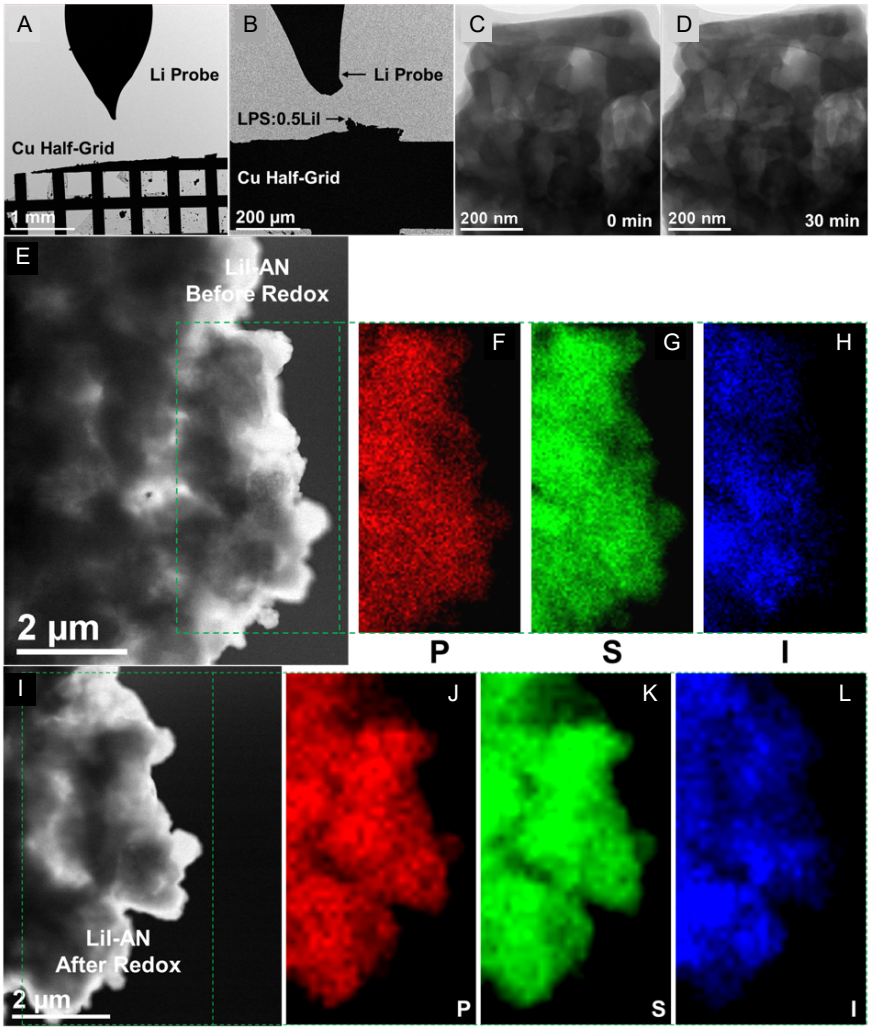

Figure 7.12: Sample Stability and additional results for TEM. (a) Low magnification *in situ* TEM image highlighting the Li probe and Cu half-grid within the in-situ TEM Nanomanipulator Holder, (b) low magnification *in situ* TEM image highlighting the position of LPS:0.5LiI on the Cu half-grid with respect to the Li probe, (c) TEM image of LPS:0.5LiI pristine material, (d) TEM image of LPS:0.5LiI pristine material after exposure to the electron beam in the HAADF STEM for 30 minutes, (e) *in situ* HAADF STEM image of LiI–AN prior to *in situ* electrochemical Li plating/stripping experiments performed in Figure 2, (f), (g), (h) phosphorus, sulfur and iodine EDS maps of LiI–AN prior to *in situ* electrochemical Li plating/stripping experiments performed in Figure 2 respectively, (i) *in situ* HAADF STEM image of LiI–AN after in-situ electrochemical Li plating/stripping experiments performed in Figure 2, (j), (k), (l) phosphorus, sulfur and iodine EDS maps of LiI–AN after *in situ* electrochemical Li plating/stripping experiments performed in Figure 2 respectively.

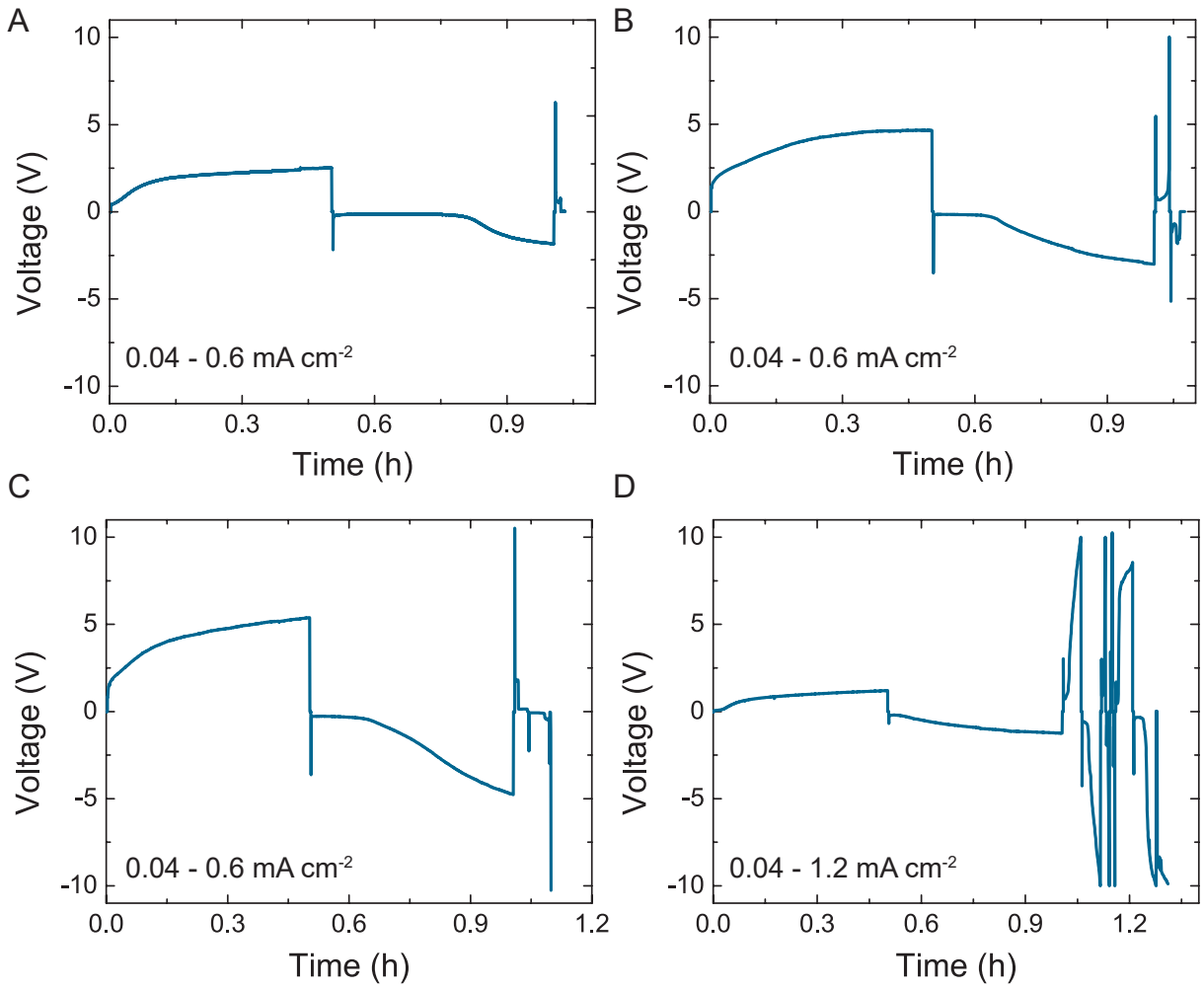

Figure 7.13: Polarization profiles for *in situ* cells. Profiles for (a) A–LPS, (b) LPS:0.5LiI, (c) LiI–AT and (d) LiI–AN. The current density employed for the tests are indicated on the graphs. All testing was carried out at room temperature.

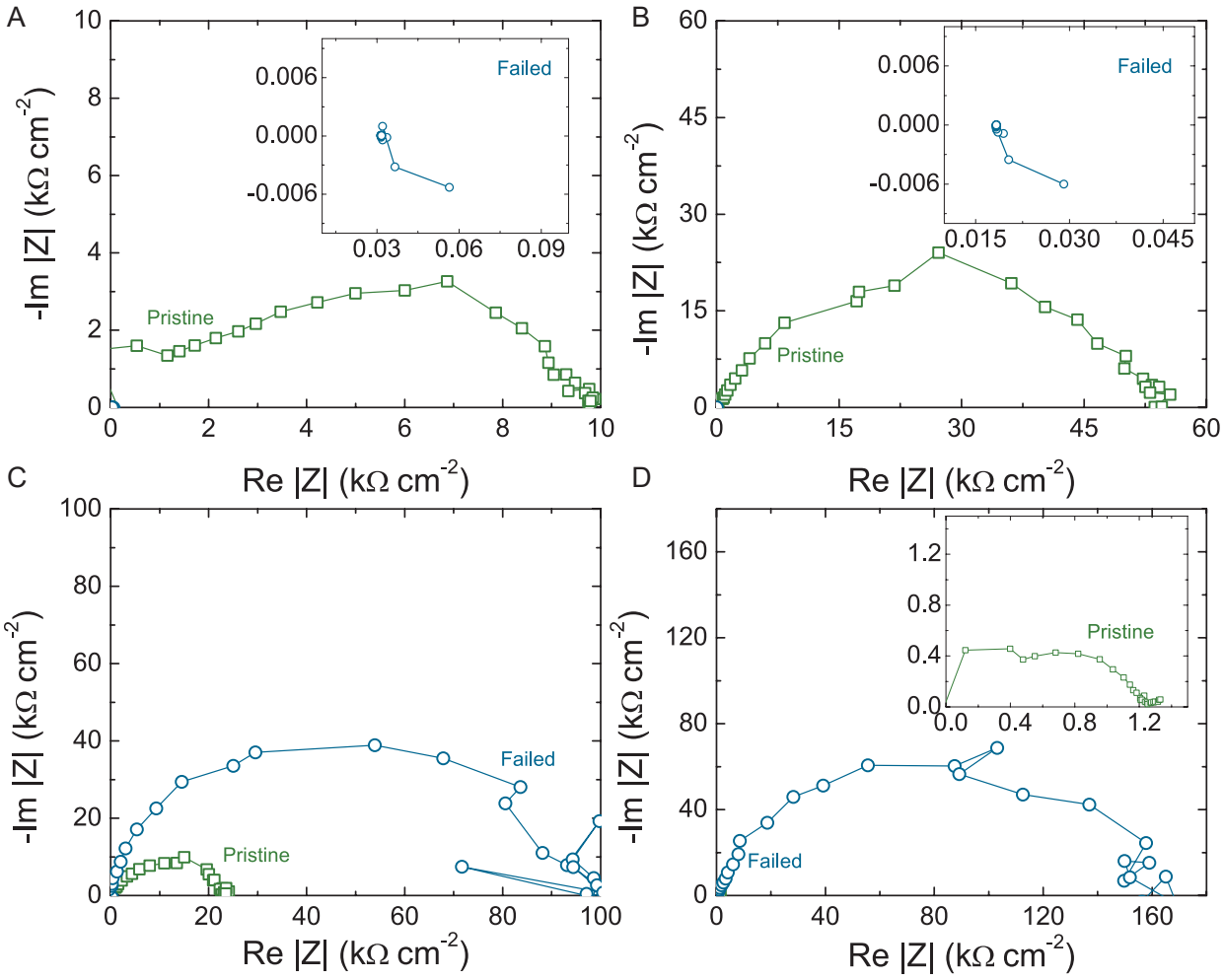

Figure 7.14: AC impedance spectroscopy for as-assembled and cycled *in situ* cells. Spectra for (a) A–LPS, (b) LPS:0.5LiI, (c) LiI–AT and (d) LiI–AN. All testing was carried out at room temperature.

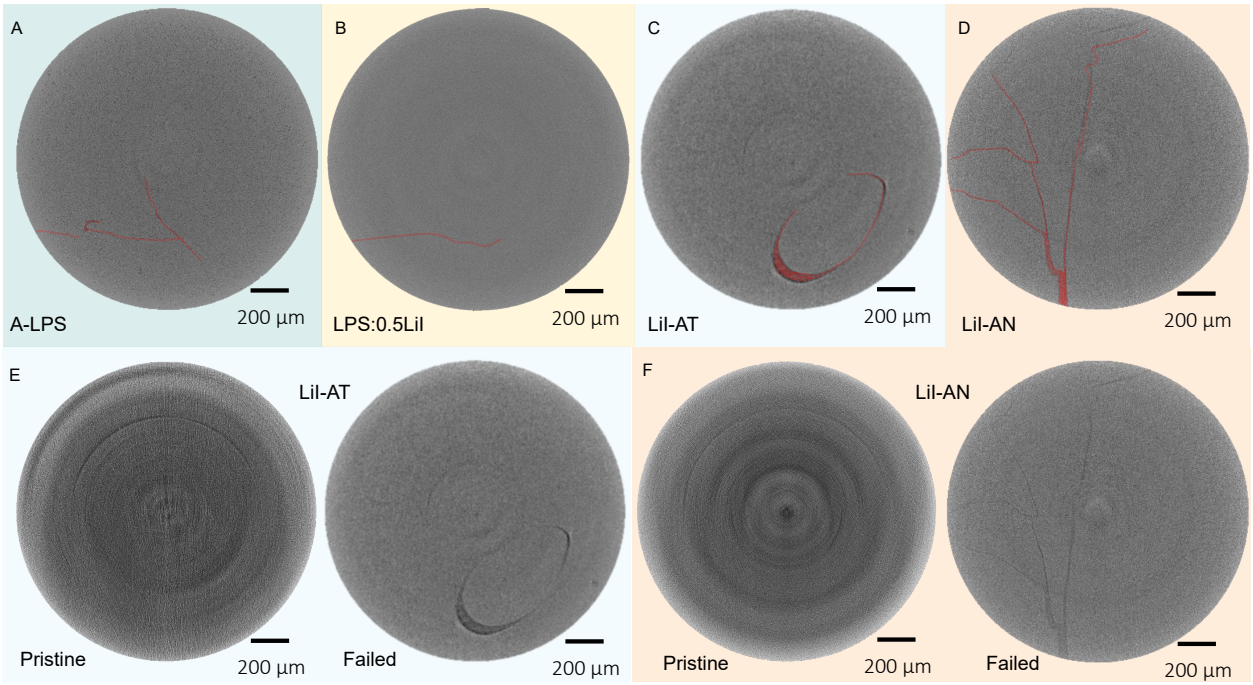

Figure 7.15: Example reconstruction slices. Images for (a) A–LPS, (b) LPS:0.5LiI, (c) LiI–AT, and (d) LiI–AN. For A–LPS and LiI–AT. The crack features in each slice are highlighted in red. Identical cross-section in pristine and failed sample for LiI-AT and LiI–AN are also shown in (e) and (f) respectively. Crack features are not highlighted to enable visualization of cracks in as-reconstructed images.

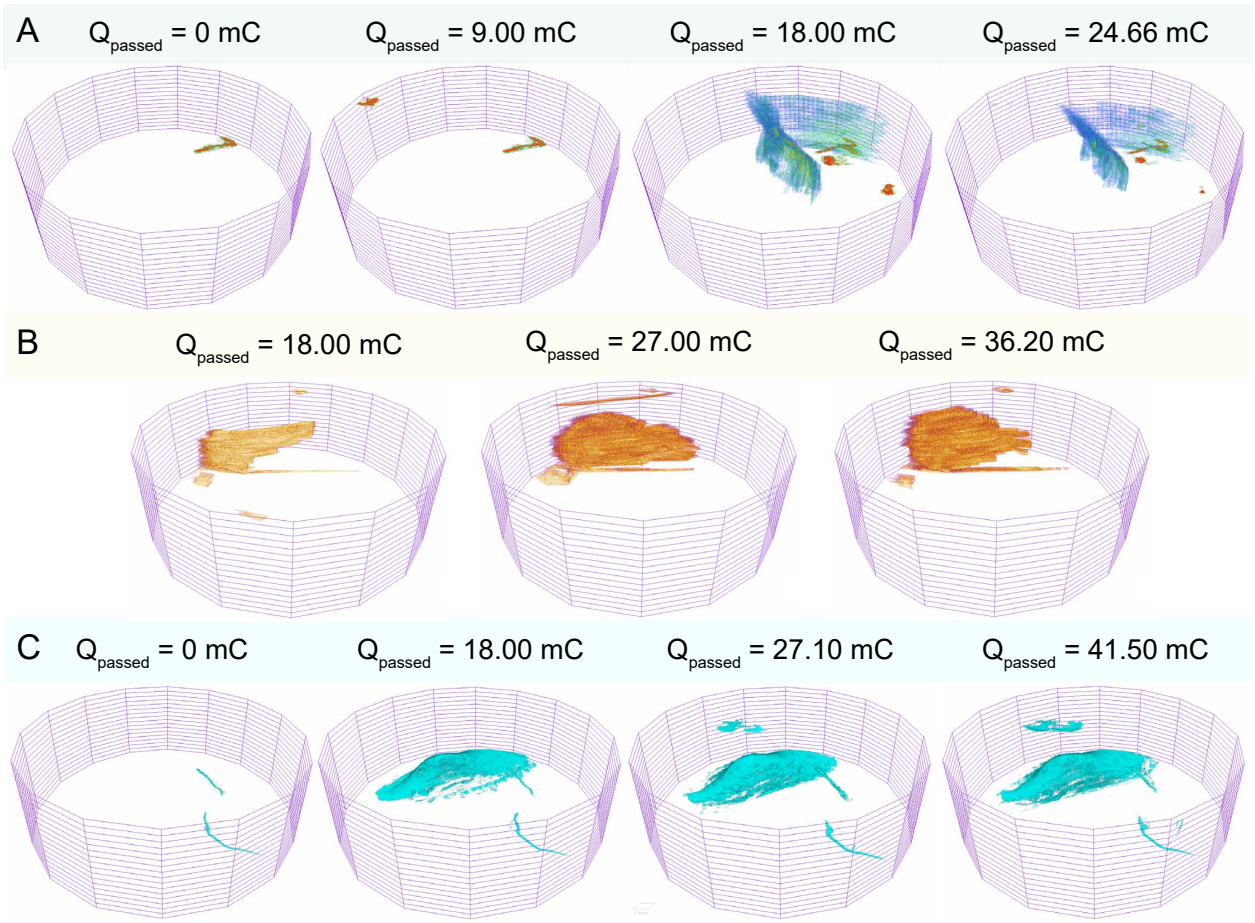

Figure 7.16: Crack propagation at various plating, stripping steps. Images shown for (a) A–LPS, (b) LPS:0.5LiI, and (c) LiI–AT. For A–LPS and LiI–AT features are shown at Q_{passed}=0 as these samples showed these microstructural features which are distinct from the general porosity of the sample.

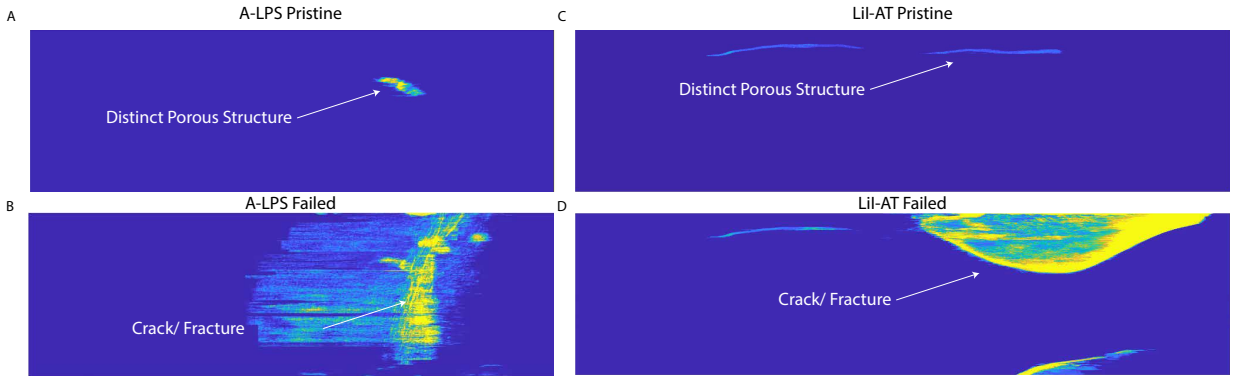

Figure 7.17: Crack propagation correlated with pristine pellet porous microstructure. (a)-(b) A–LPS pristine and failed and (c)-(d) LiI–AT pristine and failed sample. Figure shows 2D average projected porosity maps for segmented crack and pore features.

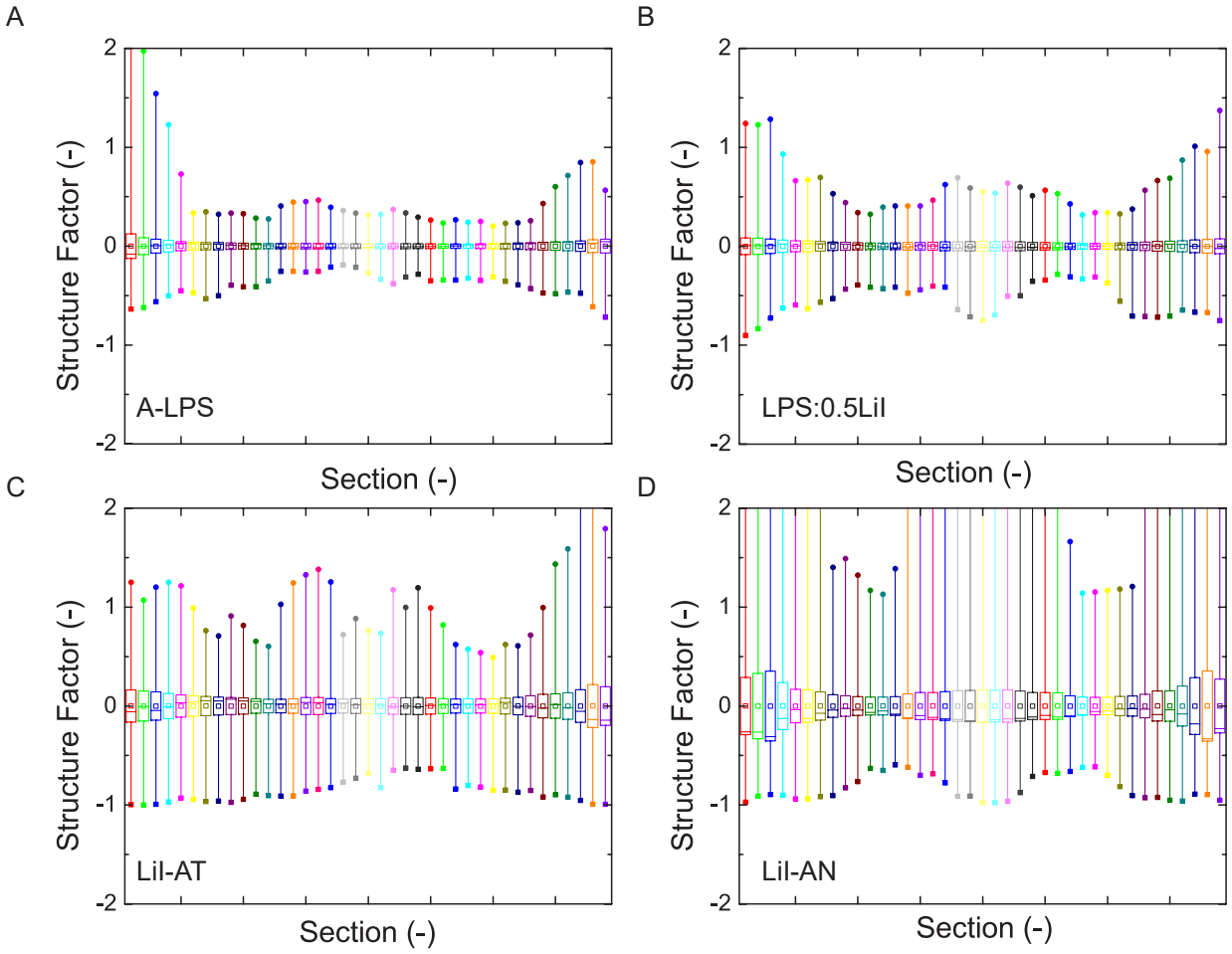

Figure 7.18: Statistics on porosity factor calculated in the through-plane direction across section of the solid electrolyte. The images are for (a) A-LPS, (b) LPS:0.5LiI, (c) LiI–AT, and (d) LiI–AN. The images shows mean of each section, with a median line and a box marking the standard deviation. Maximum and minimum porosity factor are also plotted. porosity factors are calculated on a 30x30x30 μm^3 sub-volumes across the cross-section of the electrolyte. The statistics for a single section included porosity factors for all the sub-volumes in an electrolyte cross-section, i.e. $\approx$ 24x30 porosity factors.

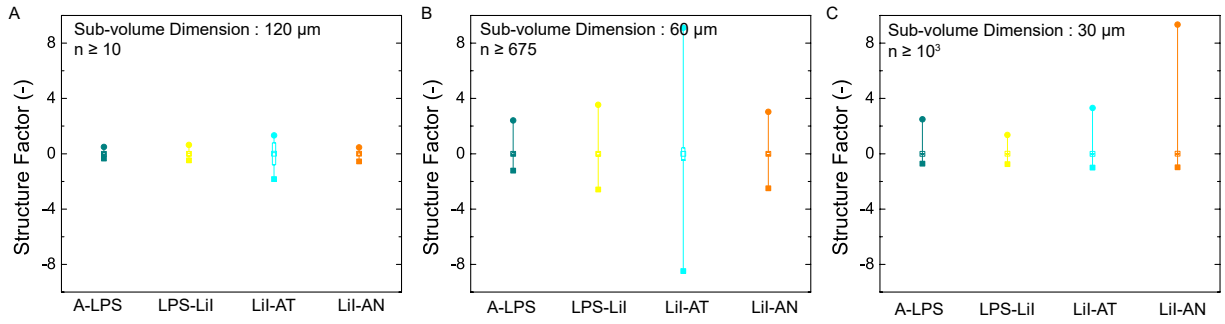

Figure 7.19: Statistics on porosity factor calculated in the in-plane direction along the direction of ion transport through the thickness of the solid electrolyte. The raw projections were used for this calculations to eliminate the errors from binarization. The images shows mean of each section, with a median line and a box marking the standard deviation. Maximum and minimum porosity factor are also plotted. porosity factors are calculated on sub-volumes of sizes (a) 30x30x30 μm^3, (b) 60x60x60 μm^3, and (c) 30x30x30 μm^3. The statistics for a single sub-volume size includes porosity factors for all the sub-volumes in an electrolyte cross-section. The approximate number of individual measurements are noted in the graph. Moving to larger sub-volumes normalizes the local heterogeneity and a uniform spread of porosity factors is observed.

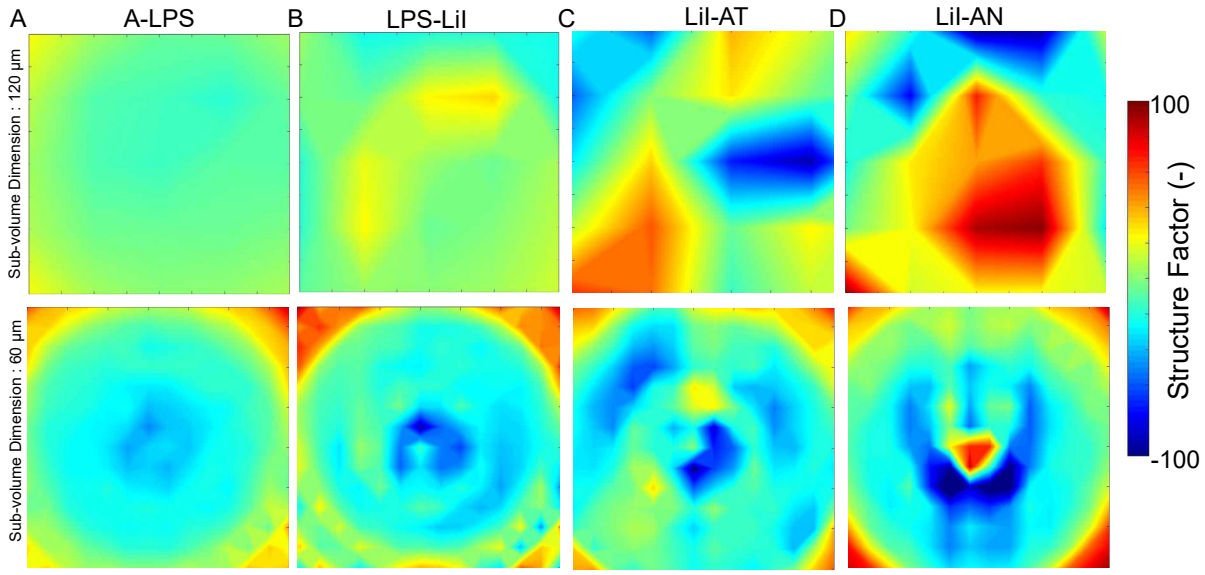

Figure 7.20: Porosity factor calculated in the in-plane direction along the direction of ion transport through the thickness of the solid electrolyte. The raw projections were used for this calculations to eliminate the errors from binarization. As the full reconstruction was used, the corners of the image are extraneous. The images are for (a) A-LPS, (b) LPS:0.5LiI, (c) LiI–AT, and (d) LiI–AN for 60x60x60 μm^3 and 120x120x120 μm^3 sub-volume size.

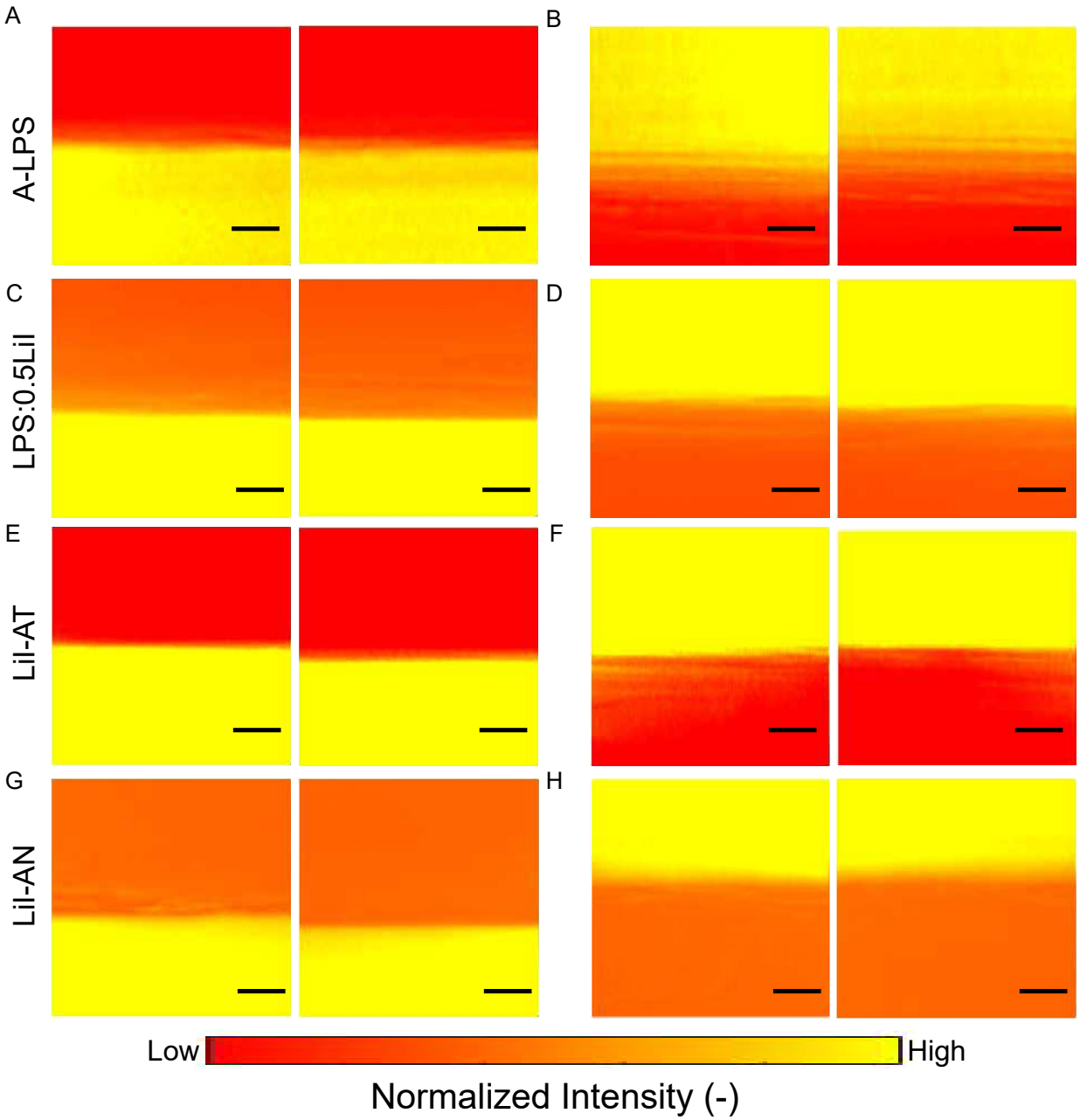

Figure 7.21: Statistics on interfacial intensity map at the solid | solid interface. Intensity map are for (a) top Li | SE and (b) bottom SE | Li interfaces in A-LPS, (c) top Li | SE and (d) bottom SE | Li interfaces in LPS-LiI, (e) top Li | SE and (f) bottom SE | Li interfaces in LiI-AT, (g) top Li | SE and (g) bottom SE | Li interfaces in LiI-AN. All the scale bars in the figure are 30 μm.

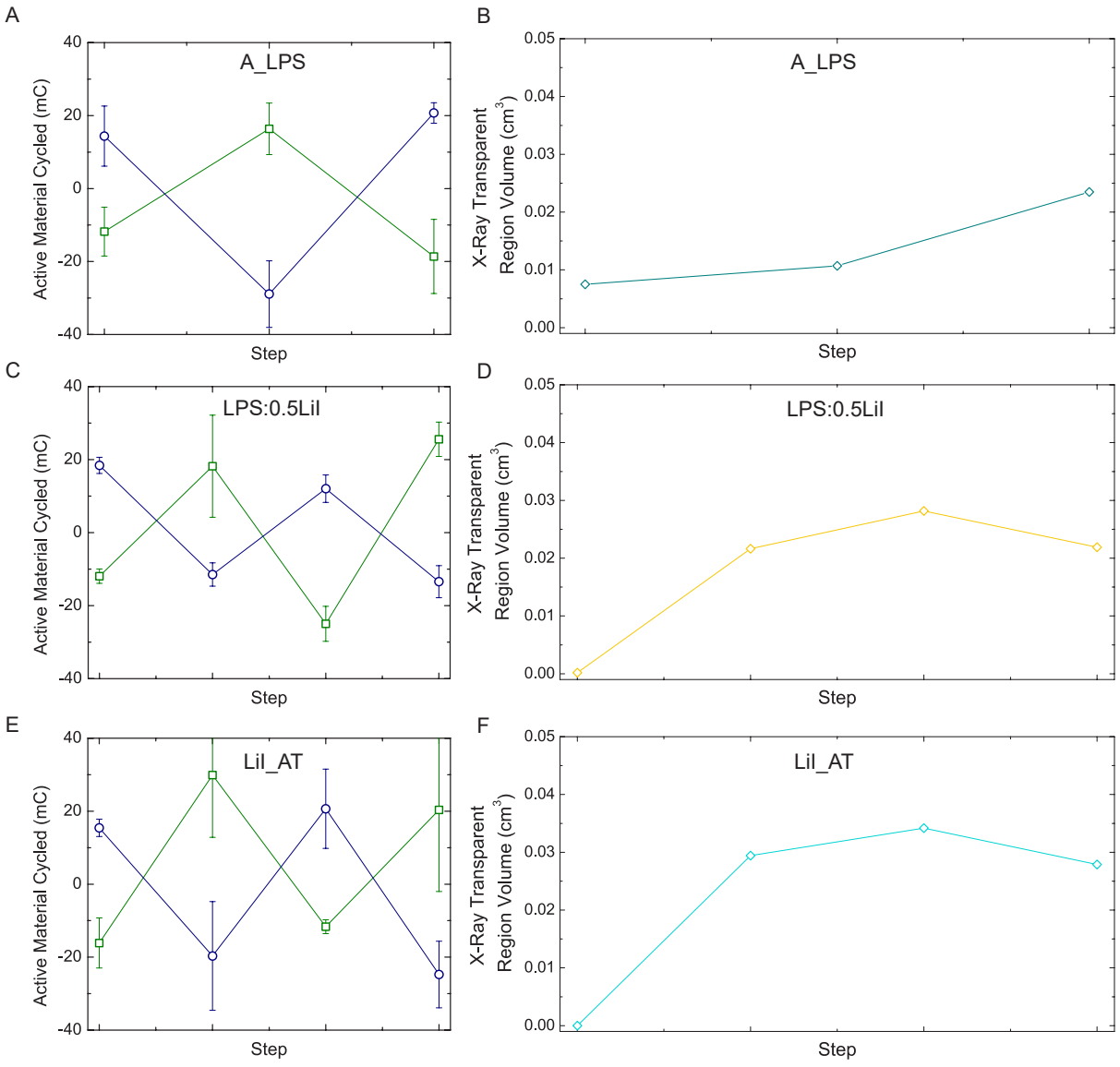

Figure 7.22: Active material cycled during plating and stripping cycles. Plots for (a) A–LPS, (c) LPS–LiI and (e) LiI–AT. Variation in X-ray transparent region volume during plating and stripping cycles for (b) A–LPS, (d) LPS–LiI and (f) LiI–AT.

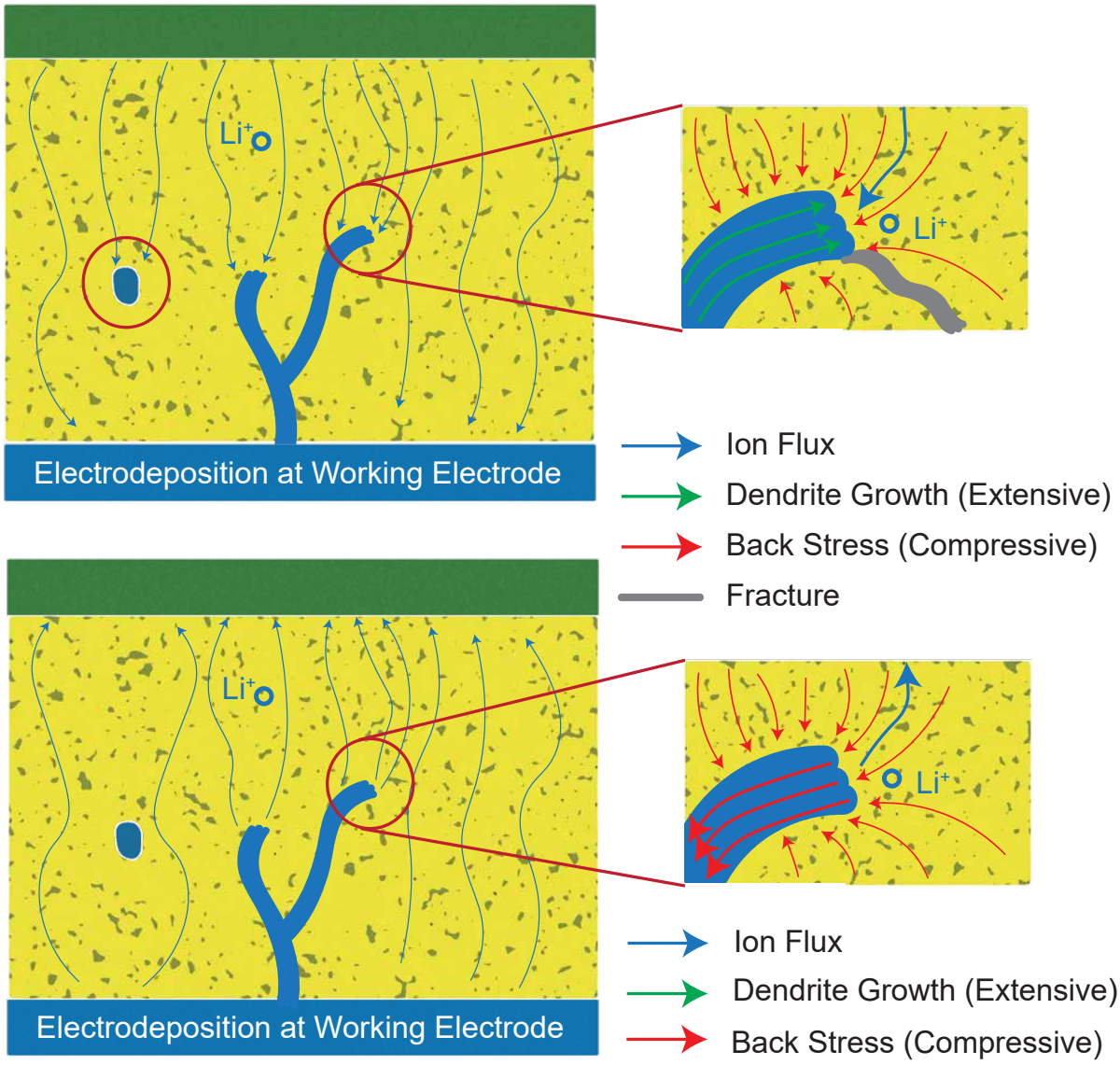

Figure 7.23: Schematic diagram depicting ion flux and stress generation during electrodeposition and electrodissolution. Preferential plating and stripping from the filament generates local stresses. If this stress exceeds the restoring stress offered by the material's fracture strength, fracture can propagate.

Chapter 8

Scalable Manufacturing of Hybrid Solid Electrolytes with Interface Control

8.1 Introduction

Lithium metal batteries can achieve high energy densities because lithium metal has a high theoretical capacity (3860 mAh/g) and low reduction potential (3.04 V) Janek & Zeier (2016); Cheng et al. (2017b). However, lithium metal suffers from consumptive side effects in liquid electrolytes and thus solid electrolytes are one approach toward mitigating these effectsShen et al. (2018). Solid electrolytes are broadly classified into two material categories (1) organic (polymer) and (2) inorganic (ceramic/glass)Sun et al. (2017); Zheng & Hu (2018); Fan et al. (2018) Organic solid electrolytes are easy to manufacture into thin films and are mechanically robust and flexible compared to inorganic electrolytes Keller et al. (2018)(Fig. 8.1a). However, these materials posses low ionic conductivities in comparison to inorganic superionic conductors. Inorganic ceramic and glass-type solid electrolytes possess high ionic conductivity, mechanical strength and electrochemical stabilityLiu et al. (2018)(Fig. 8.1a). However, processing inorganic solid electrolytes is comparatively difficult. Hybrid electrolytes, which combine organic and inorganic ion conducting materials, represent an emerging family of solid electrolytes that can potentially achieve the advantages of both types of solid ion conductors for scalable applications of solid state batteries. However, overcoming transport resistances between inorganic and organic phases remains a challenge.

Hybrid electrolytes contain three different material regions: (1) polymer, (2) inorganic, and (3) interfacial region. The interfacial region is a region adjacent to the inorganic material which contains disparate material properties (Fig. 8.1b). Ion transport in these electrolyte systems is fundamentally dependent on the underlying arrangement of inorganic particles within a polymer matrix and the interactions between the two materials

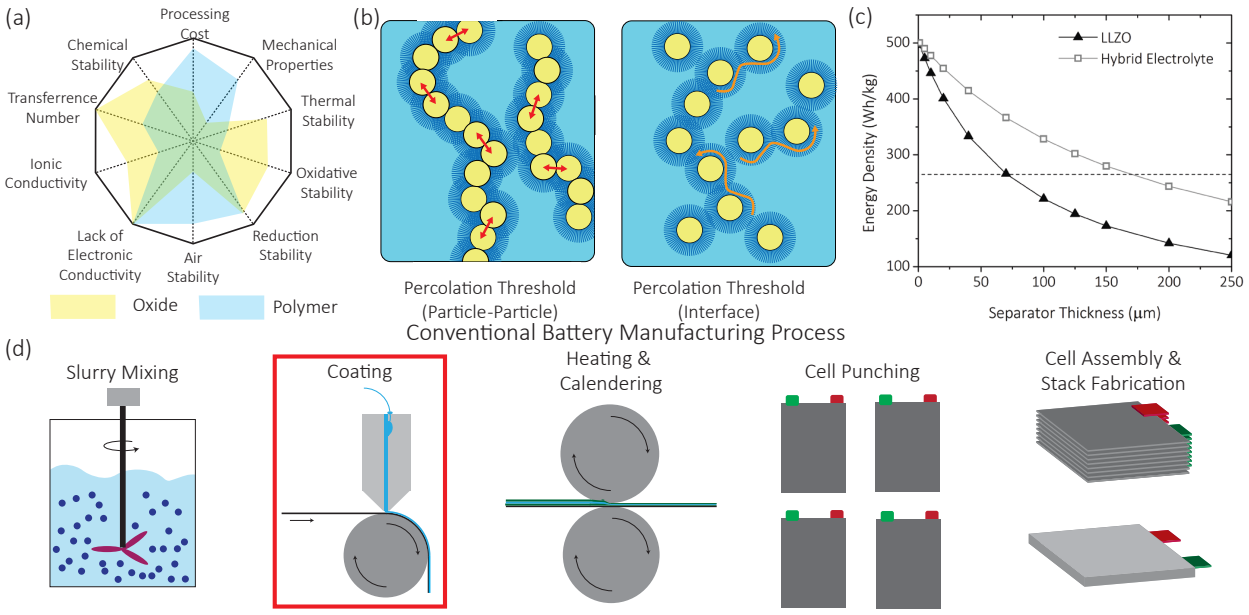

Figure 8.1: (a) Desired properties for solid electrolytes and relative strengths of oxide and polymer type solid electrolytes (b) Gravimetric energy density calculations for LLZO and hybrid electrolytes at 10 mg/cm^2 cathode loading. Active material:binder:C ratio of 96:2:2 is assumed as the cathode composition. Graphite-NCA based battery system is considered the state of the art. Energy density calculations are based on the outline provided in McCloskey (2015). (c) Particle and interfacial percolation thresholds observed in hybrid electrolytes. (d) Manufacturing process line for conventional liquid-electrolyte based batteries.

phasesZaman et al. (2019). Hybrid electrolytes demonstrate two percolation thresholds depending on the inorganic phase content: a) connected particle network at inorganic loading >33% and b) connected interfacial region at inorganic loading of <4% (Fig. 8.1b). The addition of inorganic constituents to the polymer matrix leads to Lewis acid-base interactions in the vicinity of the particlesZhang et al. (2017c). This leads to well dissociated lithium salts that can increase the free Li^+ concentration in the vicinity of the particles. Additionally, interactions between the polymer and particles leads to lower polymer crystallinity which improves the ion transport properties of the polymerTang et al. (2018); Liu et al. (2010); Deka & Kumar (2011); Wu et al. (2011); Chen et al. (2019). Solid state NMR has shown that ion transport pathways are strongly dependent on the the composition

of the electrolyteZheng et al. (2017); Zheng & Hu (2018); Zheng et al. (2016). Lithium ions are shown to prefer plasticizer phaseZheng et al. (2017), ceramic phase in some systemsZheng et al. (2016) and transitions from polymer phase to ceramic phase with some systemsZheng & Hu (2018). Currently, a knowledge gap exists concerning ion transport pathways in inorganic/organic hybrid solid electrolytes. Furthermore, the confined and nano-scale nature of these solid|solid interfaces makes it experimentally difficult to study. Thus, engineering model systems in order to isolate the organic|inorganic interfaces at a macro-scale can provide a way to study ion transport limitations and pathways in hybrid electrolytes.

Aside from transport, scalable manufacturing is one of the most significant challenges facing the adoption of solid state batteries. Keller et al. (2018); Schnell et al. (2018); Kerman et al. (2017). In 2017, there was approximately 3.1x10^9 m^2 of separator material manufactured for battery applications Bloomberg (2017). This scale demonstrates a large potential market for solid electrolytes and the need for tailored manufacturing processes that can achieve these scales. Solid electrolyte production methods must merge in this existing production chain to ensure economic viability (Fig. 8.1d). Gravimetric calculations show that electrolytes with $\leq$ 60 μm (inorganic) and $\leq$ 160 μm (hybrid) thicknesses are necessary to achieve energy densities comparable to the state-of-the-art lithium ion batteriesMcCloskey (2015)(Fig. 8.1c). Furthermore, in order for solid state batteries to displace the current state of the art, lithium metal anodes are necessary. Currently, non-uniform stripping and plating mechanisms limit the coulombic efficiency of Li-metal anodes in solid state batteries. Thus, control over local concentration gradients at solid|solid interfaces is desired to improve coulombic efficiencies. One route toward achieving this, is through micro- and meso-structural control of solid electrolytes.

Currently, hybrid solid electrolytes are processed from a homogenized dispersion of polymer, lithium salt, and ceramic filler. This dispersion is solution cast onto a polytetraflu-

oroethylene or teflon substrate to obtain free standing filmsChen et al. (2017); Langer et al. (2016). Electrolytes produced by these methods show ionic conductivities around 10^{-5} S/cm at room temperatureBan et al. (2018); Li & Johnson (2019). Changing the morphology of the inorganic material has been shown to increase transport properties. For instance, fast ionic conductivity was observed in hybrid electrolytes with inorganic materials with nanowire morphology Wan et al. (2019); Zhu et al. (2019); Zhao et al. (2019); Yang et al. (2017). Changing the morphology of the conducting inorganic filler modifies the polymer properties in the vicinity of the particles improving the overall transport. This has been further extended to develop 3D garnet-polymer frameworks that aim to tailor ion transport through the hybrid electrolyteBae et al. (2018); Fu et al. (2016). These 3D frameworks show improved thermal resistance (up to 600 °C) and ion transport properties ($\approx 10^{-4}$ S/cm @ RT). The major challenge with tailoring microstructure is control across multiple length scales. Furthermore, contradicting reports suggest Li ions favor the ceramic phase, the polymer phase or the interface region, and thus the ideal microstructure is not knownTang et al. (2018); Liu et al. (2010); Deka & Kumar (2011); Wu et al. (2011). For future adoption of hybrid electrolytes, manufacturing processes that can control the arrangement and order of the inorganic phase is necessary.

Herein, a manufacturing platform is engineered to explore the role material interfaces play on transport. This method employs a novel slot-die that is compatible with current battery manufacturing approaches. This technique is versatile and can enable control over material composition, density, and structure, during roll-to-roll scale processing. This technique can be leveraged towards processing of multi material solid electrolytes with tailored microstructural compositions to ameliorate various detrimental interfacial effects in solid-state batteries. We use this platform to engineer macro-scale interfaces in hybrid electrolytes to study ion transport through these intrinsic interfaces. In this study we investigate hybrid solid electrolytes composed of 25 wt.% LLZO-PEO and 75 wt.% LLZO-PEO. Single material films and coextruded films with 1 mm (CoX_1mm),

2 mm (CoX_2mm) and 3 mm (CoX_3mm) striped architecture are systematically evaluated for transport and stability (Figure 8.2c). The configurations and compositions are selected to create hybrid electrolytes with interfaces between a low ceramic containing matrix and a high ceramic loaded matrix. Coextruded electrolytes show a slight advantage over single material films which is attributed to the generation of highly conducting intrinsic interfaces within the hybrid electrolytes. The effect of manufacturing variability on the electrochemical performance of the system is investigated. The nature of these coextruded interfaces is identified using relaxation time distribution of charge transport mechanisms. This is further validated by theoretical modelling of the hybrid system using effective mean field theory as well as computational modeling.

8.2 Experimental Methods

8.2.1 Materials

Polyethylene Oxide (MW: 1,000,000 g/mol) was sourced from Across Organics and used as recieved. Lithium Perchlorate was used as the lithium salt. LLZO was prepared in-house using a mechanochemical synthesis reported previously. 25 wt.% LLZO-PEO and 75 wt.% LLZO-PEO system are considered as the two primary systems. Required amount of PEO and $LiClO_4$ was initially dissolved in acetonitrile. EO:Li ratio was maintained at 18. Subsequently, LLZO was added to the mixture which was ball-milled in a low energy ball mill until a uniform, homogenized mixture was obtained. Total solid loading for both inks was maintained constant at 15 wt.%.

8.2.2 Coextrusion Coating

The coextrusion head is mounted on a gantry system capable of XY-motion. The coating height is adjusted by moving the substrate. The gantry system has a resolution of ± 50, ± 150 and ± 10 μm in the X-, Y- and Z- direction. Standard G-codes are used for control of the CoX head during coating. All inks are fed pneumatically to the CoX head. A commercial pressure dosing system (Nordson EFD Ultimus V) is used as a constant

pressure source. A constant supply pressure of 60 psi is maintained. Subsequently, the pressure to individual inks are controlled by digital pressure regulators. 0-10 V signal is applied by a data acquisition system to control the dispensing pressures to the fluid. The pressures are correlated to the mass flow rates of respective fluids and can be controlled independently. The dispensing pressures are informed by standard simulations and subsequently validated by test runs on the system. An integrated software platform has been developed to integrate the positioning and feed of the CoX head. The software communicates with the positioning gantry and the pressure dispenser via a RS-232 interface, and to the individual regulators via serial communication. The response delays of each system component is considered in designing the software. The software can deliver continuous as well as intermittent coating over the entire print area of the positioning gantry.

Two inks are fed pneumatically to the co-extrusion die. Single material films, and coextruded films with 1 mm, 2 mm and 3 mm stripes were manufactured. The architecture of the film was modified by changing the shims within the coextrusion die. Coating speed of 300 mm/min was used. Electrolytes with thicknesses ranging from 50-70 μm have been fabricated using this coextrusion platform.

8.2.3 Direct Write Coating

Two inks are fed pneumatically to a regular syringe fitted with a nozzle with I.D. of 0.5 mm. Striped films are processed by coating the layers for both materials one after the other. Coating speed of 100 mm/min was used. Electrolytes with thicknesses ranging from 50-60 μm have been fabricated using this direct write platform.

8.2.4 Rheology

Inks used in coating experiments were rheologically studied using a DHR3 Hybrid Rheometer (TA instruments, USA). All inks were studied using a parallel plate geometry with 1000 μm gap thickness. All inks were presheared at 10 s^{-1} for 10s and allowed to rest for 5 minutes prior to any tests to remove any mechanical history in the samples. Shear sweeps were run from 200 s^{-1} to 0.01 s^{-1}. Frequency sweeps were run from 0.1 rad/s to 600 rad/s. A constant amplitude of 0.1% was applied during oscillating experiments.

8.2.5 Electrochemical Testing

Single Films were cast on a copper film for ionic conductivity measurement. After drying, the electrolyte films coated on copper were hot pressed at 100 °C and 400 psi for one hour. The hot pressing does not result in any change in the architecture of the coextruded membranes (Fig. 8.10). Free standing electrolyte films were cast on PTFE substrate for transference number measurement. All electrochemical tests were performed on a VMP3 potentiostat (Biologic, USA). Ionic conductivity of the electrolytes was measured by carrying out AC impedance measurements between 1 MHz and 1 Hz with an amplitude of 10 mV. Transference number measurements were carried out by polarization method in a Li|Elyte|Li configuration. Distribution of relaxation time characterization was carried out for Nyquist impedance spectra obtained at room temperature. Galvanostatic charge-discharge studies are carried out on symmetric cells. A constant current of 20 μA is applied for a duration of 10 minutes for 50 cycles. Cells are characterized by AC impedance spectroscopy before and after cycling.

8.2.6 Tomography Studies

Synchrotron X-ray tomography was carried out on the co-extruded membranes at 2-BM beamline at the Advanced Photon Source in Argonne National Laboratory. Coextruded samples were held by a metal clip and kept on the the rotation stage. 25 keV monochro-

matic X-rays were used for imaging with a 10x objective lens resulting in an ≈2x2 mm FOV with a resolution of 0.8 μm. The tomography data was reconstructed using TomopyGürsoy et al. (2014). Subsequent image analysis was carried out in ImageJSchneider et al. (2012a).

8.2.7 COMSOL Modelling

3D simulations are carried out on a 6 mm x 10 mm electrolyte domain with 60 μm thickness. This domain was subdivided into three domains of 2 x 10 mm each. The outer two domains were assigned physical and electrochemical properties of 25 wt.% system, while the inner domain was assigned the properties of 75 wt.% system. Steady state flux profiles through the electrolyte are evaluated. 1 mA/cm^2 current density is imposed as a boundary condition.

8.2.8 Distribution of Relaxation Times

Distribution of relaxation times is correlated to the impedance spectra by the following formula:

$$Z(\omega) = R_0 + Z_{pol}(\omega) = R_0 + R_{pol} \int_0^{\inf} \frac{g(\tau)}{1 + j\omega\tau} d\tau \tag{8.1}$$

with the condition that

$$\int_0^{\inf} g(\tau) d\tau = 1 \tag{8.2}$$

where, Z(ω) is the impedance data, R_0 is the ohmic resistance of the impedance, $Z_{pol}(\omega)$ is the polarization part of the impedance, R_{pol} is the polarization resistance of the impedance and g(τ) is the corresponding distribution of relaxation times. The method fits N RC-elements with individual relaxation time constants τ_i to the impedance spectra. The drawback of DRT method is that it is unable to account for capacitive behavior and hence preprocessing is required to fit the raw impedance spectra and substract the diffusive and capacitive tail at low frequencies. Equivalent circuits used for fitting, example raw data sets and processed data are shown in Fig. 8.11. For this study, the open-source software

DRTtools is used for this analysis.

8.3 Effective Mean Field Theory

The effective mean field theory was originally proposed by Bruggeman Bruggeman (1937) in 1935 and has been since then been extensively utilized to predict the transport properties of homogeneous material mixtures. In this theory, a mixture of two materials having independent properties is considered to be an effective medium with equivalent material properties. The original effective medium equation is given by Landauer as follows Landauer (1952):

$$\frac{f_1(\sigma_1 - \sigma^*)}{\sigma_1 + 2 * \sigma^*} + \frac{f_2(\sigma_2 - \sigma^*)}{\sigma_2 + 2 * \sigma^*} = 0 \tag{8.3}$$

where f_1 and f_2 are the volume fraction occupied by the two materials, σ_1 and σ_2 are the conductivities of the two materials and σ^* is the effective conductivity. The effective conductivity of the composite matrix can be obtained by solving this second order equation.

This equation was further improved by Granqvist and Hunderi Granqvist & Hunderi (1978) incorporating the effective depolarization factor dealing with the dipole-dipole interactions of the particulate insertions in the matrix. Above the percolation threshold (which according to the percolation theory occurs at a volume fraction of 0.33), the particulate insertions are assumed to form FCC clusters inside the matrix. The effective depolarization factor in this case for FCC clusters of particulate inserts in the composite matrix is found to be 0.0865. The effective conductivity equation for this case is given as:

$$\frac{f_1(\sigma_1 - \sigma^*)}{\sigma_1 + Li^*(\sigma_1 - \sigma^*)} + \frac{f_2(\sigma_2 - \sigma^*)}{\sigma_2 + Li^*(\sigma_1 - \sigma^*)} = 0 \tag{8.4}$$

Nakamura Nakamura (1982) and subsequently Nan and Smith Nan & Smith (1991) furthered this model by considering a system of three phases which are the matrix, inserted particles and the highly conductive interface layer covered on the grain surface. The high

conductivity layer on the surface of the inserted grains can arise from a space charge layer arising due to concentration defects as well as preferential adsorption/desorptions of certain moieties of the system. Employing the Maxwell-Garnett mixture ruleMaxwell Garnett (1904), the equivalent conductivity of the system consisting of the grain and the interfacial layer can be given as:

$$\sigma_{eff} = \sigma_{cer}\left(\frac{2\sigma_{cer} + \sigma_{int} + 2K_1^3(\sigma_{int} - \sigma_{cer})}{2\sigma_{cer} + \sigma_{int} - K_1^3(\sigma_{int} - \sigma_{cer})}\right) \tag{8.5}$$

$$where, K_1 = \frac{1}{1 + \frac{2t}{R}} \tag{8.6}$$

where, σ_{cer} and σ_{int} are the conductivities of ceramic and the interfacial layer, t is the thickness of the interface layer, R is the radius of the inserted grains. Rewritting the EMT equation (Eqn. 2) in terms of the polymer matrix and the effective conductivity of the inserted grains and the interfacial layer defined here, we get:

$$(1 - f_c)\frac{\sigma_{pol} - \sigma_{comp}}{\sigma_{comp} + Li^*(\sigma_{pol} - \sigma_{comp})} + f_c\frac{\sigma_{eff} - \sigma_{comp}}{\sigma_{comp} + Li^*(\sigma_{eff} - \sigma_{comp})} = 0 \tag{8.7}$$

where σ_{pol} is the conductivity of the polymer matrix and f_c is the volume fraction of the inserted grains. Substituting the Eqn. 3 in this, we get,

$$(1 - f_c)\frac{\sigma_{pol} - \sigma_{comp}}{\sigma_{comp} + Li^*(\sigma_{pol} - \sigma_{comp})} + f_c\frac{(\sigma_{cer}\left(\frac{2\sigma_{cer}+\sigma_{int}+2K_1^3(\sigma_{int}-\sigma_{cer})}{2\sigma_{cer}+\sigma_{int}-K_1^3(\sigma_{int}-\sigma_{cer})}\right)) - \sigma_{comp}}{\sigma_{comp} + Li^*((\sigma_{cer}\left(\frac{2\sigma_{cer}+\sigma_{int}+2K_1^3(\sigma_{int}-\sigma_{cer})}{2\sigma_{cer}+\sigma_{int}-K_1^3(\sigma_{int}-\sigma_{cer})}\right)) - \sigma_{comp})} = 0 \tag{8.8}$$

The above model has been used previously to estimate the effective conductivity of a wide range of composite polymer electrolytes using the known values of polymer matrix, grain and interfacial layer conductivityLi et al. (2018). In this study we use this equation to predict the properties of the interfacial layer using the known values of ceramic, polymer and the composite electrolyte conductivity. Further, to simplify and aid the estimation

an approximation of a very thin interfacial layer is used, that is $t << R$. This is a fairly reasonable assumption for the polymer ceramic systems under study. In this case, the factor K_1 reduces to unity and Eqn. 6 can be simplified to:

$$(1 - f_c)\frac{\sigma_{pol} - \sigma_{comp}}{\sigma_{comp} + Li^*(\sigma_{pol} - \sigma_{comp})} + f_c\frac{\sigma_{int} - \sigma_{comp}}{\sigma_{comp} + Li^*(\sigma_{int} - \sigma_{comp})} = 0 \tag{8.9}$$

The conductivity of the interface is obtained by solving this implicit equation. The Diffusion co-efficients can be obtained from the conductivity values by the Nernst-Einstein equation:

$$\sigma = \frac{F^2 C}{RT} D_{Li^+} \tag{8.10}$$

where, F is the Faraday's constant, C is the concentration of Lithium ions, R is the universal gas constant, T is the temperature, D_{Li^+} is the diffusion coefficient of lithium ion. The values of the conductivity of the polymer system and ceramic particles used for estimation of the interfacial conductivity are listed in Table 8.1.

Table 8.1: Conductivities of the composite polymer electrolytes used in this study. Temperature is in °C and conductivity values are in S/cm

Temperature	1M System	LLZO
25	1.51E-6	1.86E-4
35	2.62E-6	2.56E-4
45	7.87E-6	3.26E-4
55	2.44E-5	3.96E-4

8.4 Results and Discussion

There are two types of interfaces that govern ion transport and electrochemical properties in a solid state system: a) extrinsic interfaces and b) intrinsic interfaces. Extrinsic interfaces emerge when two materials are integrated together to serve some function, such as an electrode|electrolyte interface. In contrast, intrinsic interfaces naturally occur in a material or a composite and can affect concentration gradients, degradation pathways, and transport properties. Grain boundaries/voids are examples intrinsic interfaces or

microstructural features in inorganic materials, and organic|inorganic interfaces are examples of intrinsic interfaces in hybrid solid electrolytes. The ionic conductivity is lower in hybrid electrolytes than inorganic electrolytes and is often attributed to a formed interfacial resistance (R_{int}) at the polymer|ceramic interfacePandian et al. (2018); Chen et al. (2019); Tenhaeff et al. (2011) which prevents transport between the two materials (Fig. 8.2a)Li & Johnson (2019). Phenomenologically, this can be seen when mapping anionic and cationic flux in the polymer, ceramic and interfacial region using effective mean field theory (Fig. 8.2a). Ceramic electrolytes have a lithium ion transference number close to one that blocks all anion transport. This leads to redistribution of anions over the particles and higher effective current densities in the interfacial region (Fig. 8.2a). Thus, control over organic|inorganic interfaces during manufacturing may provide a means for directing ion transport to extrinsic interfaces (electrode). Uniform and controlled concentration gradients are important in order to mitigate degradation phenomena accelerated by the formation of local hot spots and/or lithium metal pore formation (i.e. Li excess/deficient

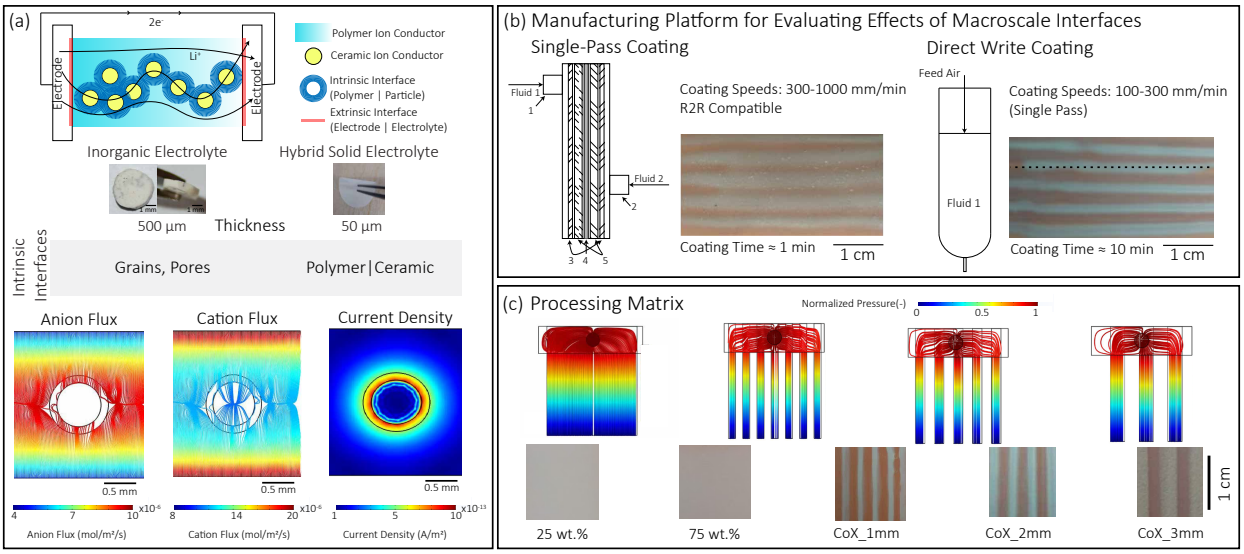

Figure 8.2: (a) Schematic diagram of interfaces in hybrid electrolytes, ion motion in hybrid electrolytes and normal current density. (b) Manufacturing platforms for generating hybrid electrolytes with macro-scale interfaces. (c) Processing matrix investigated in this study.

regions).

Slot die coaters are extensively used in roll-to-roll manufacturingEnergy (2015). Conventional slot die instruments contain flow dividers and a shim in order to control the coating fluid and coating area. Furthermore, precise mass flow regulation is necessary to maintain coating resiliency during a manufacturing pass. The co-extrusion (CoX) print head designed is an extension of a conventional slot-die head (Fig. 8.2b, 8.7a-b). The CoX head is capable of coating two layers in a single pass. Fluid one is connected to the inlet port one (1) and fluid two is connected to inlet port two(2). In the interior of CoX head, the fluid is distributed across the width of the CoX head by using a flow divider(3). Subsequently, specially designed shims(4) channel the flow in multiple configurations. The mixing of two fluids is prevented by a flow separator(5). The CoX head can deliver single material coatings and multi-material coatings with through-plane or in-plane gradation. The exact configuration is dependent on the CoX head setup and processing parameters. Similar control over local architectures are obtained by direct write coating techniques which is adapted from the 3D printing domain (Fig. 8.2b). The coextrusion platform is capable of coating areas of up to 200 cm^2/s. Direct write coating is significantly more time-consuming taking up to 10 times more time for coating the same areas (Fig. 8.2b). To ensure a uniform pressure distribution at the outlet of the CoX head, the flow dividers and the shims were designed using computational fluid dynamics simulations as a design tool. Flow divider geometry and shim configurations are designed to achieve a uniform pressure distribution at the exit(Figure 8.2c). The pressure at the exit of the flow patterns is fixed at ambient conditions and simulations are carried out at a range of viscosities (ink formulations) and inlet pressures. Typical flow patterns and pressure distribution show a uniform flow at the exit for all the configurations with uniform pressure at the outlet. This results in optimum flow paths for the two fluids resulting in well-defined co-extruded films as evidenced in the optical images. Optical picture and tomgoraphy reconstruction also show the striated nature of the coextruded membranes (Fig. 8.2c,

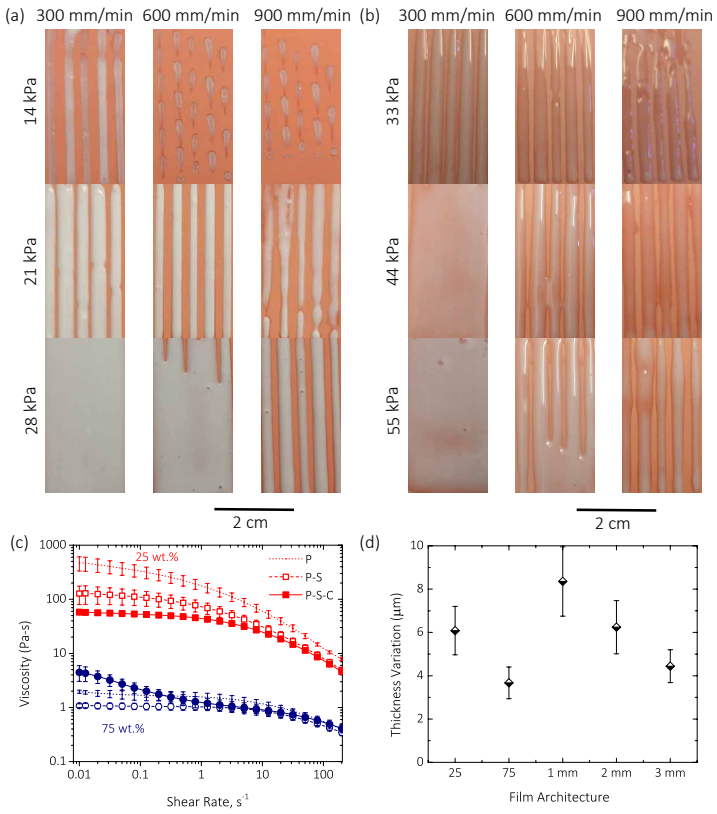

Figure 8.3: Flow stability analysis for (a) 75 wt.% system. and (b) 25 wt.% system. Rheology studies for coextrusion inks for solid electrolytes. (c) Steady shear for 25 wt.% and 75 wt.% LLZO-PEO system. P, S, and C represent polymer, salt and ceramic respectively. Rheology was measured for bare polymer ink, polymer-salt mixture and the composite ink. (d) Variation in film heights for different architectures measured using profilometer. Variations in height are calculated over at least five line scans across the coating at 5 locations along the coating length.

8.7c-d). It is important to note that all the individual configurations are obtained in a single pass coating.

The coating stability window of different ceramic:polymer inks (25 wt.% and 75 wt.%) was systematically investigated (Fig. 8.3a-b). A stable coating is obtained when the coating bead forms stable liquid-vapor interfaces with its environment (Fig. 8.8)Goda et al. (2017); Ding & Liu (2016); Hyung et al. (2011); Suk et al. (2016). If the pressure inside the bead is too large, the ink swells out in all directions leading to defect called leaking. This defect leads to loss of control over the coating width and thickness. At the other extreme,

if the pressure in the bead is too low, air can entrain in the film at the upstream meniscus leading to break up of the coating bead. The defect begins at isolated spots and can deteriorate into uncoated streaks. At very high web speeds the downstream meniscus can break up and lead to uncoated regions through the width of the slot and can manifest as ribbing/ripples in the coating. At 14 kPa and 300 mm/min, the 75 wt.% shows poor coating behavior due to low mass flow rate. At 600 and 900 mm/min the coating bead loses contact with the substrate and ribbing behavior is seen. At 21 kPa, 300 mm/min shows evidence of leaking behavior due to low coating speeds and higher mass flow rate. 600 mm/min shows a clearly coated stripes, while the stripes again show ribbing behavior at 900 mm/min. At 28 kPa, leaking behavior is seen at all coating speeds, however it reduces with increasing coating speed. Similar observations can be made about the for the 25 wt.% (ceramic:polymer) ink. Coating pressure for both inks and the coating speed was obtained for by carrying out this parametric study.

Rheological experiments are used to investigate the flow behavior of the respective inks (Fig. 8.3c, 8.9a). Effective coating is dependent on having uniform material properties during coatingMaza & Carvalho (2015); Jin et al. (2016); Tsuda (2010); Nam & Carvalho (2009); Bhamidipati et al. (2012); Lee et al. (2017); Han et al. (2014); Lin et al. (2014). Both of the inks used for coextrusion show shear thinning behavior in the regime of interest (1-100 s^{-1}). The viscosity of the 75 wt.% (ceramic:polymer) ink is two orders of magnitude lower than that of the 25 wt.% ink (22.63 Pa-s vs. 0.87 Pa-s at 12 s^{-1}). Thus, since the two inks demonstrate different rheological properties, there is a need for different operating pressures during co-extrusion (Fig. 8.7a-b). The addition of a salt (Li source) reduces the viscosity of a pure polymer solution. Salt introduces charge-screening effects in the polymeric solution leading to a reduced repulsive force in the polymer chainsSamanta et al. (2010). This leads to a reduction in the hyrdrodynamic radius of the polymer and the degree of polymer chain entanglement. Together, these factors lead to a reduction of the polymer viscosity. Subsequently, the addition of ceramic particles also reduces the

viscosity for the 25 wt.% system due to further chain disentanglement. An increase in viscosity is seen in the low shear region indicating a percolated particle network for the 75 wt.% ink (ceramic:polymer). Both systems show a higher loss moduli than storage moduli suggesting the presence of unstructured agglomerates (Fig. 8.9a).

Quality control is of significant interest in battery manufacturing, because irregularities will lead to variable material properties Mohanty et al. (2016); Heider et al. (1999); Brandt & Laman (1989); Shao et al. (2013); Kurfer et al. (2012). Thus, it is imperative to analyze the process variability in the manufacturing process. Profilometry studies were carried out on co-extruded electrolytes across multiple sections along the length of coating. The average thickness variation in the different coextruded electrolytes are reported (Fig. 8.3d, 8.9b). The average variation across all the samples is 5.75$\pm$1.2 μm. This error within the resolution limits of the gantry stage used for the co-extrusion system ($\pm$50, $\pm$150 and $\pm$10 μm in the X-, Y- and Z- direction). Moving to a dedicated coating platform with improved motor resolution and better load management can improve the variability response of the co-extrusion system. The thickness variations observed here are ≈5-10% of the average electrolyte thickness.

Electrochemical properties for the co-extruded and single material films were systemat-

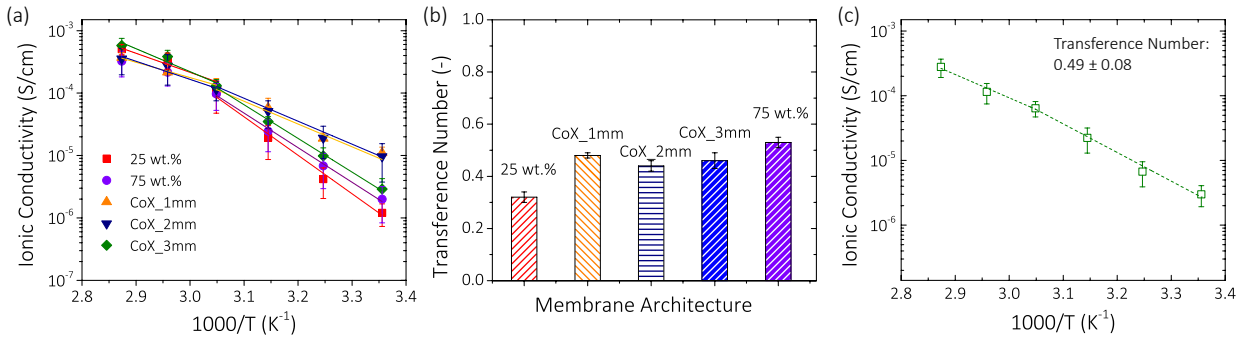

Figure 8.4: Ionic conductivity (a) and transference number (b) of coextruded membranes. Ionic conductivity and transference number of membrane processed using direct write protocol (c).

ically investigated (Fig. 8.4a-c). The ionic conductivity for the 1 mm, 2mm, and 3 mm coextruded samples were similar for temperatures between 25°C and 70°C (Fig. 8.4a), and larger than the single material electrolytes. For statistics and quality control, 10 separate samples were measured. Detailed results with errors are reported in the supporting information (Tables 8.3-8.7). The ionic conductivity reported here are generally on the lower side with a room temperature conductivity of $\approx 10^{-}5$ S/cm for the co-extruded membrane. Employing strategies like optimal loading of ceramicsZaman et al. (2019); Chen et al. (2017), addition of plasticizerZheng et al. (2017), tailoring polymer compositionZhang et al. (2017a) or moving to a bulkier anionWan et al. (2019) can help improve the ionic conductivity values. Model PEO-$LiClO_4$-LLZO inks were used for this proof-of-concept study that exhibited distinct composition and rheological properties. The relatively large spread seen in the ionic conductivity data can arise from the variability in processing discussed earlier. Even so, an improvement in the mean value of ionic conductivity is observed for coextruded membranes compared to single material films (Fig. 8.4a). The activation energy (measured on the average data) also shows an equivalent decrease for the coextruded configurations compared to the single material films below the transition temperature of the polymer (Table 8.2). The striped architecture resembles a parallel conductor network for which the equivalent conductance is equal to the sum of individual conductance in the circuit. Charges are redistributed through the individual stripes to minimize the voltage drop across the system. The equivalent circuit model de-

Table 8.2: Activation Energies (eV) for Ion Transport

Hybrid Electrolytes

Branch	25 wt.%	75 wt .%	CoX_1mm	CoX_2mm	CoX_3mm
Low Temperature	0.53	0.48	0.32	0.31	0.46
High Temperature	0.26	0.26	0.21	0.25	0.32

Interfaces

Branch	25 wt.%	75 wt .%	CoX_1mm	CoX_2mm	CoX_3mm
Low Temperature	0.42	0.43	0.25	0.21	0.46
High Temperature	0.27	0.19	0.14	0.21	0.37

scribed above considers electron motion which is not the case for the hybrid electrolytes. Ion transport through the electrolyte is limited by kinetics of ion motion through the material. Increases in ionic conductivity for coextruded solid electrolytes suggests that the addition of macro-interfaces facilitates transport pathways within the electrolyte that possess better ion transport kinetics. Generally, in hybrid electrolytes improved ion transport is ascribed to (i) increased ion-pair dissociation, (ii) enhanced Li^+ surface transport, (iii) anion attraction at inorganic phase surface due to Lewis acid-base interactions, (iv) polymer chain promoted surface transport, and (v) improved ion transport through polymer phase due to reduced crystallinityKeller et al. (2018). The architectures designed for this study are tailored so that the microstructure at the interface between the low loading ink and high loading ink are distinct than the respective bulk systems. This region can be identified as the macro-interfacial region between the two coextruded regions. The distribution of the organic, inorganic and the so-called 'space-charge' layer will be distinct from the bulk materials. The results suggest that this redistributed interfacial region between the two systems is likely the cause of improvement in the ionic conductivity. The mechanism for improved ion transport rates is likely to be described by a combination of the factors discussed above. It is extremely difficult to evaluate mechanistic information about ion transport experimentally and modelling techniques are used to provide insight into the interfacial mechanisms for improved ion transportLi & Johnson (2019). It is understood that manufacturing platforms with a higher resolution and better load management can overcome the process variation seen in this study and showcase the improvement in the co-extruded electrolytes more effectively. However, the current platform demonstrates clearly the potential value for multi-material manufacturing as a means to control electrochemical and transport properties in a part or component.

Transference number is another electrolyte property that dictates the electrochemical performanceGhosh et al. (2010); Diederichsen et al. (2017); Li et al. (2018). High transference number electrolytes minimize concentration and polarization gradients, improved power

performance and mitigate risk of catastrophic failure via shorting due to uniform concentration profiles. The transference number of the uniform coating with 25 wt.% ceramic is 0.36 while the transference number of the uniform coating with 75 wt.% system is 0.56 (Fig. 8.4b). Addition of ceramic particles to the polymer matrix improves the Li-salt dissociation and mobility of Li^+ due to charge screeningZhang et al. (2017b). Improved salt dissociation and anion immobilization on increasing the single ion conducting inorganic phase fraction leads to the higher transference number for the 75 wt.% system. The transference number for the coextruded electrolytes fall between these two systems. According to the concentrated solution theoryDoyle et al. (1994), the cation transference number is related to the effective diffusion coefficients of the binary salt in the medium, which in turn depends on the conductivityKim & Srinivasan (2016). The experimental results show an improved ionic conductivity for the coextruded films, however the transference number remains between the two boundary systems. This indicates an equal improvement in both anion and cation diffusion coefficients which results in a higher conductivity, but an effectively averaged transference number. There can be several competing mechanisms occurring at the macro-interfaces that can lead to this behavior including anion immobilization, charge screening, as well as ion redistribution. Further investigation into the differences in the bulk and interfacial microstructure and chemical morphology is needed.

In order to test the hypothesis that the improved transport is do the macro-interfaces, and not do to process related parameters, we tested a similar striped architecture using direct writing printing. Direct write printing methods are another approach capable of generating architectures similar to the coextrusion system. The primary difference between direct write and co-extrusion manufacturing platforms is speed of processing. Co-extrusion coats multiple inks at the same time, and thus is much more facile for high throughput processing. However, there is a possibility of mixing at the interfacial region in co-extrusion manufacturing. Diffusion of components within the two ink stripes during the drying step can also occur due to the composition difference between the two inks.

These phenomena have less impact with direct write coating process. The ionic conductivity of the direct-write striped electrolyte shows a slightly higher conductivity than the single-material electrolytes (75 wt% and 25 wt%) as well as a median transference number values (4.12*10^{-4} S/cm vs. 3.98*10^{-4} (25 wt%) & 2.21*10^{-4} (75 wt%)). The coextruded electrolyte with a similar stripe configuration (2 mm) show slightly higher ionic conductivities (6.31*10^{-4} S/cm vs. 4.12*10^{-4} S/cm @ 75 °C) as well as smaller activation energies (-0.966 eV vs. -1.06 eV). These results suggest that the macro-scale interfacial regions are responsible for the enhanced ion transport properties.

Deconvoluting the ion transport mechanisms between the polymer phase, ceramic phase and the interfacial region is challenging (Fig. 8.5a). Intra- and inter- chain ion hopping mechanism as well segmental motion of the polymers are known transport mechanisms through the polymer phase (Fig. 8.5a). Li transport in the garnet occurs primarily through hopping mechanisms that is driven by vacancy concentrations in the crystal structure. The improved ionic conductivity and median transference number suggests that the transport mechanisms at the interfacial regions is through a confined polymer matrix. Multi-scale modeling of battery materials is an effective tool to deconvolute experimental results.Shi et al. (2015) We employ distribution of relaxation times analysis as an experimental approach towards deconvoluting the ion transport mechanisms in these coextruded systems. This is complemented by theoretical modelling using effective mean field theory (Fig. 8.5b) as well as 3-dimensional fluid dynamics simulations (Fig. 8.6).

Distribution of relaxation time is a method for deconvoluting transport mechanisms from an impedance spectraWan et al. (2015); Mertens et al. (2017). This technique does not require any *a priori* assumptions regarding the system behavior as is necessitated in equivalent circuit modelling of the impedance spectra. Furthermore, this technique can distinguish between mechanisms with similar time constants. The distribution relaxation time spectra of the single-material 25 wt.% solid electrolytes shows one primary peak at

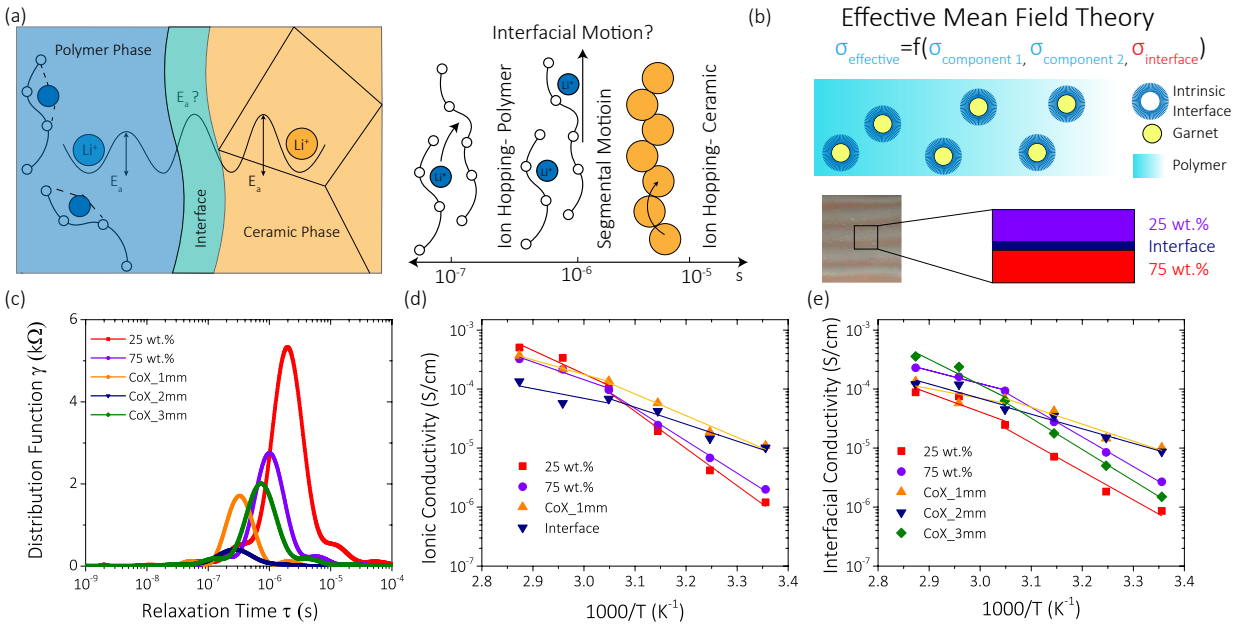

Figure 8.5: (a) Schematic diagram of Li ion transport in hybrid electrolytes with ion transport mechanisms and characteristic time-scales (b) Effective mean field theory model for estimating interfacial properties (c) Distribution of relaxation time results for all samples (d) EMFT results for CoX_1mm membrane with 25 wt.% and 75 wt.% system as the bounding components. (e) Interfacial conductivities for all samples.

≈2x10^{-6} s and shoulders at ≈1.3x10^{-5} and 3.0x0^{-7} s. These may represent the characteristic ion transport mechanisms in the polymer: inter- and intra- chain ion hopping and the segmental motion respectively. The ceramic concentration at this loading is ≈7 vol.%, which suggests a discrete network that does not contribute to ion transport significantly. Moving to the single-material 75 wt.% solid electrolyte demonstrates a shift in the relaxation time distribution curve towards smaller relaxation times (primary peak at 1x10^{-6} s), and a small shift of the peak at higher relaxation time. The shift to lower relaxation times can be attributed to the modification of the polymer phase with the addition of the ceramic particles. Coextruded electrolytes all show a shift of peaks to lower relaxation times (primary peak at 3.09*10^{-7}, 2.64x10^{-7} and 7.64x10^{-7} for CoX_1mm, CoX_2mm and CoX_3mm respectively) which suggest faster ion transport mechanisms (Fig. 8.5c). Additionally, co-extruded solid electrolytes have features at very low relaxation times (10^{-7}s)

which suggest that a region of fast transport exists in these samples.

While distribution of relaxation times helps to show presence of interfacial regions with disparate ion transport properties, the physical properties of these regions are not quantifiable. Effective mean field theory (EMFT) was originally proposed by BruggemanBruggeman (1937) to predict the effective properties of composite materials. The theory has been extensively improved since then and has been recently employed to screen mixture compositions for hybrid electrolyteLi et al. (2018). EMFT models use conductivity values for individual components of a composite matrix as well as the interface to predict the properties of the composite matrix (Fig. 8.5b). We leverage this model and use it implicitly to solve for the interfacial properties. An assumption for very thin interfaces (compared to the particle radius) is taken to simplify the analysis. This approximation is fairly safe considering the length scales interface layer is expected to propagate from the particle surface. We employ this model to predict the properties of macro-scale interfaces generated in the coextruded samples.

The interface in 25 wt.% system between the polymer phase and ceramic phase shows lower ionic conductivity than the polymer (55 °C) (Fig. 8.12a). Ion transport would favor the polymer in this case and the ionic conductivity of the hybrid membrane falls close to the bare polymer. At temperature $<T_m$, the hybrid electrolyte shows a slight improvement possibly due to the addition of the ceramic filler and a decrease the polymer crystallinity. At temperatures above the melting temperature, the bulk polymer becomes amorphous, resulting in similar transport properties between each stripe. The interface is estimated to be more conducting $<T_m$ for 75 wt.% system (Fig. 8.12b). The increased particle loading leads to generation of interfacial regions in the vicinity of the particles that possess locally amorphous polymer structure as well as strong anion suppression. This results in the improved interfacial conductivity for this system. The interfacial conductivity shows a decay after 55 °C for the 75 wt.% system. Higher ceramic loading in this

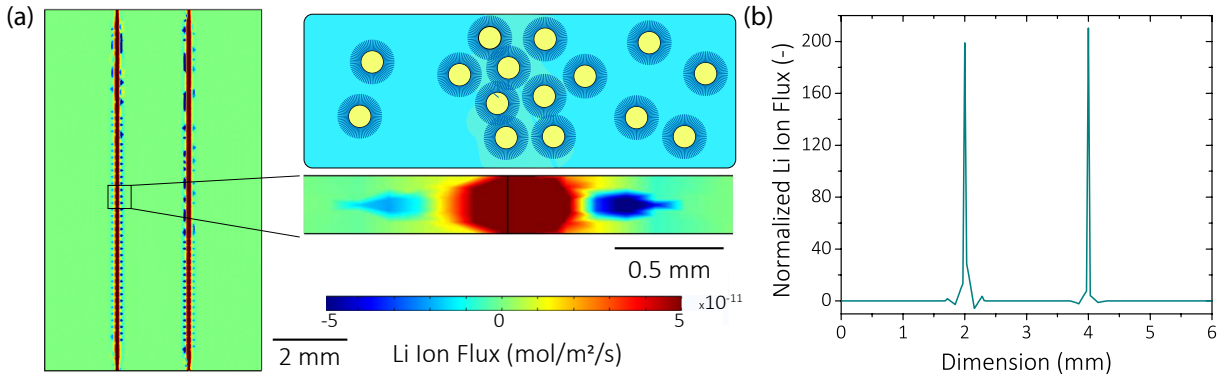

Figure 8.6: (a)Li ion flux distribution through a planar section of coextruded membrane. Flux at the interface along the transverse section is also shown. (b) Normalized Li ion flux across the width of the coextruded membrane studied using simulations. (c) Mechanical properties of single material and coextruded films.

system possibly restricts the polymer segmental motion lowering the interfacial conductivity. The model predicts that the interfacial conductivity in a 1 mm striped coextruded electrolyte is higher than the ionic conductivity of 25 wt.% and 75 wt.% system $<T_m$(Fig. 8.5d). The ionic conductivity of the interfacial layer for this configuration is slightly lower than the coextruded sample with smaller activation energies (Table 8.2). This suggests that the interfacial layer between the 25wt.% and 75wt.% sample possess an improved ion transport pathway in the co-extruded sample. Similar behavior is seen for the other co-extruded samples (Fig. 8.5e, 8.12c-d). Electrolytes with 1 mm stripe architectures show the highest interfacial conductivity and lower activation energies.

The impact of macro-interface on transport is further investigated using computational modeling. Steady state concentration flux across a domain containing three stripes 2 cm wide and 60 μm thick are evaluated (Top view seen in Fig. 8.6a). The ion transport properties of two stripes are kept equal to that obtained for 25 wt.% system while the center stripe is provided the ion transport properties of 75 wt.% system. It should be noted that the hybrid electrolytes have been modelled as a uniform phase in these simulations. A small current density is applied across the top and bottom surface of the

electrolyte domain. Steady state ion transport simulations show strong localization of lithium ion flux at the interfacial region between the two material systems (Fig. 8.6a). The cross-section across the thickness of the electrolyte at the interface highlights the lithium ion distribution at the interfacial region for the coextruded architectures. Normalized flux averaged across the entire length of the simulated domain show clear spikes in lithium ion flux at the interfacial region (Fig. 8.6b). Simulations show an enhancement factor of ≈200 in the ion flux at the interfacial regions. Figure 8.6c demonstrates how the mechanical properties of the electrolyte are altered with ceramic content and with co-extrusion. The mechanical properties appear to obey superposition. The single material 25 wt% ceramic:polymer electrolyte has the longest elongation at break (650%) and the 75 wt% ceramic:polymer solid electrolyte has the shortest elongation at break(50%). The co-extruded film which is composed of both 25 wt% and 75 wt% stripes falls in between the single-material electrolyte and breaks at 300%.

8.5 Conclusion

A novel manufacturing platform for the scalable production of hybrid solid electrolytes is demonstrated. Coating hybrid solid electrolytes with structural and compositional variation at roll-to-roll scales provides a pathway to engineering transport pathways on the fly. Herein, we demonstrate a novel architecture which introduces macro-interfaces into a polymer ceramic matrix. These interfaces demonstrate an increase in ion transport properties compared to single material films. Detailed analysis of impedance data and modeling studies provide phenomological insight into ion transport kinetics at these interfaces. Long term, control over ion transport properties and pathways are necessary to achieve uniform stripping and plating mechanisms with lithium metal anodes. This proof-of-concept study presents one potential manufacturing strategy to address this need. Achieving reliability in manufacturing is also identified as an important aspect to-

wards commercialization of solid state batteries.

8.6 Statistical Data

Table 8.3: Statistical data for 25 wt.% Sample. Temperature is in °C and conducitivity values are in S/cm

Temperature	Average	Std. Dev	Minimum	Maximum	Variance
25	1.21E-06	4.75E-07	6.65E-07	2.14E-06	2.26E-13
35	4.18E-06	2.14E-06	2.01E-06	9.18E-06	4.57E-12
45	1.94E-05	1.07E-05	9.44E-06	4.29E-05	1.16E-10
55	1.02E-04	5.45E-05	4.59E-05	2.18E-04	2.97E-09
65	3.40E-04	9.82E-05	1.28E-04	4.73E-04	9.64E-09
75	5.07E-04	9.59E-05	3.29E-04	6.10E-04	9.21E-09

Table 8.4: Statistical data for 75 wt.% Sample. Temperature is in °C and conductivity values are in S/cm

Temperature	Average	Std. Dev	Minimum	Maximum	Variance
25	2.01E-06	1.17E-06	2.96E-07	3.98E-06	1.37E-12
35	6.86E-06	3.90E-06	1.27E-06	1.35E-05	1.52E-11
45	2.46E-05	1.31E-05	5.06E-06	4.53E-05	1.71E-10
55	9.74E-05	4.45E-05	3.23E-05	1.58E-04	1.98E-09
65	2.17E-04	8.70E-05	7.56E-05	3.54E-04	7.57E-09
75	3.26E-04	1.44E-04	1.09E-04	6.18E-04	2.07E-08

Table 8.5: Statistical data for CoX_1mm Sample. Temperature is in °C and conductivity values are in S/cm

Temperature	Average	Std. Dev	Minimum	Maximum	Variance
25	1.10E-05	2.63E-06	6.99E-06	1.55E-05	6.92E-12
35	1.88E-05	4.10E-06	1.26E-05	2.62E-05	1.68E-11
45	5.80E-05	2.45E-05	4.58E-05	9.26E-05	6.00E-10
55	1.37E-04	3.43E-05	1.02E-04	2.02E-04	1.18E-09
65	2.16E-04	7.52E-05	6.58E-05	3.57E-04	5.65E-09
75	3.69E-04	7.87E-05	6.58E-05	3.57E-04	6.20E-09

Table 8.6: Statistical data for CoX_2mm Sample. Temperature is in °C and conductivity values are in S/cm

Temperature	Average	Std. Dev	Minimum	Maximum	Variance
25	9.64E-06	5.88E-06	1.82E-06	1.70E-05	3.46E-11
35	1.92E-05	1.03E-05	4.00E-06	3.48E-05	1.06E-10
45	5.12E-05	2.41E-05	2.13E-05	9.24E-05	5.82E-10
55	1.15E-04	4.00E-05	4.70E-05	1.66E-04	1.60E-09
65	2.74E-04	1.40E-04	1.47E-04	4.95E-04	1.95E-08
75	3.57E-04	1.60E-04	1.67E-04	5.01E-04	2.57E-08

Table 8.7: Statistical data for CoX_3mm Sample. Temperature is in °C and conductivity values are in S/cm

Temperature	Average	Std. Dev	Minimum	Maximum	Variance
25	2.90E-06	1.35E-06	9.17E-07	4.77E-06	1.83E-12
35	9.83E-06	3.42E-06	5.91E-06	1.45E-05	1.17E-11
45	3.50E-05	6.94E-06	2.53E-05	4.68E-05	4.82E-11
55	1.32E-04	3.26E-05	8.49E-05	1.76E-04	1.06E-09
65	3.85E-04	1.01E-04	1.88E-04	4.89E-04	1.03E-08
75	5.79E-04	1.72E-04	3.28E-04	1.01E-03	2.97E-08

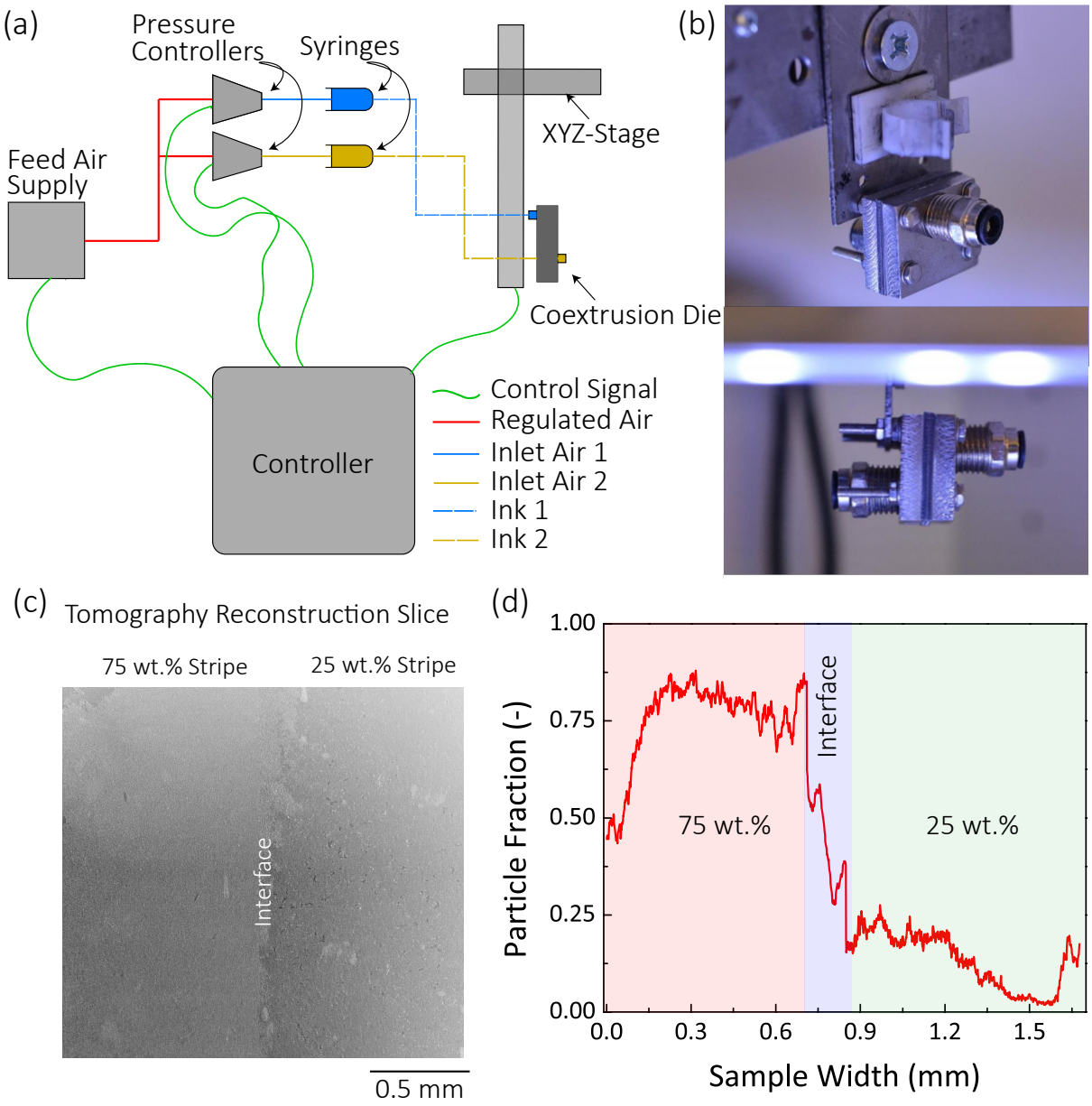

Figure 8.7: (a) Integrated setup schematic showing all the key components in the system. (b) Optical image of the coextrusion head. (c) Tomography reconstruction of coextruded membrane. (d) Ceramic fractions computed through a length of ≈ 200 μm and the entire thickness across the width of the imaged co-extrusion sample.

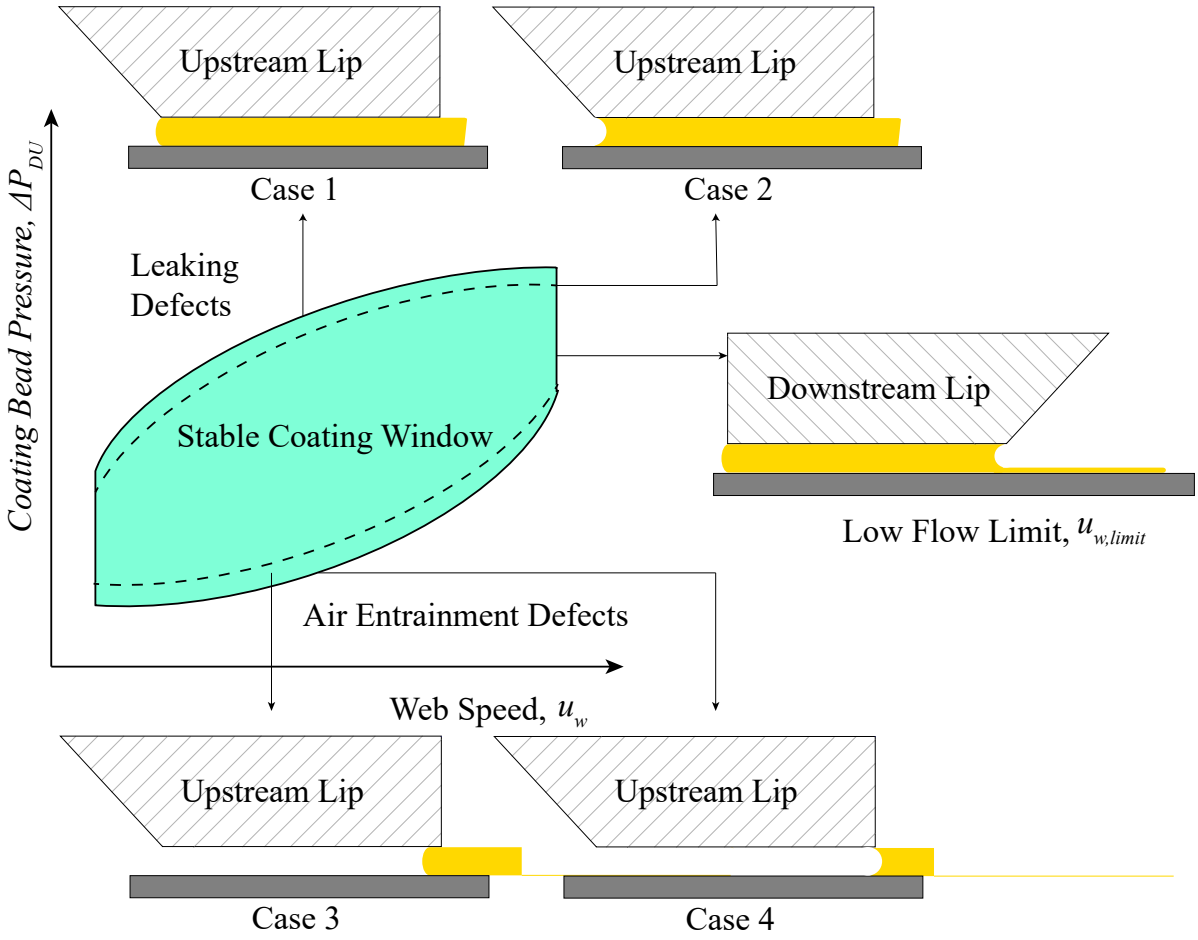

Figure 8.8: Schematic diagram showing characteristic coating defects observed in slot-die coating

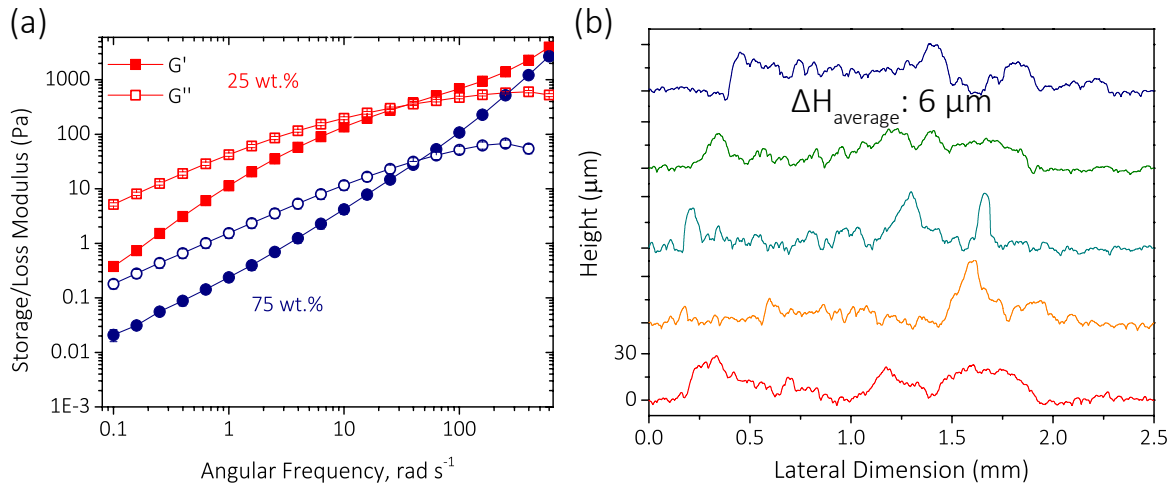

Figure 8.9: (a) Frequency shear for 25 wt.% and 75 wt.% LLZO-PEO system. P, S, and C represent polymer, salt and ceramic respectively. Rheology was measured for bare polymer ink, polymer-salt mixture and the composite ink.(b) Sample profilometry line-scans across the co-extruded membranes.

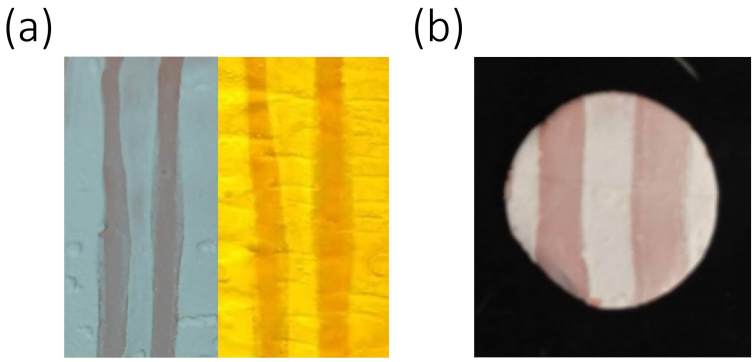

Figure 8.10: Effect of sample conditioning steps on coextruded architectures (a) Optical image of coextruded membranes before and after hot pressing (b) Optical image of coextruded membrane after thermal cycling.

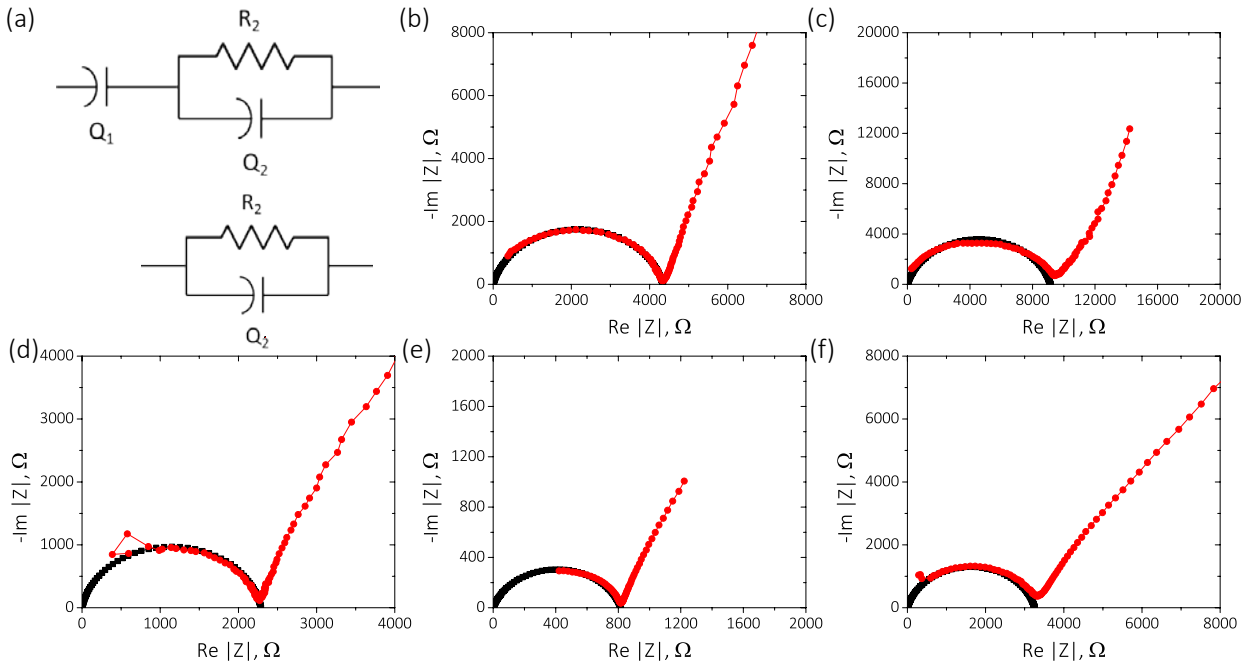

Figure 8.11: Equivalent circuit used for fitting the complete raw data and simulated circuit to extract the charge-transfer component from the nyquist plots (a) Raw data (red markers) and extracted data (black markers) used for DRT analysis for (b) 25 wt.%, (c) 75 wt.%, (d) CoX_1mm, (e) CoX_2mm and (f) CoX_3mm hybrid electrolytes.

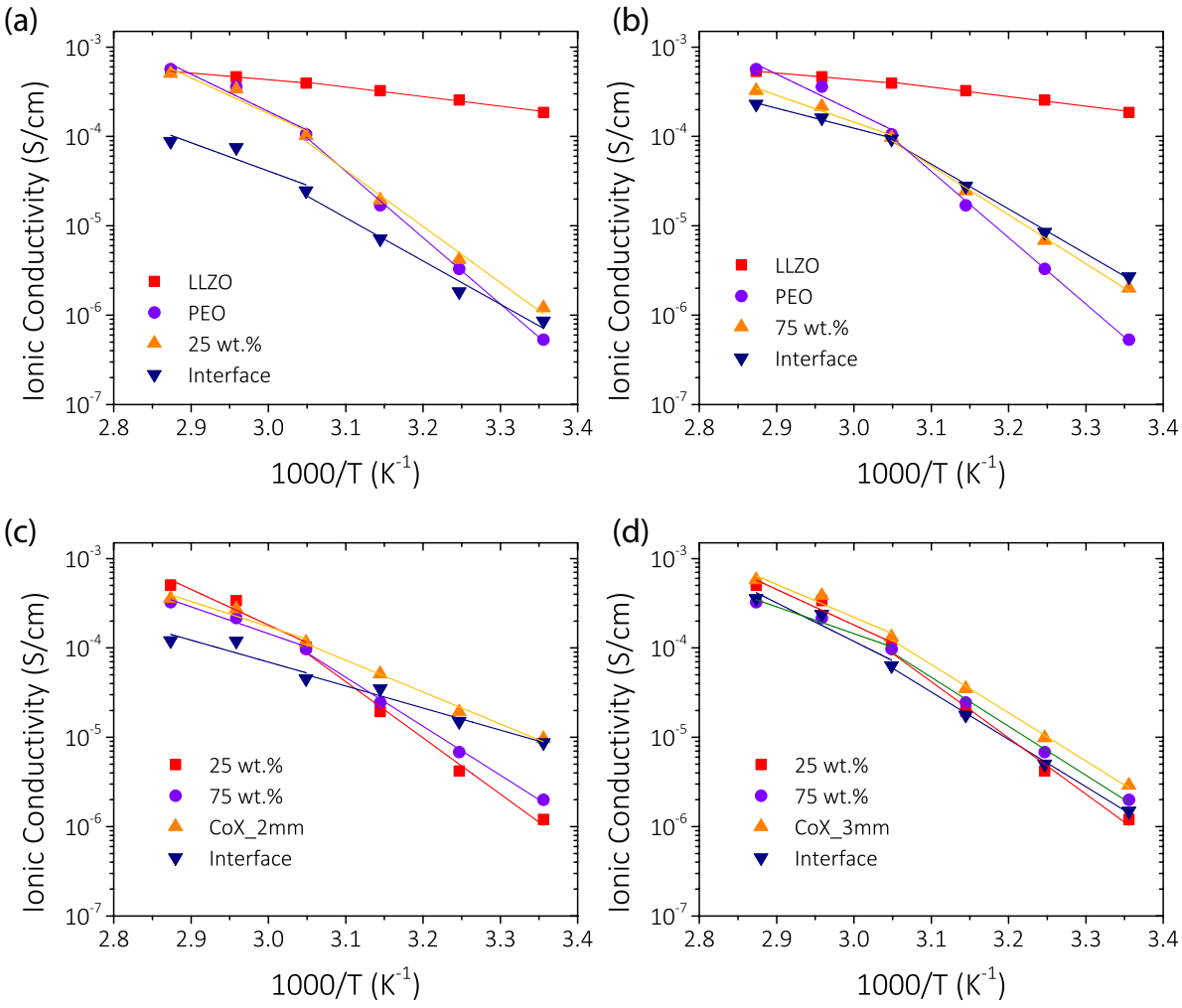

Figure 8.12: EMFT model results for 25 wt.% (a), 75 wt.% (b), CoX_2mm (c) and CoX_3mm(d) systems

Chapter 9

Conclusions

The primary aim of this work was to understand the role of processing and structure of solid electrolytes on ion transport behavior and chemo-mechanical degradation of solid-state batteries. The work compiled in this thesis illustrate the advantages and applicability of real and reciprocal space imaging techniques to assess these phenomena at buried solid|solid interfaces. In that regard, the results shown in Chapters 3, 4 represent some of the first reports on investigating the influence of the internal microstructure of a solid electrolyte on ion transport and failure characteristics. Microstructure of garnet solid electrolyte was controlled by modifying the processing conditions of the solid electrolyte. X-ray tomography was shown to be a powerful and versatile tool that can inform about sub-micron level microstructure within dense materials. The formation of isolated lithium agglomerates within the interior was identified as potentially a structurally driven phenomenon which is amplified when pore regions are connected within the electrolyte. Excess chemical potentials created within the interior of the electrolyte as a result of grain resistivity were postulated to lead to isolated lithium deposition. Solid electrolytes with connected pore regions were identified to promote dendrite formation and lower critical current densities. This work was extended by coupling Computational Fluid Dynamics modelling techniques with the measured experimental data. Garnet oxides sintered at lower temperatures had discrete pore structure with small feature sizes that led to homogeneous flux distributions within the sample. LLZO sintered at higher temperatures showed larger pore sizes with a connected pore network. These samples shower higher tortuosity as well as greater directional anisotropies. These could lead to development of large local concentration and polarization gradients that initiate and accelerate failures in these systems.

Another key challenge with solid state batteries is understanding and controlling electrodeposition and electrodissolution of the lithium metal anode. Historically, capturing Li metal anode dynamics was difficult due to the reactivity of the metal as well as low atomic number of Li making it fairly transparent to experimental probes. Chapter 5 details how careful experimental design coupled with machine learning and advanced image processing techniques enabled high resolution X-ray imaging of lithium metal in *in situ* conditions. This work was the first report that captured mesoscale electrode morphology transformations and enabled tracking of pores within lithium metal during electrochemical cycling. Heterogeneous interfacial kinetics were identified in lithium metal which were correlated with the presence of anisotropic microstructures within the solid electrolyte. The imaging resolution and contrast described here lays the ground work for future studies capable of resolving the role microstructure heterogeneities in lithium metal impact electrodeposition stability and rate performance. It is expected that this work will significantly impact subsequent anode studies in order to accurately characterize Li metal anodes and enable stable electrodeposition/dissolution for high power solid-state batteries.

Garnet oxides typically are stable against Li metal showing almost no interfacial decomposition products. In contrast, several other materials families (thiophosphates, NASICONs) show formation of a decomposed interphase against lithium metal. This interphase formation in sulfide solid electrolytes is typically ascribed as the cause for failure for sulfide solid electrolytes. Using sulfide solid electrolyte as a control material, the effect of interfacial chemistry and microstructure on the mechanical failure of LPS-based solid electrolytes is investigated using advanced multimodal characterization techniques (Chapter 7). Kinetically stable interphase and microstructural control is engineered by iodine doping, and milling and annealing respectively. *In situ* TEM results showed iodine migration to the Li metal surface and void formation at the LPS interface on electrochemical cycling. Iodine migration to the Li metal surface can stabilize the interphase

by decomposition of the SE to an ionically conducting interphase. Additionally, LiI can affords nm-scale intimate contact with Li metal resulting in improved electrochemical performance of the LiI containing materials. Material transformations during cycling are evaluated using *in situ* synchrotron X-ray tomography. A consistent failure mechanism across all materials is identified by tracking evolution of the crack features in the *in situ* tomography data. Mechanical failure is initiated with edge cracking at the interface and subsequent lateral crack growth through the surface. The onset of failure at the Li|LPS interface is consistent with the void formation observed in the TEM studies. *In situ* TEM and XRT corroborates the failure mechanism across cascading length scales. Multimodal characterization offers a unique insight into failure mechanisms of solid-state batteries. This work provided significantly new insight into fracture onset and growth mechanisms in sulfide solid electrolytes. These results are anticipated to inform future work on processing and operation of next generation solid-state batteries. While the decomposition product (e.g. interphase) between the solid electrolyte and electrode does impact failure, this work highlights the significance of microstructural heterogeneities on failure. Dense solid electrolytes with limited microstructure are imperative for high current density operation of all solid state batteries.

On the cathode side, chemo-mechanical degradation owing to active material volume changes during cycling offer a significant challenge to realization of high energy density solid-state batteries. chemo-mechanics in Li|LLZO|LFP full cells were investigated using operando synchrotron energy dispersive X-ray diffraction and in-situ tomography (Chapter 6). Chemo-mechanical response of the electrolyte (interfacial and sub-surface) are quantitatively ascertained during battery operation. Lattice strain in the electrolyte at the cathode interface is tracked during cycling. Results indicate strained interfaces that can arise due to chemo-mechanical transformations like cracking or filament formation. Delamination effects are observed in cathode sections during operation which successively deteriorate on cycling. These results suggest that the electrode|electrolyte

interfaces are pivotal in dictating the chemo-mechanical response of the all solid-state batteries. Tailoring compliant interfaces is a potentially rewarding avenue towards designing all solid-state batteries with robust chemo-mechanical performance.

Finally, a novel manufacturing platform for the scalable production of hybrid solid electrolytes is demonstrated (Chapter 8). Coating hybrid solid electrolytes with structural and compositional variation at roll-to-roll scales provides a pathway to engineering transport pathways on the fly. We demonstrated a novel architecture which introduces macro-interfaces into a polymer ceramic matrix. These interfaces demonstrated an increase in ion transport properties compared to single material films. Long term, control over ion transport properties and pathways are necessary to achieve uniform stripping and plating mechanisms with lithium metal anodes. Achieving reliability in manufacturing is also identified as an important aspect towards commercialization of solid state batteries.

Next generation energy storage systems will likely use solid state electrolytes to achieve high energy and power densities. The underlying hypothesis of this work was that the knowledge of structure-function dependence in solid electrolytes can be leveraged towards engineering of high performing systems. Using real and reciprocal space imaging: influence of microstructure and interphase chemistry on electrochemical performance of two typical solid electrolyte materials was delineated. These results bolster the need for control over solid electrolyte microstructure during processing and provide design guidelines for realizing high energy density solid-state systems. Subsequently, a scalable production method that can tailor the structure during processing for manufacturing high performing solid electrolytes is demonstrated. The overarching goal of the proposed research was aimed at understanding the fundamental processing-structure-function correlations in solid state electrolytes. The results of these studies are expected to inform rational design of next generation of solid state battery systems. Further, the research included here will contribute towards enabling scalable production of high performance

solid electrolytes and contribute towards commercialization of these systems.

Appendix A

All Data Analysis Codes

1.1 Tomography Reconstruction

```
Data Reconstruction Code for XTM Data

Author: Marm Dixit

Inks and Interfaces Laboratory, Vanderbilt University

May 2017

Developed based on the code provided by APS
```

The following set of commands imports all the pertinent python packages to run the code

[2]:
```
import tomopy
import dxchange
from tomopy.recon.rotation import write_center
from tomopy.recon.algorithm import recon
from tomopy import minus_log
import os, h5py, glob, fnmatch
import numpy as np
import matplotlib.pyplot as plt
from scipy import misc
import time
```

The following are the input parameters to various functions being called in the code. The descriptions of each variable is given with them

[3]:
```
zinger_level = 500 #Expected difference value between outlier value and␣
 ↪the median value of the array
```

```
zinger_level_w = 1000 #Expected difference value between outlier value␣
 ↪and the median value of the array
eng = 20.2 #Energy of the incident wave in KeV
pxl = 0.65e-4 #Detector size in pixel
rat = 1e-03 #Regularization parameter, used as a threshold to determine␣
 ↪the contrast between the sample and the background matris
imgPerSec = 1201 # Constants of experiment, to be used while slicing the␣
 ↪matrix into smaller chunks
secID = 1 # Constants of experiment, to be used while slicing the matrix␣
 ↪into smaller chunks
z=6 #Propogation distance of the wavefront in cm
center_shift = 200 #The absolute difference between the center of the X␣
 ↪range to be evalutated to determine the center, COARSE
center_shift_w = 5#The absolute difference between the center of the X␣
 ↪range to be evalutated to determine the center, COARSE
```

Input the file name of the HDF file with the full file path

[4]:
```
filename = 'Exp019_7.5wtPercent_pipette_r1_YPos17.
 ↪098mm_FriMar24_18_37_46_2017_edge_10x_60mm_30.
 ↪0msecExpTime_3DegPerSec_Rolling_20umLuAG_1mmC_2.657mrad_USArm1.
 ↪35_monoY_-0.399_AHutch/proj_0019.hdf'
```

h5py is the package that reads the HDF file. This following function reads the HDF file into a variable 'f'

[5]:
```
f = h5py.File(filename, 'r')
```

The respective data sets are extracted from the full data

[6]:
```
data = f['exchange/data']

white = f['exchange/data_white']

dark = f['exchange/data_dark']
```

This is the number of values in the theta-range

[7]:
```
numProj = (data.shape)[0]

numProj
```

[7]: 1201

This is the number of values in the Z-direction

[12]:
```
numSlices = (data.shape)[1]
```

[12]: 1500

This is the number of values in the r-direction

[12]:
```
imgWidth = (data.shape)[2]

imgWidth
```

[12]: 2560

Margin_slices is used to discard the defined from the top and the bottom of the stack for full reconstruction

[142]:
```
margin_slices = 100
```

This defines a linear [0-180] degree range with as many points as in data set

[143]:
```
theta = np.linspace(0,np.pi,num=numProj+1)
```

The following set of codes need to be modified to ensure that sliceStart and sliceEnd correspond to the top and bottom of the stack to be studied

[144]:
```
#n=8
#sliceStart = margin_slices + ((n-1)*margin_slices)
#sliceEnd = margin_slices +((n)*margin_slices)
sliceStart = 700
sliceEnd = sliceStart+100
```

The following set of commands extracts the respective data sets for the specified stack range from the full data

[145]:
```
data_reduced = data[(secID-1)*imgPerSec:secID*imgPerSec,sliceStart:
↪sliceEnd,:]
white_reduced = white[1:9,sliceStart:sliceEnd,:]
dark_reduced = dark[1:9,sliceStart:sliceEnd,:]
```

The following set of commands remove the outlier elements.

tomopy.misc.corr.remove_outlier(arr, dif, size=3, axis=0, ncore=None, out=None)[source]

Remove high intensity bright spots from a N-dimensional array by chunking along the specified dimension, and performing (N-1)-dimensional median filtering along the other dimensions. Parameters:

```
arr (ndarray) : Input array.
dif (float) : Expected difference value between outlier value and
the median value of the array.
size (int) : Size of the median filter.
axis (int, optional) : Axis along which to chunk.
ncore (int, optional) : Number of cores that will be assigned to jobs.
out (ndarray, optional) : Output array for result. If same as arr,
process will be done in-place.
```

[146]:
```
data_reduced_misc_corr = tomopy.misc.corr.
 ↪remove_outlier(data_reduced,zinger_level,size=15,axis=0)
white_reduced_misc_corr = tomopy.misc.corr.
 ↪remove_outlier(white_reduced,zinger_level,size=15,axis=0)
```

The following command attempts to retrieve the sample phase by adjusting the contrast of the sample based on the specified parameters.

tomopy.prep.phase.retrieve_phase(tomo, pixel_size=0.0001, dist=50, energy=20, alpha=0.001, pad=True, ncore=None, nchunk=None)[source]

Perform single-step phase retrieval from phase-contrast measurements [C6]. Parameters:

```
tomo (ndarray) : 3D tomographic data.
pixel_size (float, optional) : Detector pixel size in cm.
dist (float, optional) : Propagation distance of the wavefront in cm.
energy (float, optional) : Energy of incident wave in keV.
alpha (float, optional) : Regularization parameter.
pad (bool, optional) : If True, extend the size of the projections
by padding with zeros.
ncore (int, optional) : Number of cores that will be assigned to jobs.
nchunk (int, optional) : Chunk size for each core.
```

[147]:
```
data_reduced = tomopy.prep.phase.
 ↪retrieve_phase(data_reduced_misc_corr,pixel_size=pxl,dist=z,
energy=eng,alpha=rat,pad=True)
```

The following commands attempt to remove the stripes from the data.

Remove horizontal stripes from sinogram using the Fourier-Wavelet (FW) based method [C4].

tomopy.prep.stripe.remove_stripe_fw(tomo, level, wname, sigma, pad)

```
tomo (ndarray) : 3D tomographic data.
level (int, optional) : Number of discrete wavelet transform levels.
wname (str, optional) : Type of the wavelet filter. "haar", "db5", "sym5", etc.
sigma (float, optional) : Damping parameter in Fourier space.
pad (bool, optional) : If True, extend the size of the sinogram
by padding with zeros.
```

Remove horizontal stripes from sinogram using Titarenko's approach [C8].

tomopy.prep.stripe.remove_stripe_ti(tomo, alpha)

```
tomo (ndarray) : 3D tomographic data.
alpha (int, optional) : Damping factor.
```

Normalize raw projection data using a smoothing filter approach.

tomopy.prep.stripe.remove_stripe_sf(tomo, size)

```
tomo (ndarray) : 3D tomographic data.
size (int, optional) : Size of the smoothing filter.
```

[148]:
```
#data_reduced = tomopy.prep.stripe.remove_stripe_ti(data_reduced,alpha=5)
data_reduced = tomopy.prep.stripe.remove_stripe_ti(-1.
 ↪0*data_reduced,alpha=1.0)
#data_reduced = tomopy.prep.stripe.
 ↪remove_stripe_fw(data_reduced,level=15,wname='sym16',sigma=1,pad=True)
#data_reduced = tomopy.prep.stripe.remove_stripe_sf(data_reduced,size =␣
 ↪11)
```

The following command normalizes the 3D tomography data

tomopy.prep.normalize.normalize_bg(tomo, air=1)

```
tomo (ndarray) : 3D tomographic data.
air (int, optional) : Number of pixels at each boundary to calculate
the scaling factor.
```

[149]:
```
#data_reduced = tomopy.prep.normalize.
 ↪normalize(data_reduced,white_reduced_misc_corr,dark_reduced,cutoff=1.
 ↪1)
data_reduced_final = tomopy.prep.normalize.
 ↪normalize_bg(data_reduced,air=15)
```

The following command writes a specified slice at a range of centers as specified. A coarse and a fine code are written here, to be evaluated for each new case. Helps finding the rotation center manually by visual inspection of images reconstructed with a set of different centers.The output images are put into a specified folder and are named by the center position corresponding to the image.

tomopy.recon.rotation.write_center(tomo, theta, dpath=u'tmp/center', cen_range=None, ind=None, mask=False, ratio=1.0, sinogram_order=False)

```
tomo (ndarray) : 3D tomographic data.
theta (array) : Projection angles in radian.
dpath (str, optional) : Folder name to save output images.
cen_range (list, optional) : [start, end, step] Range of center values.
ind (int, optional) : Index of the slice to be used for reconstruction.
mask (bool, optional) : If True, apply a circular mask to the
reconstructed image to limit the analysis into a circular region.
ratio (float, optional) : The ratio of the radius of the circular mask
to the edge of the reconstructed image.
sinogram_order (bool, optional) : Determins whether data is a stack of
sinograms (True, y-axis first axis) or a stack of radiographs
```

(False, theta first axis).

[150]:
```
#write_center(data_reduced_final[:,5:7,:], theta,␣
 ↪dpath='Exp32DiffernetCenterImages/',
#           cen_range=(data_reduced.shape[2]/2-center_shift,data_reduced.
 ↪shape[2]/2+center_shift,5))
```

[151]:
```
#write_center(data_reduced_final[:,9:11,:], theta,␣
 ↪dpath='Exp32DiffernetCenterImages/Finer/',
#cen_range=(1250-center_shift_w,1250+center_shift_w,1))
```

Center determined from the permutations above

[152]:
```
rot_center = 1251
```

The following command computes the minus log of a given array.

tomopy.prep.normalize.minus_log(arr, ncore=None, out=None)

arr (ndarray) : 3D stack of projections.

ncore (int, optional) : Number of cores that will be assigned to jobs.

out (ndarray, optional) : Output array for result. If same as arr,

process will be done in-place.

[153]:
```
data_reduced_lognormalized = data = tomopy.prep.normalize.
 ↪minus_log(data_reduced_final)
```

The following command is the reconstruction command.

tomopy.recon.algorithm.recon(tomo, theta, center, algorithm)

tomo (ndarray) : 3D tomographic data.

theta (array) : Projection angles in radian.

center (array, optional) : Location of rotation axis.

algorithm (name) : One of the reconstruction algorithm, typically 'gridrec'

[154]:
```
#options = {'proj_type':'line','method':'FBP'}
#data_recon =␣
↪recon(data_reduced_lognormalized,theta,center=rot_center,algorithm=tomopy.
↪astra,options=options)
data_recon =␣
↪recon(data_reduced_lognormalized,theta,center=rot_center,algorithm='gridrec')
```

The following command attempts to remove the ring artefacts from the reconstructed data

tomopy.misc.corr.remove_ring(rec, center_x, center_y, thresh=300.0, thresh_max, thresh_min=, theta_min, rwidth)

rec : Array of reconstruction data

center_x (float, optional) : abscissa location of center of rotation

center_y (float, optional) : ordinate location of center of rotation

thresh (float, optional) : maximum value of an offset due to a ring artifact

thresh_max (float, optional) : max value for portion of image to filter

thresh_min (float, optional) : min value for portion of image to filer

theta_min (int, optional) : minimum angle in degrees (int) to be considered ring artifact

rwidth (int, optional) : Maximum width of the rings to be filtered in pixels

[155]:
```
recon_ring = tomopy.remove_ring(data_recon,(data_recon.shape)[1]/
↪2,(data_recon.shape)[2]/2,thresh = 3000,thresh_max = 3000, thresh_min␣
↪= -100, theta_min =40,rwidth=100)
```

The following command sets up a circular mask around the reconstructed object

tomopy.misc.corr.circ_mask(arr, axis, ratio=1, val=0.0, ncore=None)

```
arr (ndarray) : Arbitrary 3D array.

axis (int) : Axis along which mask will be performed.

ratio (int, optional) : Ratio of the maskâ€™s diameter in pixels

to the smallest edge size along given axis.
```

[156]:
```
data_recon_mask = tomopy.circ_mask(recon_ring,axis = 0, ratio = 1.0)

#data_recon_mask = tomopy.circ_mask(data_recon,axis = 0, ratio = 1.0)
```

The following command is used to visualize the reconstructed data inline

[157]:
```
plt.imshow(data_recon_mask[1,:,:], cmap='Greys_r',extent=[0,700,0,1],␣
↪aspect='auto')

plt.show()
```

The following command writes the reconstruced stack as a series of TIFF Images. fname is the full path where the image is to be saved.

[158]:
```
dxchange.write_tiff_stack(recon_ring,fname = 'Exp26_12%_ring_correct/
↪700-800')
```

1.2 Machine Learning Training

[ ]:
```
# This mounts the folder where raw data is present.
from google.colab import drive
drive.mount('/gdrive')
%cd /gdrive
```

[ ]:
```
# This installs the necessary segmentation models
!pip install segmentation-models
```

[ ]:
```
# This is also a repository of segmentation tools that are used in the␣
  ↪code.
!pip install -U git+https://github.com/albu/albumentations --no-cache-dir
```

[ ]:
```
# Imports the required packages for the code
import cv2
import os
import glob
import zipfile
import functools


import numpy as np
import matplotlib.pyplot as plt
import matplotlib as mpl
mpl.rcParams['axes.grid'] = False
mpl.rcParams['figure.figsize'] = (12,12)


from sklearn.model_selection import train_test_split
import matplotlib.image as mpimg
import pandas as pd
```

```
from PIL import Image
from keras.preprocessing import image


import tensorflow as tf
#import tensorflow.contrib as tfcontrib
from tensorflow.python.keras import layers
from tensorflow.python.keras import losses
from tensorflow.python.keras import models
from tensorflow.python.keras import backend as K
import keras



import albumentations as A
import segmentation_models as sm
```

[ ]:
```
# Setting the directories for raw and processed data
DATA_PATH = "/gdrive/My Drive/TrainingData/LiTraining"
FRAME_PATH = "/gdrive/My Drive/TrainingData/LiTraining/Frame/Train/"
MASK_PATH = "/gdrive/My Drive/TrainingData/LiTraining/Label/Train_Edge"


FRAME_VAL_PATH = "/gdrive/My Drive/TrainingData/LiTraining/Frame/Val/"
MASK_VAL_PATH = "/gdrive/My Drive/TrainingData/LiTraining/Label/Val_Edge/
  ↪"
TEST_PATH = "/gdrive/My Drive/TrainingData/LiTraining/Frame/Test/"
save_model_path = os.path.join(DATA_PATH,"Li_uNET.hdf5")
final_model_path = os.path.join(DATA_PATH,"Li_final_uNET.hdf5")
```

[ ]:
```
# Reading list name of all the files in the raw data directory
nFrameTrain = len(os.listdir(FRAME_PATH))
nMaskTrain = len(os.listdir(MASK_PATH))
nFrameVal = len(os.listdir(FRAME_VAL_PATH))
nMaskVal = len(os.listdir(MASK_VAL_PATH))
```

[ ]:
```
# Making variables containing full file paths
all_test = os.listdir(TEST_PATH)
all_test = [TEST_PATH + s for s in all_test]
all_train = os.listdir(FRAME_PATH)
all_train = [FRAME_PATH + s for s in all_train]
all_mask = os.listdir(MASK_PATH)
all_mask = [MASK_PATH + s for s in all_mask]
all_fVal = os.listdir(FRAME_VAL_PATH)
all_fVal = [FRAME_VAL_PATH + s for s in all_fVal]
all_mVal = os.listdir(MASK_VAL_PATH)
all_mVal = [MASK_VAL_PATH + s for s in all_mVal]
```

1.2.0.1 Data Loader and Utility Functions

[ ]:
```
# helper function for data visualization
def visualize(**images):
    """PLot images in one row."""
    n = len(images)
    plt.figure(figsize=(16, 5))
    for i, (name, image) in enumerate(images.items()):
        plt.subplot(1, n, i + 1)
        plt.xticks([])
```

```
        plt.yticks([])
        plt.title(' '.join(name.split('_')).title())
        plt.imshow(image)
    plt.show()


# helper function for data visualization
def denormalize(x):
    """Scale image to range 0..1 for correct plot"""
    x_max = np.percentile(x, 98)
    x_min = np.percentile(x, 2)
    x = (x - x_min) / (x_max - x_min)
    x = x.clip(0, 1)
    return x



# classes for data loading and preprocessing
class Dataset:
    """CamVid Dataset. Read images, apply augmentation and preprocessing␣
 ↪transformations.

    Args:
        images_dir (str): path to images folder
        masks_dir (str): path to segmentation masks folder
        class_values (list): values of classes to extract from␣
 ↪segmentation mask
```

```
        augmentation (albumentations.Compose): data transfromation␣
↪pipeline
            (e.g. flip, scale, etc.)
        preprocessing (albumentations.Compose): data preprocessing
            (e.g. noralization, shape manipulation, etc.)

    """

    CLASSES = ['lithium', 'pore']

    def __init__(
            self,
            images_dir,
            masks_dir,
            classes=None,
            augmentation=None,
            preprocessing=None,
    ):
        self.ids = os.listdir(images_dir)
        self.images_fps = [os.path.join(images_dir, image_id) for␣
↪image_id in self.ids]
        self.masks_fps = [os.path.join(masks_dir, image_id) for image_id␣
↪in self.ids]

        # convert str names to class values on masks
```

```
        self.class_values = [self.CLASSES.index(cls.lower()) for cls in␣
↪classes]

        self.augmentation = augmentation
        self.preprocessing = preprocessing

    def __getitem__(self, i):

        # read data
        image = cv2.imread(self.images_fps[i])
        image = cv2.cvtColor(image, cv2.COLOR_BGR2RGB)
        mask = cv2.imread(self.masks_fps[i], 0)

        # extract certain classes from mask (e.g. cars)
        masks = [(mask == v) for v in self.class_values]
        mask = np.stack(masks, axis=-1).astype('float')

        # add background if mask is not binary
        if mask.shape[-1] != 1:
            background = 1 - mask.sum(axis=-1, keepdims=True)
            mask = np.concatenate((mask, background), axis=-1)

        # apply augmentations
        if self.augmentation:
            sample = self.augmentation(image=image, mask=mask)
            image, mask = sample['image'], sample['mask']
```

```
        # apply preprocessing
        if self.preprocessing:
            sample = self.preprocessing(image=image, mask=mask)
            image, mask = sample['image'], sample['mask']

        return image, mask

    def __len__(self):
        return len(self.ids)


class Dataloder(keras.utils.Sequence):
    """Load data from dataset and form batches

    Args:
        dataset: instance of Dataset class for image loading and␣
 ↪preprocessing.
        batch_size: Integet number of images in batch.
        shuffle: Boolean, if `True` shuffle image indexes each epoch.
    """

    def __init__(self, dataset, batch_size=1, shuffle=False):
        self.dataset = dataset
        self.batch_size = batch_size
        self.shuffle = shuffle
```

```
        self.indexes = np.arange(len(dataset))

        self.on_epoch_end()

    def __getitem__(self, i):

        # collect batch data
        start = i * self.batch_size
        stop = (i + 1) * self.batch_size
        data = []
        for j in range(start, stop):
            data.append(self.dataset[j])

        # transpose list of lists
        batch = [np.stack(samples, axis=0) for samples in zip(*data)]

        return batch

    def __len__(self):
        """Denotes the number of batches per epoch"""
        return len(self.indexes) // self.batch_size

    def on_epoch_end(self):
        """Callback function to shuffle indexes each epoch"""
        if self.shuffle:
            self.indexes = np.random.permutation(self.indexes)
```

[ ]:
```
dataset = Dataset(FRAME_PATH, MASK_PATH, classes=['lithium','pore'])


imageX, mask = dataset[170] # get some sample
visualize(
    image=imageX,
    lithium_mask=mask[..., 0].squeeze(),
    pore_mask=mask[..., 1].squeeze(),
)
```

1.2.0.2 Augmentation

[ ]:
```
def round_clip_0_1(x, **kwargs):
    return x.round().clip(0, 1)


# define heavy augmentations
def get_training_augmentation():
    train_transform = [


        A.HorizontalFlip(p=0.5),


        A.ShiftScaleRotate(scale_limit=0.5, rotate_limit=0,␣
↪shift_limit=0.1, p=1, border_mode=0),


        A.PadIfNeeded(min_height=64, min_width=192, always_apply=True,␣
↪border_mode=0),
        A.RandomCrop(height=64, width=192, always_apply=True),


        A.IAAAdditiveGaussianNoise(p=0.2),
```

```
        A.IAAPerspective(p=0.5),

        A.OneOf(
            [
                A.CLAHE(p=1),
                A.RandomBrightness(p=1),
                A.RandomGamma(p=1),
            ],
            p=0.9,
        ),

        A.OneOf(
            [
                A.IAASharpen(p=1),
                A.Blur(blur_limit=3, p=1),
                A.MotionBlur(blur_limit=3, p=1),
            ],
            p=0.9,
        ),

        A.OneOf(
            [
                A.RandomContrast(p=1),
                A.HueSaturationValue(p=1),
            ],
            p=0.9,
```

```
        ),
        A.Lambda(mask=round_clip_0_1)
    ]
    return A.Compose(train_transform)


def get_validation_augmentation():
    """Add paddings to make image shape divisible by 32"""
    test_transform = [
        A.PadIfNeeded(min_height=64, min_width=192, always_apply=True,␣
 ↪border_mode=0),
        A.RandomCrop(height=64, width=192, always_apply=True)
    ]
    return A.Compose(test_transform)

def get_preprocessing(preprocessing_fn):
    """Construct preprocessing transform

    Args:
        preprocessing_fn (callbale): data normalization function
            (can be specific for each pretrained neural network)
    Return:
        transform: albumentations.Compose

    """
```

```
    _transform = [
        A.Lambda(image=preprocessing_fn),
    ]
    return A.Compose(_transform)
```

[ ]:
```
dataset = Dataset(FRAME_PATH, MASK_PATH, classes=['lithium','pore'],␣
 ↪augmentation=get_training_augmentation())


imageX, mask = dataset[230] # get some sample
visualize(
    image=imageX,
    pore_mask=mask[..., 0].squeeze(),
    lithium_mask=mask[..., 1].squeeze(),
)
```

1.2.0.3 Segmentation Model Training

[ ]:
```
BACKBONE = 'resnet34'
BATCH_SIZE = 10
CLASSES = ['lithium','pore']
LR = 0.0001
EPOCHS = 500


preprocess_input = sm.get_preprocessing(BACKBONE)
#create model
model = sm.Unet(BACKBONE, classes=n_classes, activation=activation)
```

[ ]:
```
# define network parameters
n_classes = 1 if len(CLASSES) == 1 else (len(CLASSES) + 1)  # case for␣
 ↪binary and multiclass segmentation
activation = 'sigmoid' if n_classes == 1 else 'softmax'


#create model
model = sm.Unet(BACKBONE, classes=n_classes, activation=activation)
```

[ ]:
```
print(model.summary())
```

[ ]:
```
# define optomizer
optim = keras.optimizers.Adam(LR)


# Segmentation models losses can be combined together by '+' and scaled␣
 ↪by integer or float factor
# set class weights for dice_loss (car: 1.; pedestrian: 2.; background:␣
 ↪0.5;)
dice_loss = sm.losses.DiceLoss(class_weights=np.array([1,1,1]))
focal_loss = sm.losses.BinaryFocalLoss() if n_classes == 1 else sm.
 ↪losses.CategoricalFocalLoss()
total_loss = dice_loss + (1 * focal_loss)


# actulally total_loss can be imported directly from library, above␣
 ↪example just show you how to manipulate with losses
# total_loss = sm.losses.binary_focal_dice_loss # or sm.losses.
 ↪categorical_focal_dice_loss
```

```
metrics = [sm.metrics.IOUScore(threshold=0.5), sm.metrics.
  ↪FScore(threshold=0.5)]


# compile keras model with defined optimozer, loss and metrics
model.compile(optim, total_loss, metrics)
```

[ ]:
```
# This code is for visualization of the CNN
keras.utils.vis_utils.plot_model(model, to_file='/gdrive/My Drive/
  ↪TrainingData/LiTraining/model_plot.png', show_shapes=True,␣
  ↪show_layer_names=True)
```

[ ]:
```
# Dataset for train images
train_dataset = Dataset(
    FRAME_PATH,
    MASK_PATH,
    classes=CLASSES,
    augmentation=get_training_augmentation(),
    preprocessing=get_preprocessing(preprocess_input),
)


# Dataset for validation images
valid_dataset = Dataset(
    FRAME_VAL_PATH,
    MASK_VAL_PATH,
    classes=CLASSES,
    augmentation=get_validation_augmentation(),
    preprocessing=get_preprocessing(preprocess_input),
)
```

```
train_dataloader = Dataloder(train_dataset, batch_size=BATCH_SIZE,␣
 ↪shuffle=True)
valid_dataloader = Dataloder(valid_dataset, batch_size=1, shuffle=False)

# check shapes for errors
assert train_dataloader[0][0].shape == (BATCH_SIZE, 64, 192, 3)
assert valid_dataloader[0][1].shape == (1, 64, 192, n_classes)

# define callbacks for learning rate scheduling and best checkpoints␣
 ↪saving
callbacks = [
    keras.callbacks.ModelCheckpoint(filepath=save_model_path,␣
 ↪save_weights_only=True, save_best_only=True, mode='min'),
    keras.callbacks.ReduceLROnPlateau(),
]

cp = tf.keras.callbacks.ModelCheckpoint(filepath=save_model_path,␣
 ↪save_weights_only=True, save_best_only=True, verbose=1)
```

[ ]:
```
# train model
history = model.fit_generator(
    train_dataloader,
    steps_per_epoch=len(train_dataloader),
    epochs=EPOCHS,
    callbacks=callbacks,
    validation_data=valid_dataloader,
```

```
    validation_steps=len(valid_dataloader),
)
```

[ ]:
```
## Plot training & validation accuracy values
plt.subplot(3,1,1)
plt.plot(history.history['f1-score'])
plt.plot(history.history['val_f1-score'])
plt.title('f1-score')
plt.ylabel('f1-score')
plt.xlabel('Epoch')
plt.legend(['Train', 'Test'], loc='upper left')


plt.subplot(3,1,2)
plt.plot(history.history['iou_score'])
plt.plot(history.history['val_iou_score'])
plt.title('IoU Score')
plt.ylabel('IoU Score')
plt.xlabel('Epoch')
plt.legend(['Train', 'Test'], loc='upper left')
plt.savefig(os.path.join(DATA_PATH,'f1_score.jpg'))


plt.subplot(3,1,3)
plt.plot(history.history['loss'])
plt.plot(history.history['val_loss'])
plt.title('Loss')
plt.ylabel('Loss')
plt.xlabel('Epoch')
```

```
plt.legend(['Train', 'Test'], loc='upper left')
plt.savefig(os.path.join(DATA_PATH,'f1_score.jpg'))
plt.savefig(os.path.join(DATA_PATH,'f1_score.jpg'))
#plt.show()
```

[ ]:
```
batch_holder = np.zeros((10 ,64,192, 3))


for i,img in enumerate(os.listdir(TEST_PATH)):
  img = image.load_img(os.path.join(TEST_PATH,img), target_size=(64,192))
  batch_holder[i, :] = img
```

[ ]:
```
model.load_weights(save_model_path)
#result= np.zeros((10 ,64,192, 3))
#result=model.predict(batch_holder)
```

[ ]:
```
img = np.expand_dims(img,axis=0)
pr_mask = model.predict(img)
```

[ ]:
```
plt.imshow(pr_mask[0,:])
```

[ ]:
```

```

1.3 Machine Learning Segmentation

[ ]:
```
# This mounts the folder where raw data is present.

from google.colab import drive

drive.mount('/gdrive')

%cd /gdrive
```

[ ]:
```
# This installs the necessary segmentation models

!pip install segmentation-models
```

[ ]:
```
# Imports the required packages for the code

import time

import cv2

import os

import glob

import zipfile

import functools


import numpy as np

import matplotlib.pyplot as plt

import matplotlib as mpl

mpl.rcParams['axes.grid'] = False

mpl.rcParams['figure.figsize'] = (12,12)


from sklearn.model_selection import train_test_split

import matplotlib.image as mpimg

import pandas as pd

from PIL import Image

from keras.preprocessing import image
```

```
import tensorflow as tf
#import tensorflow.contrib as tfcontrib
from tensorflow.python.keras import layers
from tensorflow.python.keras import losses
from tensorflow.python.keras import models
from tensorflow.python.keras import backend as K
import keras



import albumentations as A
import segmentation_models as sm
```

[ ]:
```
# Setting the directories for raw and processed data, as well as the␣
  ↪saved model
DATA_PATH = "/gdrive/My Drive/TrainingData/LiTraining"
Step0_PATH = "/gdrive/My Drive/TrainingData/NetworkData/Step0Top/Data/"
Step1_PATH = "/gdrive/My Drive/TrainingData/NetworkData/Step1Top/Data/"
Step2_PATH = "/gdrive/My Drive/TrainingData/NetworkData/Step2Top/Data/"
Step3_PATH = "/gdrive/My Drive/TrainingData/NetworkData/Step3Top/Data/"
Step6_PATH = "/gdrive/My Drive/TrainingData/NetworkData/Step6Top/Data/"


L_Step0_PATH = "/gdrive/My Drive/TrainingData/NetworkData/Step0Top/Label/
  ↪"
L_Step1_PATH = "/gdrive/My Drive/TrainingData/NetworkData/Step1Top/Label/
  ↪"
```

```
L_Step2_PATH = "/gdrive/My Drive/TrainingData/NetworkData/Step2Top/Label/
  ↪"
L_Step3_PATH = "/gdrive/My Drive/TrainingData/NetworkData/Step3Top/Label/
  ↪"
L_Step6_PATH = "/gdrive/My Drive/TrainingData/NetworkData/Step6Top/Label/
  ↪"



save_model_path = os.path.join(DATA_PATH,"Li_uNET.hdf5")
```

[ ]:
```
# Reading list name of all the files in the raw data directory
Step0_slc = os.listdir(Step0_PATH)
Step1_slc = os.listdir(Step1_PATH)
Step2_slc = os.listdir(Step2_PATH)
Step3_slc = os.listdir(Step3_PATH)
Step6_slc = os.listdir(Step6_PATH)
```

[ ]:
```
# Reading Model Files
BACKBONE = 'resnet34'
CLASSES = ['lithium','pore']


# define network parameters
n_classes = 1 if len(CLASSES) == 1 else (len(CLASSES) + 1)  # case for␣
  ↪binary and multiclass segmentation
activation = 'sigmoid' if n_classes == 1 else 'softmax'


model = sm.Unet(BACKBONE, classes=n_classes, activation=activation)
model.load_weights(save_model_path)
```

[ ]:
```
pr_mask = np.zeros((500,96,992,3))
a = time.time()
for i in range(0,len(Step0_slc)):
  img = image.load_img(os.path.join(Step0_PATH,Step0_slc[i]),␣
 ↪target_size=(96,992))
  img = np.expand_dims(img,axis=0)
  pr_mask[i,:] = model.predict(img)
  #plt.imsave(os.path.join(L_Step0_PATH,Step0_slc[i]),pr_mask[0,:])


execution_time = time.time()-a
print(execution_time)
```

[ ]:
```
import time
a = time.time()
for i in range(0,len(Step1_slc)):
  img = image.load_img(os.path.join(Step1_PATH,Step1_slc[i]),␣
 ↪target_size=(96,992))
  img = np.expand_dims(img,axis=0)
  pr_mask = model.predict(img)
  plt.imsave(os.path.join(L_Step1_PATH,Step1_slc[i]),pr_mask[0,:])


execution_time = time.time()-a
print(execution_time)
```

[ ]:
```
a = time.time()
for i in range(0,len(Step2_slc)):
  img = image.load_img(os.path.join(Step2_PATH,Step2_slc[i]),␣
 ↪target_size=(96,992))
```

```
  img = np.expand_dims(img,axis=0)
  pr_mask = model.predict(img)
  plt.imsave(os.path.join(L_Step2_PATH,Step2_slc[i]),pr_mask[0,:])


execution_time = time.time()-a
print(execution_time)
```

[ ]:
```
pr_mask = np.zeros((500,96,992,3))
a = time.time()
for i in range(0,len(Step3_slc)):
  img = image.load_img(os.path.join(Step3_PATH,Step3_slc[i]),␣
 ↪target_size=(96,992))
  img = np.expand_dims(img,axis=0)
  pr_mask[i,:] = model.predict(img)
  # plt.imsave(os.path.join(L_Step3_PATH,Step3_slc[i]),pr_mask[0,:])


execution_time = time.time()-a
print(execution_time)
```

[ ]:
```
a = time.time()
for i in range(0,len(Step6_slc)):
  img = image.load_img(os.path.join(Step6_PATH,Step6_slc[i]),␣
 ↪target_size=(96,992))
  img = np.expand_dims(img,axis=0)
  pr_mask = model.predict(img)
  plt.imsave(os.path.join(L_Step6_PATH,Step6_slc[i]),pr_mask[0,:])


execution_time = time.time()-a
```

```
print(execution_time)
```

1.4 Crack Segmentation Code

```
%.....................................................................
%
%...Crack Extraction Code
%...Inks and Interfaces Laboratory
%...March 2019
%...Marm Dixit
%...Outputs Surface Areas for Input Stack
%...GNU Terry Pratchett
%.....................................................................
clc;
clear all;
close all;
%
% File Directory

fdir = 'D:\Vandy\Year2019\ToyotaResults\';
% File Names

fname = {'/media/inkslab/DATA/ToyotaRecon/RawData/LPS_LiI/011_LPS_LII_StraightenedBinary

% File Number to be Run

fno =2;
%Extracts file information

info = imfinfo(fname{fno});
```

%Identifies number of slices

num_images = numel(info);

%

%...Generating an array with N slices

parfor k = 1:num_images

A = 255-imread(fname{fno}, k, 'Info', info);

sizeA = size(A)

BW = imbinarize(A,'adaptive','sensitivity',0.05);

Sample(:,:,k) = bwareaopen(BW,1);

end

%Find number of steps

steps = floor(num_images/10);

%Identifies crack area and averages/closes up regions

for k = 1:steps

if k ==steps+1 && num_images>k*10

$trial = Sample(:,:,(k-1)*10+1:end);$

$Sample3D(:,:,(k-1)*10+1:num\_images) = bwareaopen(trial,700000,26);$

end

$trial = Sample(:,:,(k-1)*10+1:10*k);$

$Sample3D(:,:,(k-1)*10+1:10*k) = bwareaopen(trial,1000,26);$

```
end
%ConvertsDataformatstobesaves

sampleCrack = im2uint8(Sample);
%Savestheimagestack

savestack(sampleCrack,sprintf('%s_Crack.tif',fname{fno}(1:end-23)))
```

1.5 Crack Volume Estimation

%.....

%

%...Crack Volume

%...Inks and Interfaces Laboratory

%...June 2019

%...Marm Dixit

%...Outputs excel file with crack volume

%...GNU Pratchett

%.....

clc;

close all;

%%

%.....

%...Experiment Constants.....

%.....

res=0.7; % Resolution, um/pixel

%.....

%...User Input.....

%.....

fname = { 'LPS_LII/014_LPS_LII_set1b_Crack.tif',...

'LPS_LII/015_LPS_LII_set2a_Crack.tif',...

'LPS_LII/016_LPS_LII_set2b_Crack.tif',...

'LPS_LII_AT/018_LPS_LII_AT_Set1a_Crack.tif',...

'LPS_LII_AT/019_LPS_LII_AT_Set1b_Crack.tif',...

'LPS_LII_AT/020_LPS_LII_AT_Set2a_Crack.tif',...

'LPS_LII_AT/021_LPS_LII_AT_Set2b_Crack.tif',...

```
'LPS_LII_AN/024_LPS_LII_AN_Set1b_Crack.tif',...
'LPS_LII_AN/025_LPS_LII_AN_Set2a_Crack.tif',...
'LPS_LII_AN/026_LPS_LII_AN_Set2b_Crack.tif',...
'LPS_LII_AN/027_LPS_LII_AN_set6b_Crack.tif',...
'A_LPS_S2/029_A_LPS_S2_Crack.tif',...
'A_LPS_S2/029_A_LPS_S2_Set1a_Crack.tif',...
'A_LPS_S2/030_A_LPS_S2_Set1b_Crack.tif',...
'A_LPS_S2/031_A_LPS_S2_Set2a_Crack.tif'};%BinarizedTIFFfile,1 = electrolyte,0 =
pore
RoI = 25;%Subvolume Dimension, um
vol = zeros(length(fname),1);%Volume variable initialized = number of files

%For loop calculating the sum of electrolyte pixels; normalized to total pixels' for fno = 15 :
15%length(fname)
vol = 0;
fname{fno}
A = TIFFStack(fname{fno});
sizeA = size(A);
%...Generating an array with N slices
fork = 1 : sizeA(3)
vol(k) = sum(sum(A(:,:,k)));
end
crack = sum(vol)/255;
end
```

1.6 Porosity Map

%.....

%

%...Porosity Mapper

%...Inks and Interfaces Laboratory

%...June 2019

%...Marm Dixit

%...Outputs figure plots and animation for local porosity maps in full

%...electrolyte

%...Run Three Times To Sample Effectively

%...GNU Pratchett

%.....

clc;

close all;

%%

%.....

%...Experiment Constants.....

%.....

res=3; % Resolution, um/pixel

%.....

%...User Input.....

%.....

% fname = { %'011_LPS_LII_StraightenedBinary.tif',...

% % '013_LPS_LII_set1a_StraightenedBinary.tif',...

% % '014_LPS_LII_set1b_StraightenedBinary.tif',...

% % '015_LPS_LII_set2a_StraightenedBinary.tif',...

% % '016_LPS_LII_set2b_StraightenedBinary.tif',...

% % '017_LPS_LII_AT_StraightenedBinary.tif',...

% % '018_LPS_LII_AT_Set1a_StraightenedBinary.tif',...

% % '019_LPS_LII_AT_Set1b_StraightenedBinary.tif',...

% % '020_LPS_LII_AT_Set2a_StraightenedBinary.tif',...

% % '021_LPS_LII_AT_Set2b_StraightenedBinary.tif',...

% % '022_LPS_LII_AN_StraightenedBinary.tif',...

% % '023_LPS_LII_AN_Set1a_StraightenedBinary.tif',...

% '024_LPS_LII_AN_Set1b_StraightenedBinary.tif',...

% '025_LPS_LII_AN_Set2a_StraightenedBinary.tif',...

% '026_LPS_LII_AN_Set2b_StraightenedBinary.tif',...

% '027_LPS_LII_AN_Set6b_StraightenedBinary.tif',...

% '028_A_LPS_S2_StraightenedBinary.tif',...

% '029_A_LPS_S2_Set1a_StraightenedBinary.tif',...

% '030_A_LPS_S2_Set1b_StraightenedBinary.tif',...

% '031_A_LPS_S2_Set2a_StraightenedBinary.tif'}; %Binarized TIFF file, 1 = electrolyte, 0 =pore

fname = {'/media/inkslab/DATA/6-BM/S4_pellets/Pristine.tif'....

'/media/inkslab/DATA/6 − BM/S4_pellets/C1_Charged.tif'....

'/media/inkslab/DATA/6 − BM/S4_pellets/C1_Discharged.tif'....

'/media/inkslab/DATA/6 − BM/S4_pellets/C2_Charged.tif'....

'/media/inkslab/DATA/6 − BM/S4_pellets/C2_Discharged.tif'....

'/media/inkslab/DATA/6 − BM/S4_pellets/C3_1.tif'....

'/media/inkslab/DATA/6 − BM/S4_pellets/C3_Discharged.tif'....

'/media/inkslab/DATA/6 − BM/S4_pellets/C4_Charged.tif'....

'/media/inkslab/DATA/6 − BM/S4_pellets/C4_Discharged.tif'....

'/media/inkslab/DATA/6 − BM/S4_pellets/C5_Charged.tif'....

'/media/inkslab/DATA/6 − BM/S4_pellets/C5_Discharged.tif'};

$RoI = 24; \%SubvolumeDimension, um$

$for f = 1 : 1 \%length(fname)$

$\%f = 10;$

$a = cputime;$

$fname\{f\}$

$Data = TIFFStack(fname\{f\});$

%%

%.....

%...PorosityMap.....

%.....

$RoIPix = floor(RoI/res);$

$A = size(Data);$

$A = floor(A/RoIPix);$

$m = A(1); n = A(2); o = A(3);$

$porosity = zeros(m+1, n+1, o+1);$

$parfori = 1 : o+1$

$forj = 1 : n+1$

$fork = 1 : m+1$

$ifk == m+1 \&\& j \sim$=n+1 && i$\sim$=o+1

$sub\_volume = Data((k-1) * RoIPix + 1 : end, ...$

$(j-1) * RoIPix + 1 : j * RoIPix, ...$

$(i-1) * RoIPix + 1 : i * RoIPix);$

$porosity(k, j, i) = 1 - ((sum(sum(sum(sub\_volume)))) / (255 * RoIPix3));$

$break;$

$elseifk \sim$=m+1 && j==n+1 && i$\sim$=o+1

$sub\_volume = Data((k-1)*RoIPix+1:k*RoIPix,...$

$(j-1)*RoIPix+1:end,...$

$(i-1)*RoIPix+1:i*RoIPix);$

$porosity(k,j,i) = 1-((sum(sum(sum(sub\_volume))))/(255*RoIPix3));$

$break;$

$elseifk\sim$=m+1 && j$\sim$=n+1 && i==o+1

$sub\_volume = Data((k-1)*RoIPix+1:k*RoIPix,...$

$(j-1)*RoIPix+1:j*RoIPix,...$

$(i-1)*RoIPix+1:end);$

$porosity(k,j,i) = 1-((sum(sum(sum(sub\_volume))))/(255*RoIPix3));$

$break;$

$elseifk == m+1\&\&j == n+1\&\&i\sim$=o+1

$sub\_volume = Data((k-1)*RoIPix+1:end,...$

$(j-1)*RoIPix+1:end,...$

$(i-1)*RoIPix+1:i*RoIPix);$

$porosity(k,j,i) = 1-((sum(sum(sum(sub\_volume))))/(255*RoIPix3));$

$break;$

$elseifk\sim$=m+1 && j==n+1 && i==o+1

$sub\_volume = Data((k-1)*RoIPix+1:k*RoIPix,...$

$(j-1)*RoIPix+1:end,...$

$(i-1)*RoIPix+1:end);$

$porosity(k,j,i) = 1-((sum(sum(sum(sub\_volume))))/(255*RoIPix3));$

$break;$

$elseifk == m+1\&\&j\sim$=n+1 && i==o+1

$sub\_volume = Data((k-1)*RoIPix+1:end,...$

$(j-1)*RoIPix+1:j*RoIPix,...$

$(i-1)*RoIPix+1:end);$

$porosity(k,j,i) = 1 - ((sum(sum(sum(sub\_volume))))/(255 * RoIPix3));$

$break;$

$elseif k == m + 1 \&\& j == n + 1 \&\& i == o + 1$

$sub\_volume = Data((k-1) * RoIPix + 1 : end, ...$

$(j-1) * RoIPix + 1 : end, ...$

$(i-1) * RoIPix + 1 : end);$

$porosity(k,j,i) = 1 - ((sum(sum(sum(sub\_volume))))/(255 * RoIPix3));$

$break;$

end

$sub\_volume = Data((k-1) * RoIPix + 1 : k * RoIPix, ...$

$(j-1) * RoIPix + 1 : j * RoIPix, ...$

$(i-1) * RoIPix + 1 : i * RoIPix);$

$porosity(k,j,i) = 1 - ((sum(sum(sum(sub\_volume))))/(255 * RoIPix3));$

end

end

end

%%

%.....

%...$LocationMap$.....

%.....

$dataSize = size(Data);$

$size\_p = size(porosity);$

$X\_center = dataSize(1) * res/2;$

$Y\_center = dataSize(2) * res/2;$

$x\_loc = colon(RoI/2, RoI, m * RoI);$

$x\_loc(length(x\_loc) + 1) = x\_loc(end) + (((dataSize(1) * res - m * RoI)/2));$

$y\_loc = colon(RoI/2, RoI, n * RoI);$

$y\_loc(length(y\_loc)+1) = y\_loc(end) + (((dataSize(2) * res - n * RoI)/2));$

$z\_loc = colon(RoI/2, RoI, o * RoI);$

$z\_loc(length(z\_loc)+1) = z\_loc(end) + (((dataSize(3) * res - o * RoI)/2));$

$\%location = zeros(size\_p(1), size\_p(2), size\_p(3));$

$a = 1;$

$fors = 1 : size\_p(3)$

$fort = 1 : size\_p(2)$

$foru = 1 : size\_p(1)$

$x\_pos(a) = x\_loc(u);$

$y\_pos(a) = y\_loc(t);$

$z\_pos(a) = z\_loc(s);$

$a = a + 1;$

end

end

end

$R = dataSize(1) * res/2;$

$sampleData = 1 - porosity(:);$

$a = 1;$

$fore = 1 : length(sampleData)$

$dist(e) = sqrt((x\_pos(e) - X\_center)2 + (y\_pos(e) - Y\_center)2);$

$if dist(e) > R$

$index(e) = e;$

end

end

$index = nonzeros(index);$

$x\_pos(index) = [\,];$

y_pos(index) = [ ];

z_pos(index) = [ ];

sampleData(index) = [ ];

pPlane = length(z_pos)/(o+1);

figure('Renderer','painters','Position', [10 10 600 925])

for b = 1:o

$subplot(2,1,1)$

$ax = gca();$

$scatter3(x\_pos((b-1)*pPlane+1:b*pPlane),...$

$y\_pos((b-1)*pPlane+1:b*pPlane),...$

$z\_pos((b-1)*pPlane+1:b*pPlane),...$

$100, sampleData((b-1)*pPlane+1:b*pPlane),'filled')$

$xlim([-50\ 2800])$

$ylim([-50\ 2800])$

$zlim([-50\ 1000])$

$colorbar$

$caxis([0\ 1])$

$set(ax,'XLimMode','manual','YLimMode','manual');$

$view(0,90)$

$holdon$

$subplot(2,1,2)$

$ax2 = gca();$

$scatter3(x\_pos((b-1)*pPlane+1:b*pPlane),...$

$y\_pos((b-1)*pPlane+1:b*pPlane),...$

$z\_pos((b-1)*pPlane+1:b*pPlane),...$

$30, sampleData((b-1)*pPlane+1:b*pPlane),'filled')$

$xlim([-50\ 2800])$

$ylim([-50\ 2800])$

```
zlim([-50 1000])
colorbar
caxis([0 1])
set(ax2,'XLimMode','manual','YLimMode','manual');
holdon
movie(b) = getframe(gcf);
end
movie2gif(movie,sprintf('PMap_%d.gif',f),'DelayTime',0.5,'LoopCount',Inf)
slice = colon(1,o);
forg = 1 : length(slice)
figure()
ax = gca();
scatter3(x_pos((slice(g) - 1) * pPlane + 1 : slice(g) * pPlane),...
y_pos((slice(g) - 1) * pPlane + 1 : slice(g) * pPlane),...
z_pos((slice(g) - 1) * pPlane + 1 : slice(g) * pPlane),...
30,sampleData((slice(g) - 1) * pPlane + 1 : slice(g) * pPlane),'filled')
xlim([-50 2800])
ylim([-50 2800])
zlim([-50 1000])
caxis([0 1])
colorbar;
set(ax,'XLimMode','manual','YLimMode','manual');
view(0,90)
saveas(ax,sprintf('Porosity_%d_Slice_%d.jpg',f,slice(g)))
saveas(ax,sprintf('Porosity_%d_Slice_%d.fig',f,slice(g)))
end
%
```

```
%figure()
%
%fori = 1 : o
%ax = gca();
%subplot(2,1,1)
%scatter3(x_pos((i − 1) ∗ pPlane + 1 : i ∗ pPlane),...
%y_pos((i − 1) ∗ pPlane + 1 : i ∗ pPlane),...
%z_pos((i − 1) ∗ pPlane + 1 : i ∗ pPlane),...
%10,sampleData((i − 1) ∗ pPlane + 1 : i ∗ pPlane),'filled')
%xlim([-50 1650])
% ylim([-50 1650])
% zlim([-50 1050])
% set(ax,'XLimMode','manual','YLimMode','manual');
% % view(0,90)
% movie2(i) = getframe(gcf);
% hold on
%end
%movie2gif(movie2,'test2.gif','DelayTime',1,'LoopCount',Inf)
%clearDataporositysampleDataindex;
closeall
%end
cputime − a
end
```

1.7 Tortuosity Maps

```
%.....................................................................
%
%...Tortuosity Mapper
%...Inks and Interfaces Laboratory
%...June 2019
%...Marm Dixit
%...Outputs figure plots and animation for local porosity maps in full
%...electrolyte
%...Run Three Times To Sample Effectively
%...GNU Pratchett
%.....................................................................
clc;
clear all;
close all;
%%
%.....................................................................
%...Experiment Constants.....................................................
%.....................................................................
res=1; % Resolution, um/pixel
res3 = [1 1 1];
%.....................................................................
%...User Input.....................................................
%.....................................................................
% fname = {'D:\ToyotaRecon\027_LPS_LII_AN_Set6b_StraightenedBinary.tif'};%,...
%Binarized TIFF file, White domain = electrolyte
% 'D:\ToyotaRecon\002_A_LPS_StraightenedBinary_2.tif',... %Binarized TIFF file,
```

White domain = electrolyte

% 'D:\ToyotaRecon\002_A_LPS_StraightenedBinary_3.tif'}; %Binarized TIFF file, White domain = electrolyte

% fname = 'D:\ToyotaRecon\RawData\A_LPS\Data_100um_1.tiff'; %Binarized TIFF file, Supply Square Crop, W

fname = {'D:\HEDM\Reconstructions\hatzell_apr19_rec_reduced\100umCrops\S1_Pristine_Top.tif',...

'D:\HEDM\Reconstructions\hatzell_apr19_rec_reduced\100umCrops\S1_Pristine_Bottom.tif',...

'D:\HEDM\Reconstructions\hatzell_apr19_rec_reduced\100umCrops\S1_Step1_Top.tif',...

'D:\HEDM\Reconstructions\hatzell_apr19_rec_reduced\100umCrops\S1_Step1_Bottom.tif',...

'D:\HEDM\Reconstructions\hatzell_apr19_rec_reduced\100umCrops\S1_Step2_Top.tif',...

'D:\HEDM\Reconstructions\hatzell_apr19_rec_reduced\100umCrops\S1_Step2_Bottom.tif',...

'D:\HEDM\Reconstructions\hatzell_apr19_rec_reduced\100umCrops\S1_Step3_Top.tif',...

'D:\HEDM\Reconstructions\hatzell_apr19_rec_reduced\100umCrops\S1_Step3_Bottom.tif',...

'D:\HEDM\Reconstructions\hatzell_apr19_rec_reduced\100umCrops\S1_Step6_Top.tif',...

'D:\HEDM\Reconstructions\hatzell_apr19_rec_reduced\100umCrops\S1_Step6_Bottom.tif',...

'D:\HEDM\Reconstructions\hatzell_apr19_rec_reduced\100umCrops\S2_Pristine_Top.tif',...

```
'D                          :\HEDM\Reconstructions\hatzell_apr19_rec_reduced\100
umCrops\S2_Pristine_Bottom.tif',...
'D                          :\HEDM\Reconstructions\hatzell_apr19_rec_reduced\100
umCrops\S2_Step1_Top.tif',...
'D                          :\HEDM\Reconstructions\hatzell_apr19_rec_reduced\100
umCrops\S2_Step1_Bottom.tif',...
'D                          :\HEDM\Reconstructions\hatzell_apr19_rec_reduced\100
umCrops\S2_Step2_Top.tif',...
'D                          :\HEDM\Reconstructions\hatzell_apr19_rec_reduced\100
umCrops\S2_Step2_Bottom.tif',...
'D                          :\HEDM\Reconstructions\hatzell_apr19_rec_reduced\100
umCrops\S2_Step3_Top.tif',...
'D                          :\HEDM\Reconstructions\hatzell_apr19_rec_reduced\100
umCrops\S2_Step3_Bottom.tif',...
'D                          :\HEDM\Reconstructions\hatzell_apr19_rec_reduced\100
umCrops\S2_Step4_Top.tif',...
'D                          :\HEDM\Reconstructions\hatzell_apr19_rec_reduced\100
umCrops\S2_Step4_Bottom.tif'};
RoI = 25; % Subvolume Dimension, um
tau_dir1 = zeros(3,3);
tau_dir1(3,1) = 1;
tau_dir2 = zeros(3,3);
tau_dir2(3,2) = 1;
tau_dir3 = zeros(3,3);
tau_dir3(3,3) = 1;
%%
%.....................................................................
```

```
%...Read Data.....
%.....
cnt = 1;
% for i=cnt:length(fname)
% info = imfinfo(fname{i}); %Extracts file information
% num_images = numel(info); %Identifies number of slices
%
%...GeneratinganarraywithNslices
%for k = 1 : num_images
%a = imread(fname{i},k,'Info',info);
%Data(:,:,cnt) = imbinarize(a);
%cnt = cnt + 1;
%end
[Data,nImg]=imread_big(fname{cnt});
% end
%%
%.....
%...Tortuosity Map.....
%.....
RoIPix = floor(RoI/res);
A= size(Data);
A=floor(A/RoIPix);
m =A(1);n = A(2);o=A(3);
porosity = zeros(m+1,n+1,o+1);
parfor i = 1:o
for j = 1 : n + 1
for k = 1 : m + 1
```

$ifk == m+1$&&j∼=n+1 && i∼=o+1

$sub\_volume = Data((k-1)*RoIPix+1:end,...$

$(j-1)*RoIPix+1:j*RoIPix,...$

$(i-1)*RoIPix+1:i*RoIPix);$

$results1 = TauFactor('InLine',1,1,0,sub\_volume,tau\_dir1,res3);$

$results2 = TauFactor('InLine',1,1,0,sub\_volume,tau\_dir2,res3);$

$results3 = TauFactor('InLine',1,1,0,sub\_volume,tau\_dir3,res3);$

$tau\_1(k,j,i) = results1.Tau\_W1.Tau;$

$tau\_2(k,j,i) = results2.Tau\_W2.Tau;$

$tau\_3(k,j,i) = results3.Tau\_W3.Tau;$

$break;$

$elseifk$∼=m+1 && j==n+1 && i∼=o+1

$sub\_volume = Data((k-1)*RoIPix+1:k*RoIPix,...$

$(j-1)*RoIPix+1:end,...$

$(i-1)*RoIPix+1:i*RoIPix);$

$results1 = TauFactor('InLine',1,1,0,sub\_volume,tau\_dir1,res3);$

$results2 = TauFactor('InLine',1,1,0,sub\_volume,tau\_dir2,res3);$

$results3 = TauFactor('InLine',1,1,0,sub\_volume,tau\_dir3,res3);$

$tau\_1(k,j,i) = results1.Tau\_W1.Tau;$

$tau\_2(k,j,i) = results2.Tau\_W2.Tau;$

$tau\_3(k,j,i) = results3.Tau\_W3.Tau;$

$break;$

$elseifk$∼=m+1 && j∼=n+1 && i==o+1

$sub\_volume = Data((k-1)*RoIPix+1:k*RoIPix,...$

$(j-1)*RoIPix+1:j*RoIPix,...$

$(i-1)*RoIPix+1:end);$

$results1 = TauFactor('InLine',1,1,0,sub\_volume,tau\_dir1,res3);$

$results2 = TauFactor('InLine',1,1,0,sub\_volume,tau\_dir2,res3);$

$results3 = TauFactor('InLine',1,1,0,sub\_volume,tau\_dir3,res3);$

$tau\_1(k,j,i) = results1.Tau\_W1.Tau;$

$tau\_2(k,j,i) = results2.Tau\_W2.Tau;$

$tau\_3(k,j,i) = results3.Tau\_W3.Tau;$

$break;$

$elseifk == m+1 \&\& j == n+1 \&\& i \sim =$o+1

$sub\_volume = Data((k-1) * RoIPix + 1 : end,...$

$(j-1) * RoIPix + 1 : end,...$

$(i-1) * RoIPix + 1 : i * RoIPix);$

$results1 = TauFactor('InLine',1,1,0,sub\_volume,tau\_dir1,res3);$

$results2 = TauFactor('InLine',1,1,0,sub\_volume,tau\_dir2,res3);$

$results3 = TauFactor('InLine',1,1,0,sub\_volume,tau\_dir3,res3);$

$tau\_1(k,j,i) = results1.Tau\_W1.Tau;$

$tau\_2(k,j,i) = results2.Tau\_W2.Tau;$

$tau\_3(k,j,i) = results3.Tau\_W3.Tau;$

$break;$

$elseifk \sim =$m+1 && j==n+1 && i==o+1

$sub\_volume = Data((k-1) * RoIPix + 1 : k * RoIPix,...$

$(j-1) * RoIPix + 1 : end,...$

$(i-1) * RoIPix + 1 : end);$

$results1 = TauFactor('InLine',1,1,0,sub\_volume,tau\_dir1,res3);$

$results2 = TauFactor('InLine',1,1,0,sub\_volume,tau\_dir2,res3);$

$results3 = TauFactor('InLine',1,1,0,sub\_volume,tau\_dir3,res3);$

$tau\_1(k,j,i) = results1.Tau\_W1.Tau;$

$tau\_2(k,j,i) = results2.Tau\_W2.Tau;$

$tau\_3(k,j,i) = results3.Tau\_W3.Tau;$

$break$;

$elseifk == m+1 \&\& j \sim$=n+1 && i==o+1

$sub\_volume = Data((k-1)*RoIPix+1:end,...$

$(j-1)*RoIPix+1:j*RoIPix,...$

$(i-1)*RoIPix+1:end);$

$results1 = TauFactor('InLine',1,1,0,sub\_volume,tau\_dir1,res3);$

$results2 = TauFactor('InLine',1,1,0,sub\_volume,tau\_dir2,res3);$

$results3 = TauFactor('InLine',1,1,0,sub\_volume,tau\_dir3,res3);$

$tau\_1(k,j,i) = results1.Tau\_W1.Tau;$

$tau\_2(k,j,i) = results2.Tau\_W2.Tau;$

$tau\_3(k,j,i) = results3.Tau\_W3.Tau;$

$break;$

$elseifk == m+1 \&\& j == n+1 \&\& i == o+1$

$sub\_volume = Data((k-1)*RoIPix+1:end,...$

$(j-1)*RoIPix+1:end,...$

$(i-1)*RoIPix+1:end);$

$results1 = TauFactor('InLine',1,1,0,sub\_volume,tau\_dir1,res3);$

$results2 = TauFactor('InLine',1,1,0,sub\_volume,tau\_dir2,res3);$

$results3 = TauFactor('InLine',1,1,0,sub\_volume,tau\_dir3,res3);$

$tau\_1(k,j,i) = results1.Tau\_W1.Tau;$

$tau\_2(k,j,i) = results2.Tau\_W2.Tau;$

$tau\_3(k,j,i) = results3.Tau\_W3.Tau;$

$break;$

end

$sub\_volume = Data((k-1)*RoIPix+1:k*RoIPix,...$

$(j-1)*RoIPix+1:j*RoIPix,...$

$(i-1)*RoIPix+1:i*RoIPix);$

$results1 = TauFactor('InLine',1,1,0,sub\_volume,tau\_dir1,res3);$

$results2 = TauFactor('InLine',1,1,0,sub\_volume,tau\_dir2,res3);$

$results3 = TauFactor('InLine',1,1,0,sub\_volume,tau\_dir3,res3);$

$tau\_1(k,j,i) = results1.Tau\_W1.Tau;$

$tau\_2(k,j,i) = results2.Tau\_W2.Tau;$

$tau\_3(k,j,i) = results3.Tau\_W3.Tau;$

end

end

end

%%

%.....

%...LocationMap.....

%.....

$dataSize = size(Data);$

$size\_p = size(tau\_1);$

$X\_center = dataSize(1) * res/2;$

$Y\_center = dataSize(2) * res/2;$

$x\_loc = colon(RoI/2,RoI,m * RoI);$

$x\_loc(length(x\_loc)+1) = x\_loc(end) + (((dataSize(1) * res - m * RoI)/2));$

$y\_loc = colon(RoI/2,RoI,n * RoI);$

$y\_loc(length(y\_loc)+1) = y\_loc(end) + (((dataSize(2) * res - n * RoI)/2));$

$z\_loc = colon(RoI/2,RoI,o * RoI);$

$\%z\_loc(length(z\_loc)+1) = z\_loc(end) + (((dataSize(3) * res - o * RoI)/2));$

$\%location = zeros(size\_p(1),size\_p(2),size\_p(3));$

$a = 1;$

$fori = 1 : size\_p(3)$

$forj = 1 : size\_p(2)$

$fork = 1 : size\_p(1)$

i

j

k

$x\_pos(a) = x\_loc(k);$

$y\_pos(a) = y\_loc(j);$

$z\_pos(a) = z\_loc(i);$

$a = a + 1;$

end

end

end

$R = dataSize(1) * res/2;$

$sampleData1 = tau\_1(:);$

$a = 1;$

$fori = 1 : length(sampleData1)$

$dist(i) = sqrt((x\_pos(i) - X\_center)2 + (y\_pos(i) - Y\_center)2);$

$ifdist(i) > R$

$index(i) = i;$

end

end

$index = nonzeros(index);$

$x\_pos(index) =[\,];$

y_pos(index) = [ ];

z_pos(index) = [ ];

sampleData1(index) = [ ];

pPlane = length(z_pos)/(o);

figure('Renderer','painters','Position', [10 10 600 925])

for i = 1:o

$subplot(2,1,1)$

$ax = gca();$

$scatter3(x\_pos((i-1)*pPlane+1:i*pPlane),...$

$y\_pos((i-1)*pPlane+1:i*pPlane),...$

$z\_pos((i-1)*pPlane+1:i*pPlane),...$

$81, sampleData1((i-1)*pPlane+1:i*pPlane),'filled')$

$xlim([-50\ 1650])$

$ylim([-50\ 1650])$

$zlim([-50\ 1050])$

$set(ax,'XLimMode','manual','YLimMode','manual');$

$view(0,90)$

$caxis([1\ 5])$

$colorbar;$

$holdon$

$subplot(2,1,2)$

$ax2 = gca();$

$scatter3(x\_pos((i-1)*pPlane+1:i*pPlane),...$

$y\_pos((i-1)*pPlane+1:i*pPlane),...$

$z\_pos((i-1)*pPlane+1:i*pPlane),...$

$10, sampleData1((i-1)*pPlane+1:i*pPlane),'filled')$

$xlim([-50\ 1650])$

$ylim([-50\ 1650])$

$zlim([-50\ 1050])$

$set(ax2,'XLimMode','manual','YLimMode','manual');$

```
caxis([1 5])
colorbar;
holdon

movie(i) = getframe(gcf);
end
movie2gif(movie,'Tau1.gif','DelayTime',0.5,'LoopCount',Inf)
```

1.8 RoI Calculator

%.....

%

%...RoI Calculator

%...Inks and Interfaces Laboratory

%...June 2019

%...Marm Dixit

%...Outputs data plot of porosity as a function of sub-volume size

%...Also outputs image stacks used in analysis

%...Run Three Times To Sample Effectively

%...GNU Pratchett

%.....

clc;

clear all;

close all;

%%

%.....

%...Experiment Constants.....

%.....

res=1.172; % Resolution, um/pixel

%.....

%...User Input.....

%.....

% % fname = {'E:\Toyota Recons\ToyotaRecon\RawData\A_LPS_S2

\028_A_LPS_S2_SquareCrop.tif',...

% 'E:\Toyota Recons\ToyotaRecon\RawData\LPS_LiI

\011_LPS_LII_SquareCrop.tif',...

% 'E:\Toyota Recons\ToyotaRecon\RawData\LPS_LiI_AT

\017_LPS_LII_AT_SquareCrop.tif',...

% 'E:\Toyota Recons\ToyotaRecon\RawData\LPS_LiI_AN

\022_LPS_LII_AN_SquareCrop.tif'}; %Binarized TIFF file, Supply Square Crop, White Domains = Electrolyte; Black domains = Pores

fname = {'D:\LLZO_Pellet_Binary_SquareCrop.tif'};

Sizes = [50, 100,150, 200,250, 300, 400,500]; % Subvolume Dimension, um

% Data = TIFFStack(fname);

ii = 1;

[Data,Nframes]= imread_big(fname{ii});

%%

%.....

%...Generate Subvolumes.....

%.....

Pixels = round(Sizes./res); % Pixels in each subvolume dimension

DataSize = size(Data); %Size of Input TIFF

% Max = floor(min(size(Data))./Pixels);

Max1(:) = (DataSize(1)-Pixels)';

Max2(:) = (DataSize(2)-Pixels)';

Max3(:) = (DataSize(3)-Pixels)';

for i = 1:length(Sizes)

$set1 = randi([1$ Max1(i)], 3,1);

$set2 = randi([1$ Max2(i)], 3,1);

$set3 = randi([1$ Max3(i)], 3,1);

$forj = 1:3$

$\%if Max(i) > 3$

$Test\{:,:,:,j,i\} = Data(set1(j):set1(j)+Pixels(i),...$

$set2(j) : set2(j) + Pixels(i), ...$

$set3(j) : set3(j) + Pixels(i));$

$\%elseif Max(i) == 1$

$\%if j > 1$

$\%break;$

$\%end$

$\%Test\{:,:,:,1,i\} = Data(1 + Pixels(i) : 2 * Pixels(i), 1 : Pixels(i), 1 : Pixels(i));$

$\%Test\{:,:,:,2,i\} = Data(1 + Pixels(i) : 2 * Pixels(i), 1 + Pixels(i) : 2 * Pixels(i), 1 : Pixels(i));$

$\%Test\{:,:,:,3,i\} = Data(1 + Pixels(i) : 2 * Pixels(i), 1 + Pixels(i) : 2 * Pixels(i), 1 + Pixels(i) : 2 * Pixels(i));$

$\%elseif Max(i) == 2$

$\%if j > 1$

$\%break;$

$\%end$

$\%Test\{:,:,:,1,i\} = Data(1 + Pixels(i) : 2 * Pixels(i), 1 : Pixels(i), 1 : Pixels(i));$

$\%Test\{:,:,:,2,i\} = Data(1 + Pixels(i) : 2 * Pixels(i), 1 + Pixels(i) : 2 * Pixels(i), 1 : Pixels(i));$

$\%Test\{:,:,:,3,i\} = Data(1 + Pixels(i) : 2 * Pixels(i), 1 + Pixels(i) : 2 * Pixels(i), 1 + Pixels(i) : 2 * Pixels(i));$

$\%elseif Max(i) == 3$

$\%if j > 1$

$\%break;$

$\%end$

$\%Test\{:,:,:,1,i\} = Data(1 + Pixels(i) : 2 * Pixels(i), 1 : Pixels(i), 1 : Pixels(i));$

$\%Test\{:,:,:,2,i\} = Data(1 + Pixels(i) : 2 * Pixels(i), 1 + Pixels(i) : 2 * Pixels(i), 1 : Pixels(i));$

```
%Test{:,:,:,3,i} = Data(1 + Pixels(i) : 2 * Pixels(i),1 + Pixels(i) : 2 * Pixels(i),1 +
Pixels(i) : 2 * Pixels(i));
%end
end
end
%
%%
%.....
%...CalculatingPorosity.....
%.....
fori = 1 : length(Sizes)
forj = 1 : 3
porosity(j,i) = ((sum(sum(sum(Test{:,:,:,j,i}))))/(255 * Pixels(i)3));
end
end
%%
%.....
%...PlottingROIValues.....
%.....
average = sum(porosity)/3;
stdev = std(porosity);
figure()
errorbar(Sizes',average',stdev',' b − o')
xlabel('Sub − VolumeDimension(\mum)','FontSize',16)
ylabel('Porosity (-)','FontSize',16)
xlim([0 550])
%%
```

```
%.....
%...Plotting Porosity Maps.....
%.....
[l,b,h] = size(Test{:,:,:,1,5});
for i = 1:l
forj = 1 : b
fork = 1 : 3
cell = Test{:,:,:,k,5};
pMap(i,j,k) = (sum(cell(i,j,:))/(255 * l));
end
end
end
figure();imshow(pMap(:,:,1) - mean(pMap(:,:,1)));colormapjet;caxis([-0.1 0.1])
figure();imshow(pMap(:,:,2)-mean(pMap(:,:,2))); colormap jet; caxis([-0.1 0.1])
figure();imshow(pMap(:,:,3)-mean(pMap(:,:,3))); colormap jet; caxis([-0.1 0.1])
%%
%.....
%...Saving Image Stacks.....
%.....
%
% for i = 1:length(Sizes)
% for j = 1:3
% A = Test{:,:,:,j,i};
% savestack(A,sprintf('Data_%dum_%d.tiff',Sizes(i),j))
% end
% end
```

1.9 Interface Map

close all;

clear all;

clc;

fname = {'E:\A_LPS_TopInterface.tif',...

'E :\A_LPS_TopInterface2.tif',...

'E :\A_LPS_TopInterface3.tif',...

'E :\LiI_TopInterface.tif',...

'E :\LiI_TopInterface2.tif',...

'E :\LiI_TopInterface3.tif',...

'E :\LiI_AT_TopInterface.tif',...

'E :\LiI_AT_TopInterface2.tif',...

'E :\LiI_AT_TopInterface3.tif',...

'E :\LiI_AN_TopInterface.tif',...

'E :\LiI_AN_TopInterface2.tif',...

'E :\LiI_AN_TopInterface3.tif',...

'E :\A_LPS_BotInterface.tif',...

'E :\A_LPS_BotInterface2.tif',...

'E :\A_LPS_BotInterface3.tif',...

'E :\LiI_BotInterface.tif',...

'E :\LiI_BotInterface2.tif',...

'E :\LiI_BotInterface3.tif',...

'E :\LiI_AT_BotInterface.tif',...

'E :\LiI_AT_BotInterface2.tif',...

'E :\LiI_AT_BotInterface3.tif',...

'E :\LiI_AN_BotInterface.tif',...

'E :\LiI_AN_BotInterface2.tif',...

'E :\LiI_AN_BotInterface3.tif'};

jj= 2;

for fno = 1:length(fname)

% info = imfinfo(fileName{fno});

% n_Z = numel(info);

%...Loadingimagedata.....

%$fork = 1 : n\_Z$

[Data,nFrames] = imread_big(fname{fno});

[l,b,h] = size(Data);

$iMap = sum(Data,3)./h./255;$

$figure();imshow(iMap);colormapautumn;$

%end

end

1.10 Current Density Map

%...Spatial Current Density Calculator.....

%...Marm Dixit.....

%...November 2019.....

%...GNU Pratchett.....

%.....

clc;

clear all;

close all;

```
%.....................................................................
% fname = {'D:\HEDM\Pristine.tif',...
% 'D:\HEDM\Section1.tif'};

a = datetime('now');
%fname = {'/media/inkslab/DATA/HEDM/Section1.tif',...
%'/media/inkslab/DATA/HEDM/Reconstructions/Step2.tif'};


fname = {'D:\HEDM\Reconstructions\hatzell_apr19_rec_reduced\S2_Pristine.tif',...
'D:\HEDM\Reconstructions\hatzell_apr19_rec_reduced\S2_Step1.tif',...
'D:\HEDM\Reconstructions\hatzell_apr19_rec_reduced\S2_Step2.tif',...
'D:\HEDM\Reconstructions\hatzell_apr19_rec_reduced\S2_Step3.tif',...
'D:\HEDM\Reconstructions\hatzell_apr19_rec_reduced\S2_Step4.tif'};

[Data_1, num_images1] = imread_big(fname{3});
[Data_2, num_images2] = imread_big(fname{4});

fname_top = strcat(fname{1}(1:end-4),'_Plating2_Top.xlsx');
fname_bottom = strcat(fname{1}(1:end-4),'_Plating2_Bot.xlsx');
% Data_1 = TIFFStack(fname{1});
% Data_2 = TIFFStack(fname{2});

%.....................................................................
R = 1; %...Radius, mm
res = 1; %...Resolution, um
```

```
nPix = round(R*1000/res); %...No. of pixels in R mm Disc

%....Converting planar images to sections by interchaning columns
Data_Flipped = permute(Data_1, [3 1 2]);
Data2_Flipped = permute(Data_2, [3 1 2]);
[l,b,h]= size(Data_Flipped);

%...Summing over all the sections, normalized to the number of slices

Data_integrated = sum(Data_Flipped(50:714,530:540+750,530:540+750),3)./h;
Data2_integrated = sum(Data2_Flipped(50:714,530:540+750,530:540+750),3)./h;

%...Figures showing
% figure();imshow(Data_integrated,jet)
% caxis([0 1])
% % colorbar
% figure();imshow(Data2_integrated,jet)
% caxis([0 1])
% colorbar

G1_pellet = max(Data_integrated(:));
G2_pellet = max(Data2_integrated(:));

G1_pore = min(Data_integrated(:));
G2_pore = min(Data2_integrated(:));

%...Normalized Data Sets
```

```
Data_Norm = (Data_Flipped-G1_pore)./(G1_pellet-G1_pore);
Data2_Norm = (Data_Flipped-G2_pore)./(G2_pellet-G2_pore);




% l_start = round(b/2-nPix/2)+200;
% b_start = round(h/2-nPix/2)+200;

bot_zStart = 665;
bot_zEnd = 739;
bot_l_start = 680;
bot_b_start = 380;

top_zStart = 84;
top_zEnd = 665;
top_l_start = 380;
top_b_start = 740;



nPix = 780;

tE = Data_Norm(top_zStart:top_zEnd,top_l_start:top_l_start+nPix,
top_b_start:top_b_start+nPix);
tE2 = Data2_Norm(top_zStart:top_zEnd,top_l_start:top_l_start+nPix,
top_b_start:top_b_start+nPix);
```

```
bE = Data_Norm(bot_zStart:bot_zEnd,bot_l_start:bot_l_start+nPix,
bot_b_start:bot_b_start+nPix);
bE2 = Data2_Norm(bot_zStart:bot_zEnd,bot_l_start:bot_l_start+nPix,
bot_b_start:bot_b_start+nPix);

% tE = Data_Norm(1:200,l_start:l_start+nPix, b_start:b_start+nPix);
% bE = Data_Norm(end-200:end,l_start:l_start+nPix, b_start:b_start+nPix);
% tE2 = Data2_Norm(1:200,l_start:l_start+nPix, b_start:b_start+nPix);
% bE2 = Data2_Norm(end-200:end,l_start:l_start+nPix, b_start:b_start+nPix);
% clear Data_1 Data_2 Data_Flipped Data2_Flipped

tE = im2double(tE);
bE = im2double(bE);
tE2 = im2double(tE2);
bE2= im2double(bE2);
%
trial = 400;

[l b h] = size(tE);
x = 1:1:l;

trial = tE(:,:,1);



t_loc = zeros(781,781);
t2_loc = zeros(781,781);
tb_loc = zeros(781,781);
```

```
tb2_loc = zeros(781,781);
tE_pt = [ ];
x_red = [ ];
n = [ ];
diff_tE = [ ];

b1 = datetime('now');
sprintf(' Data preprocessing time =')
b1-a

parfor i = 1:b
forj = 1 : h
tE_pt = findchangepts(tE(:,i,j),'Statistic','rms','MaxNumChanges',20);
x_red = x(tE_pt);
diff_tE = x_red(2 : end) − x_red(1 : end − 1);
n = find(diff_tE == max(diff_tE'));
iflength(n) > 1
n = min(n);
end
t_loc(i,j) = (x_red(n + 1) − x_red(n)) ∗ res;
tE_pt =[ ];
x_red =[ ];
n =[ ];
diff_tE =[ ];
end
end
```

$c = datetime('now');$

$sprintf('Loop1time =')$

$c - b1$

$parfori = 1 : b$

$forj = 1 : h$

$tE\_pt = findchangepts(tE2(:,i,j),'Statistic','rms','MaxNumChanges',20);$

$x\_red = x(tE\_pt);$

$diff\_tE = x\_red(2 : end) - x\_red(1 : end - 1);$

$n = find(diff\_tE == max(diff\_tE'));$

$iflength(n) > 1$

$n = min(n);$

end

$t2\_loc(i,j) = (x\_red(n + 1) - x\_red(n)) * res;$

$tE\_pt = [\,];$

$x\_red = [\,];$

$n = [\,];$

$diff\_tE = [\,];$

end

end

$t\_change = t2\_loc - t\_loc;$

$j = t\_change. * (96485 * 0.534 * 1E - 4/6.94/30 * 60);$

$t\_change = t2\_loc - t\_loc;$

$j = t\_change. * (96485 * 0.534 * 1E - 4/6.94/30 * 60);$

$xlswrite(fname\_top, j)$

$d = datetime('now');$

$sprintf('TopElectrodetime =')$

$d - b1$

$parfori = 1 : b$

$forj = 1 : h$

$bE\_pt = findchangepts(bE(:,i,j),'Statistic','rms','MaxNumChanges',20);$

$x\_red = x(bE\_pt);$

$diff\_bE = x\_red(2 : end) - x\_red(1 : end - 1);$

$n = find(diff\_bE == max(diff\_bE'));$

$iflength(n) > 1$

$n = min(n);$

end

$tb\_loc(i,j) = (x\_red(n + 1) - x\_red(n)) * res;$

$tE\_pt = [\,];$

$x\_red = [\,];$

$n = [\,];$

$diff\_tE = [\,];$

end

end

$e = datetime('now');$

$sprintf('Loop3time =')$

$e - d$

```
parfori = 1 : b
forj = 1 : h
bE_pt = findchangepts(bE2(:,i,j),'Statistic','rms','MaxNumChanges',20);
x_red = x(bE_pt);
diff_bE = x_red(2 : end) − x_red(1 : end − 1);
n = find(diff_bE == max(diff_bE'));
iflength(n) > 1
n = min(n);
end
tb2_loc(i,j) = (x_red(n + 1) − x_red(n)) ∗ res;
tE_pt =[ ];
x_red =[ ];
n =[ ];
diff_tE =[ ];
end
end

tb_change = tb2_loc − tb_loc;
j2 = tb_change. ∗ (96485 ∗ 0.534 ∗ 1E − 4/6.94/30 ∗ 60);
xlswrite(fname_bottom, j2)

f = datetime('now');
sprintf('BottomElectrodetime =')
f − e
sprintf('TotalElapsedtime =')
f − a
%
```

```
%
%
t_el1 = reshape(j,nPix+1,nPix+1);
A = figure();
contourf(j)
xlabel('Dimension(\mu m)')
ylabel('Dimension (\mu m)')
% caxis([0 150])
colorbar

t_el2 = reshape(j2,nPix+1,nPix+1);
B = figure();
contourf(j2)
xlabel('Dimension (\mu m)')
ylabel('Dimension (\mu m)')
% caxis([0 150])
colorbar
```

1.11 EDD Analyser Loop

```
%.....
%
%...EDD DataSet Peak Fit
%...Inks and Interfaces Laboratory
%...March 2019
%...Marm Dixit
%...Outputs Images and Excel File with analyzed data set
%.....
%
clc;
clear all;
close all;
%.....
%.....
%
const.h = 6.626E-34; % Planck's constant
const.c = 299792458; %Speed of light in vacuum
%.....
%
%...User Inputs
%...Enter file name for excel sheet with EDD results
filedir = '/media/inkslab/DATA/6-BM/EDDData/';
[expDetails,fileNames] = xlsread('/media/inkslab/DATA/6-
BM/MatlabCodes/FileNames.xlsx');
i = 8;
for i =12:length(expDetails)
```

$fileName = strcat(filedir, fileNames\{i,1\}, fileNames\{i,2\}, '.xlsx');$

$outputfName = strcat(filedir, fileNames\{i,1\}, fileNames\{i,2\}, '\_Analzed.xlsx');$

$nSteps = expDetails(i,1);$

$timeSeq = expDetails(i,2);$

$rows = 4;$

$y = EDD\_Analyzer(fileName, timeSeq, nSteps, outputfName, rows);$

$sprintf('Analysisof\%sisdone', fileName)$

end

%.....

%

%...EDD DataSet Analyzer Function

%...Inks and Interfaces Laboratory

%...March 2019

%...Marm Dixit

%...Outputs Images and Excel File with analyzed data set

%.....

%

function result = EDD_Analyzer(fileName,timeSeq, nSteps, outputfName,rows)

%.....

%

const.h = 6.626E-34; % Planck's constant

const.c = 299792458; %Speed of light in vacuum

%.....

%

%...User Inputs

%...Enter file name for excel sheet with EDD results

% fileName = 'D:\Vandy\Year2019\EDXRD\Results\ssymmetric\Data.xlsx';

sheetName = 'Sheet1';

% timeSeq = 0; %...1 if sheet has transient data, 0 if steady state

% nSteps = 6; %...Number of steps EDD is taken at

% outputfName = 'D:\Vandy\Year2019\EDXRD\Results\ssymmetric\Analyzed.xlsx';

%.....

%...Reading Input Data

data = xlsread(fileName,sheetName);

data(∼any(∼isnan(data),2),:)=[ ];

%.....

%...Sorting Input Data

index = find((data(:,1,1)==1));

if timeSeq == 0

$fori = 1 : nSteps - 1$

$channel(:,i) = data(index(i) : index(i+1) - rows,1);$

$intensity\_det1(:,i) = data(index(i) : index(i+1) - rows,2);$

$intensity\_det2(:,i) = data(index(i) : index(i+1) - rows,3);$

$\%tStep(:,i) = linspace(1,nSteps,1);$

$\%i$

end

$channel(:,i+1) = data(index(i+1) : end,1);$

$intensity\_det1(:,i+1) = data(index(i+1) : end,2);$

$intensity\_det2(:,i+1) = data(index(i+1) : end,3);$

$\%tStep(:,i+1) = linspace(1,nSteps,1);$

$else$

$nTime = length(index)/nSteps;$

$q = 1;$

$for j = 1 : nTime - 1$

$for i = 1 : nSteps - 1$

$channel(:,i,j) = data(index(q) : index(q+1) - rows,1);$

$intensity\_det1(:,i,j) = data(index(q) : index(q+1) - rows,2);$

$intensity\_det2(:,i,j) = data(index(q) : index(q+1) - rows,3);$

$\%intStep(:,i) = linspace(1,nSteps,1);$

$q = q + 1;$

end

$channel(:,i+1,j) = data(index(q) : index(q+1) - rows,1);$

$intensity\_det1(:,i+1,j) = data(index(q) : index(q+1) - rows,2);$

$intensity\_det2(:,i+1,j) = data(index(q) : index(q+1) - rows,3);$

$q = q + 1;$

end

$for i = 1 : nSteps - 1$

$channel(:,i,j+1) = data(index(q) : index(q+1) - 2,1);$

$intensity\_det1(:,i,j+1) = data(index(q) : index(q+1) - 2,2);$

$intensity\_det2(:,i,j+1) = data(index(q) : index(q+1) - 2,3);$

$\%tStep(:,i) = linspace(1,nSteps,1);$

$\%i$

$q = q + 1;$

end

$channel(:,i+1,j+1) = data(index(q) : end,1);$

$intensity\_det1(:,i+1,j+1) = data(index(q) : end,2);$

$intensity\_det2(:,i+1,j+1) = data(index(q) : end,3);$

end

$\%.....$

$\%...ConvertingChanneltoEnergy$

$\%...E(keV) = p2 * (ch)2 + p1 * (ch) + p0$

$\%....Det - 1 : 3.00993824/0.00878498/0.03485164/ - 1.36990182E - 08$

$\%....Det - 2 : 4.81406202/ - 0.00602739/0.03481301/ - 5.92165984E - 09$

$Det1\_ToA = 3.00993824;$

$Det1\_p0 = 0.00878498;$

$Det1\_p1 = 0.03485164;$

$Det1\_p2 = -1.36990182E - 08;$

$Det2\_ToA = 4.81406202;$

$Det2\_p0 = -0.00602739;$

$Det2\_p1 = 0.03481301;$

$Det2\_p2 = -5.92165984E - 09;$

$E\_1 = Det1\_p2. * (channel.2) + Det1\_p1. * channel + Det1\_p0;$

$E\_2 = Det2\_p2. * (channel.2) + Det2\_p1. * channel + Det2\_p0;$

$\%.....$

$\%...ConvertingEnergytoWavelengthandD - spacing$

$\%...E(joule) = hc/lamba$

$\%....d = lambda/2sin(theta)$

$E\_joule\_1 = E\_1. * 1.60218e - 16;$

$E\_joule\_2 = E\_2. * 1.60218e - 16;$

$l\_1 = const.h * const.c./E\_joule\_1;$

$l\_2 = const.h * const.c./E\_joule\_2;$

$d\_1 = l\_1./2./sin(deg2rad(Det1\_ToA/2))./1E - 10;$

$d\_2 = l\_2./2./sin(deg2rad(Det2\_ToA/2))./1E - 10;$

$iftimeSeq == 0$

$\%.....$

$\%...ExportingDatatoExcel$

$xlswrite(outputfName, d\_1, 'd - Spacing - detector1');$

$xlswrite(outputfName, d\_2, 'd - Spacing - detector2');$

$xlswrite(outputfName, E\_1, 'energy - detector1');$

$xlswrite(outputfName, E\_2, 'energy - detector2');$

$xlswrite(outputfName, intensity\_det1, 'intensity - detector1');$

$xlswrite(outputfName, intensity\_det2, 'intensity - detector2');$

%.....

%...Plotting for single measurement

$for i = 1 : nSteps$

$figure(1)$

$plot(d\_1(:,i), intensity\_det1(:,i) + (800 * (i-1)))$

$xlim([1\ 4])$

$hold on$

%hold on

$figure(2)$

$semilogx(d\_2(:,i), intensity\_det2(:,i) + (200 * (i-1)))$

$xlim([1\ 3])$

$hold on$

end

$else$

$for i = 1 : nTime$

%.....

%...Exporting Data to Excel

$xlswrite(outputfName, d\_1(:,:,i), sprintf('d - Spacing - detector1 - tStep\%1d', i));$

$xlswrite(outputfName, d\_2(:,:,i), sprintf('d - Spacing - detector2 - tStep\%1d', i));$

$xlswrite(outputfName, E\_1(:,:,i), sprintf('energy - detector1 - tStep\%1d', i));$

$xlswrite(outputfName, E\_2(:,:,i), sprintf('energy - detector2 - tStep\%1d', i));$

$xlswrite(outputfName, intensity\_det1(:,:,i), sprintf('intensity - detector1 - tStep\%1d', i));$

$xlswrite(outputfName, intensity\_det2(:,:,i), sprintf('intensity - detector2 - tStep\%1d', i));$

end

end

$result = 'done'$

$\%surface(d\_1, tStep, intensity\_det1)$

1.12 Peak Fitting of Energy Dispersive X-Ray Diffraction Dataset

%.....

%

%...EDD Filtered Data Set Peak Fitting Analysis

%...Inks and Interfaces Laboratory

%...March 2019

%...Marm Dixit

%...GNU Terry Pratchett

%...Outputs Images and Excel File with analyzed data set

%.....

%

clc;

clear all;

close all;

%.....

%

const.h = 6.626E-34; % Planck's constant

const.c = 299792458; %Speed of light in vacuum

%.....

%

%...User Inputs

%...Enter file name for excel sheet with EDD results

work = 0; %...Use 0 for Windows and 1 for Ubuntu

if work == 1

$outputfDir = '/media/inkslab/DATA/6-BM/EDDData/S4\_Cycle2/PeakFitting/';$

$outputfName = '/media/inkslab/DATA/6-BM/EDDData/S4\_Cycle2/PeakFitting/S4\_Cycle2\_PeakFitting';$

%fileName = {'/media/inkslab/DATA/6 - BM/EDDData/sam04_charging_c3/
sam04_charging_c3_Analzed.xlsx',...
%'/media/inkslab/DATA/6 - BM/EDDData/sam04_charging_c32_1/
sam04_charging_c32_1_Analzed.xlsx',...
%'/media/inkslab/DATA/6 - BM/EDDData/sam04_discharging_c32_1/
sam04_discharging_c32_1_Analzed.xlsx',...
%'/media/inkslab/DATA/6 - BM/EDDData/sam04_discharging_c32_2/
sam04_discharging_c32_2_Analzed.xlsx'};
fileName = {'/media/inkslab/DATA/6 - BM/EDDData/sam04_charging_c2/
sam04_charging_c2_Analzed.xlsx',...
'/media/inkslab/DATA/6 - BM/EDDData/sam04_charged_c2/
sam04_charged_c2_Analzed.xlsx'};
%'/media/inkslab/DATA/6 - BM/EDDData/sam04_discharging_c2/
sam04_discharging_c2_Analzed.xlsx',...
%'/media/inkslab/DATA/6 - BM/EDDData/sam04_discharged_c2/
sam04_discharged_c2_Analzed.xlsx'};
%fileName = {'/media/inkslab/DATA/6 - BM/EDDData/sam04_charging_c4_1/
sam04_charging_c4_1_Analzed.xlsx',...
%'/media/inkslab/DATA/6 - BM/EDDData/sam04_charging_c4_2/
sam04_charging_c4_2_Analzed.xlsx',...
%'/media/inkslab/DATA/6 - BM/EDDData/sam04_discharging_c4_2/
sam04_discharging_c4_2_Analzed.xlsx',...
%'/media/inkslab/DATA/6 - BM/EDDData/sam04_discharging_c4_2/
sam04_discharging_c4_2_Analzed.xlsx'};
else
%fileName = {'/media/inkslab/DATA/6 - BM/EDDData/sam04_charging_c3/
sam04_charging_c3_Analzed.xlsx',...

%'/media/inkslab/DATA/6 − BM/EDDData/sam04_charging_c32_1/
sam04_charging_c32_1_Analzed.xlsx',...
%'/media/inkslab/DATA/6 − BM/EDDData/sam04_discharging_c32_1/
sam04_discharging_c32_1_Analzed.xlsx',...
%'/media/inkslab/DATA/6 − BM/EDDData/sam04_discharging_c32_2/
sam04_discharging_c32_2_Analzed.xlsx'};
fileName = {'D :\6-BM\EDDData\sam04_charging_c4_1/
sam04_charging_c4_1_Analzed.xlsx',...
'D :\6-BM\EDDData\sam04_charging_c4_2/
sam04_charging_c4_2_Analzed.xlsx',...
'D :\6-BM\EDDData\sam04_discharging_c4_1/
sam04_discharging_c4_1_Analzed.xlsx',...
'D :\6-BM\EDDData\sam04_discharging_c4_2/
sam04_discharging_c4_2_Analzed.xlsx'};
%fileName = {'/media/inkslab/DATA/6 − BM/EDDData/sam04_charging_c4_1/
sam04_charging_c4_1_Analzed.xlsx',...
%'/media/inkslab/DATA/6 − BM/EDDData/sam04_charging_c4_2/
sam04_charging_c4_2_Analzed.xlsx',...
%'/media/inkslab/DATA/6 − BM/EDDData/sam04_discharging_c4_2/
sam04_discharging_c4_2_Analzed.xlsx',...
%'/media/inkslab/DATA/6 − BM/EDDData/sam04_discharging_c4_2/
sam04_discharging_c4_2_Analzed.xlsx'};
end

fori = 1 : length(fileName)
[∼,Names]=xlsfinfo(fileName{i});
sheetNames{:,i} = Names;

$tSteps(i) = (length(sheetNames\{:,i\}) - 1)/6;$

$for j = 1 : tSteps(i)$

$d1\{:,:,j,i\} = xlsread(fileName\{i\},string(sheetNames\{:,i\}(6*(j-1)+2)));$

$d2\{:,:,j,i\} = xlsread(fileName\{i\},string(sheetNames\{:,i\}(6*(j-1)+3)));$

$i1\{:,:,j,i\} = xlsread(fileName\{i\},string(sheetNames\{:,i\}(6*(j-1)+6)));$

$i2\{:,:,j,i\} = xlsread(fileName\{i\},string(sheetNames\{:,i\}(6*(j-1)+7)));$

end

end

%...*ReadData*

%

[m,n]=size(d1{:,:,1,1});

%

for i =1:length(fileName)

$for a = 1 : tSteps(i)$

$for b = 1 : n$

$alpha = 0.20;$

$i1\_filt\{:,:,a,i\}(:,b) = filter(alpha,$[1 alpha-1], i1{:,:,a,i}(:,b));%sgolayfilt(i1{:,:,a}(:,b),5,9);

$alpha = 0.1;$

$i2\_filt\{:,:,a,i\}(:,b) = filter(alpha,$[1 alpha-1], i2{:,:,a,i}(:,b));%sgolayfilt(i2{:,:,a}(:,b),5,9);

end

end

end

$r = 1;$

$for p = 1 : length(fileName)$

$for q = 1 : tSteps(p)$

$i1\_appended(:,:,r) = i1\_filt\{:,:,q,p\};$

$i2\_appended(:,:,r) = i2\_filt\{:,:,q,p\};$

$r = r + 1;$

end

end

$index1 = find((d1\{:,:,1,1\}(:,1) < 4));\%d - spacingrangesupto4angstorm$

$index2 = find((d2\{:,:,1,1\}(:,1) < 4));$

$Det1\_x = d1\{:,:,1\}(index1(1) : end,1);$

$Det2\_x = d2\{:,:,1\}(index2(1) : end,1);$

$y1 = zeros(length(Det1\_x),1);$

$y2 = zeros(length(Det2\_x),1);$

$i1\_final = i1\_appended(index1(1) : end,:,:);$

$i2\_final = i2\_appended(index2(1) : end,:,:);$

[t,u,v]=size(i1_final);

Size = [size(i1_final) size(i2_final)];

% [w,x,y]=size(i2_final);

xlswrite(outputfName,Size,'Sheet1');

for i = 1:u

$forp = 1 : v$

$A = figure();$

$plot(Det1\_x, i1\_final(:,i,p));$

$x = flipud(Det1\_x);$

$y = flipud(i1\_final(:,i,p));$

$B = figure();$

$findpeaks(y,x,'MinPeakWidth',.1e-1,'MinPeakProminence',7);$

[PKS,LOCS,W,P]=findpeaks(y,x,'MinPeakWidth',.1e-1,'MinPeakProminence',7);

$xlswrite(outputfName,PKS,sprintf('Peaks-Det1-Step\%1d-Tstep\%d',i,p));$

$xlswrite(outputfName,LOCS,sprintf('Location-Det1-Step\%1d-Tstep\%d',i,p));$

$xlswrite(outputfName,W,sprintf('Width-Det1-Step\%1d-Tstep\%d',i,p));$

$xlswrite(outputfName,P,sprintf('Prominence-Det1-Step\%1d-Tstep\%d',i,p));$

$saveas(A,strcat(outputfDir,sprintf('RawData-Det1-Step\%d-Tstep\%d.jpg',i,p)))$

$saveas(B,strcat(outputfDir,sprintf('PeakFit-Det1-Step\%d-Tstep\%d.jpg',i,p)))$

$C=figure();$

$plot(Det2\_x,i2\_final(:,i,p));$

$x=flipud(Det2\_x);$

$y=flipud(i2\_final(:,i,p));$

$D=figure();$

$findpeaks(y,x,'MinPeakWidth',.1e-1,'MinPeakProminence',3);$

[PKS,LOCS,W,P]=findpeaks(y,x,'MinPeakWidth',.1e-1,'MinPeakProminence',3);

$xlswrite(outputfName,PKS,sprintf('Peaks-Det2-Step\%1d-Tstep\%d',i,p));$

$xlswrite(outputfName,LOCS,sprintf('Location-Det2-Step\%1d-Tstep\%d',i,p));$

$xlswrite(outputfName,W,sprintf('Width-Det2-Step\%1d-Tstep\%d',i,p));$

$xlswrite(outputfName,P,sprintf('Prominence-Det2-Step\%1d-Tstep\%d',i,p));$

$saveas(C,strcat(outputfDir,sprintf('RawData-Det2-Step\%d-Tstep\%d.jpg',i,p)))$

$saveas(D,strcat(outputfDir,sprintf('PeakFit-Det2-Step\%d-Tstep\%d.jpg',i,p)))$

closeall

end

end

1.13 EDD Strain Calculator

%.....

%

%...EDD Peak Fitted Data Strain Calculation

%...Inks and Interfaces Laboratory

%...May 2019

%...Marm Dixit

%...GNU Terry Pratchett

%...Outputs Images and Excel File with analyzed data set

%.....

%

clc;

clear all;

close all;

%.....

%

const.h = 6.626E-34; % Planck's constant

const.c = 299792458; %Speed of light in vacuum

%.....

%

%...User Inputs

%...Enter file name for excel sheet with EDD results

work = 0; %...Use 0 for Windows and 1 for Ubuntu

if work == 0

$%outputfDir = '/media/inkslab/DATA/6-BM/EDDData/S4\_Cycle2/StrainCalc/';$

$%fName = '/media/inkslab/DATA/6-BM/EDDData/S4\_Cycle2/PeakFitting/$

```
S4_Cycle2_PeakFitting';
outputfDir =' D :\EDXRD\S2_PeakFits\';
fName =' D :\EDXRD\EDDData\S2_AllCycles\PeakFitting\S2_AllCycles_PeakFitting.xlsx';

else
outputfDir =' /media/inkslab/DATA/6 - BM/EDDData/S4_Cycle2/StrainCalc/';
fName =' /media/inkslab/DATA/6 - BM/EDDData/S4_Cycle2/PeakFitting/
S4_Cycle2_PeakFitting';
end

size1 = xlsread(fName,' Sheet1',' A1 : C1');
size2 = xlsread(fName,' Sheet1',' D4 : F1');


fori = 1 : size1(2)

forp = 1 : size1(3)

loc1{:,i,p} = xlsread(fName,sprintf('Location - Det1 - Step%1d - Tstep%d',i,p));
width1{:,i,p} = xlsread(fName,sprintf('Width - Det1 - Step%1d - Tstep%d',i,p));

end

end

fori = 1 : size2(2)
```

$for p = 1 : size2(3)$

$loc2\{:,i,p\} = xlsread(fName, sprintf('Location - Det2 - Step\%1d - Tstep\%d', i, p));$
$width2\{:,i,p\} = xlsread(fName, sprintf('Width - Det2 - Step\%1d - Tstep\%d', i, p));$

end

end

$llzto = [3.46\ 3.24\ 2.89\ 2.64\ 2.36\ 2.100\ 2.04\ 1.79\ 1.44];$

for i = 1:size1(2)

$for p = 1 : size1(3)$

$fig = figure(i);$
$scatter(loc1\{:,i,p\}, zeros(length(loc1\{:,i,p\}),1) + p);$
$holdon$

$if p == 1$
$for r = 1 : length(loc1\{:,i,8\})$
$plot([\text{loc1\{:,i,8\}(r) loc1\{:,i,8\}(r)}],[0\ \text{size1(3)}],'-')$
end
end
end
$saveas(fig, strcat(outputfDir, sprintf('PeakMap - Det1 - Step\%d.jpg', i)))$
$saveas(fig, strcat(outputfDir, sprintf('PeakMap - Det1 - Step\%d.fig', i)))$

```
%closeall
end

fori = 1 : size2(2)

forp = 1 : size2(3)

fig = figure(i);
scatter(loc2{:,i,p},zeros(length(loc2{:,i,p}),1) + p);
holdon

ifp == 1
forr = 1 : length(loc2{:,i,8})
plot([loc2{:,i,8}(r) loc2{:,i,8}(r)],[0 size2(3)],'–')
end
end
end
saveas(fig,strcat(outputfDir,sprintf('PeakMap − Det2 − Step%d.jpg',i)))
saveas(fig,strcat(outputfDir,sprintf('PeakMap − Det2 − Step%d.fig',i)))
end
```

REFERENCES

Adair K. R., Banis M. N., Zhao Y., Bond T., Li R., Sun X., 2020, Advanced Materials, 2002550, 2002550

Adeli P., Bazak J. D., Park K. H., et al., 2019, Angewandte Chemie International Edition, 58, 26, 8681

Agency E. P., 2020, Inventory of U.S. greenhouse gas emissions and sinks: 1990-2009, Tech. Rep. 36

Aguesse F., Manalastas W., Buannic L., et al., 2017, ACS Apllied Materials & Interfaces, 9, 4, 3808

Åhman M., Nilsson L. J., Johansson B., 2017, Climate Policy, 17, 5, 634

Al-Amleh B., Lyons K., Swain M., 2010, Journal of oral rehabilitation, 37, 8, 641

Armstrong R. D., Dickinson T., Turner J., 1974, Electrochimica Acta, 19, 5, 187

Athanasiou C. E., Jin M. Y., Ramirez C., Padture N. P., Sheldon B. W., 2020, Matter, 3, 1, 212

Bae J., Li Y., Zhang J., et al., 2018, Angewandte Chemie - International Edition, 57, 8, 2096

Bak S. M., Shadike Z., Lin R., Yu X., Yang X. Q., 2018, NPG Asia Materials, 10, 7, 563

Ban X., Zhang W., Chen N., Sun C., 2018, Journal of Physical Chemistry C, 122, 18, 9852

Barai P., Higa K., Srinivasan V., 2017, Physical Chemistry Chemical Physics, 19, 31, 20493

Barroso-Luque L., Tu Q., Ceder G., 2020, Journal of The Electrochemical Society, 167, 2, 020534

Bartsch T., Kim A. Y., Strauss F., et al., 2019, Chemical Communications, 55, 75, 11223

Bartsch T., Strauss F., Hatsukade T., et al., 2018, ACS Energy Letters, 3, 10, 2539

Basak S., Basak S., Migunov V., et al., 2020, ACS Applied Energy Materials, 3, 6, 5101

Berner E. K., Berner R. A., 2012, Global Environment: Water, Air, and Geochemical Cycles, Princeton University Press

Besli M. M., Xia S., Kuppan S., et al., 2019, Chemistry of Materials, 31, 2, 491

Bhamidipati K., Didari S., Harris T. A. L., 2012, Chemical Engineering Science, 80, 195

Billaud J., Bouville F., Magrini T., Villevieille C., Studart A. R., 2016, Nature Energy, 1, 8

Billimoria S., Guccione L., Henchen M., Louis-Prescott L., 2018, Rocky Mountain Institute

Bloomberg, 2017, Lithium-ion Battery Costs and Market, Tech. rep.

Bolsen T., Leeper T. J., Shapiro M. A., 2014, American Politics Research, 42, 1, 65

Bonnick P., Niitani K., Nose M., Suto K., Arthur T. S., Muldoon J., 2019, Journal of Materials Chemistry A, 7, 42, 24173

Boyd S., 2018, Journal of The Electrochemical Society, 165, 16, A3732

Brandt K., Laman F. C., 1989, Journal of Power Sources, 25, 265

Brissot C., Rosso M., Lascaud S., 1999, J. Power Sources, 81, 925

Broek J. V. D., Afyon S., Rupp J. L. M., 2016, Advanced Energy Materials, 6, 1

Bruce P. G., Vincent C. A., 1993, Journal of the Chemical Society, Faraday Transactions, 89, 17, 3187

Bruck A. M., Wang L., Brady A. B., et al., 2019, J. Phys. Chem. C

Bruggeman D. A. G., 1937, Annalen der Physik, 421, 2, 160

Bucci G., Swamy T., Chiang Y.-m., Carter W. C., 2017, Journal of Materials Chemistry A, 5, 19422

Buschmann H., Dolle J., Berendts S., et al., 2011, Physical Chemistry Chemical Physics, 13, 43, 19378

Cai L., Zhao-Yin W., Kun R., 2015, Journal of Inorganic Materials, 30, 9, 995

Cao Y., 2001, Engineering Failure Analysis, 8, 4, 325

Carlo F. D., Xiao X., Jacobsen C., 2014, Journal of Synchrotron Radiation, 21, 1188

Carniglia S. C., 1972, Journal of the American Ceramic Society, 55, 12, 610

Chai H., 2015, International Journal of Solids and Structures, 54, 12

Chai H., Lawn B. R., 2007, Int. J. Fract., 145, 2, 159

Chang H. J., Trease N. M., Ilott A. J., et al., 2015, J. Phys. Chem. C, 119, 29, 16443

Chen C.-F., Verma A., Mukherjee P. P., 2017, Journal of The Electrochemical Society, 164, 11, E3146

Chen J., Thapa A. K., Berfield T. A., 2014, Journal of Power Sources, 271, 406

Chen L., Li Y., Li S. P., Fan L. Z., Nan C. W., Goodenough J. B., 2018, Nano Energy, 46, 176

Chen X. C., Liu X., Samuthira Pandian A., Lou K., Delnick F. M., Dudney N. J., 2019, ACS Energy Letters, 4, 1080

Chen Y., Wang Z., Li X., et al., 2020, Nature, 578, February, 251–255

Cheng E. J., Sharafi A., Sakamoto J., 2017a, Electrochimica Acta, 223, 85

Cheng L., Chen W., Kunz M., et al., 2015, ACS Applied Materials & Interfaces, 7, 3, 2073

Cheng L., Crumlin E. J., Chen W., et al., 2014, Physical Chemistry Chemical Physics, 16, 18294

Cheng S. H. S., He K. Q., Liu Y., et al., 2017b, Electrochimica Acta, 253, 430

Cheng X.-b., Zhao C.-z., Yao Y.-x., Liu H., Zhang Q., 2019, Chem, 5, 1, 74

Choi K. H., Ahn D. B., Lee S. Y., 2018, ACS Energy Letters, 3, 1, 220

Choi S., Davenport T. C., Haile S. M., 2019, Energy and Environmental Science, 12, 1, 206

Choong Z. J., Huo D., Degenaar P., O'Neill A., 2019, Journal of Manufacturing Processes, 38, 93

Chung D. W., Ebner M., Ely D. R., Wood V., Edwin García R., 2013, Modelling and Simulation in Materials Science and Engineering, 21, 7

Conder J., Marino C., Novák P., Villevieille C., 2018, Journal of Materials Chemistry A, 6, 8, 3304

Cooper S. J., Bertei A., Shearing P. R., Kilner J. A., Brandon N. P., 2016, SoftwareX, 5, 203

Culver S. P., Koerver R., Krauskopf T., Zeier W. G., 2018, Chem. Mater., 30, 4179

Danilov D. L., Chen C., Jiang M., Eichel R. A., Notten P. H., 2020, Radiation Effects and Defects in Solids, 175, 3-4, 367

David I. N., Thompson T., Wolfenstine J., Allen J. L., Sakamoto J., 2015, Journal of the American Ceramic Society, 98, 4, 1209

Dawson J. A., Canepa P., Famprikis T., Masquelier C., Islam M. S., 2018, Journal of the American Chemical Society, 140, 1, 362

Deka M., Kumar A., 2011, Journal of Power Sources, 196, 3, 1358

Diederichsen K. M., McShane E. J., McCloskey B. D., 2017, ACS Energy Letters, acsenergylett.7b00792

Ding X., Liu J., 2016, AIChE Journal, 62, 7, 2508

Dixit M., Harkey B., Shen F., Hatzell K. B., 2018a, Journal of the Electrochemical Society, 165, 5, F1

Dixit M. B., Moreno D., Xiao X., Hatzell M. C., Hatzell K. B., ????, 1–9

Dixit M. B., Regala M., Shen F., Xiao X., Hatzell K. B., 2018b, ACS Applied Materials & Interfaces, 11, 2022

Dixit M. B., Zaman W., Hortance N., et al., 2020, Joule, 4, 1, 207

Doux J. M., Nguyen H., Tan D. H., et al., 2020, Advanced Energy Materials, 10, 1

Dowd B. A., Campbell G. H., Marr R. B., et al., 1999, , September 1999, 224

Doyle M., Fuller T. F., Newman J., 1994, Electrochimica Acta, 39, 13, 2073

Doyle M., Newman J., 1996, Journal of The Electrochemical Society, 143, 6, 1890

Ebner M., Geldmacher F., Marone F., Stampanoni M., Wood V., 2013, Advanced Energy Materials, 3, 7, 845

Ebner M., Wood V., 2014, Journal of the Electrochemical Society, 162, 2, A3064

El-Shinawi H., Paterson G. W., MacLaren D. A., Cussen E. J., Corr S. A., 2017, J. Mater. Chem. A, 5, 1, 319

Endrizzi M., 2018, Nuclear Instruments and Methods in Physics Research, Section A: Accelerators, Spectrometers, Detectors and Associated Equipment, 878, 88

Energy D. o., 2015, Roll to Roll Processing Technology Assessment, Tech. rep.

Famprikis T., Canepa P., Dawson J. A., Islam M. S., Masquelier C., 2019, Nature Materials, 18, 12, 1278

Fan L., Wei S., Li S., Li Q., Lu Y., 2018, Advanced Energy Materials, 1702657, 1

Ferguson T. R., Bazant M. Z., 2012, Journal of The Electrochemical Society, 159, 12, A1967

Finegan D. P., Vamvakeros A., Tan C., et al., 2020, Nature Communications, 11, 1, 631

Flatscher F., Philipp M., Ganschow S., Wilkening H. M. R., Rettenwander D., 2020, Journal of Materials Chemistry A, 8, 15782

Freiberg A. T. S., Siebel A., Berger A., et al., 2018, The Journal of Physical Chemistry C, 122, 10, 5303

Frenck L., Sethi G. K., Maslyn J. A., Balsara N. P., 2019, Frontiers in Energy Research, 7, 115

Fu C., Venturi V., Kim J., et al., 2020, Nature Materials

Fu K. K., Gong Y., Dai J., et al., 2016, Proceedings of the National Academy of Sciences, 113, 26, 7094

Garcia-Mendez R., Mizuno F., Zhang R., Arthur T. S., Sakamoto J., 2017, Electrochimica Acta, 237, 144

Ghosh A., Wang C., Kofinas P., 2010, J. Electrochem. Soc., 846–849

Glazer M. P., Cho J., Almer J., Okasinski J., Braun P. V., Dunand D. C., 2015, Advanced Energy Materials, 5, 14, 1

Goda T., Sasaki Y., Mizuno M., Morizawa K., Katakura H., Tomiya S., 2017, Journal of Coatings Technology and Research, 14, 5, 1053

Goonetilleke D., Sharma N., Kimpton J., Galipaud J., Pecquenard B., Le Cras F., 2018, Frontiers in Energy Research, 6, July, 1

Gowrishankar V., Levin A., 2017, Natural Resources Defense Council, , September

Granqvist C. G., Hunderi O., 1978, Physical Review B, 18, 4, 1554

Groeber M. A., Jackson M. A., 2014, Integrating Materials and Manufacturing Innovation, 3, 5

Gürsoy D., De Carlo F., Xiao X., Jacobsen C., 2014, Journal of Synchrotron Radiation, 21, 5, 1188

Haas R., Pompe C., Osenberg M., Manke I., Maitra U., Langsdorf D., 2019, Energy Technology, 7, 1801146

Han F., Westover A. S., Yue J., et al., 2019, Nature Energy, 4, 3, 187

Han F., Yue J., Chen C., et al., 2018, Joule, 2, 3, 497

Han F., Zhu Y., He X., Mo Y., Wang C., 2016, 18th International Meeting on Lithium Batteries, 12, 1727863, 4

Han G. H., Lee S. H., Ahn W. G., Nam J., Jung H. W., 2014, Journal of Coatings Technology Research, 11, 1, 19

Han X., Gong Y., Fu K., et al., 2017, Nature Materials, 16, 5, 572

Hao F., Mukherjee P. P., 2018, Journal of The Electrochemical Society, 165, 9, A1857

Hapuarachchi S. N. S., Sun Z., Yan C., 2018, Advanced Sustainable Systems, 1700182, 1700182

Harley C. D., 2011, Science, 334, 6059, 1124

Harry K. J., Hallinan D. T., Parkinson D. Y., MacDowell A. A., Balsara N. P., 2014, Nature Materials, 13, 1, 69

Hartmann P., Leichtweiss T., Busche M. R., et al., 2013, J. Phys. Chem. C, 117, 41, 21064

Hatzell K. B., Chen X. C., Cobb C., et al., 2020, ACS Energy Letters, 5, 922

Hatzell K. B., Eller J., Morelly S. L., Tang M. H., Alvarez N. J., Gogotsi Y., 2017, Faraday Discussions, 199, 511

Hatzor Y. H., Palchik V., 1997, International Journal of Rock Mechanics and Mining Sciences, 34, 5, 805

Hayashi A., Tatsumisago M., 2018, Journal of the Ceramic Society of Japan, 126, 9, 719

Heider U., Oesten R., Jungnitz M., 1999, Journal of Power Sources, 81-82, 119

Hildebrand T., Rüegsegger P., 1997, Journal of Microscopy, 185, 1, 67

Hiratani M., Miyauchi K., Kudo T., 1988, Solid State Ionics, 28-30, PART 2, 1406

Hlushkou D., Reising A. E., Kaiser N., et al., 2018, Journal of Power Sources, 396, February, 363

Howard M., 2018, Electric Power Research Institute, , April

Howell D., Cunningham B., Duong T., Faguy P., 2016, 24

Huang J., Li Z., Zhang J., 2017, Frontiers in Energy, 11, pages334–364

Huang X., Lu Y., Jin J., et al., 2018, ACS Applied Materials & Interfaces, 10, 1727863, 17147

Huang X., Lu Y., Song Z., Xiu T., Badding M. E., Wen Z., 2019, Journal of Energy Chemistry, 39, 8

Huie M. M., Bock D. C., Zhong Z., et al., 2017, Journal of The Electrochemical Society, 164, 1, A6007

Hyung S., Jung H., Kyung B., Jo S., Wook H., Chun J., 2011, Chemical Engineering Science, 66, 21, 4953

Ishiguro K., Nemori H., Sunahiro S., et al., 2014, Journal of The Electrochemical Society, 161, 5, A668

Jackson R. B., Le Quéré C., Andrew R. M., et al., 2018, Environmental Research Letters, 13, 12

Jacquet J., Jamieson D., 2016, Nature Climate Change, 6, 7, 643

Jana A., García R. E., 2017, Nano Energy, 41, July, 552

Janek J., Zeier W. G., 2016, Nature Energy, 1, 16141

Jena A., Meesala Y., Hu S.-F., Chang H., Liu R.-S., 2018, ACS Energy Letters, 3, acsenergylett.8b01564

Jin G. L., Ahn W.-g., Kim S. J., Nam J., Jung H. W., Hyun J. C., 2016, 28, May, 159

Jow T. R., Liang C. C., 1983, Solid State Ionics, 10, 695

Kaiser N., Spannenberger S., Schmitt M., Cronau M., Kato Y., Roling B., 2018, Journal of Power Sources, 396, April, 175

Kanno R., Hata T., Kawamoto Y., Irie M., 2000, Solid State Ionics, 130, 1-2, 97

Kanno R., Murayama M., 2001, J. Electrochem. Soc., 148, 7, A742

Kasemchainan J., Peter G., 2018, Johnson Matthey Technology Review, 2, 2, 177

Kasemchainan J., Zekoll S., Spencer Jolly D., et al., 2019, Nature Materials, 18, 1105–1111

Kato Y., Shiotani S., Morita K., Suzuki K., Hirayama M., Kanno R., 2018, Journal of Physical Chemistry Letters, 9, 3, 607

Kawasoko H., Shirasawa T., Shiraki S., et al., 2020, ACS Applied Energy Materials, 3, 2, 1358

Kazyak E., Garcia-Mendez R., LePage W. S., et al., 2020, Matter, 2, 4, 1025

Ke X., Wang Y., Dai L., Yuan C., 2020a, Energy Storage Mater., 33, 309

Ke X., Wang Y., Dai L., Yuan C., 2020b, Energy Storage Mater., 33, 309

Kehrwald D., Shearing P. R., Brandon N. P., Sinha P. K., Harris S. J., 2011, Journal of The Electrochemical Society, 158, 12, A1393

Keller M., Varzi A., Passerini S., 2018, Journal of Power Sources, 392, April, 206

Kerman K., Luntz A., Viswanathan V., Chiang Y.-M., Chen Z., 2017, Journal of The Electrochemical Society, 164, 7, A1731

Khounsary A., Kenesei P., Collins J., Navrotski G., Nudell J., 2013, Journal of Physics: Conference Series, 425, 21, 212015

Kim S. U., Srinivasan V., 2016, Journal of the Electrochemical Society, 163, 14, A2977

Kimura Y., Fakkao M., Nakamura T., et al., 2020, ACS Applied Energy Materials, 3, 7782–7793

Kirshenbaum K. C., Bock D. C., Brady A. B., Marschilok A. C., Takeuchi K. J., Takeuchi E. S., 2015, Physical Chemistry Chemical Physics, 17, 11204

Klinsmann M., Hildebrand F. E., Ganser M., McMeeking R. M., 2019, Journal of Power Sources, 442, September, 227226

Kodama M., Komiyama S., Ohashi A., Horikawa N., Kawamura K., Hirai S., 2020, Journal of Power Sources, 462

Koerver R., Aygu I., Leichtweiß T., et al., 2017

Koerver R., Zhang W., De Biasi L., et al., 2018, Energy and Environmental Science, 11, 8, 2142

Krauskopf T., Hartmann H., Richter F. H., et al., 2019

Kurfer J., Westermeier M., Tammer C., Reinhart G., 2012, CIRP Annals - Manufacturing Technology, 61, 1

Lacaille V., Morel C., Feulvarch E., Kermouche G., Bergheau J. M., 2014, Computational Materials Science, 95, 187

Lagadec M. F., Ebner M., Zahn R., Wood V., 2016, J. Electrochem. Soc., 163, 6, A992

Lagadec M. F., Zahn R., Wood V., 2018, J. Electrochem. Soc., 165, 9, A1829

Landauer R., 1952, Journal of Applied Physics, 23, 7, 779

Landesfeind J., Ebner M., Eldiven A., Wood V., Gasteiger H. A., 2018a, J. Electrochem. Soc., 165, 3, A469

Landesfeind J., Eldiven A., Gasteiger H. A., 2018b, J. Electrochem. Soc., 165, 5, A1122

Langer F., Bardenhagen I., Glenneberg J., Kun R., 2016, Solid State Ionics, 291, 8

Larson J. M., Gillette E., Burson K., Wang Y., Lee S. B., Reutt-Robey J. E., 2018, Science Advances, 4, 6, 1

Lau J., DeBlock R. H., Butts D. M., Ashby D. S., Choi C. S., Dunn B. S., 2018, Advanced Energy Materials, 8, 27, 1

Leahy R. M., Clackdoyle R., Noo F., 2009, in The Essential Guide to Image Processing, 741–776

Lee Y. W., Ahn W.-g., Nam J., Jung H. W., Hyun J. C., 2017, Rheologica Acta, 56, 707

Leite M. S., Ruzmetov D., Li Z., et al., 2014, Journal of Materials Chemistry A, 2, 48, 20552

LePage W. S., Chen Y., Kazyak E., et al., 2019, Journal of The Electrochemical Society, 166, 2, A89

Lewis J. A., Javier F., Cortes Q., et al., 2019, ACS Energy Letters, 4, 591

Li H., Li M., Siyal S. H., et al., 2018, Journal of Membrane Science, 555, March, 169

Li J., Johnson G., 2019, Joule, 3, 1, 4

Li Y., Xu B., Xu H., et al., 2017, Angewandte Chemie - International Edition, 56, 3, 753

Lin C.-f., Wang B.-k., Lo S.-h., Wong D. S.-h., Liu T.-j., Tiu C., 2014, Asia-Pacific Journal of Chemical Engineering, 9, 134

Lin F., Liu Y., Yu X., et al., 2017, Chemical Reviews, 13123–13186

Liu D. X., Cao L. R., Co A. C., 2016, Chem. Mater., 28, 556–563

Liu M., Wang C., Cheng Z., et al., 2020, ACS Materials Letters, 665–670

Liu Q., Geng Z., Han C., et al., 2018, Journal of Power Sources, 389, April, 120

Liu S., Imanishi N., Zhang T., et al., 2010, J. Phys. Chem. Lett., 1092–1098

Lotsch B. V., Maier J., 2017, J. Electroceram., 38, 2-4, 128

Løvvik O. M., Vegge T., Wenzel W., Hahlin M., Hartmann S., Latz A., 2019, Deliverable 2.1 BATTERY 2030+ Roadmap, Tech. rep.

Lu C., Danzer R., Fischer F. D., 2004, Journal of the European Ceramic Society, 24, 14, 3643

Lu Y., Meng X., Alonso J., Fernández-Díaz M. T., Sun C., 2018, ACS Applied Materials & Interfaces, 11, 2042–2049

Lu Y.-C., Crumlin E. J., Veith G. M., et al., 2012, Scientific Reports, 2, 1, 715

Luo W., Gong Y., Zhu Y., et al., 2016, Journal of the American Chemical Society, 138, 37, 12258

Ma C., Cheng Y., Yin K., et al., 2016, Nano letters, 16, 11, 7030

Ma J., Chen B., Wang L., Cui G., 2018, Journal of Power Sources, 392, 189, 94

Mai T. T., Jadun P., Logan J. S., et al., 2018, National Renewable Energy Laboratory, 151

Mai W., Yang M., Soghrati S., 2019, Electrochimica Acta, 294, 192

Manthiram A., Yu X., Wang S., 2017, Nature Reviews Materials, 2, 4

Marbella L. E., Zekoll S., Kasemchainan J., Emge P., Bruce P. G., Grey C. P., 2019, Chemistry of Materials, 31, 8, 2762

Marschilok A. C., Bruck A. M., Abraham A., et al., 2020, Phys. Chem. Chem. Phys., 22,

Maslyn J. A., Frenck L., Loo W. S., Parkinson D. Y., Balsara N. P., 2019, ACS Applied Energy Materials, 2, 11, 8197

Masquelier C., 2011, Nature Materials, 10, 9, 649

Matsuyama T., Deguchi M., Mitsuhara K., et al., 2016, Journal of Power Sources, 313, 104

Maxwell Garnett J. C., 1904, Phil. Trans., 203, 385

Maza D., Carvalho M. S., 2015, AIChE Journal, 61, 5, 1699

Mcbreen J., 2009, Journal of Solid State Electrochemistry, 13, 1051

McCloskey B. D., 2015, Journal of Physical Chemistry Letters, 6, 22, 4581

McGrogan F. P., Swamy T., Bishop S. R., et al., 2017, Advanced Energy Materials, 7, 12, 1602011

Mercier R., Malugani J.-P., Fahys B., Robert G., 1981, Solid State Ionics, 5, 663

Mertens A., Yu S., Schön N., et al., 2017, Solid State Ionics, 309, July, 180

Mistry A., Mukherjee P. P., 2020a, J. Electrochem. Soc., 167, 082510

Mistry A. N., Mukherjee P. P., 2020b, J. Electrochem. Soc., 167, 8, 082510

Mohanty D., Hockaday E., Li J., Hensley D. K., Daniel C., Wood D. L., 2016, Journal of Power Sources, 312, 70

Mohn K., 2018, Economics of Energy and Environmental Policy, 8, 2, 1

Monroe C., Newman J., 2003, Journal of The Electrochemical Society, 150, 10, A1377

Monroe C., Newman J., 2005, Journal of The Electrochemical Society, 152, 2, A396

Munch B., Holzer L., 2008a, Journal of American Ceramics Society, 91, 12, 4059

Munch B., Holzer L., 2008b, Journal of Americal Ceramics Society, 91, 12, 4059

Münch B., Trtik P., Marone F., Stampanoni M., 2009, Optics Express, 17, 10, 8567

Murugan R., Thangadurai V., Weppner W., 2007, Angew. Chem. Int. Ed., 46, 41, 7778

Nadel S., Ungar L., 2019, ACEEE Report, , September

Nakamura M., 1982, Journal of Physics C: Solid State Physics, 15, 23

Nam J., Carvalho M. S., 2009, Journal of Fluid Mechanics, 631, 397

Nan C.-W., Smith D. M., 1991, Materials Science and Engineering: B, 10, 2, 99

Narayan S., Anand L., 2020, Journal of The Electrochemical Society, 167, 4, 040525

Needell Z. A., McNerney J., Chang M. T., Trancik J. E., 2016, Nature Energy, 1, 9

Neumann A., Randau S., Becker-Steinberger K., et al., 2020, ACS Applied Materials and Interfaces, 12, 8, 9277

Newman J., Thomas-Alyea K. E., 2012, Electrochemical Systems, Wiley

Nie K., Hong Y., Qiu J., et al., 2018, Frontiers in Chemistry, 6, 1

Nose M., Kato A., Sakuda A., Hayashi A., Tatsumisago M., 2015, Journal of Materials Chemistry A, 3, 44, 22061

Ohno S., Koerver R., Dewald G., et al., 2019, ChemRxiv

Ohta N., Takada K., Sakaguchi I., et al., 2007, Electrochem. Commun., 9, 7, 1486

O'Rourke C., Morgan B. J., 2018, Physical Review Materials, 2, 4, 1

Oudenhoven J. F., Labohm F., Mulder M., Niessen R. A., Mulder F. M., Notten P. H., 2011, Advanced Materials, 23, 35, 4103

Paganin D., Mayo S. C., Gureyev T. E., Miller P. R., Wilkins S. W., 2002, Journal of Microscopy, 206, 1, 33

Pandian A. S., Chen X. C., Chen J., et al., 2018, Journal of Power Sources, 390, 153

Patra S., Narayanasamy J., Chakravarty S., Murugan R., 2020, ACS Applied Energy Materials, 3, 3, 2737

Paxton W. A., Akdoan E. K., Sąvkliyildiz I., et al., 2015, Journal of Materials Research, 30, 3, 417

Pecher O., Carretero-Gonzalez J., Griffith K. J., Grey C. P., 2017, Chemistry of Materials, 29, 1, 213

Pelt D. M., De Andrade V., 2016, Advanced Structural and Chemical Imaging, 2, 1

Pervez S. A., Cambaz M. A., Thangadurai V., Fichtner M., 2019, ACS Applied Materials and Interfaces, 11, 22029

Pesci F. M., Brugge R. H., Hekselman A. K., Cavallaro A., Chater R. J., Aguadero A., 2018, Journal of Materials Chemistry A, 6, 40, 19817

Pietsch P., Ebner M., Marone F., Stampanoni M., Wood V., 2017, 1

Pietsch P., Ebner M., Marone F., Stampanoni M., Wood V., 2018, Sustainable Energy & Fuels, 2, 598

Porz L., Swamy T., Sheldon B. W., et al., 2017, Advanced Energy Materials, 7, 20, 1701003

Quartarone E., Mustarelli P., 2011, Chemical Society Reviews, 40, 5, 2525

Raj R., Wolfenstine J., 2017, Journal of Power Sources, 343, 119

Randau S., Weber D. A., Kötz O., et al., 2020, Nature Energy, 5, 3, 259

Ren C. E., Hatzell K. B., Alhabeb M., Ling Z., Mahmoud K. A., Gogotsi Y., 2015, Journal of Physical Chemistry Letters, 6, 20, 4026

Rivers M. L., 2012, in Proc. SPIE, vol. 8506, 85060U

Rogora M., Mosello R., Arisci S., 2003, Water, Air, and Soil Pollution, 148, 1-4, 347

Sakuda A., Hayashi A., Tatsumisago M., 2010, Chemistry of Materials, 22, 949

Samanta A., Bera A., Ojha K., Mandal A., 2010, Journal of Chemical and Engineering Data, 55, 10, 4315

Sang L., Bassett K. L., Castro F. C., et al., 2018, Chemistry of Materials, 30, 24, 8747

Santhanagopalan D., Qian D., McGilvray T., et al., 2013, The journal of physical chemistry letters, 5, 2, 298

Schiffer Z. J., Manthiram K., 2017, Joule, 1, 1, 10

Schlenker R., Stpień D., Koch P., et al., 2020, ACS Applied Materials and Interfaces, 12, 17, 20012

Schleussner C. F., Rogelj J., Schaeffer M., et al., 2016, Nature Climate Change, 6, 9, 827

Schmalzried H., Janek J., 1998, Ber. Bunsmges. Phys. Chem, 102, 127

Schneider C. A., Rasband W. S., Eliceiri K. W., 2012a, Nature Methods, 9, 7, 671

Schneider C. A., Rasband W. S., Eliceiri K. W., 2012b, Nature Methods, 9, 7, 671

Schnell J., Günther T., Knoche T., et al., 2018, Journal of Power Sources, 382, December 2017, 160

Seitzman N., Guthrey H., Sulas D. B., Platt H. A. S., Al-Jassim M., Pylypenko S., 2018, Journal of The Electrochemical Society, 165, 16, A3732

Shao C., Paynabar K., Kim T. H., et al., 2013, in Journal of Manufacturing Systems, vol. 32, 550–555

Shao Y., Wang H., Gong Z., et al., 2018, ACS Energy Letters, 3, 6, 1212

Sharafi A., Haslam C. G., Kerns R. D., Wolfenstine J., Sakamoto J., 2017, Journal of Materials Chemistry A, 5, 40, 21491

Sharafi A., Meyer H. M., Nanda J., Wolfenstine J., Sakamoto J., 2016, Journal of Power Sources, 302, 135

Shen F., Dixit M., Xiao X., Hatzell K., 2018, ACS Energy Letters, 3, 4, 1056

Shen H., Yi E., Amores M., et al., 2019, Journal of Materials Chemistry A, 7, 36, 20861

Shen L., Chen Z., 2007, Chemical Engineering Science, 62, 14, 3748

Shi Y., Zhang X., Liu G., 2015, ACS Sustainable Chemistry and Engineering, 3, 9, 2237

Shiraki S., Shirasawa T., Suzuki T., Kawasoko H., Shimizu R., Hitosugi T., 2018, ACS Applied Materials and Interfaces, 10, 48, 41732

Shutthanandan V., Nandasiri M., Zheng J., et al., 2019, Applications of XPS in the characterization of Battery materials

Singh N., Horwath J. P., Bonnick P., et al., 2020, Chemistry of Materials

Spencer Jolly D., Ning Z., Darnbrough J. E., et al., 2020, ACS Applied Materials and Interfaces, 12, 1, 678

Strauss F., Teo J. H., Schiele A., et al., 2020, ACS Applied Materials and Interfaces, 12, 18, 20462

Su J., Huang X., Song Z., et al., 2019, Ceramics International, 45, 12, 14991

Sudo R., Nakata Y., Ishiguro K., et al., 2014, Solid State Ionics, 262, 151

Suk H., Ahn W.-g., Kwon I., Nam J., Wook H., 2016, Chemical Engineering Science, 143, 122

Sun B., Xu C., Mindemark J., Gustafsson T., Edström K., Brandell D., 2015, J. Mater. Chem. A, 3, 26, 13994

Sun C., Liu J., Gong Y., Wilkinson D. P., Zhang J., 2017, Nano Energy, 33, January, 363

Sun F., Osenberg M., Dong K., et al., 2018, ACS Energy Letters, 3, 2, 356

Taiwo O. O., Finegan D. P., Paz-Garcia J. M., et al., 2017, Physical Chemistry Chemical Physics, 19, 33, 22111

Takada K., Nakano S., Inada T., et al., 2003, J. Electrochem. Soc., 150, 3, A274

Tan J., Tiwari A., 2012, Electrochemical and Solid-State Letters, 15, 3, 37

Tang W., Tang S., Zhang C., Ma Q., Xiang Q., Yang Y.-w., 2018, 1800866, 1

Taylor N. J., Stangeland-Molo S., Haslam C. G., et al., 2018, Journal of Power Sources, 396, June, 314

Tenhaeff W. E., Yu X., Hong K., Perry K. A., Dudney N. J., 2011, Journal of the Electrochemical Society, 158, 10, A1143

Thangadurai V., Narayanan S., Pinzaru D., 2014, Chemical Society Reviews, 43, 13, 4714

Thielmann A., Sauer A., Isenmann R., Wietschel M., 2013, Fraunhofer Institute for Systems and Innovation Research ISI, , 1, 32

Thorat I. V., Stephenson D. E., Zacharias N. A., Zaghib K., Harb J. N., Wheeler D. R., 2009, Journal of Power Sources, 188, 2, 592

Tian H.-K., Chakraborty A., Talin A. A., Eisenlohr P., Qi Y., 2020, Journal of The Electrochemical Society, 167, 9, 090541

Tian H. K., Xu B., Qi Y., 2018, Journal of Power Sources, 392, March, 79

Tian Y., Sun Y., Hannah D. C., et al., 2019, Joule, 3, 4, 1037

Tippens J., Miers J. C., Afshar A., et al., 2019, ACS Energy Letters, 4, 6, 1475

Tjaden B., Brett D. J., Shearing P. R., 2018, International Materials Reviews, 63, 2, 47

Tomandl I., Vacik J., Kobayashi T., et al., 2020, Radiation Effects and Defects in Solids, 175, 3-4, 394

Tripathi A. M., Hwang B. J., 2018, Chemical Society Reviews

Tsai C.-L., Roddatis V., Chandran C. V., et al., 2016, ACS Apllied Materials & Interfaces, 8, 16, 10617

Tsuda T., 2010, Journal of the Society of Rheology, 38, 223

Tsukasaki H., Uchiyama T., Yamamoto K., et al., 2019, Journal of Power Sources, 434

Tu Q., Barroso-Luque L., Shi T., Ceder G., 2020, Cell Reports Physical Science, 1, 7, 100106

Ujiie S., Hayashi A., Tatsumisago M., 2012, Solid State Ionics, 211, 42

Ujiie S., Hayashi A., Tatsumisago M., 2013, Journal of Solid State Electrochemistry, 17, 3, 675

Ujiie S., Inagaki T., Hayashi A., Tatsumisago M., 2014, Solid State Ionics, 263, 57

Ulvestad A., Clark J. N., Singer A., et al., 2015, Phys. Chem. Chem. Phys., 17, 16, 10551

United Nations T., 2015, Paris Agreement

Vadakkepatt A., Trembacki B., Mathur S. R., Murthy J. Y., 2016, Journal of The Electrochemical Society, 163, 2, A119

Vardar G., Bowman W. J., Lu Q., et al., 2018, Chemistry of Materials, 30, 6259

Vijayaraghavan B., Ely D. R., Chiang Y.-M., Garcia-Garcia R., Garcia R. E., 2012, Journal of The Electrochemical Society, 159, 5, A548

Walther F., Koerver R., Fuchs T., et al., 2019, Chemistry of Materials, 31, 3745

Wan T. H., Saccoccio M., Chen C., Ciucci F., 2015, Electrochimica Acta, 184, 483

Wan Z., Lei D., Yang W., et al., 2019, Advanced Functional Materials, 29, 1, 1

Wang M., Sakamoto J., 2018, Journal of Power Sources, 377, November 2017, 7

Wang M., Wolfenstine J. B., Sakamoto J., 2019, 296, 842

Wang X., Jiang M., Zhou Z., Gou J., Hui D., 2017, Composites Part B: Engineering, 110, 442

Wang Z., Lee J. Z., Xin H. L., et al., 2016, Journal of Power Sources, 324, 342

Wenzel S., Leichtweiss T., Krüger D., Sann J., Janek J., 2015a, Solid State Ionics, 278, 98

Wenzel S., Metelmann H., Raiß C., Dürr A. K., Janek J., Adelhelm P., 2013, J. Power Sources, 243, 758

Wenzel S., Randau S., Leichtweiß T., et al., 2016a, Chemistry of Materials, 28, 7, 2400

Wenzel S., Randau S., Leichtweiß T., et al., 2016b, Chemistry of Materials, 28, 7, 2400

Wenzel S., Sedlmaier S. J., Dietrich C., Zeier W. G., Janek J., 2018, Solid State Ionics, 318, February 2017, 102

Wenzel V., Nirschl H., Nötzel D., 2015b, Energy Technology, 3, 7, 692

Whitney S., Biegalski S. R., Huang Y. H., Goodenough J. B., 2009, 886–890

Wiemers-Meyer S., Winter M., Nowak S., 2019, in Annual Reports on NMR Spectroscopy, vol. 97, 121–162, Academic Press Inc.

Willmott P., 2011, An Introduction to Synchrotron Radiation: Techniques and Applications, Wiley, Germany

Wu F., Tan G., Chen R., Li L., Xiang J., Zheng Y., 2011, Advanced Materials, 23, 43, 5081

Wu H.-l., Hu L. A., Gewirth A. A., 2015, 7, 1709–1719

Wu X., Billaud J., Jerjen I., et al., 2019, Advanced Energy Materials, 9, 1901547

Xia W. H., Xu B. Y., Duan H. N., et al., 2016, ACS Apllied Materials & Interfaces, 8, 8, 5335

Xiao Y., Wang Y., Bo S.-H., et al., 2020, Nature Reviews Materials, 5, 1, 105

Xu L., Tang S., Cheng Y., et al., 2018, Joule, 2, 10, 1991

Yakubovskiy P., 2019, Segmentation Models, https://github.com/qubvel/segmentation_models

Yamada H., Ito T., Hongahally Basappa R., 2016, Electrochimica Acta, 222, 648

Yamamoto K., Iriyama Y., Asaka T., et al., 2010, Angewandte Chemie - International Edition, 49, 4414

Yang J. F., Ohji T., Kanzaki S., Díaz A., Hampshire S., 2002, Journal of the American Ceramic Society, 85, 6, 1512

Yang T., Zheng J., Cheng Q., Hu Y. Y., Chan C. K., 2017, ACS Applied Materials and Interfaces, 9, 26, 21773

Yonemoto F., Nishimura A., Motoyama M., Tsuchimine N., Kobayashi S., Iriyama Y., 2017, Journal of Power Sources, 343, 207

Yu S., Schmidt R. D., Garcia-Mendez R., et al., 2016, Chemistry of Materials, 28, 1, 197

Yu S., Siegel D. J., 2018, ACS Applied Materials & Interfaces, 10, 38151

Yu X., Manthiram A., 2017, Acc. Chem. Res., 2653

Yulaev A., Oleshko V., Haney P., et al., 2018, Nano Lett.

Zahn R., Lagadec M. F., Hess M., Wood V., 2016, ACS Appl. Mater. Interfaces, 8, 48, 32637

Zaman W., Hortance N., Dixit M. B., De Andrade V., Hatzell K. B., 2019, Journal of Materials Chemistry A, 7, 41, 23914

Zhang J., Hatzell K. B., Hatzell M. C., 2017a, Environmental Science and Technology Letters, 4, 11, 470

Zhang L., Guo X., Huang J., Qu Y., Niu C., Chen Y., 2018, 6, March, 16

Zhang X., Wang Q. J., Harrison K. L., Roberts S. A., Harris S. J., 2020, Cell Reports Physical Science, 1, 2, 100012

Zhang Y., Lee J. J., Srikanth R., Lawn B. R., 2013, Dental Materials, 29, 12, 1201

Zhang Y., Zhang F., Yan Z., Ma Q., Li X., Huang Y., 2017b, Nature Reviews Materials, 2, 17019

Zhang Z., Zhang Q., Shi J., et al., 2017c, Advanced Energy Materials, 7, 4, 1

Zhao Y., Yan J., Cai W., et al., 2019, Energy Storage Materials, , January

Zheng J., Dang H., Feng X., Chien P.-H., Hu Y.-Y., 2017, J. Mater. Chem. A, 5, 18457

Zheng J., Hu Y.-y., 2018, ACS Applied Materials & Interfaces, 10, 4, 4113

Zheng J., Tang M., Hu Y. Y., 2016, Angewandte Chemie - International Edition, 55, 40, 12538

Zhu L., Zhu P., Yao S., Shen X., Tu F., 2019, International Journal of Energy Research, , May, er.4638

Zhu W., Wang Y., Liu D., et al., 2018, Energies, 11, 11, 2963

Zhu Y., He X., Mo Y., 2015, ACS Applied Materials and Interfaces, 7, 42, 23685